

STUDIES OF ION CHANNELLING
AND DECHANNELLING IN DIAMOND

by

ROGER WORSLEY FEARICK

a thesis submitted
to the Faculty of Science,
University of the Witwatersrand, Johannesburg,
for the degree of

DOCTOR OF PHILOSOPHY

May, 1980

ABSTRACT

The dechannelling of protons in diamond has been investigated, in good crystals, in crystals containing high concentrations of defects, and in crystals overlaid with amorphous surface layers. The energy loss of light ions in diamond has also been investigated.

Measurements have been made of the dechannelling in good diamond crystals for the three major axes $\langle 110 \rangle$, $\langle 111 \rangle$ and $\langle 100 \rangle$, at room temperature, over a range in energy of 1.0 MeV to 8.9 MeV, and at 1.0 MeV, at room temperature, at 300 °C and at 600 °C. Measurements are also reported for planar channelling along $\{110\}$, $\{111\}$ and $\{100\}$ at 1.0 MeV and room temperature. The energy dependence of the axial dechannelling is found to scale with a length z_e which depends on electronic scattering; it is concluded that this is the major source of dechannelling in good crystals. The temperature dependence of dechannelling is found to be rather small compared with other crystals. The experimental results are compared with calculations based on the diffusion model. The relative effect of various approximations in the diffusion model is explored.

The effect of surface layers of carbon, gold and aluminium on the 1.0 MeV, $\langle 110 \rangle$, yield, both at the surface and as a function of depth, has been investigated. The yield at the surface is compared with calculations based on Thomas-Fermi multiple scattering theory, with a number of approximations for the yield as a function of angle. The yield calculated with the experimental azimuthal-averaged angular yield is in good agreement with experiment. The yield as a function of depth is

compared with diffusion model calculations, and good agreement is found. Approximations have been derived for the increase in yield due to thin layers, and are found to be in reasonable agreement with experiment. The application of a scaling law for different layers, based on a power-law scattering potential has been investigated and is applied to compensate the aluminium measurements for a small amount of oxygen present in the layer.

Dechannelling by defects, namely platelets and nitrogen aggregates, in Type Ia diamond has been investigated and it is shown that the increase in yield in these diamonds can be explained in terms of the defects known to be present in the diamond from infra-red spectroscopy. Models are derived for the dechannelling effect of stacking faults and of dislocation loops, and are applied to the dechannelling by platelets. The relation between platelets and B-aggregates of nitrogen is considered.

The energy loss, in thin diamond crystals, of 3 to 12 MeV protons, 12 to 18 MeV alpha particles and 24 MeV lithium ions has been measured, both in random and in channelled directions. Results are also reported for the random straggling of protons. For random stopping, the results are in agreement with a recent compilation of stopping data. The ratio of channelled to random stopping-power is compared with the predictions of the theories of Esbensen and Golovchenko and of Dettmann. An expression has been derived for the stopping power of a periodic electron gas and is used to modify the theory of Dettmann. The results suggest that the channelled energy loss is determined in this case by the energy loss in the major plane passing through the axis under study.

I declare that the results presented in this thesis are my own work performed under the supervision of Professor J.P.F. Sellschop.

None of the material has been submitted for a degree at any university.

A handwritten signature in black ink, consisting of a stylized, cursive script that appears to be the initials 'A. L.' or similar.

To Creina

ACKNOWLEDGEMENTS

This work could not have been concluded without the co-operation of many people. To all those at the Nuclear Physics Research Unit, in the Physics Department, and elsewhere, who have so freely offered their advice and assistance, I extend my appreciation. In particular, I would like to thank:

- Professor J P F Sellschop, my supervisor, for his constant support, guidance and encouragement.
- Trevor Derry, for many valuable discussions and for his companionship and assistance in many data-taking sessions.
- Mick Rebak, for diamond polishing and precision engineering.
- The generations of accelerator technicians; Lieb Verga and the Workshop Staff; and Hugo Andeweg and the Staff of the Electronics Workshop, for technical support.
- Joe Malkin and Rory Leahy for assistance with computing.
- Dr Michael Seal and Dr Eddie Burgemeister of D. Drukker & Zn, Amsterdam, for the supply of thin diamonds, for confirming some infra-red measurements, and for many useful discussions.
- Jeannette Menasce, who deciphered my handwriting and produced this thesis.

- The University of the Witwatersrand, and de Beers Diamond Research Laboratory, for financial support.
- The Atomic Energy Board and the Council for Scientific and Industrial Research for material support.

C O N T E N T S

<u>CHAPTER</u>		<u>PAGE</u>
1	INTRODUCTION	1
2	THEORY	6
2.1	INTRODUCTION	6
2.2	THE CONTINUUM MODEL	8
	2.2.1 Axial Channelling	8
	2.2.2 Planar Channelling	25
2.3	STATISTICAL EQUILIBRIUM CHANNELLING THEORY	27
	2.3.1 Introduction	27
	2.3.2 Transverse Energy Distribution and Reaction Yields	30
	2.3.3 Particle Flux	42
	2.3.4 Limitations of the Equilibrium Continuum Model	45
2.4	ENERGY LOSS OF CHANNELLED IONS	49
	2.4.1 Introduction	49
	2.4.2 Nuclear Stopping	50
	2.4.3 Electronic Stopping in Random Solids	54
	2.4.4 Energy Loss of Channelled Ions	63
	2.4.5 Energy Loss in a Spatially Periodic Electron Gas	77
2.5	DECHANNELLING OF IONS	86
	2.5.1 Introduction	86
	2.5.2 Scattering by Nuclei and Thermally Vibrating Atoms	88
	2.5.3 Scattering by Electrons	97
	2.5.4 Damping	103
	2.5.5 Steady Increase Model of Dechannelling	104
	2.5.6 Diffusion Model of Axial Dechannelling	106
	2.5.7 Dechannelling by Defects	115
	2.5.8 Planar Dechannelling	122
2.6	THERMAL VIBRATION AMPLITUDES	124

<u>CHAPTER</u>		<u>PAGE</u>
3	APPARATUS AND METHODS	126
3.1	INTRODUCTION	126
3.2	APPARATUS	126
3.2.1	Accelerators	126
3.2.2	Channelling Beam Line and Scattering Chamber	127
3.2.3	Goniometer	129
3.2.4	Detectors and Pulse Handling	130
3.2.5	Beam Current Measurement	134
3.3	METHODS	137
3.3.1	Location of Channels	137
3.3.2	Angular Scans across Channels	138
3.3.3	Data Handling	139
3.3.4	Random Spectra	139
3.3.5	Determination of Depth Scale	140
3.3.6	Radiation Damage to Targets	143
4	DIAMONDS: PROPERTIES, SELECTION AND PREPARATION	144
4.1	INTRODUCTION	144
4.2	PROPERTIES	145
4.2.1	General Properties	145
4.2.2	Impurities in Diamond	147
4.2.3	Classification of Diamonds	149
4.3	SELECTION OF DIAMONDS	157
4.3.1	Selection Procedures	157
4.3.2	Assessment of Selection Procedures	159
4.4	PREPARATION	160
4.4.1	Aims	160
4.4.2	Polishing	160
4.4.3	Gas-Etching	161
4.4.4	Cleaning	161
4.4.5	Assessment	162
4.4.6	Thin Diamonds	162

<u>CHAPTER</u>		<u>PAGE</u>
5	DECHANNELLING IN GOOD CRYSTALS	164
	5.1 INTRODUCTION	164
	5.2 EXPERIMENTAL METHODS AND DATA ANALYSIS	166
	5.3 CALCULATIONS	168
	5.3.1 Diffusion Model	168
	5.3.2 Steady Increase Model	172
	5.4 RESULTS AND DISCUSSION	172
	5.4.1 Energy Dependence	172
	5.4.2 Axial Dependence	179
	5.4.3 Temperature Dependence	182
	5.4.4 Planar Dechannelling	182
	5.5 COMPARISON WITH THEORY	188
	5.5.1 Axes: The Diffusion Model	188
	5.5.2 Axes: The Steady Increase Model	201
	5.5.3 Planes	204
	5.6 CONCLUSIONS	206
6	EFFECT OF AMORPHOUS SURFACE LAYERS ON CHANNELLING	207
	6.1 INTRODUCTION	207
	6.2 EXPERIMENTAL METHOD	209
	6.3 TREATMENT OF DATA	209
	6.3.1 Determination of Layer Thickness	209
	6.3.2 Minimum Yield	213
	6.3.3 Depth Conversion	214
	6.4 THEORY	214
	6.4.1 Plural and Multiple Scattering	214
	6.4.2 Yield in Channelling Measurements	218
	6.4.3 Dechannelling	220
	6.5 INFLUENCE OF AMORPHOUS LAYERS ON MINIMUM YIELD AT THE SURFACE	224
	6.5.1 Results	224
	6.5.2 Calculations	224
	6.5.3 Discussion	229

<u>CHAPTER</u>	<u>PAGE</u>
6.6 DECHANNELLING IN DIAMONDS COVERED WITH AMORPHOUS LAYERS	231
6.6.1 Results	231
6.6.2 Calculations	235
6.6.3 Discussion	236
6.7 APPROXIMATIONS	237
6.7.1 Effect of Thin Contamination Layers	237
6.7.2 An Approximate Scaling Rule	242
6.8 CONCLUSIONS	248
7 DECHANNELLING BY DEFECTS IN TYPE Ia DIAMONDS	250
7.1 INTRODUCTION	250
7.2 EXPERIMENTAL PROCEDURES AND RESULTS	251
7.2.1 Infra-Red Measurements	251
7.2.2 The Diamonds	251
7.2.3 Channelling Measurements	255
7.3 DATA ANALYSIS AND DISCUSSION	255
7.3.1 Extraction of Dechannelling Probability	255
7.3.2 Results	262
7.3.3 Discussion	266
7.4 SOME REMARKS ON PLATELET STRUCTURE	288
7.5 CONCLUSIONS	293
8 ENERGY LOSS OF LIGHT IONS IN DIAMOND	295
8.1 INTRODUCTION	295
8.2 EXPERIMENTAL METHODS	297
8.2.1 Experiment	297
8.2.2 Thin Diamonds	298
8.2.3 Data Analysis	300
8.3 THEORY	305
8.3.1 Random Stopping	305
8.3.2 Straggling of the Random Beam	306
8.3.3 Energy Loss of Channelled Ions	307

<u>CHAPTER</u>		<u>PAGE</u>
8.4	RESULTS AND DISCUSSION	311
8.4.1	Random Stopping	311
8.4.2	Straggling	311
8.4.3	Channelled Ion Stopping-Power	315
8.5	CONCLUSION	320
9	CONCLUSION	323
	APPENDIX 1 CHANSPEC	329
	APPENDIX 2 LISTING OF DECHANNELLING PROGRAM	338
	REFERENCES	341

LIST OF FIGURES

<u>FIGURE</u>		<u>PAGE</u>
2.1	Comparison of Lindhard and Molière $\langle 110 \rangle$ single string axial continuum potentials for protons incident on diamond.	12
2.2	Continuum model potential energy contours in units of $\frac{1}{2}E\psi_1^2 = 54$ eV for protons incident on diamond along $\langle 110 \rangle$.	18
2.3	Continuum model potential energy contours in units of $\frac{1}{2}E\psi_1^2 = 28$ eV for protons incident on diamond along $\langle 111 \rangle$.	19
2.4	Continuum model potential energy contours in units of $\frac{1}{2}E\psi_1^2 = 24$ eV for protons incident on diamond along $\langle 100 \rangle$.	20
2.5	Single- and multi-string transmission factors for three major axes in diamond, calculated with the Lindhard potential.	38
2.6	Schematic diagram of integrand of equation (2.4.7)	57
2.7	Schematic representation of quantities in equation (2.4.31).	80
2.8	Schematic representation of quantities in equation (2.5.4).	92
2.9	Two dimensional thermal vibration amplitude for diamond as a function of temperature.	125
3.1	Schematic diagram of channelling lines for Cockcroft-Walton and Tandem accelerators.	128
3.2	Block diagram of electronics.	133
3.3	Arrangement used for target current monitoring while preventing target charging.	156
3.4	Schematic representation of relationship between ion beam penetration and scattering, and the back-scattering spectrum.	141
5.1	Energy spectra for 1.0 MeV protons incident on diamond in random and channelled directions.	165

<u>FIGURE</u>		<u>PAGE</u>
5.2	Experimental energy and depth dependence of the normalized yield, for protons along $\langle 110 \rangle$.	173
5.3	Scaled depth dependence of the normalized yield for $\langle 110 \rangle$.	176
5.4	Scaled depth dependence of the normalized yield for $\langle 111 \rangle$.	177
5.5	Scaled depth dependence of the normalized yield for $\langle 100 \rangle$.	178
5.6	Dependence of the normalized yield on depth for the three major axes.	180
5.7	Scaled depth dependence of the experimental normalized yield for three major axes.	181
5.8	Dependence of normalized yield in $\langle 110 \rangle$ on depth, at various temperatures.	183
5.9	Dependence of normalized yield in $\langle 111 \rangle$ on depth, at various temperatures.	184
5.10	Dependence of normalized yield in $\langle 100 \rangle$ on depth, at various temperatures.	185
5.11	Dependence of normalized yield in $\langle 110 \rangle$ on zu_2^2 , for various temperatures.	186
5.12	Dependence of channelled fraction of beam, $1 - \chi$, on depth for three major planes.	187
5.13	Rate of change of transverse energy with depth, due to nuclear scattering, for 1.0 MeV protons in $\langle 110 \rangle$.	190
5.14	Rate of change of transverse energy with depth, due to electronic scattering, for 1.0 MeV protons in $\langle 110 \rangle$.	194
5.15	Effect of changes in electronic scattering on the yield calculated using the diffusion model, for 1.0 MeV protons in $\langle 110 \rangle$.	195
5.16	Effect of changes to various terms on the yield calculated using the diffusion model, for 1.0 MeV protons in $\langle 110 \rangle$.	197
5.17	Effect of changes to various terms on the yield calculated using the diffusion model, for 1.0 MeV protons in $\langle 110 \rangle$.	199

<u>FIGURE</u>		<u>PAGE</u>
5.18	Temperature dependence of normalized yield in $\langle 110 \rangle$ on depth.	202
5.19	Comparison of steady increase model and diffusion model.	203
6.1	Deconvolution of spectrum of carbon layer on diamond	211
6.2	Dependence of normalized yield on angle.	221
6.3	Dependence of normalized yield on reduced thickness, τ , for carbon layer.	225
6.4	Dependence of normalized yield on reduced thickness, τ , for aluminium layer.	226
6.5	Dependence of normalized yield on reduced thickness, τ , for gold layer.	227
6.6	Experimental and theoretical dependence of normalized yield on depth, for various values of τ , as indicated.	232
6.7	Experimental and theoretical dependence of normalized yield on depth, for various values of τ , as indicated.	233
6.8	Experimental and theoretical dependence of normalized yield on depth, for various values of τ , as indicated.	234
6.9	Dependence of normalized yield on τ for thin layers.	243
6.10	Dependence of $(c\tau)^{1/2m}$ on τ .	246
6.11	Scaling of the dependence of normalized yield on layer thickness τ .	247
7.1	Typical Type Ia diamond infra-red absorption spectrum in the one-phonon region, with approximate decomposition into A and B components.	252
7.2	Dependence of normalized yield on depth, for Type Ia diamonds with differing absorption at 1370 cm^{-1} .	256
7.3	Experimental energy and depth dependence of the normalized yield, for a diamond with high Type Ia absorption.	257
7.4	Determination of dechannelling probability, $n_D\sigma$.	260
7.5	Variation of dechannelling probability with measured total nitrogen concentration.	263

<u>FIGURE</u>		<u>PAGE</u>
7.6	Relation of dechannelling probability in $\langle 111 \rangle$ to that in $\langle 110 \rangle$.	264
7.7	Relation of dechannelling probability in $\langle 100 \rangle$ to that in $\langle 110 \rangle$.	265
7.8	Dependence of dechannelling probability on absorption at 1282 cm^{-1} due to B-aggregates.	267
7.9	Dependence of dechannelling probability on absorption at 1370 cm^{-1} .	268
7.10	Energy dependence of dechannelling probability.	269
7.11	Displacement of rows by $(a_0/3)$ $[100]$ fault, viewed along $[101]$ and $[111]$.	272
7.12	Dependence of n on depth, for $\langle 110 \rangle$ and $\langle 111 \rangle$.	277
7.13	Comparison of transverse energy distribution as used by Kudo and multi-string distribution calculated for $\langle 110 \rangle$.	282
7.14	View in $\{110\}$ of Lang model platelet compared with diamond.	289
8.1	Thin diamonds viewed in sodium light.	299
8.2	Spectra of 10.0 MeV protons transmitted through $19.7 \mu\text{m}$ diamond in $\langle 110 \rangle$ and random directions, showing position of the leading edge of the channelled spectrum.	301
8.3	Random stopping power of light ions in diamond.	313
8.4	Straggling of protons transmitted through thin diamond in random orientations.	314
8.5	Ratio of channelled to random stopping powers.	317

LIST OF TABLES

<u>TABLE</u>		<u>PAGE</u>
2.1	Constants for diamond single-string potentials	23
2.2	Critical angles and energies for diamond at room temperature.	39
2.3	Fourier component of stopping number, $L = L_R + L_S$ for silicon, as calculated by Desalvo and Rosa, and from equation (2.4.33).	83
3.1	Scan plane orientations for angular scans.	138
4.1	Physical constants for diamond.	147
5.1	Electron scattering length, z_e , for major axes of diamond.	175
5.2	Parameters s_c and s_T for $\left. \frac{d\epsilon_1}{dz} \right)_e$.	191
5.3	Planar dechannelling half-lengths, x_1 , in diamond.	204
7.1	Absorption coefficients and dechannelling probabilities in Type Ia suite.	254
8.1	Valence electron scattering and structure factors for diamond.	309
8.2	Random stopping powers in diamond.	312
8.3	Ratio of channelled to random stopping power.	316

INTRODUCTION

The phenomenon of channelling, the guided motion of energetic ions injected into crystals close to principal lattice directions, was discovered in computer simulations of the slowing down of ions in crystals by Robinson and Oen [Rob 63a,b] in the early 'sixties', and is now well-established. (The historical development is discussed in [Ge 74] and [Th 73].) It was soon shown that the channelling effect manifested itself in various ion-crystal interactions, for instance, in the form of reduced stopping-powers for channelled ions [Ne 63, Dea 64] and in reduced nuclear reaction yields [Ne 63, Bøg 64].

The theoretical basis for channelling was laid by several workers [Ne 63, Le 63, Er 65] but particularly by Lindhard [Lin 64a, 65]. In his 1965 paper, Lindhard introduced a criterion for channelling in the form of a critical angle of the incident ion beam with respect to the crystal direction and introduced the concept of 'transverse energy' of a channelled ion, which together with a statistical treatment, allowed great theoretical simplification. He also discussed the energy loss of channelled ions and dechannelling, that is, the scattering of channelled ions beyond the critical angle by processes in the crystal.

These channelling effects have been studied in many crystals (for example, see [Ge 74]) and have been applied to the study of other phenomena including radiation damage [Ei 73], foreign atom location

2.

[Das 73], surface studies [Bøg 73, Jac 76, Tu 76], the study of defects in solids [Del 70] and the measurement of nuclear lifetimes [Gi 73]. The subject is reviewed by Gemmel [Ge 74] and discussed in detail in a book edited by Morgan [Mog 73b].

In this thesis, the dechannelling, both inherent and defect-produced, and energy loss of ions channelled in diamond are studied. Relatively few diamond channelling experiments have been reported and these have been concerned with initial measurements of basic parameters [Pic 69, Sel 73] or the effect of ion implantation damage [Dad 69, Dad 71]. Only recently have comprehensive and systematic measurements of critical angles and minimum yields been made [Der 78]. This work was undertaken as an extension of the work of T.E. Derry [Der 78], partly in order to extend measurements to diamond, since much work had been done on the other diamond-structure crystals, silicon and germanium, and also because the unique properties of diamond allow measurements to be extended to regions somewhat different to those usually encountered.

The dechannelling of ions has been much studied, particularly in silicon and germanium [Cam 71, Fot 71, Mor 71, Fu 71a, 71b, 72, Fon 72]. This work indicates that there are two processes inherent in the crystal that lead to dechannelling, namely, multiple scattering by electrons in the channel ('electronic scattering') and the perturbation of the channelled ion trajectory by atoms displaced from lattice sites by thermal vibrations (usually termed 'nuclear scattering' because of its relation to the usual multiple scattering by nuclear collisions in random materials). In silicon and germanium, axial dechannelling is dominated by nuclear scattering [Fot 71, Cam 71]. Diamond has both an unusually low thermal

vibration amplitude at room temperature and an exceptionally high Debye temperature so that the thermal vibration amplitude increases slowly with temperature in the region of room temperature. Also, the majority (that is, two thirds) of the electrons in diamond are valence electrons, which are predominantly responsible for electronic scattering. This leads to the expectation that electron scattering will be more important in dechannelling in diamond, and this has indeed been found to be the case.

Additional sources of dechannelling in imperfect crystals are radiation-damaged regions and crystal defects. Layers evaporated onto the crystal surface have been used to investigate the scattering mechanisms in amorphised damage regions [Rim 72, Cam 73, Lug 73] and the scattering has been found to be well described by Thomas-Fermi plural scattering theory [Mey 71, Si 74]. The use of diamond has enabled these measurements to be extended to the case of carbon layers, while gold and aluminium layers have also been studied. Furthermore, the measurements have been extended to relatively thin layers in order to study the effect of surface contamination layers on dechannelling.

The diamonds used in this study were natural crystals and the best diamonds were selected from a large group. This raises the question of the role of defects in the dechannelling in these crystals. The defect dechannelling in a group of diamonds was studied and it was found that it could be related to the presence of certain characteristic defects, as revealed by infrared absorption spectroscopy.

Finally, measurements have been made of the energy loss of light ions transmitted in channelling and random directions through thin

4.

diamond crystals. The large fraction of valence electrons in diamond allows the role of these electrons to be explored in relation to theories of channelled ion energy loss.

The general theoretical background to the work is given in Chapter 2 and certain results relevant to dechannelling and energy loss are derived.

In Chapter 3, the experimental apparatus and techniques used are described.

The properties of diamond relevant to the work in this thesis are discussed in Chapter 4. The classification system for natural diamonds and the defects characteristic of these classes are also discussed. The selection and preparation of target crystals is described.

Investigation of dechannelling in 'perfect' crystals over a range of energies and temperatures is reported in Chapter 5, and comparisons are made with theoretical models.

Dechannelling by surface layers of carbon, aluminium and gold is studied in Chapter 6. An approximate scaling relationship between different layer species, and the expressions describing the effect of contaminant layers on the minimum yield are discussed.

Investigations into the additional dechannelling in diamonds that failed the selection criteria are reported in Chapter 7. It is shown that this dechannelling can be related to the presence of known defects

in the diamonds, and some inferences can be drawn about these defects.

Energy loss of light ions in thin diamond crystals is reported in Chapter 8, and compared with various theoretical predictions.

The conclusions of the thesis are summarised in Chapter 9.

THEORY2.1 INTRODUCTION

The idea that directional effects would manifest themselves in the interaction of fast heavy particles with crystalline matter is, at first glance, appealing but becomes less so on further contemplation. The intuitive picture of a crystal containing vacant channels parallel to major axial and planar directions invites the application of simple transparency arguments to such interactions, but a little thought shows that any effects will depend on the thickness of the crystal, and will be confined to extremely small angles of incidence with respect to a channel. Diffraction effects in the interaction of energetic heavy particles are also likely to be small: a proton of MeV energies has a wavelength of some 30 fm, compared with typical lattice parameters which are four orders of magnitude larger. Thus, it is not surprising that such effects were neglected between their first suggestion by Stark in 1912 [Sta 12] and the discovery of channelling, in range measurements and in computer simulations of these, in the early 1960's. It became clear that particles incident close to a major crystal direction were steered through the crystal along the channels by a series of correlated glancing collisions with crystal atoms, and thus avoided close collisions with these atoms [Le 63, Ne 63, Lin 64a, Er 65]. This leads to a decrease in energy loss, multiple scattering and reaction yields, and similar processes that require close collisions with atoms.

In a major paper, which has remained the theoretical foundation of channelling, Lindhard [Lin 65] introduced the idea of a string, an idealised picture of a row of atoms in a crystal as a smeared-out continuum string of potential. He derived a criterion for the validity of this model in terms of the angle of incidence of particles on the string, which led to the idea of a critical angle separating the angular region in which particles would become channelled, from the region in which they would travel as though in a random array of atoms.

Lindhard also introduced a statistical description of the motion which allowed a simplified treatment of reaction yields and angular distributions, under conditions of statistical equilibrium. He discussed the energy loss of charged particles in a crystal, and the dechannelling of ions, that is, the scattering of ions from channels into the random beam by interactions with electrons and thermally vibrating crystal atoms.

In this Chapter, these ideas are discussed, together with their extension by other authors. The basic theory of channelling, of energy loss and of dechannelling, is outlined below, while the application of this theory to channelling in diamond is discussed in the relevant experimental chapters. The basic string model is discussed in Section 2.2 and the statistical description is discussed in Section 2.3. The theory of energy loss of ions in channels is discussed in Section 2.4 and the theory of dechannelling, which relies to some extent on the theory of energy loss, is discussed in Section 2.5. Finally, the model for thermal vibration amplitudes in crystals, used generally in channelling theories, is given in Section 2.6.

2.2 THE CONTINUUM MODEL.

2.2.1 Axial Channelling

It is clear that, for a channelled ion, the angles through which it is scattered in successive collisions with crystal atoms must be small. In the classical approach which is generally adopted, this means that the impact parameter in each collision is relatively large, that is, much larger than nuclear dimensions, and thus the ion interacts with each atom via a Coulomb potential partially screened by the electron cloud surrounding the atom. This screened potential may be written, for an ion of charge Z_1e and an atom of charge Z_2e , in terms of the separation, r , as

$$V(r) = \frac{Z_1 Z_2 e^2}{r} \phi\left(\frac{r}{a}\right)$$

where ϕ is a screening function, a is a screening length setting the scale of ϕ and Gaussian e.s.u. have been used.

In order to retain simplicity of the theory, a form of the screening function which is generally applicable is desirable, and a Thomas-Fermi screening function, based on a statistical description of the atom, is generally used to give a good approximation (that is, accurate to about 10 %) to the true ion-atom interaction [Gom 56, Lin 63]. With this screening function, the screening length becomes [Lin 68]:

$$a = 0.8853 a_0 (Z_1^{2/3} + Z_2^{2/3})^{-1/2}$$

or, for $Z_1 = 1$,

$$a = 0.8853 a_0 Z_1^{-1/3}$$

where a_0 is the Bohr radius ($a_0 = 52.9$ pm). (An alternative form due to Firsov [Fi 58] is often used:

$$a = 0.8853 a_0 (Z_1^{1/2} + Z_2^{1/2})^{-2/3}$$

The differences are within the accuracy of the basic Thomas-Fermi description.) For protons incident on diamond, $a = 25.8$ pm.

The Thomas-Fermi screening function can only be evaluated numerically, and approximations are generally used. Molière [Mol 47] has given a good approximation:

$$\phi_M\left(\frac{r}{a}\right) = \sum_{i=1}^3 \alpha_i \exp\left(-\frac{\beta_i r}{a}\right) \quad (2.2.1)$$

where

$$\{\alpha_i\} = \{0.1, 0.55, 0.35\}$$

$$\{\beta_i\} = \{6.0, 1.2, 0.3\}$$

Another approximation was introduced by Lindhard [Lin 65], which is less accurate than (2.2.1) but is particularly simple:

$$\phi_L \left(\frac{r}{a} \right) = 1 - \left(1 + \frac{C^2 a^2}{r^2} \right)^{-1/2} \quad (2.2.2)$$

where C is a constant which may be chosen to fit the region of the Thomas-Fermi function of interest. In practice, it is usually taken to be $C = \sqrt{3}$.

The basis of the continuum model of channelling is that a channelled ion is steered by successive collisions, of approximately the same impact parameter, with a row of atoms in a crystal, each collision producing only a very small deflection of the ion [Le 63, Lin 65, Er 65]. Thus the orbit of the ion is determined by many correlated collisions, and the structure of the row of atoms is not felt by the ion. In this case the row of atoms can be replaced by a continuum string, interacting with the ion via the average atomic potential along the string, that is [Lin 65],

$$U(r) = \frac{1}{d} \int_{-\infty}^{\infty} V(\sqrt{z^2 + r^2}) dz \quad (2.2.3)$$

where r is the perpendicular distance of the ion from the string and d is the (average) distance between atoms in the string.

With the choice of Lindhard's screening function (2.2.2), the string potential is [Lin 65]

$$U(r) = \frac{Z_1 Z_2 e^2}{d} \ln \left(\frac{C^2 a^2}{r^2} + 1 \right) \quad (2.2.4)$$

This is generally termed 'Lindhard's standard potential'. This form of the string potential will be generally used throughout this work as it lends itself to easy mathematical manipulations and gives simple results. The form arising from the Molière potential is a more accurate approximation to the Thomas-Fermi string potential, although not necessarily to the actual ion-string potential, but is mathematically difficult to use and leads to expressions that must be evaluated numerically. It is

$$U_M(r) = \frac{Z_1 Z_2 e^2}{d} \sum_{i=1}^3 \alpha_i K_0 \left(\beta_i \frac{r}{a} \right)$$

where K_0 is the modified Bessel function of the second kind and zero-th order [Abr 70]. The two are shown for comparison in Figure 2.1.

The conditions for the validity of the continuum string approximation have been investigated by Lindhard [Lin 65], and his treatment is outlined below. He demanded that the scattering in the vicinity of the minimum distance of approach, r_{\min} , to a string be due to many atoms. This requires that the distance travelled by the ion during the interaction is large compared with the separation, d , of atoms in the string. For a particle approaching the string at a small angle, ψ , with respect to the string, this distance is given by the collision time, Δt , multiplied by the velocity component parallel to the string, $v \cos \psi \approx v$.

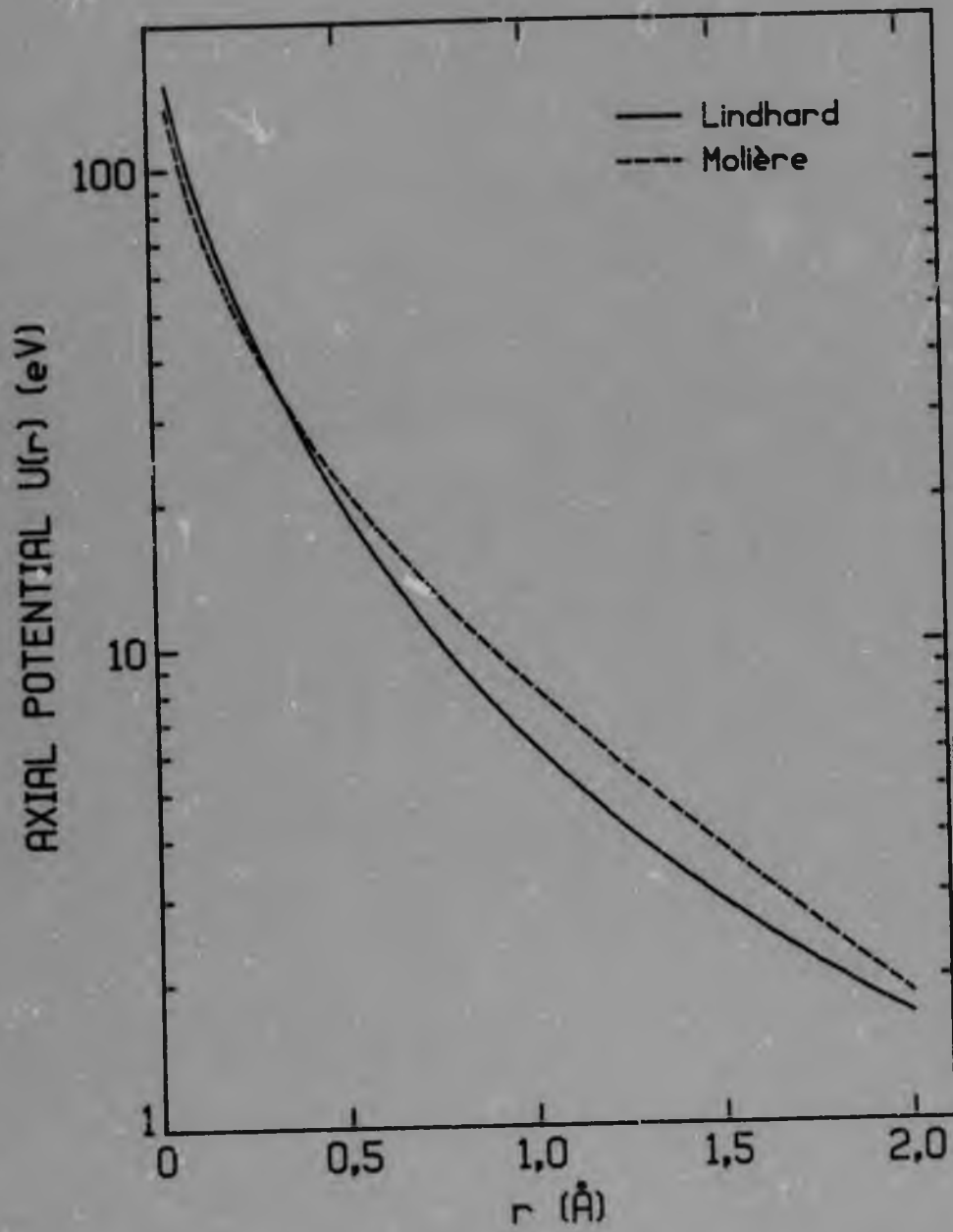


Figure 2.1: Comparison of Lindhard and Molière $\langle 110 \rangle$ single-string axial continuum potentials for protons incident on diamond.

The collision time is of the order of $r_{\min}/v \sin \psi$, leading to the condition for validity of the continuum model

$$\Delta t \quad v \cos \psi \approx \frac{r_{\min}}{\psi} > d . \quad (2.2.5)$$

The minimum distance of approach is determined by

$$\begin{aligned} U(r_{\min}) &= \frac{1}{2} M_1 (v \sin \psi)^2 \\ &= \frac{1}{2} M_1 v^2 \psi^2 \\ &= E \psi^2 \end{aligned}$$

where M_1 is the mass and E is the kinetic energy of the ion.

For small distances $r \ll Ca$, the string potential may be approximated as

$$U(r) = 2 \frac{Z_1 Z_2 e^2}{d} \ln \frac{Ca}{r} \quad (2.2.6)$$

and, determining r_{\min} from this, equation (2.2.5) becomes

$$\frac{Ca}{\psi d} \cdot \exp \left\{ - \frac{\psi^2}{\psi_1} \right\} > 1$$

where

$$\psi_1 = \left(\frac{2 Z_1 Z_2 e^2}{Ed} \right)^{\frac{1}{2}}$$

As ψ increases from zero, the inequality is first violated by the decrease in the exponential, provided $Ca/\psi d$ remains large, and thus the model is valid for

$$\psi \leq \psi_1$$

if $\psi \leq \frac{a}{d}$

or $E \geq 2Z_1 Z_2 e^2 \frac{d}{a^2} \sim 10 \text{ keV}$ for diamond.

At lower energies, another condition applies: this will not be considered as energies in this region were not used in this work. More detailed considerations [Lin 65] also lead to similar conditions for validity.

Lindhard [Lin 65] has pointed out the great importance of the angle ψ_1 in channelling. If the angle of incidence of an ion on the string is smaller than $\sim \psi_1$, the ion motion will be governed by the

continuum potential and the ion will be channelled. The ion will be steered away from the string and will not approach it closer than distances of the order of the screening length. Thus, processes requiring a close encounter with a crystal atom, such as nuclear reactions, will be suppressed. For incident angles much larger than ψ_1 , the particle will no longer be influenced by the continuum potential, and will travel as though in a random medium. The critical angle, ψ_c , which divides the regime of channelling from that of random motion, is thus of the order of ψ_1 and Lindhard gave this as $\psi_c = \alpha\psi_1$, where $\alpha \sim 1 - 2$. This critical angle is difficult to measure directly: a convenient measured quantity is the angle ψ_1 defined as that angle of incidence at which the yield in a close encounter process is mid-way between the random yield and the minimum yield measured at zero angle of incidence to the channel.

It may be noted that, with the above definition of ψ_1 , the Lindhard standard potential becomes

$$U(r) = \frac{E\psi_1^2}{2} \ln \left(\frac{C^2 a^2}{r^2} + 1 \right)$$

Within the continuum model, the motion of an ion of mass M moving at a small angle ϕ to a string in the z direction, may be described using the Hamiltonian

$$H = \frac{1}{2M} (p_z^2 + p_\perp^2) + U(r)$$

where p_z is the momentum component along the string, $p_\perp = (p_x, p_y)$ is the momentum component transverse to the string, and $r_\perp = (x, y)$ is the position of the ion in the plane perpendicular to the string, and where U is the total crystal continuum potential. It follows that, since U is independent of z , p_z is a constant of the motion and the motion can be described using the motion in the transverse x - y plane. Also, $U(r_\perp)$ is independent of the velocity so that the 'transverse energy',

$$E_\perp = U(r_\perp) + \frac{p_\perp^2}{2M}$$

$$= U(r_\perp) + E\phi^2$$

is also a constant of the motion.

A detailed theory of channelling would entail the solution of the equations of motion, which would be a formidable task, even with the reduction to two dimensions brought about by the continuum model. However, the principle of conservation of transverse energy, combined with statistical concepts, allows great simplification to be achieved, as outlined in the next section.

The continuum potential that occurs in the Hamiltonian is the net continuum potential of the crystal, which it is useful to define in such a way that the minimum potential is zero. Two models of the continuum potential may be distinguished:

- i) The multi-string model [Kok 76, Pic 76]. The potential is obtained as the sum of the string potentials due to the two dimensional lattice of strings in the transverse plane:

$$U_m(\underline{r}) = \sum_i U(\underline{r} - \underline{r}_i) - U_{\min}$$

where U_{\min} is a constant chosen so that $\min(U_m(\underline{r})) = 0$. This is a detailed two-dimensional periodic potential that requires numerical computation, and the sum is taken over a sufficient number of strings so that any further contributions are negligible. The calculated potentials for the three major axes in diamond are shown in Figures 2.2 to 2.4.

- ii) The single string model [Lin 65]. Because channelling theory is often concerned with processes close to strings (for example, nuclear reactions), a detailed knowledge of the transverse potential in the vicinity of the minimum is often not necessary, and an approximation may be used in which only one string in a unit cell of the transverse lattice is considered. The unit cell may be replaced by a circular region with the same area, of radius, r_0 , defined by

$$\pi r_0^2 = \frac{1}{Nd} \quad (2.2.7)$$

where N is the atomic density of the crystal. Choosing the

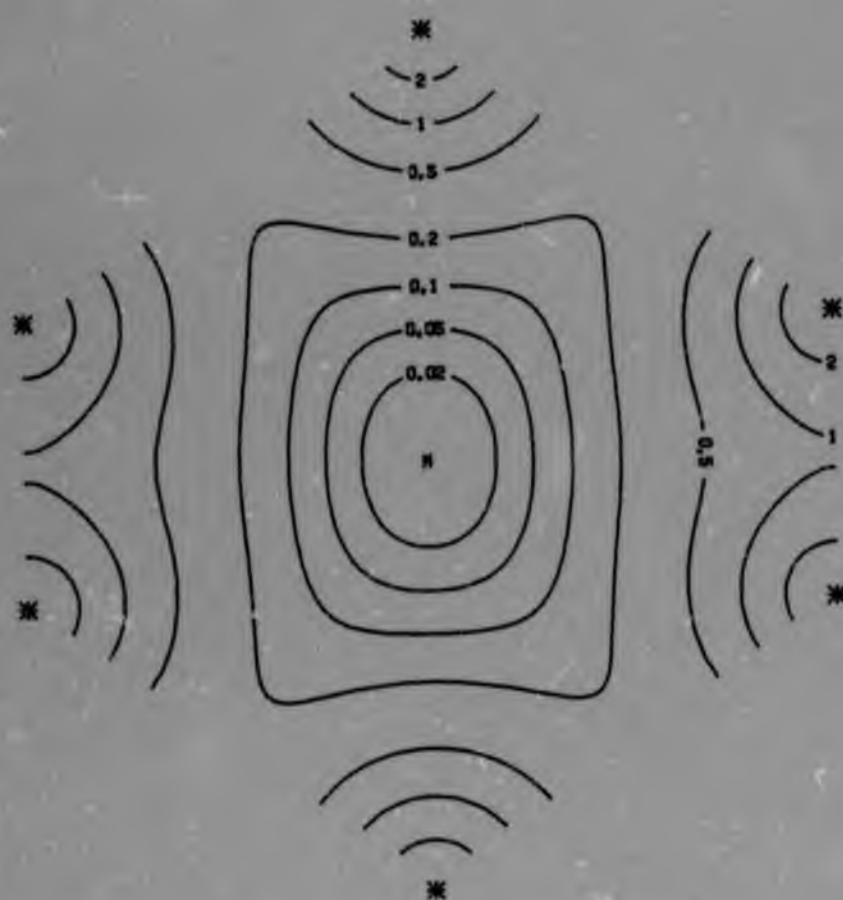


Figure 2.2: Continuum model potential energy contours in units of $\frac{1}{2}E_p^2 = 34$ eV for protons incident on diamond along $\langle 110 \rangle$. The positions of rows in the transverse plane are indicated by (*) and the minimum of potential by (M).

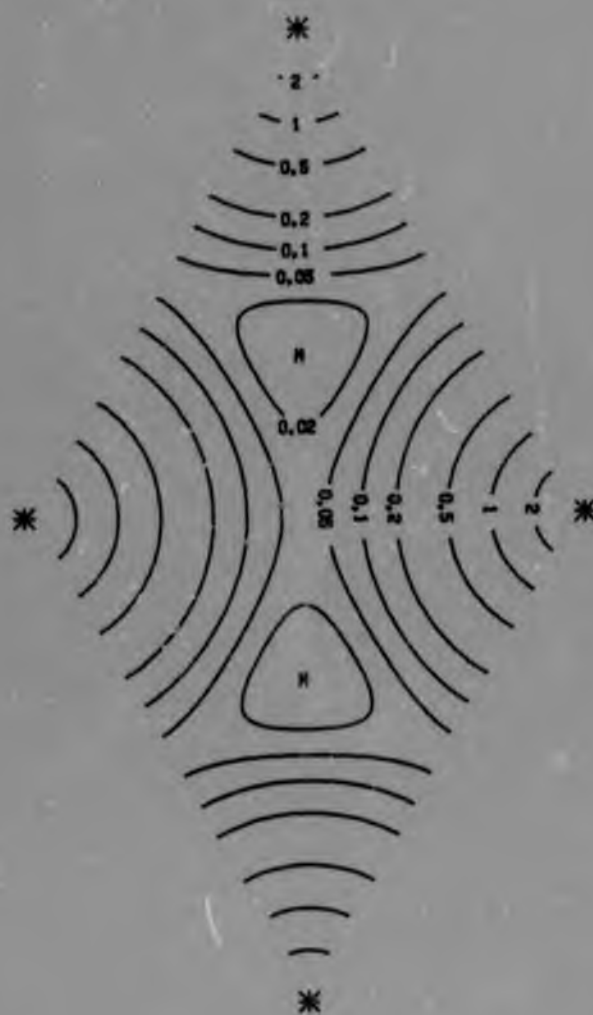


Figure 2.3: Continuum model potential energy contours in units of $\frac{1}{2} E v_1^2 = 28 \text{ eV}$ for protons incident on diamond along $\langle 111 \rangle$. The positions of rows in the transverse plane are indicated by (*) and the minimum of potential by (M).

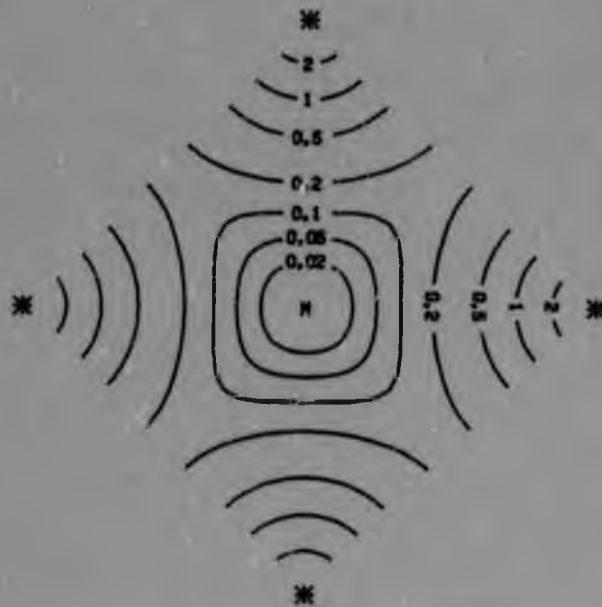


Figure 2.4: Continuum model potential energy contours in units of $\frac{1}{2}E v_1^2 = 24$ eV for protons incident on diamond along $\langle 100 \rangle$. The positions of rows in the transverse plane are indicated by (*) and the minimum of potential by (M).

standard potential (2.2.4) and defining $U_1(r_0) = 0$, the single-string potential, U_1 , is

$$U_1(r) = \frac{E\psi_1^2}{2} \ln \left[\left(\frac{C^2 a^2}{r^2} + 1 \right) / A \right] \quad (2.2.8a)$$

where

$$A = \frac{C^2 a^2}{r_0^2} + 1 \quad (2.2.9a)$$

With this potential, the distance of closest approach, r_{\min} , to a string, of a particle with transverse energy E_1 is given by

$$U_1(r_{\min}) = E_1$$

which may be solved to give

$$r_{\min}^2 = C^2 a^2 \left(A e^{\frac{2E_1}{E\psi_1^2}} - 1 \right) \quad (2.2.10)$$

The single string model is valid for $r_{\min} \ll r_0$.

The above definition of A is often used; however, a closer approximation to the multi-string potential near the string position may be obtained with a different definition. The potential close to a particular string, n , may be written

$$\begin{aligned}
 U_m(r) &= U(r) + \sum_{i \neq n} U(|r - r_i|) - U_{\min} \\
 &= U(r) + \sum_{i \neq n} U(|r_n - r_i|) - U_{\min} \\
 &= U(r) - U_0
 \end{aligned}$$

where $U_0 = U_{\min} - \sum_{i \neq n} U(|r_n - r_i|)$.

Thus, close to the string,

$$U_m(r) = U_1(r)$$

with $U_1(r) = \frac{E\psi_1^2}{2} \ln \left[\left(\frac{C^2 a^2}{r^2} + 1 \right) / A_{\text{eff}} \right]$ (2.2.8b)

where $A_{\text{eff}} = \exp \left(\frac{2U_0}{E\psi_1^2} \right)$. (2.2.9b)

Values of A_{eff} calculated from this definition converge rapidly to a limit as the number of rows in the summation is increased, and are somewhat different from the values calculated from (2.2.9a). Using these values will give results closer to that of the multistring potential than

(2.2.9a) for processes that depend on close approach to the string. The values for the three major axes in diamond are given in Table 2.1.

Table 2.1

CONSTANTS FOR DIAMOND SINGLE-STRING POTENTIALS

Axis	A (eqn 2.2.9a)	A _{eff} (eqn 2.2.9b)
<110>	1.278	1.151
<111>	1.340	1.615
<100>	1.394	1.595

It has been suggested [Er 65] that the effect of thermal vibrations of crystal atoms on the potential should be taken into account, and that a temperature-dependent continuum potential can be determined by averaging the continuum potential (2.2.3) over the distribution of thermal vibration amplitudes. Thus the thermally modified string potential becomes [Er 65]

$$U_T(r) = \int_0^{\infty} dP(s) U(|r-s|)$$

where $dP(s)$ is the distribution of thermal vibration amplitudes in

the transverse plane,

$$dP(s) = \frac{2s}{u_2} e^{-s^2/u_2^2} ds \quad (2.2.11)$$

where u_2 is the r.m.s thermal vibration amplitude in the (two dimensional) transverse plane.

The potential, $U_T(r)$, cannot be calculated analytically for the standard potential (2.2.4). The effect of thermal vibration is important only for small r , so that the approximation (2.2.6) may be used. This yields:

$$U_T(r) = \frac{E\psi_1^2}{2} \left[\ln \frac{C^2 a^2}{r^2} - E_1 \left(\frac{r^2}{u_2^2} \right) \right]$$

$$= \frac{E\psi_1^2}{2} \left[\ln \frac{C^2 a^2}{u_2^2} + \gamma - \frac{r^2}{u_2^2} + \frac{1}{2} \frac{r^4}{u_2^4} - \dots \right]$$

where $E_1(x)$ is the function [Abr 70],

$$E_1(x) = \int_x^\infty \frac{e^{-u}}{u} du$$

and $\gamma = 0.577215$ is Euler's constant. For $r = 0$, the thermally modified potential has a finite value,

$$U_T(0) = \frac{E\psi_1^2}{2} \left(\ln \frac{C^2 a^2}{u_2} + \gamma \right). \quad (2.2.12)$$

This gives a thermal bound to the validity of the continuum approach as, for transverse energies higher than $U_T(0)$, the ion will be able to penetrate to the centre of strings, and is more likely to suffer a large angle deflection. In general, however, thermally modified potentials are rarely used, as the complicated expressions that arise are difficult to handle analytically, and the effects are large only for $r \ll u_2$, whereas the region $r \gg u_2$ is generally more important in channelling.

2.2.2 Planar Channelling

Similar considerations to those outlined above apply to ions incident on a crystal in a direction far from an axis, but still nearly parallel to a plane of the lattice. The continuum model of these planar effects is discussed only briefly in this section, as planar channelling is only touched upon in this work.

In a similar fashion to axial channelling, a planar continuum potential may be derived by averaging the potential due to a large number of atoms lying in a plane. This planar continuum potential is [Lin 65]

$$Y(y) = N d_p \int_0^{\infty} 2\pi r dr V(\sqrt{r^2 + y^2})$$

where $N d_p$ is the average number per unit area of atoms in the plane and d_p is the (average) planar spacing. The potential (2.2.2) gives [Lin 65]

$$Y(y) = 2\pi Z_1 Z_2 e^2 N d_p [(y^2 + C^2 a^2)^{1/2} - y] . \quad (2.2.13)$$

The establishment of a criterion for the validity of the continuum approach to planar channelling is more complicated than in the axial case, because of the essentially random distribution of ions in the plane and because of their two-dimensional distribution, and is discussed by Lindhard [Lin 65]. The planar potential (2.2.13) is finite at the plane ($y = 0$), and ions with transverse energies much greater than this barrier energy $Y(0)$ will travel essentially as though in a random medium. This leads to a characteristic angle for planar effects

$$\psi_a = \left(\frac{2\pi Z_1 Z_2 N d_p C a}{E} \right)^{1/2}$$

and, as with the axial case, the critical angle dividing channelled from random motion is expected to be of this order.

2.3 STATISTICAL EQUILIBRIUM CHANNELLING THEORY

2.3.1 Introduction

The detailed motion of ions in a crystal lattice is extremely complicated, even when the two-dimensional motion in a lattice of strings is considered rather than the full three-dimensional case, and can only be studied using elaborate computer simulations [Mog 73a, Ge 74 and references therein] or computer time consuming integrations of the equations of motion [Els 78, Bot 78]. Lindhard [Lin 65] has, however, shown that the assumption of statistical equilibrium on the transverse energy shell, together with the principle of conservation of transverse energy, offers a powerful framework for estimating average properties of the motion, such as reaction yields.

A beam of ions entering a crystal will have some initial probability distribution in transverse momentum space. As time, or depth of penetration into the crystal, proceeds there will be a trend towards statistical equilibrium in the transverse phase space. Lindhard [Lin 65] has estimated that the depth within which equilibrium is attained is of the order of 1000 atomic layers.

An ion with transverse energy E_1 is restricted to an accessible area $A(E_1)$ in a unit cell of the transverse lattice of area $A_0 = 1/Nd$. This accessible area is

$$A(E_1) = \int_{U(r) \leq E_1} d^2r \quad (2.3.1)$$

since the ion can approach a string no closer than \hat{r} given by $U(\hat{r}) = E_1$. In the single-string model, this gives

$$A(E_1) = \pi(r_0^2 - \hat{r}^2)$$

(with $A_0 = 1/Nd = \pi r_0^2$). Once equilibrium on the transverse energy shell is attained, the ion is found with equal probability at all points in the transverse phase space accessible to it. For axial channelling, this leads to the probability for finding an ion with transverse energy E_1 at position \underline{r} being given by [Lin 65].

$$P_0(E_1, \underline{r}) = \begin{cases} 1/A(E_1) & E_1 > U(\underline{r}) \\ 0 & E_1 < U(\underline{r}) \end{cases} \quad (2.3.2)$$

This simple form of the distribution is a result of the two-dimensional nature of the transverse momentum space. If the motion is restricted to the one-dimensional case of planar channelling, the distribution becomes

$$P_0(E_1, y) = \begin{cases} \frac{C}{d_P} \left(\frac{E_1}{E_1 - Y(y)} \right)^{1/2} & E_1 > Y(y) \\ 0 & E_1 < Y(y) \end{cases}$$

where C is a normalising constant. The discussion that follows will deal mainly with the axial case.

The average, on a transverse energy shell, of any property of the ion trajectory that is a function $f(\underline{r})$ of position in the transverse plane may be determined using equation (2.3.2) [Lin 65]. Thus

$$\begin{aligned} f(E_1) &= \int P_0(E_1, \underline{r}) f(\underline{r}) d^2r \\ &= \frac{1}{A(E_1)} \int_{U(\underline{r}) \leq E_1} f(\underline{r}) d^2r \end{aligned} \quad (2.3.3a)$$

or, within the single string model,

$$f(E_1) = \frac{2}{(r_0^2 - \bar{r}^2)} \int_{\bar{r}}^{r_0} f(r)r dr \quad (2.3.3b)$$

Furthermore, if the distribution of transverse energy, $g(E_1)$, is known, the average of f for all ions is given by [Lin 65]

$$\langle f \rangle = \int_0^{\infty} g(E_1) f(E_1) dE_1 \quad (2.3.4)$$

2.3.2 Transverse Energy Distribution and Reaction Yields

One of the aims of any channelling theory is to predict the effective cross-section of a close-encounter process, such as a nuclear reaction, for a beam of ions of energy E impinging on a crystal at a small angle ψ_{in} to an axis.

There are essentially three stages involved in the particle motion [Lin 65].

- i) The transmission through the crystal surface, which results in the ion beam having some initial transverse energy distribution $g(E_1, 0)$ (which depends generally on ψ_{in}).
- ii) The passage to some depth z in the crystal, during which the transverse energy distribution $g(E_1, z)$ is modified by multiple scattering and other processes. This will be considered in Section 2.5.
- iii) Thirdly, the occurrence of the physical close encounter process, with probability as a function of E_1 given by a reaction function $\Pi(E_1)$.

Thus the effective cross-section σ_{eff} of a process with a random cross-section σ (here taken to be much smaller than any dimension typical of channelling, that is $\sigma \ll a^2$) is, from (2.3.4) [Lin 65]

$$\sigma_{\text{eff}}(z, \psi_{\text{in}}) = \int dE_1 g(E_1, \psi_{\text{in}}, z) \Pi(E_1) \sigma .$$

It is usually convenient to consider the yield χ of the reaction relative to the random yield, and thus

$$\chi(z, \psi_{\text{in}}) = \int dE_1 g(E_1, \psi_{\text{in}}, z) \Pi(E_1) . \quad (2.3.5)$$

Thus, in order to determine the relative yield, the functions g and Π must be known.

An ion entering the crystal at position \underline{r} with (small) angle ψ_{in} to the axis, will have a transverse energy

$$E_1 = U(\underline{r}) + E\psi_{\text{in}}^2 .$$

The distribution in transverse energy due to transmission through the surface is thus given by the transmission factor [Lin 65].

$$T(E_1, \psi_{\text{in}}) = \frac{1}{\Lambda_0} \int \delta(E_1 - E\psi_{\text{in}}^2 - U(\underline{r})) d^2r \quad (2.3.6)$$

where $\delta(x)$ is the Dirac δ function.

In general, there will be some initial angular distribution $P(E\psi_{in}^2) dE\psi_{in}^2$ of incident angles about the incident direction ψ_{in} , due to lack of perfect beam collimation and due to multiple scattering by surface impurity layers. Then, the initial transverse energy distribution is given by [Lin 65].

$$g(E_1, \psi_{in}) = \int P(\psi_{in}, E\psi^2) T(E_1, \psi) dE\psi^2. \quad (2.3.7)$$

If $P(\psi_{in}, E\psi^2)$ is normalised to unity, it follows that

$$\int_0^{\infty} g(E_1, \psi_{in}) dE_1 = 1.$$

It follows from equation (2.3.6) that

$$T(E_1, \psi_{in}) = T(E_1 - E\psi_{in}^2)$$

and $T(E_1, \psi_{in}) = 0$ for $E_1 < E\psi_{in}^2$.

Similarly, for $\psi_{in} = 0$,

$$P(0, E\psi_{in}^2) = 0 \quad \text{for} \quad E_1 < 0.$$

Thus, for $\psi_{in} = 0$, (2.3.7) becomes

$$g(E_1, 0) = \int_0^{E_1} P(E\psi^2) T(E_1 - E\psi^2) dE\psi^2 \quad (2.3.8a)$$

and, provided $P(0)$ is finite,

$$g(0, 0) = 0.$$

Suppose that the effects of collimation, etc, can be represented by a gaussian distribution with standard deviation ψ_{col} :

$$P(E\psi^2) dE\psi^2 = \frac{1}{2E\psi_{col}^2} e^{-\psi^2/2\psi_{col}^2} dE\psi^2.$$

Then, if ψ_{col} is small (for example, $\psi_{col} \ll \psi_1$) and T does not vary much

over the range of P (for example, for the usual tight experimental collimation) then g may be written approximately as (from (2.3.8a)),

$$g(E_1, 0) = T(E_1 - \overline{E\psi^2}) \int_0^{E_1} P(E\psi^2) dE\psi^2$$

$$= T(E_1 - 2E\psi_{col}^2) \left(1 - e^{-\frac{E_1}{2E\psi_{col}^2}}\right) \quad (2.3.8b)$$

(where $\overline{E\psi^2}$ is the average value of $E\psi^2$).

Note that beam divergence and multiple scattering are often neglected, and thus

$$P(\psi_{in}, E\psi^2) = \delta(E\psi_{in}^2 - E\psi^2)$$

giving

$$g(E_1, \psi_{in}) = T(E_1, \psi_{in})$$

with, in general, $T(0,0) \neq 0$.

The transmission function may be related to the accessible area:
(2.3.1) and (2.3.6) give:

$$T(E_1, 0) = \frac{d}{dE_1} A(E_1)$$

where

$$A(E_1) = \frac{A(E_1)}{A_0}$$

The transmission factor may be evaluated explicitly in the single-string model, using the potential (2.2.8) to give [Fot 71]

$$T(\epsilon_1, \psi_{in}) = (A - 1) \frac{Ae^{(\epsilon_1 - \epsilon_{in})}}{[Ae^{(\epsilon_1 - \epsilon_{in})} - 1]^2} \quad (2.3.9)$$

where the reduced energy ϵ_1 is defined by

$$\epsilon_1 = \frac{2E_1}{E\psi_1} \quad (2.3.10)$$

and

$$\epsilon_{in} = \frac{2\psi_{in}^2}{\psi_1^2}$$

This model also gives [Fot 71]

$$A(\epsilon_1) = \frac{A(e^{\epsilon_1} - 1)}{\lambda e^{\epsilon_1} - 1}$$

For the multi-string model, the transmission factor must be evaluated numerically, but certain general features may be deduced. The transmission factor (2.3.6) may be written, using the properties of the δ function,

$$T(E_1, 0) = \frac{1}{\Lambda_0} \int d^2r \frac{\delta(\underline{r} - \hat{\underline{r}})}{|\nabla U|}$$

$$= \frac{1}{\Lambda_0} \int ds \frac{1}{|\nabla U|_{\underline{r} = \hat{\underline{r}}}}$$

where ∇U is the gradient of U and ds is a line element of the curve c in the unit cell along which $U(\underline{r}) = E_1$. The potential $U(\underline{r})$ is a periodic function of the argument \underline{r} and thus a theorem of van Hove [Ho 53] may be applied to show that

- i) $T(E_1, 0)$ must have discontinuities corresponding to minima or maxima of U , that is, at $E_1 = 0$ and at $E_1 = U(0)$ if a thermally modified potential is used.

- ii) $T(E_1, 0)$ must have logarithmic singularities corresponding with saddle points in U .

Thus $T(E_1, 0)$ will be non-zero for all $E_1 > 0$. In practice the logarithmic singularities in T are unobservable, as $g(E_1)$ remains integrable and, furthermore, they will rapidly be rendered finite by multiple scattering, beam divergence due to imperfect collimation, etc. The functions $T(E_1, 0)$ for the three major axes are shown in Figure 2.5 for the single- and multi- string models. The single-string transmission factors use the effective A -values of Table 2.1; the multi-string factors have been calculated numerically and thus the logarithmic peaks are only approximately rendered, because of the finite grid employed in the computation. It is clear that the models agree for high transverse energy, but are rather different for low energies. That portion of the multi-string factors from $E_1 = 0$ to the energy of the first peak represent those particles that are trapped within one unit cell: these are sometimes referred to as 'hyperchannelled' [Ap 72].

Channelling effects are usually studied using nuclear reactions with cross-sections very much smaller than typical dimensions involved in determining the channelled motion, such as a^2 or u^2 , and thus the reaction function is determined by the density of scattering atoms in the transverse plane. These atoms are usually the crystal atoms; they may, however, be interstitials or foreign species.

A simple estimate of the reaction function may be obtained by noting that channelled ions are steered away from the crystal axis, and therefore reactions are suppressed, while above a certain critical transverse

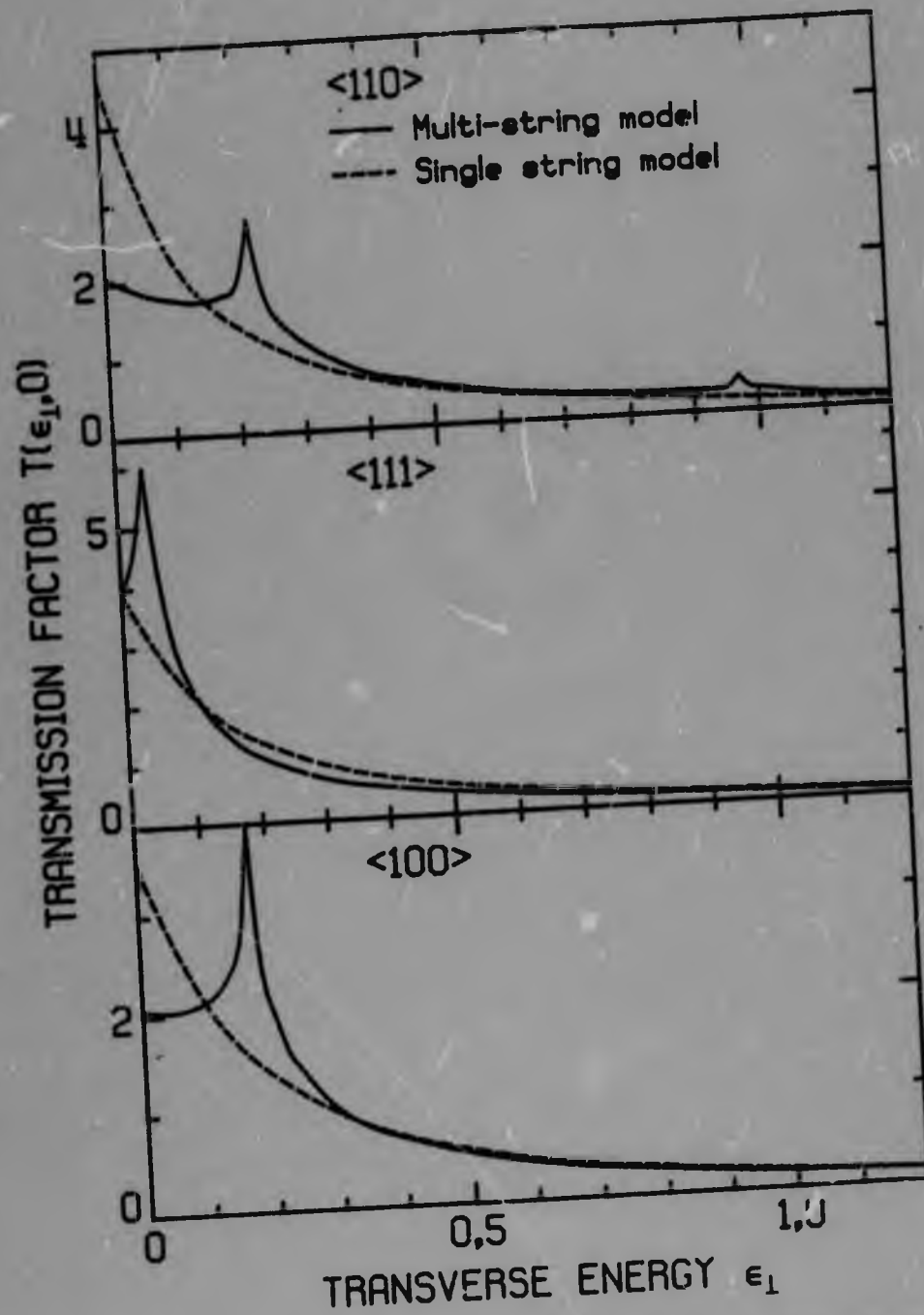


Figure 2.5: Single- and multi-string transmission factors for three major axes in diamond, calculated with the Lindhard potential.

energy, the ions travel as though in a random medium, with the random reaction yield. This leads to the 'square-well' approximation to the reaction function [Bod 72]

$$\Pi(E_1) = \begin{cases} 1 & E_1 \geq E_1^* \\ 0 & E_1 < E_1^* \end{cases} \quad (2.3.11)$$

The 'critical' energy E_1^* is often taken to be defined by the (measured) half-angle of the dip, that is, $E_1^* = E\psi_1$, but a more consistent definition is that it should reproduce the measured half-angle via equation (2.3.5). This leads to values typically about 10 % higher than $E\psi_1^2$. The values of the reduced critical energy ϵ_1^* for the multi-string model for diamond at room temperature are given in Table 2.2; the values of ψ_1 determined by Derry [Der 78] have been used.

Table 2.2

CRITICAL ANGLES AND ENERGIES FOR DIAMOND AT ROOM TEMPERATURE

Axis	ψ_1	ϵ_{11}	ϵ_1^*
<110>	0.55°	2.69	2.96
<111>	0.49°	2.62	2.75
<100>	0.42°	2.21	2.44

In general, the reaction function is determined by the distribution of the scattering atoms in the transverse plane. Suppose that $P(\underline{r})d^2r$ is the probability of finding an atom in the area d^2r at \underline{r} . Then, from (2.3.3) the reaction function is given by

$$\Pi(E_1) = \frac{1}{A(E_1)} \int_{U(\underline{r}) \leq E_1} P(\underline{r}) d^2r \quad (2.3.12)$$

The crystal atom density in the transverse plane will be governed by the thermal vibration distribution (2.2.11). This may be used, together with the single string model, which is adequate since the atoms are concentrated close to the string, to give [Lin 65]

$$\Pi(E_1) = \frac{1}{A(E_1)} \left[e^{-\frac{r_0^2}{u_2^2}} - e^{-\frac{r_0^2}{u_2^2}} \right] \quad (2.3.13a)$$

This expression is not small only for large E_1 where $A(E_1) = 1$. Then, with the use of (2.2.10) and taking $r_0 \gg u_2$, it becomes

$$\Pi(\epsilon_1) = \exp\left(-\frac{C^2 a^2}{u_2}\right) [Ae^{\epsilon_1} - 1]^{-1} \quad (2.3.13b)$$

Finally, a 'square-well' approximation can be determined for

interstitial atoms located at \underline{r}' in the transverse plane by assuming their density to be given by a delta function, $\delta(\underline{r} - \underline{r}')$, that is, their thermal vibrations are ignored. This gives, using (2.3.3)

$$\pi_{\text{int}}(E_1) = \begin{cases} \frac{1}{A(E_1)} & E_1 > U(\underline{r}') \\ 0 & E_1 < U(\underline{r}') \end{cases}$$

Lindhard [Lin 65] used (2.3.12) and (2.3.5) together with the single-string model (with $A = 1$, that is, $r_0 = \infty$), to obtain an estimate of the minimum yield $\chi(\psi_{\text{in}} = 0)$:

$$\chi(0) = \pi N d u_2^2 \equiv \chi_1$$

This is typically 1 to 5 % of the random yield. Lindhard also estimated a second, less well defined, contribution to the yield due to ions scattered from within a distance, a , from the string which could, after little multiple scattering, hit crystal atoms. This contribution is

$$\chi_2 = \pi N d a^2$$

He further considered the effect of impurity layers on the surface, and by assuming these scattered with the Rutherford cross-section, he obtained their contribution to the yield:

$$X_3 = \frac{\pi}{\psi_1^2} \sum_i n_i \left(\frac{Z_1 Z_i e^2}{E} \right)^2$$

where n_i is the areal density of the i -th impurity, with charge $Z_i e$. The effect of impurity layers on the yield will be further considered in Chapter 6.

The reaction function (2.3.13b) has been used to calculate approximately the half-angle of the dip [Pic 69, And 70]. With $A = 1$, $g(E_1)$ approximated by $\delta(E_1)$ and ψ_1 determined from

$$\Pi(E\psi_1^2) = 0.5$$

this gives

$$\begin{aligned} \psi_1 &= [U_1(u_2 \sqrt{\ln 2})/E]^{\frac{1}{2}} \\ &= [U_1(1.18 u_1)/E]^{\frac{1}{2}} \end{aligned} \quad (2.3.14)$$

2.3.3 Particle Flux

The channelling effect must lead to a redistribution of ion flux in the channel: a beam of ions impinges on a crystal with a uniform flux distribution. The reduced reaction rate of close-encounter processes due to channelling implies that the flux near the strings is reduced below

that in a random material. Thus the flux at other points in the transverse plane must be increased above the random [And 71, VI 71, Kom 75].

The flux at a point r can only receive contributions from ions with $E_1 > U(r)$. These ions are distributed uniformly over their accessible area and it follows that $F(r, z, \psi_{in})$, the flux relative to random at position r and depth z for incident angle ψ_{in} is [Bel 73, Ge 74]

$$F(r, z, \psi_{in}) = \int_{U(r)}^{\infty} \frac{g(E_1, \psi_{in}, z)}{A(E_1)} dE_1 \quad (2.3.15)$$

For zero angle of incidence and depth this becomes, if multiple scattering and beam divergence are ignored [And 71],

$$\begin{aligned} F(r) = F(r, 0, 0) &= \int_{U(r)}^{\infty} \frac{1}{A(E_1)} \frac{dA(E_1)}{dE_1} dE_1 \\ &= \ln \frac{1}{A(U(r))} \end{aligned}$$

This diverges logarithmically at the minimum of the potential ($U(r) \rightarrow 0$).

In practice, the maximum flux is rendered finite by the beam divergence and any multiple scattering, which results in $g(0) = 0$. The flux is

also limited by the multiple scattering in the crystal resulting in fluctuations in the transverse energy: these effects are discussed extensively by van Vliet [V1 71].

In terms of the flux, the relative yield of a reaction is given by

$$x(z, \psi_{in}) = \int F(\underline{r}, z, \psi_{in}) P(\underline{r}) d^2r$$

where $P(\underline{r}) d^2r$ is the probability of an atom being in d^2r at \underline{r} .

This is consistent with (2.3.5):

$$x(z, \psi_{in}) = \int g(E_1, \psi_{in}, z) \Pi(E_1) dE_1$$

as may be seen by using (2.3.15), (2.3.2) and (2.3.12).

The flux peaking effect, that is, the rise of the flux to a maximum at the minimum of the potential, is important for lattice location work, where it allows the position of interstitial atoms to be determined [And 71] and in the calculation of scattering by defects such as stacking faults [V1 71]. In these cases, it is clear that the apparent cross-section of a defect will depend on its position in the transverse plane.

2.3.4 Limitations of the Equilibrium Continuum Model

Certain limitations of the equilibrium continuum model can be found when the predictions of the model are compared with theory, and with more detailed calculations such as computer simulations. Many workers have noted deviations between the Lindhard minimum yield χ_1 or $\chi_1 + \chi_2$ and experiment. Andersen and Laegsgård [And 72] found for a wide range of crystals and axes, that (2.3.14) overestimates the critical angle by ~20 %.

Barrett, in a wide-ranging study of channelling, mainly in tungsten, by computer simulation, found semi-empirical relations for the minimum yield and for the half-angle [Ba 71] that agree with experiment on many crystals [Ba 71, Mog 73a].

These are, for the minimum yield

$$\chi_{\min} = \chi_{1B} + \chi_{2B}$$

Here,
$$\chi_{1B} = C_1 N d \pi u_2^2 (1 + \xi^{-2})^{\frac{1}{2}} \quad (2.3.16a)$$

where
$$\xi = \frac{\kappa u_1}{\psi_1 d}$$

is usually small at MeV energies, and

$$x_{2B} = C_2 N d \pi a^2 .$$

Here C_1 , C_2 and κ are fitting parameters, the first two depending on beam divergence. For zero beam divergence, Barrett found [Ba 71]

$$C_1 = 3.0 \pm 0.2$$

$$C_2 = 0.2 \pm 0.1 \quad \text{and}$$

$$\kappa = 2.2 .$$

At MeV energies (2.3.16a) becomes

$$x_{\min} = N d \pi (C_1 u_2^2 + C_2 a^2) . \quad (2.3.16b)$$

For diamond, Derry [Der 78] found from experiment,

$$C_1 = 3.2 \pm 0.6$$

$$C_2 = 0.05 \pm 0.05 .$$

For the half-angle, Barrett found [Ba 71]

$$\psi_{\frac{1}{2}} = k [U_1(\mu_1)/E]^{\frac{1}{2}} \quad (2.3.17)$$

where k and m are fitting parameters,

$$k = 0.8$$

$$m = 1.2$$

Thus (2.3.17) agrees with (2.3.14) found with the continuum model, except for the factor k . This factor cannot be accounted for by the difference in the potential used by Andersen [And 72] and Barrett [Ba 71]. For diamond, Derry [Der 78] found

$$k = 0.83 \text{ (<110>, <111>) or } 0.76 \text{ (<100>)}$$

$$m = 1.2$$

The cause of the difference between the equilibrium model calculations and the computer simulations has been traced to the existence of focussing effects in the transverse plane for ions with certain transverse energies [Ba 73]. It was found that these ions, after a close collision with a string, would be focussed by collisions with neighbouring strings into a close collision with another string. The energy of these ions was of the order of $E_{w_1}^2$ and the enhancement of the number of these ions in the vicinity of this closest approach to the string leads to an increase in yield or decrease in critical angle. This amounts to a breakdown of the statistical equilibrium model outlined above.

This effect can be taken into account by modifying the reaction function [Kub 73]. This, however, leads to expressions that must be evaluated numerically, and which can only give an approximate description.

For this reason, it seems best to use the simplest approximation for the reaction function, that is, the square-well model (2.3.11) which can be fitted to the experimentally measured critical angles. The minimum yields found with this procedure give reasonable (numerical) agreement with (2.3.16b).

Another limitation of the model is that yields cannot rise above random, and thus shoulders on dips cannot be obtained. Andersen [And 67, And 70] has shown that these can be obtained using the 'halfway plane model' [Lin 65], a refinement of the continuum model in which the transverse energy is conserved only if measured on the planes halfway between adjacent atoms in the string. It was found that, for values of $\frac{u_2}{\psi_{1d}} > 1$, the continuum model was approached. For diamond, this parameter is of the order of 3 and half-way plane calculations for diamond do show very little shoulder in the reaction function. Thus, the application of the more complicated half-way plane model to diamond does not seem warranted.

The shoulders that appear on measured angular yield functions do not immediately result from the half-way plane model shoulders: they appear to result from complicated effects in the transition from axial to planar channelling [Ba 68]. The equilibrium continuum model does not allow for any planar effects: these can be treated in a separate planar model, but the transition from one to the other is not described. Thus, angular yields, for instance, can at best represent some sort of average over all azimuthal angles and planar effects. These effects do, however, only come into play for angles $2\theta_1$, so that the minimum yield

and calculations involving the half-angle are generally not affected.

Finally, the equilibrium model does not allow any description of the depth region before equilibrium is obtained. Fluctuations in flux and yield are expected and have been found both experimentally [Bog 72, Abe 72a] and in computer simulations [Ba 71, Vl 71]. However, the depth resolution of typical experiments does not allow these oscillations to be seen. The equilibrium model, can in this respect, be regarded as a depth-averaged model. The effect of these oscillations can be important, for instance, in lattice location studies on foreign species implanted close to the surface [Wag 78].

2.4 ENERGY LOSS OF CHANNELLED IONS

2.4.1 Introduction

In a random solid, at the energies considered in this work, an ion may lose energy by two mechanisms, firstly by elastic collisions with heavy nuclei of atoms and, secondly, by excitation of the electrons of atoms. At the energies under consideration, the latter mechanism is by far the most important, the energy loss exceeding that by the former mechanism by a factor of the order of 1000. At lower energies, in the keV region, the first mechanism becomes important; at higher energies, relativistic effects and nuclear reactions become important.

Under channelling conditions, the energy loss by elastic collision with nuclei (generally called nuclear stopping) is greatly reduced as the ions are steered away from atoms [Lin 65]. The effect of channelling on nuclear stopping will not be discussed further, but the theory of nuclear stopping in random materials will be outlined below, as it is important

in the discussion of multiple scattering mechanisms in dechannelling.

The energy loss to electrons ('electronic stopping') is also influenced by channelling, although not as much as are close collision processes. From a classical viewpoint there are two contributions to the energy loss: large impact parameters or distant, resonance, collisions with electrons and small-impact parameters or close collisions which are essentially elastic and where binding effects are small [Boh 48].

From the quantum mechanical viewpoint which must be applied the distinction must be between small and large momentum transfers which corresponds roughly with the classical separation [Boh 48]. Thus, if the orbit of an ion is outside the orbital of an electron the cross-section for high momentum transfers is negligible and the energy loss of the ion is small. In an initial discussion of the energy loss of channelled ions Lindhard [Lin 65] applied an 'equipartition rule' [Lin 64b], according to which the contributions to the stopping-power of 'close' and 'distant' collisions approach equality for high velocities. From this, he deduced that the stopping would be reduced by a factor of $\sim \frac{1}{2}$. The equipartition rule does not apply strictly to stopping at the energies considered here [Er 68, Br 70] and more detailed theories of stopping have been derived. The major theories are outlined below.

2.4.2 Nuclear Stopping

Let $d\sigma(E,T)$ be the differential cross-section for the transfer of energy T to an atom by an ion with kinetic energy E , in an elastic collision. Then, in a pathlength Δx in a medium of atomic density N the average energy loss is [Boh 48].

$$\langle \Delta E \rangle = N \Delta x \int_0^{T_m} T \, d\sigma(E, T)$$

where T_m is the maximum energy loss in an elastic collision, given from the conservation of momentum and energy (see, for example [Man 68])

$$T_m = \frac{4M_1 M_2}{(M_1 + M_2)^2} E$$

where M_1 and M_2 are the mass of the ion and atom. It follows that, taking infinitesimals,

$$\left(- \frac{dE}{dx} \right)_n = N \int_0^{T_m} T \, d\sigma(E, T)$$

$$= N S_n(E)$$

where

$$S_n(E) \equiv \int_0^{T_m} T \, d\sigma(E, T)$$

is the nuclear stopping cross-section and $\left(- \frac{dE}{dx} \right)_n$ is the nuclear stopping

power (the minus sign is introduced as energy is lost by the ion).

The nuclear energy loss has been treated extensively by Lindhard and co-workers [Lin 63, Lin 68], using a Thomas-Fermi approach. In a general approach, the elastic cross-section depends on two variables, E and T (where T is given by $T = T_m \sin^2 \frac{\theta}{2}$, where θ is the centre-of-mass scattering angle). Lindhard et al showed that it can be written to a good approximation as a function of one variable

$$t = \epsilon^2 \frac{T}{T_m} \quad (2.4.1)$$

where ϵ is a dimensionless reduced energy

$$\epsilon = \frac{a}{Z_1 Z_2 e^2} \frac{M_2}{M_1 + M_2} E$$

Then the cross-section $d\sigma(E, T)$ may be written

$$d\sigma(E, T) = d\sigma(t) = \pi a^2 \frac{1}{2t^{3/2}} f(t^{1/2}) dt \quad (2.4.2)$$

where $f(t^{1/2})$ is a function that depends on the scattering potential and is tabulated for the Thomas-Fermi potential in [Lin 68]. An interpolation formula has been given by Winterbon et al [Win 70]

$$f(t^{1/2}) = \lambda t^{1/6} [1 + (2\lambda t^{2/3})^{2/3}]^{-3/2}$$

with $\lambda = 1.309$

which is a good fit to the tabulated Thomas-Fermi function [Lin 68].

Lindhard et al have also introduced a dimensionless measure of the path length

$$\rho = 4N\pi a^2 \frac{M_1 M_2}{(M_1 + M_2)^2} x$$

and with this definition, the nuclear stopping power becomes [Lin 68]

$$-\frac{d\epsilon}{d\rho} = S_n(\epsilon) = \frac{1}{\epsilon} \int_0^{\epsilon} f(t^{1/2}) dt^{1/2} \quad (2.4.3)$$

Thus a universal description of nuclear stopping is obtained in terms of the Thomas-Fermi variables ϵ and ρ . The function $S_n(\epsilon)$ is tabulated in [Lin 68]. It can be approximated in certain regions [Lin 68] as

$$S_n(\epsilon) = \begin{cases} 0.981\epsilon^{1/3} & \epsilon \leq 0.01 \\ 0.327 & 0.2 \leq \epsilon \leq 2 \\ \frac{1}{2\epsilon} \ln(1.29\epsilon) & 5 \leq \epsilon \end{cases} \quad (2.4.4)$$

The interpolation formula may also be used to calculate

$S_n(\epsilon)$ and gives

$$S_n(\epsilon) = \frac{9}{4} \frac{\lambda}{r} \left[\frac{1}{b^{3/2}} \ln \left[(1 + b\epsilon^{8/9})^{1/2} + b^{1/2} \epsilon^{4/9} \right] - \frac{\epsilon^{4/9}}{b(1 + b\epsilon^{8/9})^{1/2}} \right]$$

$$b = (2\lambda)^{2/3} = 1.89$$

For high energies this gives

$$S_n(\epsilon) = \frac{1}{2\epsilon} \ln(1.03 \epsilon) \quad (2.4.5)$$

The differences in the logarithmic terms in (2.4.4) and (2.4.5) become unimportant at high energies ($\epsilon \gg 5$). For protons incident on diamond at 1 MeV, $\epsilon = 2756$.

2.4.3 Electronic Stopping in Random Solids

The energy loss of ions in random matter by electronic excitation has been studied for many years, and a good description in the energy region considered in this work is given by the well-known Bethe-Bloch result [Bet 30, Bl 33 a, b]

$$-\frac{dE}{dx} = \frac{4\pi Z_1^2 e^4}{m_e v^2} NZ_2 \ln \frac{2m_e v^2}{I} \quad (2.4.6)$$

where m_e is the mass of the electron, v is the velocity of the ion and I is the mean ionisation potential of the atom, defined by

$$Z_2 \ln I = \sum_n f_n \ln \hbar\omega_n$$

where f_n is the oscillator strength for a transition in the atom of energy $\hbar\omega_n$.

Using a Thomas-Fermi statistical treatment of the atom, Bloch obtained for the ionization potential

$$I = I_B = I_0 Z_2$$

with $I_0 \approx 10$ eV.

In an alternative approach to energy loss phenomena, Lindhard [Lin 54] and Lindhard and Winther [Lin 64] have considered the energy loss of an ion to a uniform electron gas in terms of the complex wave vector and frequency-dependent dielectric function $\epsilon(k, \omega)$ in the random-phase approximation.

The stopping power is then [Dat 67]

$$-\frac{dE}{ix} = \frac{2Z_1^2 e^2}{\pi v^2} \int_0^{\infty} \frac{dk}{k} \int_0^{kv} \omega \, d\omega \operatorname{Im} \left\{ \frac{1}{\epsilon(k, \omega)} \right\} \quad (2.4.7)$$

where $\operatorname{Im}(\dots)$ represents the imaginary part.

In the high velocity region, this may be evaluated using the Bethe sum rule [Lin 64, Dat 67]

$$\int_0^{\infty} \omega \, d\omega \operatorname{Im} \left\{ \frac{1}{\epsilon(k, \omega)} \right\} = -\frac{\pi}{2} \omega_p^2 \quad (2.4.8)$$

where ω_p is the plasma frequency of the electron gas, given by

$$\omega_p = \left(4\pi n_e e^2 / m_e \right)^{1/2}$$

where n_e is the gas density.

The integrand of equation (2.4.7) has been given by Lindhard [Lin 64] and vanishes over large areas of the k - ω plane. The form of the integrand is sketched in Figure 2.6. The integrand is zero except in the single-particle excitation region and along the plasmon line which corresponds with collective excitations of the gas. The Fermi velocity and momentum of the gas are v_F and $k_F = \frac{m_e}{\hbar} v_F = (3\pi^2 n_e)^{1/3}$. For a

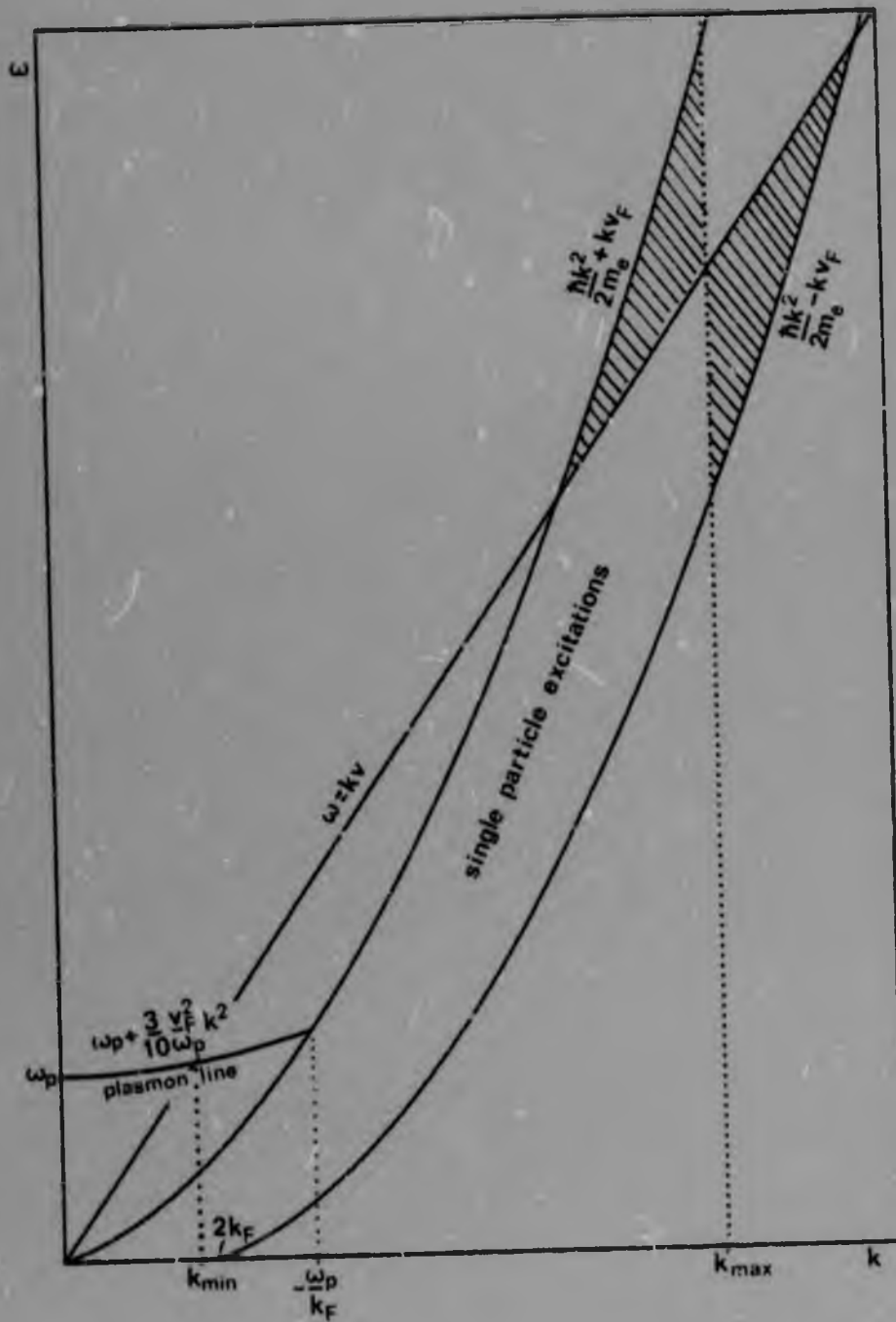


Figure 2.6: Schematic diagram of integrand of equation (2.4.7).

degenerate gas, excitations with $\omega < 0$ are forbidden by the Pauli exclusion principle.

The integration in (2.4.7) extends over the region below the line $\omega = kv$. For high velocities, the cross-hatched regions are small and approximately equal; the single particle region below $k = k_{\min}$ vanishes as k^4 [Lin 64]. Thus the limits of integration in (2.4.7) may be restricted to between k_{\min} and k_{\max} , and the ω integration extended to infinity. The sum rule (2.4.8) may then be used to perform the integration, giving

$$-\frac{dE}{dx} = \frac{4\pi Z_1^2 e^4}{m_e v^2} n_e \ln \frac{k_{\max}}{k_{\min}} \quad (2.4.9)$$

Inspection of Figure 2.6 shows that $k_{\min} = \frac{\omega_p}{v}$ and $k_{\max} = \frac{2m_e v}{\hbar}$. The former is recognised as the adiabatic limit to the momentum transfer to a system oscillating at frequency ω_p [Jak 62] and the latter as the maximum momentum transfer to a free electron.

Thus, the stopping power of the electron gas is

$$-\frac{dE}{dx} = \frac{4\pi Z_1^2 e^4}{m_e v^2} n_e \ln \frac{2m_e v^2}{\hbar \omega_p} \quad (2.4.10)$$

Lindhard and Winther also proved an equipartition rule in which the logarithmic term

$$L = \ln \frac{2m_e v^2}{\hbar \omega_p}$$

receives equal contributions from the resonance and single particle regions for a change in v . This has been stated in the form [Br 70]

$$\frac{dL_R}{dv} = \frac{dL_S}{dv}$$

where

$$L = L_R + L_S$$

Here, L_R is the resonance term and L_S is the single particle excitation term. At high velocities, the two contributions differ by a constant, that is, [Br 70]

$$L_S(v) = L_R(v) + C$$

and thus approximate equipartition of energy loss holds only if

$$C \ll L_S \quad \text{and} \quad C \ll L_R$$

The energy loss of an ion in an electron gas with an energy gap E_g , as a model of a semiconductor, has been examined by Brandt and Reinheimer [Br 70]. In this case the plasmon line is given approximately by [Br 70, Des 77]

$$\hbar^2 \omega^2 = \hbar^2 \omega_p^2 + E_g^2 + \frac{3}{5} v_F^2 \hbar^2 k^2 \quad (2.4.11)$$

and k_{\min} is given by

$$k_{\min} = \frac{\sqrt{\omega_p^2 + E_g^2/\hbar^2}}{v}$$

while k_{\max} is as for the case $E_g = 0$. Then the sum rule gives [Br 70]

$$-\frac{dE}{dx} = \frac{4\pi Z_1^2 e^4}{m_e v^2} n_e \ln \frac{2m_e v^2}{\sqrt{\hbar^2 \omega^2 + E_g^2}} \quad (2.4.12)$$

The energy loss to an electron gas has also been discussed by Pines [Pin 53, Pin 63]. He showed that, below the value $k = k_c$ where the plasmon line meets the single particle spectrum (Figure 2.6), the energy loss is mainly to the plasma oscillations, and above this value it is mainly to the single particle excitations. This dividing wave number is, approximately, [Pin 63]

$$k_c = \frac{\omega_p}{v_F}$$

Thus, it follows that [Er 67]

$$L_R = \ln \frac{v}{v_F}$$

(2.4.13)

$$L_S = \ln \frac{2m_e v v_F}{\hbar \omega_F}$$

A similar division can be performed for the case of the gas with an energy gap [Des 77]. In this case, the dividing wave-number, k_c , is determined by the intersection of the plasmon line (2.4.11) and the upper edge of the single particle spectrum, given approximately by [Des 77]

$$\omega = \frac{\hbar^2 k^2}{2} + \hbar^2 k k_F + \frac{E}{2} \left(1 - \frac{E}{4\hbar^2 k_F^2} \right) \quad (2.4.14)$$

The values of L_R and L_S for high velocities obtained using (2.4.9) and k_c from (2.4.14) and (2.4.11) agree with those calculated numerically from equation (2.4.7) by Brandt and Reinheimer to within about 10%. (The sum rule result (2.4.12) agrees well with their numerical results [Br 70].)

Contact between the Bethe-Bloch and the electron gas models can be made via the 'local density' approximation. In this approximation, the electron gas surrounding an atom is treated locally as a uniform electron gas, and the stopping power is determined by integrating over the whole atom [Lin 53], giving from (2.4.10),

$$-\frac{dE}{dx} = \frac{4\pi Z_1^2 e^4}{m_e v^2} N \int_0^{\infty} \rho(r) 4\pi r^2 \ln \frac{2m_e v^2}{\alpha \hbar \omega_p(r)} dr \quad (2.4.15)$$

where $\rho(r)$ is the density of electrons as a function of radius, $\omega_p(r)$ is the local plasma frequency $\omega_p(\rho(r))$ and $\alpha = \sqrt{2}$ is a constant introduced to take account of binding effects [Lin 53].

It follows from (2.4.15) that the local density approximation for the ionization potential is [Lin 53]

$$Z_2 \ln I = \int_0^{\infty} \rho(r) 4\pi r^2 \ln(\alpha \hbar \omega_p(r)) dr \quad (2.4.16)$$

The approximation may also be used to define an oscillator strength distribution [Es 78, Br 77]

$$\frac{df}{d\omega} = \int_0^{\infty} \rho(r) 4\pi r^2 \delta(\omega - \alpha \omega_p(r)) dr \quad (2.4.17)$$

which, with (2.4.6a), gives (2.4.16).

The local density approximation has been found to give good agreement with experimentally determined values of I , when Hartree-Fock wave-functions are used to calculate $\rho(r)$ [Chu 72].

2.4.4 Energy Loss of Channelled Ions

Two approaches to the calculation of the stopping powers of channelled ions may be distinguished. In the first, the valence electrons are treated separately from the core electrons. In some treatments the effects of core electrons are neglected [Ap 67, Bcl 70, Des 77]; this is expected to be valid at lower energies: the maximum distance at which a particular electron shell may be excited can be estimated with an adiabaticity criterion

$$b_{\text{max}} = \frac{\hbar v}{\Delta E} \quad [\text{Ap 67}]$$

where ΔE is the binding energy. In other treatments, the core electrons are included [Lun 68, Kom 74, Mel 75, Bel 78, Det 75, Kit 72]. In the second approach, the stopping to all electrons is considered on the same basis and no a priori separation is made between core and valence electrons [Det 74, Es 78]. At this time, both of these approaches appear to be valid.

In a first attempt to provide a more detailed theory of channelled ion energy loss than Lindhard's estimates [Lin 65], Appleton et al considered the energy loss to valence electrons, using the electron gas model together with the Bohm-Pines separation into resonance and single-particle excitations, for example, (2.4.13). They argued that resonance losses

would be to all the valence electrons, while single-particle losses would depend on the local electron density, and obtained [Ap 67]

$$-\left(\frac{dE}{dx}\right)_{\text{val}} = \frac{4\pi Z_1^2 e^4}{m_e v^2} N [Z_V L_R + Z_{\text{LCC}} L_S] \quad (2.4.18)$$

with

$$L_R = \ln \frac{v}{v_F}, \quad L_S = \ln \frac{2m_e v v_F}{\hbar \omega_p}$$

where Z_V is the number of valence electrons and NZ_{LCC} is the local electron density on the ion path. They used an adiabaticity criterion to estimate the contribution of core electrons to the stopping and found it negligible. The contribution of core electrons was considered by Datz et al [Dat 67], who used the well-known result for the energy loss to a harmonically bound charge in the dipole approximation (for example, [Jak 62]):

$$\Delta E(b) = \frac{2}{m_e} \left(\frac{Z_1 e^2}{v^2} \right) \omega^2 \left\{ K_0^2 \left(\frac{\omega b}{v} \right) + K_1^2 \left(\frac{\omega b}{v} \right) \right\} \quad (2.4.19a)$$

$$= \frac{2Z_1^2 e^4}{m_e v^2 b} ; \quad \frac{\omega b}{v} \ll 1 \quad (2.4.19b)$$

where ω is the frequency of the electron, b is the impact parameter,

K_0 and K_1 are the modified Bessel functions of the second kind and zero-th and first orders, and ΔE is the energy lost in a single collision. The approximation (2.4.19b) was used together with the valence electron treatment of Appleton et al [Ap 67] by Luntz and Bartram [Lun 68] and Melvin and Tombrello [Mel 75]. The latter authors found good agreement with the experimental energy loss of protons in silicon, using local electron densities calculated from Molière's approximation to the Thomas-Fermi potential.

While this theory does appear to give good results, it does represent a rather simplified picture. Thus, it has been pointed out [Bon 70] that the range of impact parameters for single particle collisions extends from

$$b_{\min} = \frac{1}{k_{\max}} = \frac{\hbar}{2m_e v} \quad \text{to} \quad b_c = \frac{1}{k_c} = \frac{v_F}{\omega_p}$$

The latter can be of the order of channel dimensions, and thus the local electron density NZ_{LOC} should actually be averaged over some area of the channel. Furthermore, there is some effect of channelling on the plasmon losses [Bon 70]. Finally, the Thomas-Fermi approach (via the Molière potential) to the local electron density can lead to large errors at the channel centre.

For this reason, Bonsignori and Desalvo [Bon 69, Bon 70] treated the valence electron as a spatially periodic electron gas and calculated

the stopping power using the dielectric function in the random phase approximation [Ad 62, Wis 63]. Bonsignori and Desalvo obtain [Bon 69]

$$-\frac{dE}{dx}(\underline{r}) = \frac{Z_1^2 e^2}{\pi^2 v} \int_{-\infty}^{\infty} \frac{d^3 k}{k^2} \int_{-\infty}^{\infty} d\omega \operatorname{Im} \{K(\underline{k}, \omega, \underline{r})\} \delta(\omega - \underline{k} \cdot \underline{v}) \quad (2.4.20)$$

where \underline{r} is the position of the orbit of the ion in the transverse plane, and K is the response function, which in the translationally invariant case reduces to $K = \frac{1}{\epsilon(\underline{k}, \omega)}$. The response function may be expanded in a Fourier series [Bon 69]:

$$K(\underline{k}, \omega, \underline{r}) = \sum_{\underline{G}} K(\underline{k}, \omega, \underline{G}) e^{i \underline{G} \cdot \underline{r}}$$

where the sum runs over all reciprocal lattice vectors \underline{G} which are perpendicular to the channel. (Other reciprocal lattice vectors drop out in averaging along the channel. Thus

$$f(\underline{r}) = \frac{1}{d} \int_{-\infty}^{\infty} f(\underline{r}, z) dz$$

$$\begin{aligned}
 f(\underline{r}) &= \frac{1}{d} \int_{-\infty}^{\infty} \sum_{(\underline{G}, \underline{G}_z)} f(\underline{G}, \underline{G}_z) e^{i(\underline{G} \cdot \underline{r} + \underline{G}_z z)} dz \\
 &= \frac{1}{d} \sum_{(\underline{G}, \underline{G}_z)} f(\underline{G}, \underline{G}_z) \delta(\underline{G}_z) e^{i\underline{G} \cdot \underline{r}} \\
 &= \sum_{\underline{G}} f(\underline{G}, 0) e^{i\underline{G} \cdot \underline{r}}.
 \end{aligned}$$

In the weak binding approximation [Fa 60] the response function is

$$\kappa(\underline{k}, \omega, \underline{G}) = \delta_{\underline{G}, 0} \frac{1}{\epsilon(\underline{k}, \omega, 0)} - (1 - \delta_{\underline{G}, 0}) \frac{\epsilon(\underline{k}, \omega, \underline{G})}{\epsilon(\underline{k}, \omega, 0)} \quad (2.4.21)$$

where $\epsilon(\underline{k}, \omega, \underline{G})$ are the Fourier components of the periodic dielectric function $\epsilon(\underline{k}, \omega, \underline{r})$ [Ad 62, Wis 63] in which local field effects are considered. If these are averaged over, only the $\underline{G} = 0$ term is retained, which is identical to the case treated by Brandt and Reinheimer [Br 70] in their investigation of the stopping power of an electron gas with an energy gap.

In this theory, the path-dependent channelled ion stopping power

is obtained directly, without recourse to separation into resonance and single-particle excitations, although these can be examined. The theory has been applied with good results [Bon 70, Kom 74, Des 77]; however, the application has involved complicated numerical calculations, required to calculate the response function χ and to evaluate the integrals in (2.4.20). In fact, sum rules can be used to perform an approximate evaluation of equation (2.4.20) for high velocities; this is discussed in Section 2.4.5.

Recently, attempts have been made to calculate the stopping power of channelled ions in the high velocity (Bethe-Bloch) region using a more fundamental approach [Det 74, Det 75, Es 78]. Both of these theories treat the stopping power in first Born approximation but differ somewhat in philosophy and approach.

Dettmann [Det 75] treats the valence electrons separately from the core electrons; the former are treated as a uniform electron gas, for which the Lindhard result (equation (2.4.10)) applies: the latter are treated in an independent particle model using a Hartree-Fock approach. Thus the core contribution is a sum over independent contributions from each electron.

For random impact, the energy loss to each core electron is determined by using a generalised oscillator strength sum rule together with an interchange of the limits of integration in a similar manner to the treatment for the electron gas, outlined above. The low momentum transfer limit is determined by demanding that the region of the integrand

which is neglected in this procedure is compensated by that added: this condition determines a mean excitation energy in terms of the Hartree-Fock wave-functions of the atom. The random stopping power is determined as [Det 75]:

$$S_r = - \left. \frac{dE}{dx} \right|_{\text{ran}} = \frac{4\pi Z_0^2 e^4}{m_e v^2} N \left[Z_V \ln \frac{2m_e v^2}{\hbar \omega_p} + \sum_{j=1}^{Z_C} \ln \frac{2m_e v^2}{\hbar \omega_j'} \right]$$

where Z_C is the number of core electrons and

$$\omega_j'^2 = \frac{\langle j | p^2 | j \rangle}{\langle j | r^2 | j \rangle}$$

where p and r are the momentum and position operators and $|j\rangle$ is the Hartree-Fock wave function for electron j . Note that ω_p is determined using the valence electron density. This equation can be written in the Bethe-Bloch form (2.4.6), with the mean ionization potential

$$I = \hbar \left[\omega_p \prod_{j=1}^{Z_C} \omega_j' \right]^{1/Z_2} \quad (2.4.22)$$

An equipartition rule for core electrons was also derived by dividing the stopping into contributions from high core excitations and low core excitations. This gives [Det 75]

$$S_{r,H} = \frac{2\pi Z_1^2 e^4}{m_e v^2} N \sum_{j=1}^{Z_C} \ln \frac{2m_e v^2}{\hbar |\omega_j|}$$

$$S_{r,L} = \frac{2\pi Z_1^2 e^4}{m_e v^2} N \sum_{j=1}^{Z_C} \ln \frac{2m_e v^2 |\omega_j|}{\hbar \omega_j^2} \quad (2.4.23)$$

where $S_{r,H}$ and $S_{r,L}$ are the random high excitation and low excitation contributions and $\hbar \omega_j$ is the binding energy of the j -th electron. At high velocities, the differences in the logarithmic terms become negligible and

$$S_{r,H} = S_{r,L}$$

For the case of channelled ions, Dettmann considered the high and low core excitations separately. The energy loss for low excitations was calculated using a self-consistency condition that the average over all impact parameters should give the random result (2.4.23). This condition supplied a mean excitation energy

$$\overline{\omega_j} = \frac{3}{2 \langle j | r^2 | j \rangle}$$

for low excitations. The energy loss to a single atom was then evaluated

as a function of impact parameter b , and for $b \gg \langle j|r|j \rangle$ the dipole result (namely equation (2.4.19)) was obtained [Det 75]

$$\Delta E_L(b) = \frac{2}{m_e} \frac{Z^2 e^4}{v^4} \sum_{j=1}^{Z_C} \frac{1}{\omega_j^2} \left\{ K_0^2 \left(\frac{b}{b_j} \right) + K_1^2 \left(\frac{b}{b_j} \right) \right\} \quad (2.4.24)$$

where

$$b_j = \frac{v}{\omega_j} = \frac{2}{3} v \langle j|r^2|j \rangle$$

$\Delta E(b)$ decreases exponentially for $b \gg b_j$; and thus b_j plays the part of a critical impact parameter. For $b = 0$, a finite result for $\Delta E(b)$ was obtained, and the full b dependence can be obtained by scaling from results obtained using a hydrogen-like ground state [Det 74]. However, the region $b \ll \langle j|r|j \rangle$ for core electrons is less important for channelled ions and need not be considered in detail. The high core excitations were treated using an impulse approximation and found to be highly local in the electron density, giving [Det 75]

$$\Delta E_H(b) = \frac{2\pi Z^2 e^4}{m_e v^2} \sum_{j=1}^{Z_C} \rho_j(b) \ln \frac{v^2}{|\omega_j|}$$

where $\rho_j(b)$ is the density of the j -th electron, averaged along the channel. The core electron density is very small for most channelled ions, and this contribution is usually negligible. The core contribution to the stopping of channelled ions is then obtained by summing (2.4.24) over all atoms in

the range $b \leq b_j$. This can result in contributions from atoms far from the immediate axial channel being included, especially at high velocities, where b_j becomes large. Dettmann regarded the valence electrons as a uniform electron gas, that gave equal stopping to channelled and random ions, and thus the same valence stopping was used for both cases.

Certain features of the theory as given by Dettmann appear to be unsatisfactory. The use of a uniform electron gas to treat the valence electrons is the most important of these. Arguments have been advanced to support this, based on the long range b -dependence obtained from (2.4.24) [Jar 77], and it is claimed that variations in electron density are averaged out. This is contradicted by calculations using a spatially periodic electron gas [Bon 70, Des 77]. Furthermore, at high velocities, the contribution of core electrons far from the channel would seem to be important. However, it is probable that polarization effects would become important for these, and a treatment similar to that of Fermi [Fer 40] for the density effect would be needed.

Esbensen and Golovchenko [Es 78], while also starting from the first Born approximation, choose to treat the atom as a whole and calculate the stopping in terms of the dipole oscillator strengths f_{n0} . The periodicity of the crystal is exploited to expand the stopping power as a function of position \underline{b} in the transverse plane in a Fourier series [Es 78].

$$-\frac{dE}{dx}(b) = \frac{4\pi Z_1^2 e^4}{m_e v^2} N \sum_{\underline{G}} e^{i\underline{G} \cdot \underline{b}} S(\underline{G}) \quad (2.4.25)$$

where the sum is over all transverse reciprocal lattice vectors \underline{G} .

The function $S(\underline{G})$ is given by [Es 78]

$$S(\underline{G}) = \frac{1}{2\pi} \sum_n \int dk \frac{(k^2 - \frac{1}{2}G^2) \delta(k_x - \frac{\omega_{n0}}{v})}{|k + \frac{1}{2}\underline{G}|^2 |k - \frac{1}{2}\underline{G}|^2} F_{n0}(\underline{k}, \underline{G})$$

for a unit transverse lattice cell containing one atom. The ion motion has been chosen in the x direction. The function $F_{n0}(\underline{k}, \underline{G})$ is a generalised oscillator strength, satisfying the sum rule [Es 78]

$$\sum_n F_{n0}(\underline{k}, \underline{G}) = \langle 0 | e^{i\underline{G} \cdot \underline{r}} | 0 \rangle$$

which, for $\underline{G} = 0$ reduces to the Bethe sum rule [Bet 30]. On averaging equation (2.4.25) over all positions in the transverse cell, only the $\underline{G} = 0$ term is non-vanishing and thus the Bethe result is obtained (see, equation (2.4.6))

$$-\frac{dE}{dx} \Big|_{\text{trans}} = \frac{4\pi Z_1^2 e^4}{m_e v^2} N Z_2 \ln \frac{2m_e v^2}{I}$$

with

$$Z_2 \ln I = \sum_n F_{n0} \ln(\hbar \omega_{n0})$$

For channelled ions the function $S(G)$ must be evaluated for $G \neq 0$. Golovchenko and Esbensen accomplished this approximately by using, for small G , a dipole approximation for small k and a sum rule for large k and for large G by using the sum rule. The small G and large G regions were joined by constructing an expression which matched both regions, giving [Es 78]

$$S(G) = \langle 0 | e^{iG \cdot \mathbf{r}} | 0 \rangle \left(\frac{\ln \left(1 + \left[\frac{2m_e v}{\hbar G} \right]^2 \right)}{2 \sqrt{1 + \left(\frac{\hbar G}{2m_e v} \right)^2}} + \phi(Gv) \right) \quad (2.4.26)$$

where

$$\phi(Gv) = \sum_n \frac{J_{n0}(G)}{\langle 0 | e^{iG \cdot \mathbf{r}} | 0 \rangle} \left(\ln \frac{Gv}{\omega_{n0}} - \frac{\ln \left(\frac{Gv}{\omega_{n0}} + \sqrt{\left(\frac{Gv}{2\omega_{n0}} \right)^2 + 1} \right)}{\sqrt{1 + \frac{2\omega_{n0}}{Gv}}} \right)$$

where $J_{n0}(G)$ is a generalised dipole oscillator strength which satisfies a sum rule

$$\sum_n J_{n0}(G) = \langle 0 | e^{iG \cdot \mathbf{r}} | 0 \rangle$$

and which tends to the dipole oscillator strength f_{n0} for $G \rightarrow 0$. For $G = 0$, the expression (2.4.26) gives the random result (2.4.6).

Certain difficulties arise in the evaluation of this expression, especially as regards the dipole oscillator strength $J_{n0}(G)$ and the transition frequencies ω_{n0} . For this reason, an approximation for J_{n0} was introduced [Es 78].

$$J_{n0}(G) = \frac{1}{Z_2} f_{n0} \langle 0 | e^{iG \cdot \mathbf{r}} | 0 \rangle \quad (2.4.27)$$

which satisfies the sum rule, gives the correct random result, and is exact for electrons bound in a harmonic oscillator potential and initially in the ground state. Esbensen and Golovchenko then evaluated the sum in (2.4.26) using the local density approximation for the oscillator strength distribution (equation (2.4.17)). The Fourier transforms of the charge density, $\langle 0 | e^{iG \cdot \mathbf{r}} | 0 \rangle$, are given by kinematic X-ray scattering factors.

Esbensen and Golovchenko used the Lenz-Jensen model [Je 32] to define the electron density for the local density approximation. Thus (2.4.26) may be written

$$S(G) = F(G) \left(\frac{\ln \left(1 + \left(\frac{2m_e v^2}{\hbar G} \right)^2 \right)}{2 \sqrt{1 + \left(\frac{\hbar G}{2m_e v^2} \right)^2}} + \phi(Gv) \right) \quad (2.4.28)$$

with

$$\phi(Gv) = \frac{1}{Z_2} \int_0^{\infty} 4\pi\rho(r)r^2 dr \left\{ \ln \frac{Gv}{\omega'} - \frac{\ln \left(\frac{Gv}{\omega'} + \sqrt{\left(\frac{Gv}{2\omega'}\right)^2 + 1} \right)}{\sqrt{1 + \frac{2\omega'}{Gv}}} \right\}$$

where

$$\omega' \equiv \sqrt{2} \omega_p(\rho(r))$$

and $F(G)$ is the kinematic X-ray structure factor, which takes account of the distribution of atoms within the unit cell.

For high velocities, the function $\phi(Gv)$ becomes very small for $G \neq 0$ and the stopping power may be written [Es 78]

$$-\frac{dE}{dx} (b) = \frac{4\pi Z_1^2 e^4}{m_e v^2} N \left\{ Z_2 \ln \frac{2m_e v^2}{I} \right. \quad (2.4.29)$$

$$\left. + \sum_{G \neq 0} e^{iG \cdot b} F(G) \ln \left(\frac{2m_e v}{\hbar G} \right) \right\}.$$

This is valid for $v \gg Z_2 \frac{v_B}{G_0 a_B}$ where v_B and a_B are the Bohr velocity and radius and G_0 is the minimum non-zero transverse reciprocal lattice vector.

Esbensen and Golovchenko found good agreement of the theory with stopping of α -particles in silicon $\langle 110 \rangle$ and $\langle 111 \rangle$ determined experimentally

by Eisen et al [Ei 72]. They do point out, however, that the model (2.4.27) is likely to be rather crude at lower velocities; they do not give any range of velocity over which (2.4.27) is expected to be valid.

2.4.5 Energy Loss in a Spatially Periodic Electron Gas

As mentioned above, the stopping power of a spatially periodic electron gas is given by equation (2.4.20) and may be written in the form, for a gas of density n_0 ,

$$-\frac{dE}{dx}(\underline{r}) = \frac{4 Z_1^2 e^4}{m_e v} \frac{n_0}{\pi \omega_p^2} \int e^{i\mathbf{G}\cdot\mathbf{r}} \cdot I(\mathbf{G})$$

$$\text{where } I(\mathbf{G}) = \int_0^\infty \frac{d^3k}{k^2} \int \omega \operatorname{Im} \{K(\underline{k}, \omega, \mathbf{G})\} \delta(\omega - \underline{k}\cdot\mathbf{v})$$

with $K(\underline{k}, \omega, \mathbf{G})$ given by (2.4.21).

In the high velocity region, a sum rule may be applied in the approximate evaluation of the integral $I(\mathbf{G})$. The dielectric response of non-metals (with application to diamond) has been examined by Johnson [Jo 74] using the dielectric formulation of Adler and Wiser [Ad 62, Wis 63]. He found [Jo 74]

$$\lim_{\omega \rightarrow \infty} \epsilon(\underline{k}, \omega, \mathbf{G}) = \delta_{0, \mathbf{G}} - \frac{\omega_p^2}{\omega^2} F_V^1(\mathbf{G}) \hat{\mathbf{e}}(\underline{k}) \cdot \hat{\mathbf{e}}(\underline{k} + \mathbf{G})$$

where $F_V^i(\underline{G})$ is the valence electron X-ray structure factor, normalised so that $F_V^i(0) = 1$, and $\hat{e}(\underline{x})$ is a unit vector in the direction of \underline{x} . From this a sum rule [Jo 74]

$$\int_0^{\infty} \omega \operatorname{Im} \{ \epsilon(\underline{k}, \omega, \underline{G}) \} d\omega = -\frac{\pi}{2} \omega_p^2 F_V^i(\underline{G}) \hat{e}(\underline{k}) \cdot \hat{e}(\underline{k} + \underline{G})$$

follows from the principle of causality (for example, [Pin 63, Lin 64]).

Similarly, it follows that

$$\lim_{\omega \rightarrow \infty} K(\underline{k}, \omega, \underline{G}) = \delta_{0, \underline{G}} + \frac{\omega_p^2}{\omega^2} F_V^i(\underline{G}) \hat{e}(\underline{k}) \cdot \hat{e}(\underline{k} + \underline{G})$$

from which may be derived the sum rule

$$\int_0^{\infty} \omega \operatorname{Im} \{ K(\underline{k}, \omega, \underline{G}) \} d\omega = \frac{\pi}{2} \omega_p^2 F_V^i(\underline{G}) \hat{e}(\underline{k}) \cdot \hat{e}(\underline{k} + \underline{G}) \quad (2.4.30)$$

Because reciprocal lattice vectors \underline{G} perpendicular to the channel axis and to the velocity vector \underline{v} need only be considered,

$$\cos\psi = \hat{e}(\underline{k}) \cdot \hat{e}(\underline{k} + \underline{G})$$

is given by (see Figure 2.7)

$$\cos\psi = \frac{k^2 + kG \cos\phi \sin\theta}{k\sqrt{k^2 + G^2 + 2kG \cos\phi \sin\theta}} \quad (2.4.31)$$

In an isotropic system, K is independent of θ . In the periodic valence electron gas, the departure from isotropy is not large, and the variation of K with θ can be ignored in a first approximation to obtain, after integrating over θ ,

$$I(G) = \frac{1}{v} \int_0^{2\pi} \int_0^{\pi} \frac{dk d\phi}{k} \int_0^{kv} \omega d\omega \operatorname{Im}\{K(\underline{k}, \omega, \underline{G})\} \quad (2.4.32)$$

Now, considering (2.4.31) for large k , \underline{k} is approximately parallel to \underline{y} and $\sin\theta = 0$ so that

$$\cos\psi = \frac{k}{\sqrt{k^2 + G^2}}$$

Integrating over ϕ gives

$$\overline{\cos \psi} = \frac{2\pi k}{\sqrt{k^2 + G^2}} \xrightarrow{k \rightarrow \infty} 2\pi .$$

For small k , k is approximately perpendicular to y and $\sin \theta = 1$. Then

$$\cos \psi = \frac{k + G \cos \phi}{\sqrt{k^2 + G^2 + 2kG \cos \phi}} .$$

This can be integrated over ϕ to yield

$$\begin{aligned} \overline{\cos \psi} &= 4 \left(\frac{k}{G} K \left(\frac{k}{G} \right) + \frac{G}{k} \left(K \left(\frac{k}{G} \right) - E \left(\frac{k}{G} \right) \right) \right) \text{ for } \frac{k}{G} \leq 1 \\ &= \pi \frac{k}{G} ; \quad k \rightarrow 0 \end{aligned}$$

where K and E are elliptic functions. A simple function that may be chosen to join the high k and low k regions is

$$\overline{\cos \psi} = \frac{2\pi k}{\sqrt{k^2 + 4G^2}} .$$

Then (2.4.32) may be used with the sum rule (2.4.30) to give, with an interchange of limits of integration as for the uniform electron gas,

$$I(G) = \frac{\pi^2}{v} \omega_p^2 \int_{k_{\min}}^{k_{\max}} \frac{dk}{\sqrt{k^2 + 4G^2}} F'_v(G)$$

where, as for the case of the electron gas with a gap

$$k_{\min} = \frac{\sqrt{\omega_p^2 + E^2/\hbar^2}}{v} ; \quad k_{\max} = \frac{2m_e v}{\hbar} .$$

Thus the stopping power is given by

$$-\frac{dE}{dx}(r) = \frac{4\pi Z_1^2 e^4}{m_e v^2} n_e \int_G^{\infty} e^{-iG \cdot r} F'_v(G)$$

$$\cdot \ln \frac{2m_e (v^2 + \sqrt{v^4 + \frac{G^2 v^2 \hbar^2}{m_e^2}})}{\hbar(\omega_g + \sqrt{\omega_g^2 + 4G^2 v^2})} \quad (2.4.33)$$

where

$$\omega_g^2 = \omega_p^2 + E^2/\hbar^2 .$$

A separation into close and distant collisions can be made if k_c is determined as for the electron gas with a gap, that is,

$$L_R = \int_{\underline{G}}^{\overline{G}} e^{iG \cdot r} F_V'(G) \ln \frac{k_c + \sqrt{k_c^2 + 4G^2}}{k_{\min} + \sqrt{k_{\min}^2 + 4G^2}} \cdot \quad (2.4.34)$$

$$L_S = \int_{\underline{G}}^{\overline{G}} e^{iG \cdot r} F_V'(G) \ln \frac{k_{\max} + \sqrt{k_{\max}^2 + 4G^2}}{k_c + \sqrt{k_c^2 + 4G^2}} \cdot$$

The results of this approximate theory are compared in Table 2.3 with the numerically calculated values of Desalvo and Rosa [Des 77] for

Table 2.3

FOURIER COMPONENTS OF STOPPING NUMBER, $L = L_R + L_S$, FOR SILICON AS CALCULATED BY DESALVO AND ROSA AND FROM EQ 2.4.33

Energy (keV)	G	L [Des 77]	L (eqn 2.4.33)
100	{000}	2.373	2.511
100	{111}	0.355	0.359
100	{222}	0.055	0.042
2000	{000}	5.622	5.50
2000	{111}	0.906	0.819
2000	{222}	0.139	0.117

protons in silicon. The results are found to be quite good, considering the approximations made, even at 100 keV. (It may be noted, that for the random 2 MeV case ($G = \{000\}$) the results of Desalvo and Rosa are about 5 % above those of Brandt and Reinheimer.)

The result (2.4.33) has certain interesting consequences. Averaging over the unit cell to determine the random energy loss leaves only the term $G = 0$, giving

$$-\frac{dE}{dx} \Big|_{\text{ran}} = \frac{4\pi Z_1^2 e^4}{m_e v^2} n_e \ln \frac{2m_e v^2}{\hbar\omega_g}$$

which is, as is to be expected, just the result for the electron gas with a gap, equation (2.4.12). For large $v \gg G$ (2.4.33) reduces to

$$-\frac{dE}{dx} \Big|_{\text{ran}} = \frac{4\pi Z_1^2 e^4}{m_e v} n_e \left[\ln \frac{2m_e v^2}{\hbar\omega_g} + \sum_{G \neq 0} e^{iG \cdot \mathbf{r}} F_V'(G) \ln \frac{2m_e v}{\hbar G} \right]. \quad (2.4.35)$$

This is clearly related to the result (2.4.29) of Esbensen and Golovchenko, and may be seen to give the latter on application of the local density approximation. The result (2.4.35) has also been obtained for the periodic electron gas by Burenkov and Komarov [Bun 79].

A re-arrangement of (2.4.35) gives, with $n_e = Z_V N$,

$$L = Z_V \ln \frac{v}{v_F} + \sum_{G \neq 0} e^{iG \cdot \mathbf{r}} \ln \frac{2m_e v v_F}{\hbar\omega_g} F_V'(G) + \sum_{G \neq 0} e^{iG \cdot \mathbf{r}} F_V'(G) \ln \frac{\hbar\omega_g}{v_F G}$$

that is,

$$L = Z_V \ln \frac{v}{v_F} + Z_{\text{LOC}}(\underline{r}) \ln \frac{2m_e v v_F}{\hbar \omega_g} + \sum_{G \neq 0} e^{i\mathbf{G} \cdot \underline{r}} F_V(G) \ln \frac{\hbar \omega_g}{v_F G}$$

where $F_V(G) = Z_V F'_V(G)$ and

$$Z_{\text{LOC}}(\underline{r}) = \int_{\underline{G}} e^{i\mathbf{G} \cdot \underline{r}} F_V(G) \quad .$$

This gives the result (2.4.18) of Appleton et al [Ap 67], together with a correction term which takes into account the varying gas density; the Appleton et al result is valid in the high velocity region, where the correction term can be neglected. However, the slow variation of the logarithmic term with velocity implies that this region is not reached except for extremely high velocities where, in any case, the expression must be modified to take into account relativistic effects.

Finally, (2.4.35) may be written

$$-\frac{dE}{dx}(\underline{r}) = \frac{2\pi Z_1^2 e^4}{m_e v^2} N \{ (Z_V + Z_{\text{LOC}}(\underline{r})) \ln \frac{2m_e v}{\hbar \omega_g} + C(\underline{r}) \}$$

$$C(\underline{r}) = \sum_{G \neq 0} e^{i\mathbf{G} \cdot \underline{r}} F_V(G) \ln \frac{2m_e \omega_g}{\hbar G^2}$$

which is related to an expression derived from (2.4.29) by Esbensen and Golovchenko [Es 78; their equation 24].

The result (2.4.33) (or (2.4.35)) can be combined with a suitable treatment of core electrons (for example, that of Dettmann [Det 75]) to supply a complete theory of channelled stopping power.

2.5 DECHANNELLING OF IONS

2.5.1 Introduction

It was pointed out by Lindhard [Lin 65] that the transverse energy of an ion is not strictly conserved. This non-conservation can arise from several sources. The force seen by an ion must fluctuate due to thermal vibrations; this gives rise to a multiple scattering of the ion away from the orbit it would follow if there were no vibrations and thus to an increase in the transverse energy. A similar increase arises from multiple scattering from electrons in the channel. Similar, though smaller, effects arise from the fact that the string is made up of a discrete assemblage of atoms, and yet another source of scattering is the presence of defects in the crystal. All these lead, on the average, to an increase in the transverse energy. A decrease in the transverse energy is brought about by electronic stopping which is directed against the motion. If an ion of transverse energy E_{\perp} loses energy δE then the transverse energy will change by an amount $\delta E_{\perp} \sim \delta E \frac{E_{\perp}}{E}$ [Lin 65]. Lindhard [Lin 65] has also considered the effect of deviations from classical motion.

All these effects, of which the most important in 'defect-free' crystals are multiple scattering by thermally vibrating atoms and by electrons, lead to changes in the transverse energy of an ion as it proceeds

into a crystal. In general, the transverse energy increases, with the result that the distribution of transverse energies shifts to higher values, and the relative yield in close encounter processes increases. The ion beam is said to become dechannelled.

In a random system, multiple scattering of an ion beam, on a pathlength δz leads to a mean-square fluctuation in angle $\delta\Omega^2$ about the initial direction [Boh 48]. If the scattering processes result in only small deviations in direction, the change in angular distribution with depth can be treated as a diffusion process, with the diffusion coefficient being governed by $\frac{d\Omega^2}{dz}$. If the continuum description applies to the ions, the mean-square fluctuation in angle gives rise to a mean fluctuation in transverse kinetic energy $\delta E\Omega^2$ and, hence, as $\delta z \rightarrow 0$, a mean fluctuation in transverse energy, δE_1 . In the random system, the multiple scattering will be independent of position and, thus, by (2.3.3), independent of the transverse energy.

Under channelling conditions, however, the multiple scattering will vary with position, and thus the mean change in transverse energy with depth $\frac{dE_1}{dz}$, when averaged over the accessible area in the transverse plane, will depend on the transverse energy. The diffusion in the angle can then become small compared with the change in the average direction, or the spread in transverse energy small compared with the change in transverse energy, for ions with initially well-defined transverse energy [Lin 65].

These considerations lead to two models of dechanneling, within the equilibrium continuum model, both of which require knowledge of $\frac{dE_1}{dz}$.

In the first and more general model (the 'diffusion model' [Lin 65, Ap 67, Bod 72, Bel 72]), the dechannelling is regarded as a diffusion process in transverse energy space (or sometimes transverse momentum space) with the transverse energy distribution being governed by a Fokker-Planck equation. In the second, simpler model (the 'steady increase' model [Lin 65, For 71]), the diffusion is neglected and the transverse energy of a particle is regarded as increasing steadily according to the function $\frac{dE_1}{dz}$. This, in turn, governs the change in distribution with depth. In both of these models, the yield at a given depth can then be obtained from equation (2.3.5):

$$\chi(z, \psi_{in}) = \int g(E_1, \psi_{in}, z) \Pi(E_1) dE_1$$

These two models, and the functions $\frac{dE_1}{dz}$ for the two main scattering processes, due to thermally vibrating atoms and due to electrons, are discussed below. The effect of defects on the yield is also considered.

2.5.2 Scattering by Nuclei and Thermally Vibrating Atoms

In a random solid, the mean-square fluctuation in angle due to elastic collisions with nuclei ('nuclear collision') is given approximately by [Boh 48, Lin 65]

$$\delta\Omega_n^2 = \frac{M_2}{M_1} \frac{1}{E} \delta E_n$$

that is,

$$\delta\Omega_n^2 = \frac{M_2}{M_1} \left(\frac{1}{E} \frac{dE}{dz} \right)_n \delta z$$

$$= \frac{M_2}{M_1} \frac{1}{E} N S_n(E) \delta z \quad (2.5.1)$$

where δE_n is the energy lost in nuclear collision on the path-length δz , and $N S_n(E)$ is the nuclear stopping power. (This expression contains contributions from large-angle scattering and is thus not strictly applicable to a diffusion treatment. It is convenient to neglect these for the meantime, but this point will be considered again below.)

This leads to a mean fluctuation in transverse energy

$$\overline{\delta E_1} = E \delta\Omega_n^2 = \frac{M_2}{M_1} N S_n(E) \delta z$$

where $\overline{\delta E_1}$ is the average fluctuation in transverse energy on the pathlength δz for a particle with initial transverse energy E_1 .

Thus a rate of change of transverse energy with depth may be defined

$$\left(\frac{dE_1}{dz} \right)_R = \frac{M_2}{M_1} N S_n(E) \quad (2.5.2a)$$

where R indicates that it is for a random system. It is convenient to write this in terms of the reduced transverse energy $\epsilon_1 = \frac{2E_1}{E\psi_1^2}$

$$\left(\frac{d\epsilon_1}{dz}\right)_R = \frac{2M_2}{M_1} \frac{N}{E\psi_1^2} S_n(\epsilon) \quad (2.5.2b)$$

A channelled ion will be steered away from atoms in the crystal, and thus the multiple scattering and rate of change of transverse energy will be much reduced. For a first estimate, the multiple scattering can be regarded as a close-encounter process, with the multiple scattering at a point in the transverse plane being determined by the density of scatterers at that point. Then a square-well approximation can be defined in which ions with $E_1 < E_1^*$ are regarded as channelled, with no multiple scattering and those with $E_1 > E_1^*$ are regarded as travelling at random, when (2.5.2a) applies. A somewhat better approximation is given by taking the density of atoms as given by the thermal vibration amplitude distribution (2.2.11). The scattering may then be averaged over the accessible area to give [Ki 73, Sc 75]

$$\begin{aligned} \left(\frac{d\epsilon_1}{dz}\right)_n &= \frac{2M_2}{M_1} \frac{S_n(\epsilon)}{E\psi_1^2} \quad \epsilon = \epsilon_1 \\ &= \left(\frac{d\epsilon_1}{dz}\right)_R \Pi(\epsilon_1) \end{aligned} \quad (2.5.3)$$

where $\Pi(\epsilon_1)$ is given by (2.3.13) and n indicates that the scattering is due to nuclei.

However, large impact parameters of the order of the screening length, a , are important in multiple scattering and thus the process cannot be regarded as a close-encounter process. Thus (2.5.3) will under-estimate the scattering, especially for low transverse energies (that is, large distance from the string). Lindhard [Lin 65] has treated this latter case by summing the squares of the force fluctuations along the string to obtain

$$\overline{\delta E_1} = \frac{d}{4E} \langle (\delta F(\underline{r}))^2 \rangle \delta z$$

where $\underline{F}(\underline{r})$ is the transverse force at \underline{r} , $\underline{F}(\underline{r}) = -\text{grad } U(\underline{r})$, and $\langle \dots \rangle$ denotes the average over the accessible area, equation (2.3.3), and $\delta F(\underline{r})$ is the force fluctuation at \underline{r} , averaged over the thermal distribution, that is (see Figure 2.8)

$$\begin{aligned} (\delta F(\underline{r}))^2 = & \int_0^{2\pi} \frac{d\phi}{2\pi} \int_0^{\infty} \frac{ds^2}{u_2^2} e^{-s^2/u_2^2} [F^2(\underline{r}) \\ & + F^2(\underline{r} - \underline{s}) - 2\underline{F}(\underline{r}) \cdot \underline{F}(\underline{r} - \underline{s})] . \end{aligned} \quad (2.5.4)$$

Lindhard expanded this to first order in $\frac{E}{u_2^2}$ to obtain [Lin 65]

$$\langle (\delta F(\underline{r}))^2 \rangle = \frac{u_2^2}{2} \left\langle \frac{F^2(\underline{r})}{r^2} + F'^2(\underline{r}) \right\rangle .$$

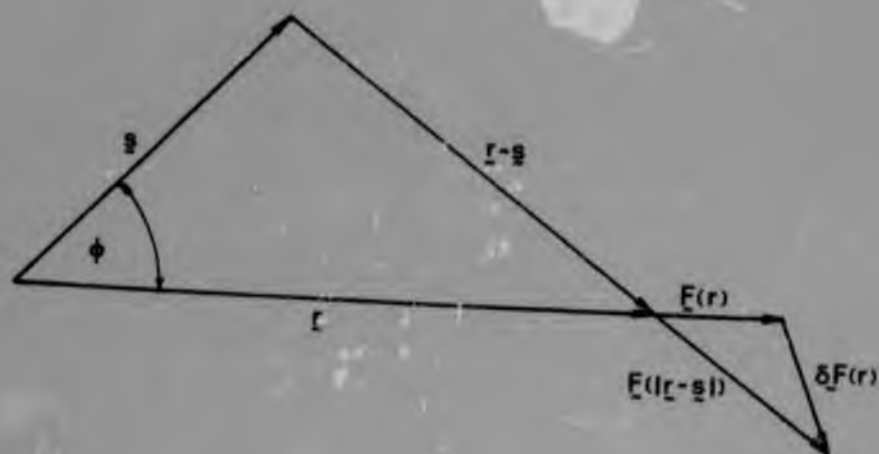


Figure 2.8: Schematic representation of quantities in equation (2.5.4).

Expansions to second order have also been performed [Sc 75, Got 75a].
 The expressions can be evaluated in the single-string model (2.2.15) to
 give [Lin 65, Sc 75, Got 75a, Cam 71, Bel 72]

$$\left. \frac{d\epsilon_1}{dz} \right)_n = \left. \frac{d\epsilon_1}{dz} \right)_R (\gamma_1 + \gamma_2) \quad (2.5.5a)$$

where the reduction factors $\gamma_1(\epsilon_1)$ (first order expansion) and $\gamma_2(\epsilon_1)$
 (second order expansion) are given by

$$\begin{aligned} \gamma_1 = & \frac{1}{A(\epsilon_1)} \frac{1}{2L_n} \frac{u_2^2}{C^2 e^2} [(Ae^{\epsilon_1} + 2/3) (1 - \frac{e^{-\epsilon_1}}{A})^3 \\ & - (A + 2/3) (1 - 1/A)^3] \end{aligned} \quad (2.5.5b)$$

$$\begin{aligned} \gamma_2 = & \frac{1}{A(\epsilon_1)} \frac{1}{2L_n} \frac{u_2^4}{C^4 a^4} [(A^2 e^{2\epsilon_1} - 2Ae^{\epsilon_1} - \frac{4}{A} e^{-\epsilon_1} \\ & - \frac{7}{A^2} e^{-2\epsilon_1} + \frac{26}{A^3} e^{-3\epsilon_1} - \frac{24}{A^4} e^{-4\epsilon_1} + \frac{36}{5A^5} e^{-5\epsilon_1}) \\ & - (A^2 - 2A - 4/A - 7/A^2 + 26/A^3 - 24/A^4 + 7.2/A^5)] \end{aligned}$$

(2.5.5c)

where $L_n = \ln 1.29e$ is the logarithmic term in (2.4.4).

If only the first order expansion is used, $\left. \frac{d\epsilon_1}{dz} \right)_n$ may be written [Bod 72, Bel 72],

$$\left. \frac{d\epsilon_1}{dz} \right)_n = \frac{1}{A(\epsilon_1)} \frac{1}{4z_n} \left[(Ae^{\epsilon_1} + 2/3) \left(1 - \frac{e^{-\epsilon_1}}{A} \right)^3 - (A + 2/3) \left(1 - 1/A \right)^3 \right]$$

where

$$z_n = \frac{C^2 a^2}{u_2^2} \frac{1}{\pi N d^2 \psi_1^2}$$

is a characteristic length, scaling the thermal term to different axes (if differences in A are small), energies and temperatures. With the inclusion of the second order expansion, and the limiting of the random scattering to small angles, discussed below, z_n loses its generality, but may still be used to set the approximate scale for the phenomena.

The expansions leading to (2.5.5) are valid for $r \ll u_2$, that is, (2.5.5) is valid for $E_1 \ll U_1(u_2)$. At high transverse energies, for example, for transverse energies greater than the maximum value of the thermally modified potential (2.2.12) [Sc 75], the rate of increase of the transverse energy with depth should tend to the random value.

The random value (2.5.2b), however, contains contributions from

large angle scattering and thus overestimates the diffusion [Sc 75]. Schjøtt et al [Sc 75] found, in the case of their calculations for silicon, that the mean-square fluctuation in angle, as calculated from (2.5.1), was about two to three times larger than the Gaussian part (due to small angle multiple scattering) and they, therefore, reduced the random term by this amount. They further suggested that the single scattering term (that is, large angle scattering) could be treated as an absorption term in their diffusion treatment, but found that it turned out to be negligible.

A systematic way in which this problem may be treated is to consider, in (2.5.1) or (2.5.2), the energy loss restricted to collisions with scattering angle smaller than some cut-off value ψ_D . Collisions with scattering angles greater than ψ_D could then be treated with an absorption term, that is, they would be regarded as being transferred irrevocably to the random beam. For channelled ions, the angular scale is set by the angle ψ_1 , and it seems reasonable to take ψ_D of this order. A convenient choice is $\psi_D = \psi_1$, and it turns out that the value is not critical. Then the nuclear stopping-power for collisions with angles less than ψ_D is given by

$$-\left(\frac{dE}{dx}\right)_{n,D} = N \int_0^{\psi_D} T \, d\sigma(E,T)$$

where, for the mass of the ion \ll mass of the atom,

$$T_D = T_m \sin^2 \frac{\psi_D}{2} = \frac{1}{4} T_m \psi_D^2 .$$

Using the Thomas-Fermi approach, the stopping-power becomes, with (2.4.3) and (2.4.1)

$$-\frac{d\epsilon}{d\rho} \Big)_{n,D} = S_{n,D}(\epsilon) = \frac{1}{\epsilon} \int_0^{t_D^{1/2}} f(t^{1/2}) dt^{1/2}$$

where

$$t_D = \frac{\epsilon^2 \psi_D^2}{4}.$$

This may be written

$$\begin{aligned} S_{n,D}(\epsilon) &= \frac{t_D^{1/2}}{\epsilon} \int_0^{t_D^{1/2}} \frac{1}{t_D^{1/2}} f(t^{1/2}) dt^{1/2} \\ &= \frac{t_D^{1/2}}{\epsilon} S_n(t_D^{1/2}). \end{aligned}$$

Thus, the transverse energy change, due to diffusion only, for random motion is

$$\frac{d\epsilon_1}{dz} \Big)_{R,D} = 2 \frac{M_2}{M_1} \frac{N}{E\psi_1^2} \frac{t_D^{1/2}}{\epsilon} S_n(t_D^{1/2}). \quad (2.5.6)$$

This is also, typically, a factor of 2 to 3 smaller than (2.5.2). For

1 MeV protons incident on diamond <110> axis, (2.5.6) is smaller than (2.5.2) by a factor of 3.04; doubling or halving ψ_D leads to a change in the value given by (2.5.6) of about 25 %.

With this value for the random scattering, and with (2.5.5) providing the values for small transverse energy, a suitable function for all transverse energies can be found by bridging the gap. Schjøtt et al [Sc 75] have proposed an expression, based on the series expansion (2.5.5) and which gave good results in a number of crystals [Ped 75]. This is

$$\left. \frac{d\epsilon_1}{dz} \right|_n = \left. \frac{d\epsilon_1}{dz} \right|_R \gamma \quad (2.5.7)$$

with

$$\gamma = \gamma_1 + \gamma_2 + \left(1 + \frac{k\gamma_2}{\gamma_1} \right)$$

where $k = 1$. This expression was applied for all values of ϵ_1 below the value for which

$$\left. \frac{d\epsilon_1}{dz} \right|_R \gamma = \left. \frac{d\epsilon_1}{dz} \right|_{R,D}$$

The application of this to diamond is considered in Chapter 5.

2.5.3 Scattering by Electrons

For random motion in matter containing electrons, the mean-square

fluctuation in angle of an ion is given by [Boh 48, Lin 65, Vli 73]

$$\begin{aligned} \delta\Omega_e^2 &= c \frac{m_e}{M_1} \frac{1}{E} \delta E_e \\ &= c \frac{m_e}{M_1} \frac{1}{E} \left(\frac{dE}{dz} \right)_e \delta z \\ &= c \frac{m_e}{M_1} \frac{1}{E} \rho S_e \delta z \end{aligned}$$

where δE_e is the energy loss to electrons on a path-length δz , ρ is the density of electrons, S_e is the stopping power per electron and c is a constant included to take account of the differences between close and distant energy losses. The multiple scattering is produced mainly by close collisions with electrons, while distant resonance collisions lead to relatively large energy transfers with small momentum transfers, and do not contribute much to multiple scattering. For an electron gas, Kitagawa and Ohtsuki [Ki 73] have obtained the ratio of multiple scattering by one-electron excitations and by plasma excitations as (for high velocities), with E_F the Fermi energy of the gas,

$$\frac{\delta\Omega_{\text{one el}}^2}{\text{plasma}} = \frac{4E_F Z_1}{\hbar\omega_p} \ln \frac{2m_e v^2}{\hbar\omega_p}$$

For 1 MeV protons in the valence electron gas of diamond, this gives

$$\delta\Omega_{one\ e1}^2 = 16 \delta\Omega_{plasma}^2$$

The multiple scattering by plasmons can, therefore, be ignored in a first approximation.

For a channelled ion, the electron density varies relatively slowly across the channel and the rate of change of transverse energy with depth, due to electrons, becomes [Lin 65]

$$\left(\frac{dE_1}{dz}\right)_e = c \frac{m_e}{M_1} S_e \langle \rho(\underline{r}) \rangle$$

where $\langle \dots \rangle$ represents the averaging over the accessible area, and $\rho(\underline{r})$ is the electron density at \underline{r} in the transverse plane, averaged along the string. With an electron density obtained from the string potential by applying Poisson's equation, this becomes [Lin 65, Bod 72, Bel 72]

$$\left(\frac{dE_1}{dz}\right)_e = \frac{1}{z_e} \left(1 - \frac{e^{-c_1}}{\Lambda}\right) \tag{2.5.8}$$

(with $c = \frac{1}{2}$), where

$$z_e = \frac{E}{\pi Z_1 e^2 L_e N d} \tag{2.5.9}$$

and

$$L_e = \ln \frac{2m_e v^2}{I}$$

or, for use with experimental stopping powers,

$$L_e = \frac{m_e v^2}{4\pi Z_1^2 e^4 N Z_2} \left(\frac{dE}{dz} \right)_e$$

This expression is expected to lead to a value for $\left(\frac{dc_1}{dz} \right)_e$ that is too small for small ϵ_1 , as it uses a mean ionization potential and does not take into account the reduction in ionization for tightly bound electrons [Bj 72]. An electron gas model has, therefore, been suggested, in which the plasmon frequency, ω_p , depends on the local electron density [Bj 72, Bod 72]. The electron density obtained from the Lindhard standard potential in the single-string model, Bonderup et al [Bod 72] obtained

$$\left(\frac{dc_1}{dz} \right)_e = \frac{1}{Z_e} \left(1 - \frac{e^{-\epsilon_1}}{A} \right) \left[1 - \frac{1}{L_e} \ln \left(1 - \frac{e^{-\epsilon_1}}{A} \right) \right] \quad (2.5.10)$$

These expressions ((2.5.8) and (2.5.10)) depend on the strict equipartition of close and distant collisions (that is, $c = \frac{1}{2}$), which does not hold, in general. Furthermore, electron density outside a radius r_0 (equation 2.2.7) is ignored, and the use of the standard Lindhard potential under-estimates the actual electron density by a factor, in some cases, of ~ 4 [Sc 75]. Corrections to take into account these last two problems

are discussed by Schiøtt et al [Sc 75]. However, an approach based on the separation of the stopping power into close and distant collisions as, for instance, in equation (2.4.34) seems to offer the best estimate for the electronic multiple scattering. In common with the above treatments, the contribution of resonance (distant) collisions is neglected, but equipartition is not demanded, which can lead to an increase in the random multiple scattering of 20 % to 40 %. Also, a realistic electron density can be incorporated into the theory through the use of X-ray structure factors related to experiment.

If the stopping power is separated into contributions from single particle and resonance collisions,

$$\frac{dE}{dz}(\vec{r}) = \left. \frac{dE}{dz} \right|_S(\vec{r}) + \left. \frac{dE}{dz} \right|_R(\vec{r})$$

the rate of change of transverse energy with depth can be written

$$\begin{aligned} \left. \frac{d\epsilon_1}{dz} \right|_e(\epsilon_1) &= \frac{2}{E\psi_1^2} \frac{m_e}{M_1} \left\langle \left. \frac{dE}{dz} \right|_S(\vec{r}) \right\rangle \\ &= \frac{2}{E\psi_1^2} \frac{m_e}{M_1} \frac{1}{\Lambda(\epsilon_1)} \int_{U(\vec{r}) \leq E_1} \left. \frac{dE}{dz} \right|_S(\vec{r}) d^2r \end{aligned}$$

(2.5.11)

It is obvious that

$$\left. \frac{d\epsilon_1}{dz} \right|_e (0) = \frac{2}{\psi_1^2} \frac{m_e}{M_1} \left. \frac{dE}{dz} \right|_{S, \min} \quad (2.5.12)$$

where $\left. \frac{dE}{dz} \right|_{S, \min}$ is the single particle stopping power at the position of the potential minimum.

Equation (2.5.11) can, in general, be evaluated numerically using the many string model. However, $\left. \frac{d\epsilon_1}{dz} \right|_e$ only varies by a factor of ~ 2 over the full range of transverse energies, increasing from a minimum at $E_1 = 0$ to a constant value for $E_1 \gg E\psi_1^2$.

Such elaborate calculations to determine the exact dependence of $\left. \frac{d\epsilon_1}{dz} \right|_e$ on ϵ_1 seem out of place in a treatment which must, of necessity, contain many approximations, especially as the calculated yields do not depend too much on how the regions $E_1 = 0$ and $E_1 \sim E\psi_1^2$ are joined, because of the slow increase of $\left. \frac{d\epsilon_1}{dz} \right|_e$ with ϵ_1 . The function $\left. \frac{d\epsilon_1}{dz} \right|_e$ can be expected to vary in the same general fashion as (2.5.8) and (2.5.10), which suggests as an approximation for $\left. \frac{d\epsilon_1}{dz} \right|_e$

$$\left. \frac{d\epsilon_1}{dz} \right|_e = \frac{1}{z_e} s_r \left(1 - \frac{e^{-\epsilon_1}}{s_c} \right) \quad (2.5.13)$$

where

$$s_r = \left. \frac{d\epsilon_1}{dz} \right|_e (\epsilon_1 \rightarrow \infty)$$

$$s_c = \frac{s_r}{s_r - \left. \frac{d\epsilon_1}{dz} \right|_e (0) z_e}$$

and where z_e , as obtained from (2.5.9), has been retained as a standard length characteristic of the scattering. The values of $\left. \frac{d\epsilon_1}{dz} \right|_e$ for $\epsilon_1 = 0$ and $\epsilon_1 \rightarrow \infty$ may be obtained from (2.5.12) and from the random scattering.

This expression clearly contains (2.5.8) (that is, $s_r = 1$, $s_c = A$) and, when applied to the electron gas model, gives very good agreement with the expression (2.5.10). It may, therefore, be expected to give a reasonable approximation to equation (2.5.11). The expression has been applied to the case of diamond in this work. The application of this function is discussed further in Chapter 5.

2.5.4 Damping

A reduction in transverse energy is brought about by electronic energy loss of the ion. In a pathlength dz a loss of energy dE will lead to a reduction in transverse energy [Bj 72]:

$$\frac{dE_1}{dz}(r) = - \frac{dE}{dz} \psi^2$$

where

$$E_1 = E\psi^2 + U(r)$$

Averaging this over the accessible area leads to [Bj 72]

$$\left. \frac{dE_1}{dz} \right)_{\text{damp}} = -\beta \frac{E_1}{E} \left\langle \frac{dE}{dz} \right\rangle$$

where $\beta = 0.5$ and $\left\langle \frac{dE}{dz} \right\rangle$ is the electronic energy loss averaged over $A(E_1)$. Since this term has a relatively small effect on the dechannelling [Bj 72], a relatively crude approximation is justified and $\left\langle \frac{dE}{dz} \right\rangle$ may be represented in a manner similar to equation (2.5.13)

$$\left\langle \frac{dE}{dz} \right\rangle = \frac{dE}{dz} \left(1 - \frac{e^{-\epsilon_1}}{\alpha} \right)$$

where α is a constant adjusted to fit the minimum energy loss at the channel centre.

2.5.5 Steady Increase Model of Dechannelling

If the rate of change of transverse energy with depth, $\frac{d\epsilon_1}{dz}$, is changing rapidly with transverse energy, the spread about some initial transverse energy will be much smaller than the nett change in transverse energy, along some pathlength δz [Lin 65]. In this case, the diffusion in transverse energy can be neglected, and the transverse energy of an ion will increase steadily according to $\frac{d\epsilon_1}{dz}$. In practice, the thermal contribution to the rate of change in transverse energy with depth greatly exceeds the electronic contribution, for large transverse energies, and increases rapidly in the region $E_1 \sim E\psi^{\frac{1}{2}}$. For this reason, the steady

increase model [Fot 71, Bj 72, Gr 73] has been applied to dechannelling calculations, in order to determine the yield as a function of depth.

The total change of transverse energy with depth is given by

$$\frac{d\epsilon_1}{dz} = \left(\frac{d\epsilon_1}{dz} \right)_n + \left(\frac{d\epsilon_1}{dz} \right)_e \quad (2.5.14)$$

(The inclusion of a damping term is considered by Björkvist et al [Bj 72]; its effect is found to be small.)

The transverse energy of an ion with initial transverse energy E_{10} will increase according to (2.5.14) until, at a depth z^* , the transverse energy is E_1^* and the ion is considered to be dechannelled into the random beam (that is, the square-well approximation (2.3.11) is applied) [Fot 71]. The function (2.5.14) increases monotonically and thus an ion with $E_1 > E_{10}$ will dechannel at a depth of $z < z^*$. The yield at z^* is thus [Fot 71]

$$\chi(z^*) = \int_{E_{10}}^{\infty} g(E_1) dE_1 \quad (2.5.15)$$

$$\equiv G(E_{10})$$

where

$$E_{10} = E_{10}(z^*),$$

The depth z^* is determined by [Fot 71]

$$z^*(E_{10}) = \int_{E_{10}}^{E_1^*} \frac{1}{\frac{dE_1}{dz}} dE_1. \quad (2.5.16)$$

The yield at any depth z^* may thus be found from $G(E_{10})$ and $E_{10}(z^*)$, defined implicitly by (2.5.16). The functions (2.5.15) and (2.5.16) may be easily computed by numerical integration, and the yield

$$\chi(z) = G(E_{10}(z))$$

determined most conveniently by graphical solution of $z^*(E_{10}) = z$.

2.5.6 Diffusion Model of Axial Dechannelling

A more general approach to the dechannelling of ions in the continuum equilibrium model is given by the diffusion model [Lin 65, Bod 72, Bel 72]. In this approach, the motion of ions to higher transverse energies is treated as a diffusion in transverse energy space, governed by the multiple scattering through the function (2.5.14).

From an approach based on the kinetic equation for transverse motion, the following Fokker-Planck-like equation (the 'diffusion equation') has been derived [Bod 72, Bel 72, Sc 75]

$$\frac{\partial f(\epsilon_1, z)}{\partial z} = \frac{1}{A(\epsilon_1)} \frac{\partial}{\partial \epsilon_1} \left[A(\epsilon_1) D(\epsilon_1) \frac{\partial f(\epsilon_1, z)}{\partial \epsilon_1} \right] + \frac{\partial}{\partial \epsilon_1} \left[A(\epsilon_1) f(\epsilon_1, z) \left. \frac{d\epsilon_1}{dz} \right|_{\text{damp}} \right] \quad (2.5.17)$$

where

$$f(\epsilon_1, z) = \frac{g(\epsilon_1, z)}{A(\epsilon_1)}$$

and where the diffusion function $D(\epsilon_1)$ is given by [Bod 72]

$$\frac{d\epsilon_1}{dz} = \frac{1}{A(\epsilon_1)} \frac{d}{d\epsilon_1} [A(\epsilon_1) D(\epsilon_1)] \quad (2.5.18a)$$

with $D(0) = 0$. Thus

$$D(\epsilon_1) = \frac{1}{A(\epsilon_1)} \int_0^{\epsilon_1} A(\epsilon_1') \left. \frac{d\epsilon_1}{dz} \right|_{(\epsilon_1')} d\epsilon_1' \quad (2.5.18b)$$

Here $\left. \frac{d\epsilon_1}{dz} \right|_{(\epsilon_1)}$ is given by equation (2.5.15) and $\left. \frac{d\epsilon_1}{dz} \right|_{\text{damp}}$ is the rate of

change of transverse energy due to damping of the transverse motion. The effect of the damping term is small [Bj 72, Sc 75] and it may often be neglected, to give

$$\begin{aligned} \frac{\partial f}{\partial z} &= \frac{1}{A(\epsilon_1)} \frac{\partial}{\partial \epsilon_1} \left[A(\epsilon_1) D(\epsilon_1) \frac{\partial f}{\partial \epsilon_1} \right] \\ &= D(\epsilon_1) \frac{\partial^2 f}{\partial \epsilon_1^2} + \frac{d\epsilon_1}{dz} \frac{\partial f}{\partial \epsilon_1} \end{aligned} \quad (2.5.19)$$

For small depths, the region of transverse energy in the neighbourhood of $E\psi_1^2$ is the most important in the variation of close encounter yields. Then $A(\epsilon_1) \approx 1$ and (2.5.19) reduces to [Bod 72]

$$\frac{\partial g(\epsilon_1, z)}{\partial z} = D(\epsilon_1) \frac{\partial^2 g}{\partial \epsilon_1^2} + \frac{d\epsilon_1}{dz} \frac{\partial g}{\partial \epsilon_1} \quad (2.5.20)$$

with

$$D(\epsilon_1) = \int_0^{\epsilon_1} \frac{d\epsilon_1}{dz} (\epsilon_1') \quad .$$

These equations must, in general, be solved numerically for $g(\epsilon_1)$ and the yield can then be determined from

$$\chi(z) = \int_0^{\infty} g(\epsilon_1, z) \Pi(\epsilon_1) d\epsilon_1 .$$

The numerical solution will be discussed in Chapter 5.

Simple solutions to equation (2.5.20) have appeared in various guises in the literature. Suppose that the multiple scattering is independent of position. Then it may be written in the form

$$\delta\Omega^2 = \frac{\psi_1^2}{z_D} \delta z \quad (2.5.21a)$$

where z_D is the distance in which $\delta\Omega^2$ becomes equal to ψ_1^2 . Then

$$\frac{d\epsilon_1}{dz} = \frac{2}{z_D} . \quad (2.5.21b)$$

With this, equation (2.5.20) may be solved using Laplace transforms to give, with an initial transverse energy distribution $g(\epsilon_1, 0) = \delta(0)$,

$$g(\epsilon_1, z) = \frac{z_D}{2z} e^{-\frac{\epsilon_1^2 z_D}{2z}} .$$

Using the square-well approximation to the reaction function

$\Pi(\epsilon_1)$ the yield is

$$\chi(z) = \exp \left\{ -\frac{\epsilon_1^2 z_D}{2z} \right\}$$

and, with $E_1^* = E\psi_1^2$ ($\epsilon_1^* = 2$),

$$\chi(z) = \exp \left\{ -\frac{z_D}{z} \right\} \quad (2.5.22)$$

This equation has been derived by Ellegaard and Lassen [El 67] by a simpler route from equation (2.5.21a) (and also using $\epsilon_1^* = E\psi_1^2$); their approach has sometimes been considered distinct from the diffusion approach [Ge 74]. Equation (2.5.22) predicts $\chi(0) = 0$, and therefore Ellegaard and Lassen incorporated the measured $\chi(0) = \chi_{\min}$ and wrote [El 67]

$$\chi(z) = \chi_{\min} + (1 - \chi_{\min}) \exp \left\{ -\frac{z_D}{z} \right\} .$$

They obtained a good fit to their experimental measurements of 5 MeV protons dechannelling in bismuth by varying z_D ; reasonable values of the fitting parameter were obtained. This approach was extended by Fujimoto et al [Fu 71 a,b] who allowed some initial spread in the transverse energy distribution and obtained [Fu 71 a,b]

$$x(z) = x_{\min} + (1 - x_{\min}) \exp \left\{ - \frac{z_D}{z + \Delta z} \right\} .$$

Both z_D and Δz were regarded as fitting parameters and good fits were obtained with experimental measurements of the dechannelling of protons in silicon [Fu 71a] and germanium [Fu 72]. Recently, Kitagawa [Ki 76] attempted to relate this approach to the general diffusion approach, by determining z_D from an average of the general $\frac{d\epsilon_1}{dz}(\epsilon_1)$ over the 'channelled' region of transverse energy space, $\epsilon_1 \leq \epsilon_1^*$.

Because of this interest in simple solutions of equation (2.5.20), using (2.5.21b), it is of interest to note that the equation can be solved using the transverse energy distribution for the single-string model, which in the absence of beam divergence and for $\psi_{in} = 0$, may be written, from (2.3.9)

$$g(\epsilon_1, 0) = (A - 1) \frac{Ae^{\epsilon_1}}{(Ae^{\epsilon_1} - 1)^2} .$$

Because $\frac{e^{-\epsilon_1}}{A} < 1$ this may be expanded as

$$g(\epsilon_1, 0) = (A - 1) \sum_{n=1}^{\infty} \frac{n}{A^n} e^{-n\epsilon_1} . \quad (2.5.23)$$

Equation (2.5.20) combined with (2.5.21b) may be written

$$\frac{\partial g}{\partial z} = \epsilon_1 \frac{\partial^2 g}{\partial \epsilon_1^2} + \frac{\partial g}{\partial \epsilon_1} \quad (2.5.24)$$

where the factor $\frac{z_D}{2}$ has been absorbed in the depth scale, that is, z is measured in units of $\frac{z_D}{2}$. This equation may be solved using Laplace transforms and the initial distribution (2.5.23); only one term of (2.5.25) need be considered owing to the linearity of the transform. Thus, introducing the two-dimensional transform

$$\bar{g}(n, s) = \int_0^{\infty} \int_0^{\infty} g(\epsilon_1, z) e^{-\epsilon_1 n - sz} d\epsilon_1 dz$$

equation (2.5.24) becomes, with $g(\epsilon_1, 0) = e^{-n\epsilon_1}$

$$n^2 \frac{d\bar{g}(n, s)}{dn} + (s + n)\bar{g}(n, s) = \frac{1}{n + n}$$

which has the solution,

$$\bar{g}(n, s) = \frac{1}{nn} e^{s(\frac{1}{n} + \frac{1}{n})} E_1(s(\frac{1}{n} + \frac{1}{n}))$$

where

$$E_1(x) = \int_x^{\infty} \frac{e^{-u}}{u} du .$$

Applying the inverse transform gives

$$g(\epsilon_1, z) = \frac{1}{zn + 1} e^{-\frac{n\epsilon_1}{zn+1}} .$$

Restoring the explicit dependence on z_D/z , the transverse energy distribution at depth z is

$$g(\epsilon_1, z) = (A-1) \sum_{n=1}^{\infty} \frac{1}{A^n} \frac{nz_D}{2nz + z_D} \exp \left\{ -\frac{nz_D \epsilon_1}{2nz + z_D} \right\}$$

and the yield, with the square-well approximation, is

$$\chi(z) = (A-1) \sum_{n=1}^{\infty} \frac{1}{A^n} \exp \left\{ -\frac{nz_D \epsilon_1^*}{2nz + z_D} \right\} . \quad (2.5.25)$$

This equation is applicable at small depths where (2.5.20) applies. At these depths, the change in yield is determined mainly by diffusion in the region $\epsilon_1 = \epsilon_1^*$, and a diffusion constant, z_D , which applies in this case is sought. The averaged value of Kitagawa [Kit 76] may be used; however, it is possible to find a value more suitable for the depth region

under consideration. Thus, taking the more general case, the square-well approximation may be applied to (2.5.19) for $z = 0$, with the result, after integration by parts

$$\begin{aligned} \left. \frac{d\chi}{dz} \right|_{z=0} &= A(\epsilon_1^*) D(\epsilon_1^*) \left. \frac{\partial f}{\partial \epsilon_1} \right|_{\epsilon_1 = \epsilon_1^*} \\ &= D(\epsilon_1^*) \left. \frac{\partial g}{\partial \epsilon_1} \right|_{\epsilon_1 = \epsilon_1^*} \end{aligned}$$

since $A(\epsilon_1^*) = 1$. This also holds for (2.5.24). Thus, for small depths, z_D can be determined by

$$\frac{1}{z_D} = \frac{D(\epsilon_1^*)}{2\epsilon_1^*} \quad (2.5.26)$$

where $D(\epsilon_1^*)$ is determined from equation (2.5.18). Thus (2.5.25), with (2.5.26), is expected to be a good approximation for the yield as a function of depth, for small depths. The analytical solution of the diffusion calculation is also useful for checking programs for numerical solution.

Another version of a diffusion equation has been given by Kitagawa and Ohtsuki [Kit 73]. However, results with this equation are not in agreement with experiment [Om 77].

2.5.7 Dechannelling by Defects

If defects are present in the crystal (for example, atoms displaced by radiation damage, dislocations or stacking faults, etc) these will scatter ions and lead to an increase in yield. The distribution of defects is usually regarded as random, and a simplified treatment based on the square-well approximation is used. In this approximation, the portion of the beam with $\epsilon_1 \leq \epsilon_1^*$ may be regarded as channelled, and that with $\epsilon_1 > \epsilon_1^*$ as random. There are then two contributions to the dechannelled yield: a contribution $\chi_R(z)$ from the random portion of the beam, which will depend on the concentration of defects from the surface to the depth z , and a contribution from direct scattering from the defects at depth z . If $n_D(z)$ is the probability of back-scattering of a random beam from the defects at z , the total yield at z becomes [Bøg 67]

$$\chi_T(z) = \chi_R(z) + (1 - \chi_R(z)) n_D(z) . \quad (2.5.27)$$

Extended defects such as dislocation have a large dechannelling effect and a small contribution to the direct yield, and then

$$\chi_T(z) = \chi_R(z) .$$

The random yield $\chi_R(z)$ contains contributions from the beam dechannelled by the defects up to depth z , and the main problem of the theory is to predict $\chi_R(z)$. The yield at depth z in a perfect crystal, $\chi_p(z)$, is usually assumed known. Three models are used [Beh 76]: a single scattering model [Bøg 67] which applies for small defect concentrations, a multiple

scattering model [Bøg 67, Fel 70] which applies for large concentrations of randomly displaced atoms, and a plural scattering model [Wes 70] which is applied to all concentrations of randomly displaced atoms, and approaches the single scattering and multiple scattering models in the limits of small or large defect concentrations.

The single scattering model may be applied to cases in which the concentration of displaced atoms is small, or in which the scattering cross-section is large (that is, larger than the 'area', $1/Nd$, of a channel) and small perturbations of the ion orbits do not need to be considered. Ions that are scattered through angles larger than $\psi_{\frac{1}{2}}$ are regarded as being dechannelled. Suppose that the concentration of defects is $n_D(z)$ and the cross-section for scattering through angles larger than $\psi_{\frac{1}{2}}$ is σ_D . Then the fraction of the beam that has been scattered at depth z is [Bøg 67]

$$P_S(z) = 1 - \exp \left\{ - \int_0^z n_D(z) \sigma_D dz \right\}$$

and thus, from (2.5.27) applied to χ_p ,

$$\chi_R(z) = \chi_p(z) + (1 - \chi_p(z)) P_S(z).$$

In the multiple and plural scattering models [Bøg 67, Fel 70, Wes 70], the channelled portion of the beam is assumed to be spread in angle from an initial delta-function distribution by plural or multiple scattering by the

defects, usually considered to be an amorphous layer. If the plural or multiple scattering distribution at depth z is $f(\psi, z)$, the fraction of the beam that has been scattered beyond ψ_2 and is dechannelled is [Bog 67]

$$P_M(z) = \int_{\psi_2}^{\infty} \psi \, d\psi \, f(\psi, z)$$

and the yield at z is thus

$$x_R(z) = x_p(z) + (1 - x_p(z)) P_M(z)$$

The multiple and plural scattering treatments differ in the description used for $f(\psi, z)$, which is a function of

$$\int_0^z n_D(z) \, dz$$

The multiple scattering model assumes a Gaussian distribution with a mean-square deviation in angle integrated from equation (2.5.1). Thus

[Beh 76]

$$P_M(z) = \exp \left\{ - \frac{\psi_2^2}{\Omega^2(z)} \right\}$$

This neglects the contribution of single scattering to the tail of the distribution, and thus under-estimates the yield at small defect concentrations. This is taken into account in plural scattering models, where the distribution must be obtained from a plural scattering treatment such as that of Meyer [Mey 71, Si 74].

Both of these latter models suffer from the defect that the spread in transverse energies is neglected, and the channelled beam is considered to be spread only by the defects. The dechannelled fraction of the beam in the perfect crystal is then included as an independent quantity. A better approximation may be to assume (in the multiple scattering model)

$$x_R(z) = \exp \left\{ - \frac{\psi_d^2}{\Omega^2(z) + \Omega_p^2(z)} \right\}$$

where

$$x_p(z) = \exp \left\{ - \frac{\psi_d^2}{\Omega_p^2(z)} \right\}$$

defines the function $\Omega_p^2(z)$. This treats the diffusion in the perfect and damaged crystals on the same basis, although it in effect assumes a constant rate of transverse energy increase with depth in the perfect crystal. A similar approximation might be applied to the plural scattering model.

The best way of describing the scattering effects of defects is to include them in the diffusion model of dechanneling. This has been attempted by Matsunami and Itoh [Mas 73, Mas 75] who calculated a diffusion function for defects located in specific interstitial sites in KCl crystals.

A cut-off procedure was applied to limit the scattering to small angles, and large angle scattering was neglected.

A general treatment of the dechannelling by defects would be based on the diffusion model and would include the effect of single scattering. Scattering through angles smaller than some cut-off ψ_c are included in the diffusion term, while scattering angles larger than ψ_c contribute to the single scattering term. These ions may be regarded as lost to the channelled beam (that is, they are scattered to a large angle and the probability of diffusing to small transverse energies is negligible) and may be included in an absorption term. Scattering through an angle larger than $\psi_c \sim \psi_1$ requires a small impact parameter, and the reaction function for these ions may be determined from the distribution $P_D(r)$ of defect atoms in the transverse plane, that is

$$\Pi_D(\epsilon_1) = \frac{1}{A(\epsilon_1)} \int_{U(r) \leq E_1} P_D(r) d^2r$$

If the cross-section of the defects is σ_D , the change in the transverse energy distribution due to the single scattering is

$$\frac{\partial g(\epsilon_1, z)}{\partial z} = -\sigma_D \Pi_D g(\epsilon_1, z)$$

Scattering through angles smaller than ψ_c contributes to the rate of

change of transverse energy with depth through a term $\left. \frac{d\epsilon_1}{dz} \right|_D$. Thus the diffusion equation becomes (from 2.5.17)

$$\begin{aligned} \frac{\partial f}{\partial z} = & D_T \left(\frac{\partial^2 f}{\partial \epsilon_1^2} + \frac{\partial \epsilon_1}{\partial z} \right)_T \frac{\partial f}{\partial \epsilon_1} \\ & + \frac{\partial}{\partial \epsilon_1} \left[A(\epsilon_1) f \left. \frac{\partial \epsilon_1}{\partial z} \right|_{\text{damp}} \right] - \sigma_D \Pi_D(\epsilon_1) f(\epsilon_1, z) \end{aligned} \quad (2.5.28)$$

where

$$\left. \frac{\partial \epsilon_1}{\partial z} \right|_T = \frac{\partial \epsilon_1}{\partial z} + \left. \frac{\partial \epsilon_1}{\partial z} \right|_D$$

$$D_T(\epsilon_1) = D(\epsilon_1) + D_D(\epsilon_1)$$

With the inclusion of the last term in (2.5.28), the transverse energy distribution is no longer normalised to unity, and the fraction of ions absorbed is

$$x_A(z) = 1 - \int_0^{\infty} g(\epsilon_1, z) dz$$

The yield at depth z then becomes

$$\chi_R(z) = \int_0^{\infty} \Pi(\epsilon_1) g(\epsilon_1, z) d\epsilon_1 + \chi_A(z). \quad (2.5.29)$$

This equation may be applied to take account of the single scattering by thermally vibrating atoms discussed in Section 2.5.2. The cross-section for scattering through an angle larger than ψ_c may be determined using the impulse approximation to the scattering angle [Lin 65]. This gives the scattering angle ψ as a function of impact parameter b as [Lin 65]

$$\psi(b) = -\frac{d}{2E} \left. \frac{dU(r)}{dr} \right|_{r=b}.$$

With the approximation (2.2.6) valid for small r , this gives

$$\psi(b) = \frac{Z_1 Z_2 e^2}{E} \frac{1}{b}$$

and, thus,

$$\sigma = \pi \left[\frac{Z_1 Z_2 e^2}{E} \right]^2 \frac{1}{\psi_c^2}. \quad (2.5.30)$$

In the application of (2.5.30) to thermal vibration scattering, the

distribution of vibrating atoms as a function of ϵ_1 is given by (2.3.13) that is,

$$\sigma_T \Pi_T = \pi \left[\frac{Z_1 Z_2 e^2}{E} \right]^2 \frac{1}{\psi_c^2} \exp \left(\frac{C^2 a^2}{v_2^2} [Ae^{\epsilon_1} - 1]^{-1} \right) . \quad (2.5.31)$$

2.5.8 Planar Dechannelling

Considerations similar to those for axial dechannelling apply to planar dechannelling, except that the motion and scattering are one-dimensional: scattering parallel to the plane having no effect on the dechannelling. Thus the yield, as a function of depth, may be determined from a diffusion model or a steady-increase model similar to those for the axial case. However, it is observed experimentally (for example, [Ap 68]) that the channelled fraction of the beam (that is, $1 - \chi(x)$) decreases exponentially as the depth x increases, that is, $\chi(x)$ may be represented as

$$(1 - \chi(x)) = (1 - \chi(0)) e^{-0.693 \frac{x}{x_1}}$$

where x_1 is a dechannelling half-length.

Such behaviour can be obtained theoretically from solutions to a simple diffusion equation with constant scattering as a function of position in the channel, and with fixed boundary conditions $n(\theta_c, x) = 0$, where $n(\theta, x)$ is the distribution in crossing angle θ defined by $E\theta^2 = E_1$,

x is the depth, and θ_c is the critical crossing angle $\theta_c = \theta_{\frac{1}{2}}$. Neglecting the nuclear scattering term which is relatively small under planar channelling conditions (for $\theta < \theta_c$) and assuming equipartition between close and distant electronic collisions, Feldman et al [Fel 68] obtained such a solution, which yields

$$\frac{F}{x_{\frac{1}{2}}} = 0.62 \frac{M_1}{m_e} E \theta_c^2 \frac{1}{\frac{dE}{dx}} \quad (2.5.32)$$

Similar results have been obtained by Morita and Itoh [Mor 71], and Beloshitsky et al [Bel 73]. It should be noted that this approach assumes that the channelled and random fractions of the beam are independent and does not allow rechannelling of the dechannelled portion.

Morgan [Mog 79] has pointed out that the initial dechannelling rate obtained from this approach is a factor of 24 too large compared with experiment and computer simulations or, equivalently, the half-length is too small by this factor. He has pointed out that the whole dechannelling curve is determined by the initial dechannelling rate and has evaluated this in a steady-increase approximation. This approach [Mog 79] yields

$$\frac{M}{x_{\frac{1}{2}}} = 0.693 \frac{M}{m_e} d_p Y'(y_c) \frac{1}{\frac{dE}{dx}} \quad (2.5.33)$$

where $Y'(y_c)$ is the slope of the continuum planar potential at the critical approach distance y_c defined by $Y(y_c) = E \theta_c^2$, and

where equipartition has been assumed. Morgan found that this approach gave closer agreement with experiment. The validity of both of these approaches for diamond is considered in Chapter 5.

2.6 THERMAL VIBRATION AMPLITUDES

The mean thermal vibration amplitude is often required in calculating quantities in channelling theories. This is denoted u_1 for vibrations in one dimension and u_2, u_3 for vibrations in two or three dimensions, with

$$u_3 = \sqrt{3} u_1 \quad \text{and} \quad u_2 = \sqrt{2} u_1$$

In common with other works on channelling, this has been calculated from the Debye approximation (for example, [Ge 74])

$$u_1 = 12.1 \left(\left[\frac{\phi(x)}{x} + \frac{1}{2} \right] / M_2 \theta_D \right)^{\frac{1}{2}} \text{ \AA}$$

where $\phi(x)$ is the Debye function plotted, for example, in [Ge 74] and tabulated in [Abr 70], $x = \frac{\theta_D}{T}$ where T is the crystal temperature in Kelvin, and θ_D is the Debye temperature. The value used for θ_D for diamond was $\theta_D = 1860$ K [Vic 62]. The calculated thermal vibration amplitude, u_2 , as a function of temperature is shown in Figure 2.9.

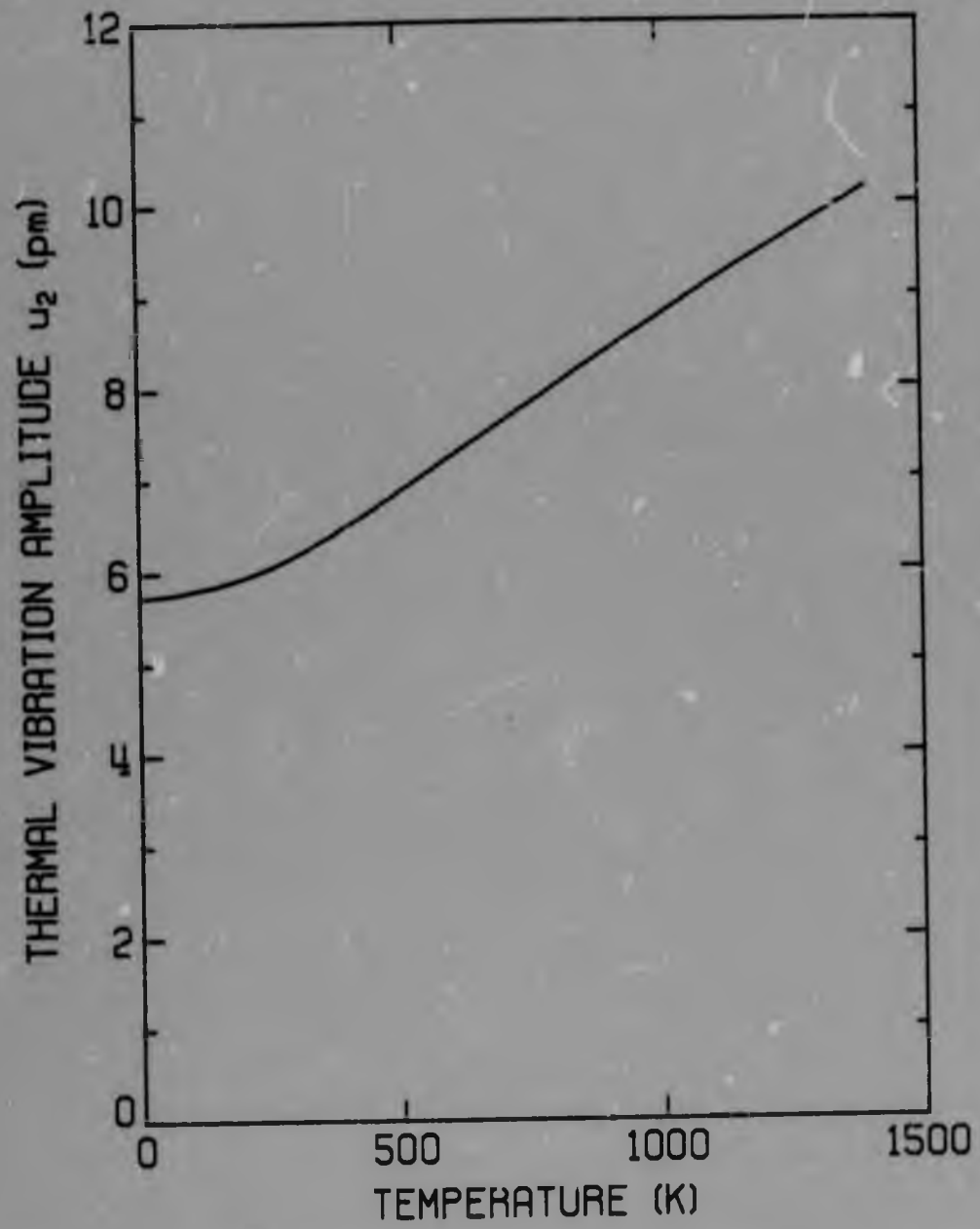


Figure 2.9: Two-dimensional thermal vibration amplitude for diamond as a function of temperature.

APPARATUS AND METHODS

3.1 INTRODUCTION

The basic requirements for the performance of ion-channelling experiments are well known [Ge 74]. In addition to the usual experimental apparatus of accelerator-based ion-beam experiments (that is, evacuated beam lines and scattering chambers, suitable detectors and associated electronic hardware), channelling experiments require a high degree of collimation of the ion beam incident on the target, and some means of accurately aligning the target with respect to the ion beam, that is, a goniometer which must be capable of operation under vacuum.

The experiments described in this work were performed on the channelling lines of the two accelerators of the Nuclear Physics Research Unit (NPRU). The apparatus used in these measurements, and the general experimental methods are described in this Chapter.

3.2 APPARATUS

3.2.1 Accelerators

Two accelerators were used for the measurements. 'Low' energy experiments, with beam energies less than 1.4 MeV were performed on a Philips PWS121 pressurised Cockcroft-Walton accelerator. Beams of protons, deuterons or alpha particles could be obtained from an Ortec R F ion source. 'High' energy experiments, with beam energies greater than 2 MeV were performed on a HVEC EN Tandem van de Graaff accelerator. Protons, alpha's or ${}^7\text{Li}$ ions were produced from a duoplasmatron ion source.

Beam energies were calibrated using nuclear reactions, with an accuracy of 0.4% for the low energy machine and 0.06% for the high energy machine. The beam energy was stabilised in the usual way, with feedback from the slits located after the analysing magnet. The energy spread of the beam, as defined by the slits and analysing magnet, was 0.3% for the low energy machine and 0.06% for the high energy machine.

3.2.2 Channelling Beam Line and Scattering Chamber

The beam line is shown diagrammatically in Figure 3.1. The beam was collimated before entering the chamber by two apertures, spaced 2.4 m apart on the low energy machine and 5.1 m apart on the high energy machine. The downstream collimator was formed by a circular aperture 0.5 mm or 0.7 mm in diameter, in a tantalum disc. This was followed by an antiscatter collimator. The upstream collimator was formed by two sets of slits, placed at right angles to one another. These slits were adjusted to give an aperture of 0.5 to 1.0 mm, so that the half angle of beam divergence defined by the collimator system was less than 5% of the critical angle of the channel under study. Typical values of the half-angle used were 0.3 m rad at 1 MeV and 0.1 m rad at 12 MeV. The slit edges and bore of the downstream collimator were polished to a high finish to minimise slit edge scattering [Res 69]. This procedure reduced the scattering to negligible proportions, as determined by backscattering from a target with an aperture which allowed the non-scattered beam to pass through.

The scattering chambers were pumped with Balzers turbo-pumps. Copper cold shields cooled with liquid nitrogen surrounded the target in order to minimise deposition of organic vapour onto the target. Measured operating vacua were less than 10^{-6} torr. The chambers were provided

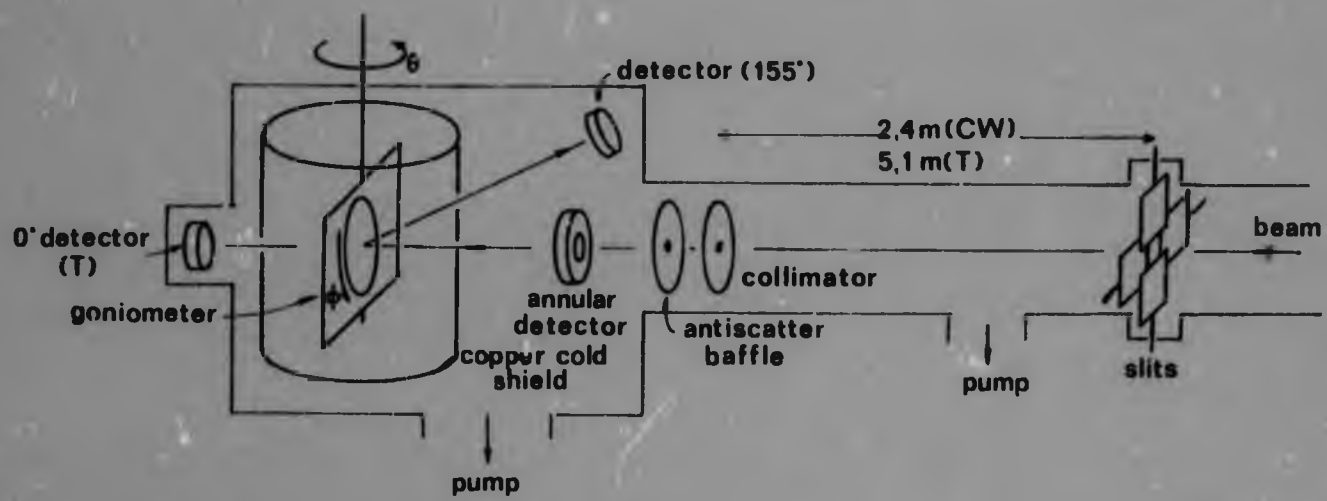


Figure 3.1: Schematic diagram of channelling lines for Cockcroft-Walton (CW) and Tandem (T) accelerators.

with a number of ports for windows and feed-throughs. In the low energy chamber a PHI ion sputtering gun was mounted in one of these ports in a sliding holder which enabled it to be positioned 2 cm from the target if sputtering was required, or to be retracted when it was not required. When this gun was in use, the chamber was back-filled with spectrographic quality argon to a pressure of 5×10^{-5} torr.

3.2.3 Goniometer

The goniometer design has been fully described by Derry [Der 78]. It is a two-axis design, designed and built at the NPRU, with full 360° rotation on both polar (θ) and azimuthal (ϕ) axes, in steps of 0.01° . Settings were always made by approaching the required value in the direction of increasing angle, in order to minimise the effects of backlash; this allowed an accuracy of $\pm 0.01^\circ$ to be achieved. The goniometer motions were driven from outside the vacuum by stepping motors controlled from the data gathering area of the accelerator control room. The controls provided variable speeds, allowed the setting of upper and lower limits to 0.01° and gave a digital readout of the current angular position.

The target was mounted in a translation stage contained in the ϕ spool of the goniometer. The position of the beam on the target could be adjusted to an accuracy of 0.1 mm along two mutually perpendicular axes, while maintaining the coincidence of the goniometer axes and the beam position. Adjustment could be made from outside the vacuum and covered a range of 4 mm on both axes. The translation stage was designed for both transmission and back-scattering work and provided thermal and electrical insulation of the target by means of a pyrophyllite or Makor

(Dow Corning Inc) insert. The goniometer design, including the translation stage, permitted angles of incidence up to 70° from the target normal to be used.

The target holder was designed so that it could be inserted in the goniometer in a unique orientation, as an aid to alignment of the target. The target was clamped rigidly between two sections, with the target surface in the place of the goniometer axes. Provision was made for clamping an insulated chromel-alumel thermocouple in the region of the target and a resistive target heater could be bolted to the back of the target holder. This used an insulated Thermocoax element and temperatures of 750°C could be achieved with a power input of 100 W. The goniometer spool temperature was monitored close to the bearing surface and rose to 120°C at the maximum target temperature of 750°C . The heater was powered by lead-acid batteries as it was found that leakage currents from mains-powered power supplies interfered with beam current measurements.

3.2.4 Detectors and Pulse Handling

Backscattered particles were detected in both chambers by silicon detectors mounted at a scattering angle of 155° . Collimators in front of the detectors ensured that the detector resolution was not compromised by the kinematic spread in energy introduced by the angle subtended by the detector. Solid angles subtended were of the order of 5 m steradians. The detectors were mounted in the plane defined by the beam and the goniometer θ axis (Figure 3.1). The particle pathlengths for scattering from a fixed depth as measured along the beam, were thus independent of the θ setting.

For room-temperature studies, an Ortec BE-014-050-100 detector (14 keV resolution) was used on the low energy apparatus and a BE-012-050-500 on the high energy apparatus. At elevated temperatures Ortec ruggedised series (BR-016-050-100 or 016-050-1000) were used, as the reflective aluminium front electrode of these rendered them insensitive to the infra red radiation from the target which causes an increase in the noise level from standard gold electrode detectors.

The low energy chamber also contained an Ortec TC-018-150-500 annular detector mounted concentrically with the beam at a mean scattering angle of 177° . This subtended a larger solid angle than the 155° detector ($\sim 10^{-2}$ sr) but had worse resolution. It was generally used for alignment of the target, where the higher count rate at a given beam fluence, compared with the 155° detector (the increase in solid angle more than compensating for the decrease in cross-section due to the larger scattering angle) meant that less target damage occurred.

The high energy chamber contained, in addition, two detectors at forward angles for transmission studies. An Ortec BA-016-050-1000 detector was positioned at 0° , 600 mm from the target, and was collimated to subtend a solid angle of 2μ steradians. This detector was mounted on a stage which enabled it to be translated along two axes perpendicular to the beam direction for accurate alignment, which was performed by aligning the detector for maximum transmission of the beam with no target in the goniometer. It was confirmed that the situation was unchanged with the target in a random orientation. An Ortec annular detector was placed concentric with the beam path at a distance of 100 mm to 250 mm from the target, corresponding to scattering angles of 10° to 4° . This

detector was used as a monitor in aligning the target for transmission studies, and the distance from the target was chosen to give a count rate comparable with the 0° detector, this distance depending on the multiple scattering produced by the target.

Standard nuclear electronics were used to amplify and analyse the detector pulses as shown in Figure 3.2. At higher energies, it was found advantageous to use a pile-up rejector (Canberra 1468), even though the count-rate was not exceptionally high, as it was found to clean up the spectrum above the carbon edge considerably, while rejecting only a small proportion (typically 5%) of the pulses. The system dead-time was monitored with scalers and the spectrum could be corrected for it.

Pile-up rejection was not used at lower energies as it introduced additional low-energy cut-off and some distortion of the lower edge of the spectrum. This was not serious at higher energies as the larger portion of the beam was generally dechannelled at the depths corresponding with these energies.

Pulses were analysed in Nuclear Data 4420 or 2400, or Canberra 8180 analysers. The pulse-height analysers (PHA) were calibrated by backscattering particles from a graphite target with thin (<1 keV energy loss) layers of ^{27}Al , ^{56}Ni and ^{197}Au evaporated onto it. ^{16}O was also present, probably associated with the ^{27}Al . For convenience, the system was usually adjusted for a gain of 5.00 keV per PHA channel, with a zero base-line intercept. The system was found to be linear within ± 2 keV overall.

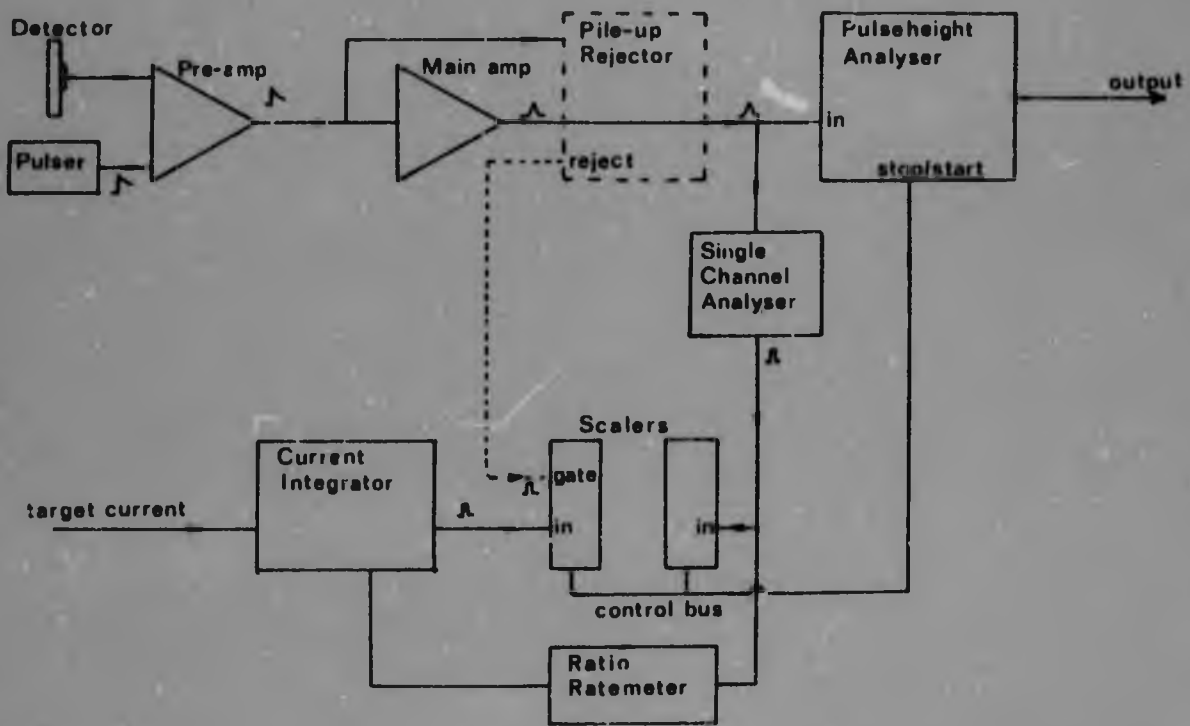


Figure 3.2: Block diagram of electronics.

3.2.5 Beam Current Measurement

An important consideration in ion beam experiments, especially when spectra are to be compared with one another as in channelling measurements of yield relative to random, is the accurate measurement of beam currents. This is generally complicated by the emission of secondary electrons from the target, which adds to the measured beam current, and those electrons are often 'suppressed' by some means, such as placing a ring at high potential in front of the target to prevent electrons from leaving the target or occasionally by using magnetic suppression with the same aim. A further complication arises with insulating targets where charge build-up on the target occurs, which leads, in the worst cases, to beam current being 'measured' only as a series of sporadic discharges through the current measuring system.

It proved possible to obtain a continuous measure of beam current on most diamonds, with only a few showing drastic discharges and noticeable flashes across the diamond surface. When a conventional 'ring' type electron suppression system was used, consisting of a plate with a shaped aperture held at a negative potential in front of the target, it was found that the measured target current was independent of the suppression potential, except on semiconducting (type IIb) diamonds or on diamonds with a surface damaged by ion milling. It was thus evident that the targets were charging and providing a source of self-suppression once equilibrium was reached. The potential reached was also presumably sufficient to drive an equilibrium current to the metal target holder. This target charging was also sufficient to affect channelling measurements by producing a beam current dependent deflection of the beam, if the target surface was not normal to the beam (that is, for $\theta \neq 0$). Thus

it was found that the position of an axis at $\theta \sim 45^\circ$ would shift by about 0.1° in θ for a change in beam current of 4 nA, the change being such that the beam was deflected away from the target as the beam current increased. The target potential required for this was estimated at 2 keV [Der 78].

A method of target neutralisation was thus developed, which still allowed the beam current to be easily measured (Figure 3.3). A filament and grid assembly from a valve was used as an electron source after carefully breaking the glass envelope and removing the anode structures. This was then mounted about 3 cm from the target. The filament was powered from a lead-acid accumulator and the grid was biased at about +120 V in order to provide some acceleration of the electrons towards the target; the HT for the grid was supplied from a simple DC to DC convertor [Bol 65] powered from the lead-acid battery. The entire chamber was insulated and protected against any flux of secondary electrons from the collimation line. The beam current was then measured from the chamber which acted as a Faraday cup.

Other sources of electrons were initially tried, that is, a tungsten filament and a carbon filament [Ah 75]. Those both led to rapid contamination of the target with tungsten or carbon. The valve, with its indirectly heated cathode, was found to produce no contamination, as measured by alpha backscattering from a diamond target, even after 24 hours with the filament voltage over-run by 50%.

It was found important to insulate the batteries from the concrete floor: the small current across the battery surface, which is difficult

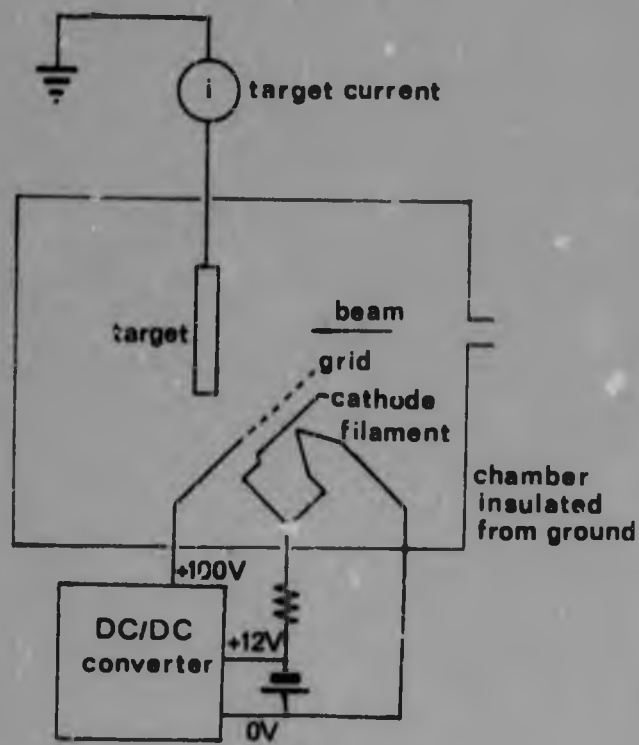


Figure 3.3: Arrangement used for target current monitoring while preventing target charging.

to keep free of small quantities of electrolyte, was grounded through the concrete and caused random fluctuations in the beam current. On the high energy machine, target charging effects were found to be negligible. This is understandable in terms of the energy dependence of secondary electron emission [Ste 57] and the surface deflection. These combine to give an energy dependence of the deflection of E^{-a} , where a is approximately 1.75 to 2 in the Bethe-Bloch stopping region. This decreases much more rapidly than the critical angle ($E^{-1/2}$) and so becomes negligible at high energies. Conventional electron suppression techniques were thus used; a plate in front of the target was held at a potential of 1.5 keV. The size of the plate and its aperture, and the distance from the target holder were determined so as to maximize the suppression efficiency [Der 78].

3.3 METHODS

3.3.1 Location of Channels

The location of channels was facilitated by the use of Laue backscatter photographs of the crystal, taken with the crystal mounted in the target holder. The angular position of the desired channel was then read off the photograph to within 1° by means of a Geringer net. Once the target was mounted in the goniometer, the region of the channel was slowly scanned and the channel located more precisely with the aid of a ratio-ratemeter, which measured the ratio of the backscattered counts in a region of the spectrum selected with a single-channel analyser (SCA), to the signal from the beam current integrator. Thus the channel was indicated by a decrease in the ratio. Finally, the region was scanned in small steps on both axes (or perhaps one axis for planes), while the pulses from the SCA were counted for a fixed beam charge. This final

procedure was iterated until the minimum had been found. This enabled the channel to be located to $\pm 0.01^\circ$.

Occasionally a channel was sought at such an angle that the related spot was located off the X-ray photograph. The position was first estimated from the pattern on the photograph and if it was not found in the estimated position, the position was predicted by spherical trigonometry from the position of known axes.

3.3.2 Angular Scans across Channels

The yield as a function of angle from a channel position is sensitive to the azimuth of the plane in which the scan is made for axial channels and to the (angular) distance from the axis for planar scans. It is also important that scans be made along a great circle path. The question of optimal scan orientations was considered by Derry [Der 78] and his recommendations are adhered to in this work: the planes used for scans across axes and planes are reported in Table 3.1.

Table 3.1

SCAN PLANE ORIENTATIONS FOR ANGULAR SCANS

<u>axis</u>	<u>angle from {110}</u>	<u>plane</u>	<u>angle from <110></u>
<110>	$75^\circ \pm 5^\circ$	{110}	$9.2^\circ \pm 0.2^\circ$
<111>	$17^\circ \pm 2^\circ$	{111}	$10.0^\circ \pm 0.3^\circ$
<100>	$30^\circ \pm 1^\circ$	{110}	$8.6^\circ \pm 0.2^\circ$

in order to perform the scan along a desired great circle path,

both axes on the goniometer had to be varied together. The setting for the θ and ϕ axes for a given scan angle were determined by calculation [Der 78].

3.3.3 Data Handling

Energy spectra recorded in the pulse-height analysers were rarely in a form suitable for direct analysis. In particular, it is often desirable to normalise a spectrum to a random orientation spectrum (in order to eliminate the effect of energy dependence of reaction cross-section and stopping-power on the spectrum shape) and to relate the energy scale of a spectrum to the depth of interaction in the target crystal. Spectra from pulse-height analysers were recorded on tape or printed out. A computer program (see Appendix 1) was written to allow the analysis of these on the NPRU's Perkin Elmer 7/32 computer. The program allowed a great degree of flexibility in performing the routine data manipulation required, that is, normalisation to random, conversion from an energy to a depth scale, deconvolution of the spectrum edge and surface peak, and data smoothing.

3.3.4 Random Spectra

The obtaining of a 'random' spectrum using a crystalline target is not without problems. The method of Ziegler and Crowder [Z1 72] was used in this work: the crystal was offset by about 10° from a major axis and rotated about this axis through an angle related to the crystal symmetry. By using this method, a repeatable random spectrum could be obtained, and spectra recorded at different times on different crystals agreed within $\pm 3\%$. Ziegler and Crowder reported small differences between spectra taken with this method on silicon crystals, and spectra

taken on amorphous silicon targets, and suggested correcting for this. It is possible, however, that this difference is not due to crystal effects on the scattering, as they suggested, but to differences in stopping-power in the two silicon forms due to chemical bonding effects [Sof 61, Mat 76], and similar corrections were not used in this work. The corrections are, in any case, small.

3.3.5 Determination of Depth Scale

In a thick-target backscattering spectrum (for example, Figure 5.1) the energy E_2 at which an ion of initial energy E_0 leaves the target may be used to determine the depth of scattering in the target, and hence to assign a depth scale to the spectrum. The relationship between energy and depth is illustrated in Figure 3.4. An ion of energy E_0 loses energy at a rate of $\frac{dE}{dx}$ along the incident path to a depth, z , where the energy is E_1 . The ion is then elastically scattered, losing energy $(1 - k^2)E_1$ and then loses energy along the emergent path, leaving the crystal with energy E_2 . The backscattering factor k^2 may be determined from the usual scattering kinematics [Man 68]

$$k^2 = \left[\frac{M_1 \cos \theta_s + \sqrt{M_2^2 - M_1^2 \sin^2 \theta_s}}{M_1 + M_2} \right]^2$$

where M_1 is the mass of the incident ion, M_2 the mass of the scattering atom and θ_s the scattering angle in laboratory co-ordinates. Thus

$$E_2 = k^2 \left[E_0 - \int_0^{z/\cos \theta_1} \frac{dE}{dx} dx \right] - \int_0^{z/\cos \theta_2} \frac{dE}{dx} dx .$$

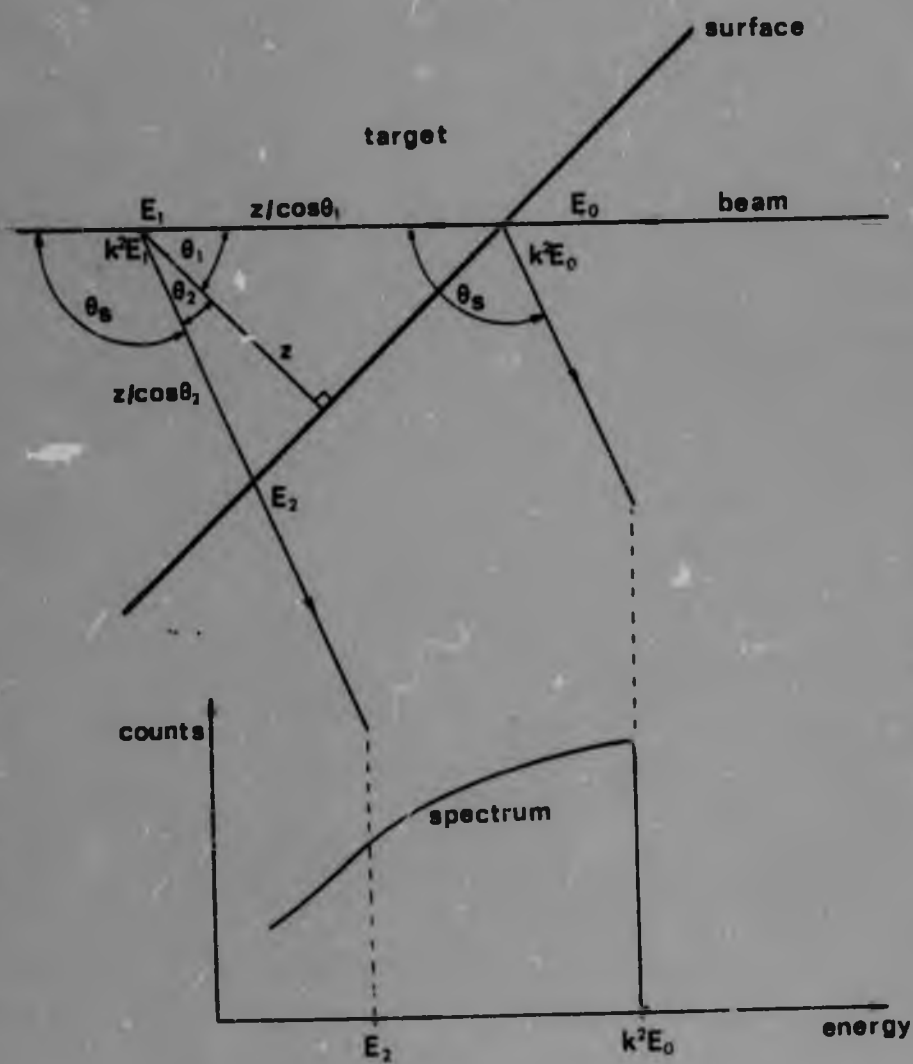


Figure 3.4: Schematic representation of relationship between ion beam penetration and scattering, and the backscattering spectrum.

This equation is often approximated in linear form by ignoring the slow variation of $\frac{dE}{dx}$ (for small depths z) to obtain [Bøg 67]

$$E_2 = k^2(E_0 - \frac{dE}{dx}(E_0)\frac{z}{\cos\theta_1}) - \frac{dE}{dx}(E_2)\frac{z}{\cos\theta_2}$$

Hence, z may be obtained from E_2 . Since $\frac{dE}{dx}$ is a function of E and not z , a more general depth determination requires solution of the equations:

$$z = \frac{1}{\cos\theta_1} \int_{E_0}^{E_1} \frac{-1}{\frac{dE}{dx}} dE = \frac{1}{\cos\theta_2} \int_{k^2 E_1}^{E_2} \frac{-1}{\frac{dE}{dx}} dE$$

Depth-energy tables were constructed by solving these equations using numerical integration and Newton-Raphson iteration.

The range of the ion is given by

$$R(E) = \int_E^0 \frac{-1}{\frac{dE}{dx}} dE$$

and hence the depth may also be found by using

$$\int_E^{E'} \frac{-1}{\frac{dE}{dx}} = R(E) - R(E')$$

if a suitable expression for the range is available [Za 74]. This method due to Zaidins, was incorporated in the program CHANSPEC (Appendix 1) with [Za 74]:

$$R(E) = \frac{0.585 E^{7/4}}{C[1 - \exp(-\frac{3}{7} \alpha E)]}$$

with parameters for protons in diamond

$$C = 0.09026 \text{ MeV}^{7/4} \text{ } \mu\text{m}^{-1}$$

$$\alpha = 8.9 \text{ MeV}^{-1}$$

The accuracy of this expression is $\sim 5\%$ at high energies.

3.3.6 Radiation Damage to Targets

In order to minimize the effect of radiation damage on the spectra obtained, the limits of beam fluence recommended by Derry were adhered to [Der 78]. That is, the beam-spot was changed if the fluence at that point on the target exceeded $\sim 10^{16}$ ions. cm^{-2} for protons at 1 MeV.

This limit was extended to higher energies by assuming that the damage rate scaled in energy with the nuclear stopping-power [Lin 68]. In addition, because the major portion of the damage lies at the end of the particle path, for high energy light ions, spectra were never taken at higher energies on a spot which had been used at lower energies, and proton spectra were never taken on a spot that had been used to take alpha spectra.

DIAMONDS: PROPERTIES, SELECTION AND PREPARATION

4.1 INTRODUCTION

The adoption of diamond as a target in channelling experiments implies the use of natural crystals. Synthetic diamonds are indeed grown, but these are rarely large enough to use without microbeam techniques, and furthermore contain metallic inclusions in quantities ranging from several tenths of a percent to several percent by weight [Wo 73]. They are not, therefore, good crystals for channelling purposes. The use of natural diamond means that there can be no control over crystal perfection or purity, and consideration must thus be given to the extent to which the results are characteristic of diamond itself rather than the product of the defects and impurities in a given sample.

Fortunately, the defects and impurities of natural diamond have been studied for many years, and many simplifying relationships have been brought to light. In particular, it is possible to divide diamonds into two types, each with two subdivisions, namely Types Ia, Ib, IIa and IIb. This classification is made on the relatively restricted basis of nitrogen-dependent optical properties and on electrical properties and, although there can be some mixing between the types, the members of each class are broadly similar in terms of the nature of their predominant impurities and defects. A more detailed characterisation of an individual diamond can be obtained by thorough study of the optical properties from

the infra-red to the ultra violet [Dav 77], by X-ray topographic studies to determine lattice perfection and internal structure [Fr 65, Lan 79], and by careful microscopic examination to locate any visible inclusions. This is, however, a formidable programme and it has proved simpler to select a group of diamonds which might, from relatively crude criteria, be expected to be good channelling crystals and then to refine the selection using channelling measurements. There is some evidence that the channelling characteristics of diamonds so selected are those intrinsic to diamond: the results are independent of type (all four subtypes were measured) and deviations from these results in a set of diamonds displaying higher yields can be explained quantitatively in terms of the defects characteristic of these diamonds. This latter investigation is reported in Chapter 7.

Finally, the selected crystals must be prepared as targets with clean and preferably flat surfaces. Relatively simple and standard cleaning and polishing procedures were found to lead to good results.

4.2 PROPERTIES

4.2.1 General Properties

The properties of diamond are reviewed extensively in the books edited by Berman [Ber 65] and Field [Fie 79]. The latter contains a useful compilation of data. A brief summary of relevant data is given below.

Diamond is a crystalline form of carbon with a cubic lattice (diamond cubic O_h^7 space group) with eight atoms per unit cell and a lattice constant of 356.7 pm. In many of its physical properties diamond is an extreme and thus attractive to the physicist. It is the hardest substance

known; it is the most elastic and least compressible substance known and has the highest thermal conductivity at room temperature, about five times that of copper. It has an extremely high Debye temperature, 1860 K at temperatures of 0 °C to 810 °C [Vi 62], and thus has a relatively small thermal vibration amplitude.

Diamond is an unstable allotrope of carbon and will transform irreversibly to graphite if heated above about 1800 °C in ultra high vacuum or extremely pure argon at atmospheric pressure [Eva 64]. It may be annealed at higher temperatures if a sufficiently high pressure is applied to keep it within the diamond stability region. In general, diamond is rather inert and is only attacked chemically by oxidising agents at elevated temperatures, for example, molten sodium nitrate above 450 °C, oxygen above 600 °C or carbon dioxide above 950 °C [Eva 62a], leading to some difficulties in the chemical etching of diamond.

Electrically, diamond is a semiconductor with an indirect band gap of 5.48 eV. Nitrogen is present as a donor in all diamonds but the donor levels are deep enough that most diamonds are extremely good insulators at room temperature in the dark. Photoconductivity is induced by ultra-violet radiation. A rare class of natural diamonds, type IIb, have an excess of boron [Lig 76, Sel 77] acceptors over the compensating nitrogen and exhibit p-type semiconductivity, with resistivities in the range $10 \Omega\text{cm}$ to $10^3 \Omega\text{cm}$.

The values of particular physical constants used in this work are given in Table 4.1.

Table 4.1

PHYSICAL CONSTANTS FOR DIAMOND

Lattice constant	a_0	356.7 pm
Nearest neighbour distance		145.45 pm
Density	ρ	$3.515 \cdot 10^3 \text{ kg} \cdot \text{m}^{-3}$
Atomic density	N	$1.76 \cdot 10^{29} \text{ m}^{-3}$
Debye temperature (0 - 800 °C)	θ_D	1860 K
(0 K)		2220 K
Energy gap	E_g	5.48 eV
Dielectric constant		5.70
Refractive index ($\lambda = 581 \text{ nm}$)		2.42
($\lambda = 7 - 10 \text{ }\mu\text{m}$)		2.27 - 2.33

4.2.2 Impurities in Diamond

Impurities in diamond may be divided into two classes: those that are present in the lattice and those that are present in inclusions. Diamonds containing inclusions visible in microscopic examinations have been rejected for use in this work, but it can be expected that inclusions of sizes down to almost atomic dimensions may be present in all diamonds [Fes 75].

The major impurities in (visible) inclusion-free diamonds have been found to be nitrogen [Ka 59], oxygen [Fes 75] and hydrogen [Hu 77a, Sel 78]. Nitrogen is found in quantities ranging from 10 ppm to as much as 5000 ppm [Ka 59, Lig 64, Sel 78]. From spectroscopic studies it is known to be incorporated in the lattice, the concentration and form being related to diamond type. Hydrogen has been found in quantities up to 1000 ppm. A

small portion of this is suspected to be in the lattice; lines in the infra-red spectra of some diamonds have been ascribed to hydrogen [Run 71] and small effects on the thermal conductivity have also been attributed to the presence of hydrogen [Bur 79]. It appears, however, that most of the hydrogen is in inclusions, possibly water-rich magma droplets [Sel 78]. Oxygen has been found in quantities of up to 200 ppm [Fes 75]. There is no evidence that any of this is in the lattice. Much of it can be related to the general trace element chemistry and can be associated with mineral inclusions [Fes 75]; the remainder is probably in gaseous inclusions [Sel 75a].

Many other elements have been found in diamond [Sea 66, Fes 73, 75, Sel 75a, 77, 78]. Most of these are present in quantities much smaller than the above impurities and are probably present in inclusions. Boron is known to be present substitutionally in the lattice in quantities of up to 100 ppm in Type IIb diamonds [Lig 76, Sel 77], and in lesser amounts in other types.

With the exception of nitrogen, therefore, no impurities are present in the lattice in any quantities sufficient to influence channelling. The possible influence of sub-microscopic inclusions is more difficult to assess. The numbers given above for inclusion-related impurities are maxima; the amount of these impurities is related to diamond colour and clear and yellow diamonds, which predominated amongst those used, are expected to contain lower amounts [Fes 75]. From the results of Fesq and co-workers [Fes 75], the diamonds used in this work are expected to contain ≤ 40 ppm of inclusion-related impurity, isolated in small inclusions scattered throughout the diamonds. The effect of these on channelling is thus expected to be small and no evidence for any such effect was found.

4.2.3 Classification of Diamonds

It remains to consider the possible effect on channelling of nitrogen and any lattice defects that may be present. These may be conveniently considered together, as it is found that diamonds may be classified into four groups, essentially on the basis of nitrogen concentration and form, and that the major crystal defects found are related to these groups.

The classification is made predominantly on the basis of spectroscopic features in the infra-red and ultra-violet regions. Pure diamond is expected to have no absorption in the ultra-violet below the band-gap energy of 5.5 eV [Dav 77] and to have absorption in the infra-red caused by two-phonon processes coupling lattice vibrations to the incident radiation in the region 3 - 6 μm , while one-phonon absorption (7 - 10 μm) is forbidden by symmetry [Lax 55]. Diamonds were originally classified into Type I or Type II, depending on the presence or absence of infra-red absorption in the range 7 - 10 μm and the corresponding presence or absence of a secondary absorption edge in the ultra-violet, below the absorption edge at 5.5 eV. The presence of infra-red absorption in the one-phonon region is now known to be caused by some impurity [Lax 55], which has been shown to be nitrogen [Ka 59, Sob 72]. The levels introduced in the band-gap by the nitrogen are responsible for the secondary absorption edge [Dav 73]. About 98 % of natural diamonds are of Type I.

About 0.1 % of Type I diamonds are found to have a large proportion of their nitrogen in the form of single substitutional atoms, as revealed by electron spin resonance [Dy 65]. These have been classified as Type Ib, while the rest, which have only a very small fraction of their nitrogen in this form are classified as Type Ia. In contrast to natural diamonds,

most synthetic diamonds are of Type Ib [Dav 77].

Some Type II diamonds are found to be p-type semiconductors and are classified Type IIb [Cu 52]. These are generally the purest of diamonds [Dav 77]. The rest are classified Type IIa. Type II diamonds do contain nitrogen [Sel 75a], the amount present being insufficient to produce measurable infra-red absorption. Type IIa diamonds exhibit a tail on the absorption edge extending from 5.5 eV down into the blue region, but have no secondary absorption edge; Type IIb diamonds show no ultra-violet absorption below the absorption edge [Dav 77].

The general characteristics of these classes are summarised below:

1) Type Ia

The one-phonon infra-red absorption spectrum in the region 7 - 10 μm ($1000 - 1332 \text{ cm}^{-1}$) shows two sets of characteristic features, the 'A' features and the 'B' features [Su 54]. (A typical Ia one-phonon absorption spectrum is shown in Figure 7.1.) Davies has shown that the spectrum can be decomposed into a mixture of an A spectrum and a B spectrum, related to an A form and a B form of nitrogen, and has given a prescription for determining the ratio of A and B present [Dav 73, 77]. A third feature characteristic of Type Ia diamonds is a peak in the absorption at 7.3 μm (1370 cm^{-1}), denoted B'. This is above the Raman energy of 1332 cm^{-1} and thus above the one-phonon region.

The absorption in the infra-red due to the A and B nitrogen is proportional to the concentration of the respective forms. From experiments using diamonds with predominantly A nitrogen it has been found that

$$\mu_A (1282 \text{ cm}^{-1}) = 300 \pm 20 N_A$$

where μ_A is the absorption coefficient in cm^{-1} at 1282 cm^{-1} ($7.8 \mu\text{m}$) and N_A is the percentage atomic concentration of A form nitrogen [Ka 59, Lig 64].

The position for B nitrogen is less clear. From a consideration of the amount of B nitrogen present in the diamonds used in the A correlation, Davies concluded that [Dav 73, 77] (in the above units)

$$\mu_B (1282 \text{ cm}^{-1}) = 330 \pm 150 N_B$$

Sobolev has found, using diamonds with predominantly B features, that [Sob 72]

$$\mu_B (1175 \text{ cm}^{-1}) = 250 N_B$$

which implies [Dav 77]

$$\mu_B (1282 \text{ cm}^{-1}) = 85 N_B$$

From a group of diamonds, including some used in this work, with nitrogen measured using a $^{14}\text{N}(\alpha, n)$ reaction [Sel 75b], the relation

$$\mu_B (1282 \text{ cm}^{-1}) = 150 \pm 20 N_B$$

has been obtained.

The absorption in the ultra-violet secondary absorption region is also related to the A and B forms of nitrogen. For the A nitrogen it is found that

$$\nu_A (4.04 \text{ eV}) = 0.5 \nu_A (1282 \text{ cm}^{-1}) \quad [\text{Ka } 59]$$

and

$$\nu_A (4.76 \text{ eV}) = 8.4 \pm 1.5 \nu_A (1282 \text{ cm}^{-1}) \quad [\text{Dav } 73].$$

The absorption produced by the 'N9' system at 5.25 eV has been found to be proportional to the B nitrogen concentration but it has been concluded that the N9 system is not a transition of the B nitrogen but is due to a defect present in much smaller quantities [Dav 73].

The A form of nitrogen has been identified as a pair of nearest neighbour nitrogen atoms in substitutional sites [Dav 76], although some relaxation from the lattice site by 5 to 20 % is indicated [Sto 78]. The structure of the B centre is at present unknown. Lack of paramagnetism implies that it must contain an even number of nitrogen atoms [Dav 73]. Optical and radiation damage studies indicate that the centre should be relatively simple, perhaps 4 to 8 atoms [Dav 77]. Low temperature (<20 K) thermal conductivity measurements have suggested that the B nitrogen is in clusters about 6 nm in diameter [Va 78], but this is to some extent contradicted by near room temperature measurements (320 - 450 K) in which it is found that phonons are scattered by B nitrogen in much the same way as A nitrogen [Bur 78]. Evans [Eva 78] has suggested that the B nitrogen is related to defects known as platelets. Some diamonds have B nitrogen

and no platelets: in these it is concluded that the platelets have degenerated and the B nitrogen is related to the small (6 nm) clusters [Eva 78], which have been observed in these diamonds. (The diamonds used by Vandersande were of this kind [Va 80].)

Platelets are defects that take the form of precipitates on {100} planes which displace the lattice on either side, normal to the platelets, with a total displacement of $\frac{a_0}{3} \langle 100 \rangle$ [Cat 58, Lan 64]. The presence of these was predicted by Frank [Fr 56] to explain anomalous spikes on X-ray photographs of Type Ia diamonds [Ra 40, Lo 65]. They were found by electron microscopy by Evans and Phaal [Eva 62b] and range in size from 20 nm to 50 μm across [Eva 62b, Wo 76]. The distribution is often inhomogeneous [Eva 62b] and the platelets are often found in alternating growth bands tens of microns wide [Lan 77]. It has been found that the integrated X-ray spike intensity is proportional to the platelet area per unit volume [Eva 73] and the 7.3 μm (B') absorption coefficient [Sob 63, Eva 75]. From the data given by Evans and Phaal [Eva 62b], the relation between the absorption coefficient μ_p at 7.3 μm and the platelet area per unit volume (A_p), can be estimated as

$$A_p = 10^3 \mu_p (7.3 \mu\text{m}).$$

This agrees with an estimate by Hudson based on his own data [Hu 76]. The B' peak is only found in the presence of the A and/or B absorption features; however, diamonds showing A and/or B absorption features with no B' peak are also found.

The nature of the precipitated layer is not known. When large

quantities of nitrogen were discovered in Ia diamonds [Ka 59], nitrogen was suggested as the platelet species [Elt 50]. Lang [Lan 64] has given an elegant model for a nitrogen platelet. However, it was found that nitrogen was associated with A and B spectra; although the B and B' peaks are often correlated in sets of diamonds, diamonds can be found which negate this correlation (for example, showing B features with no B'). It has, therefore, been suggested that little or no nitrogen is present in the platelets, and that the species present is probably carbon [Eva 73, Dav 73, Wo 76]. Recently, Evans and Rainey have found that annealing above 2200°C can depress the B' peak without altering the integrated spike intensity [Eva 75]. Evans has suggested that the B nitrogen is associated in some way with the platelets and that, in B diamond with little or no B' peak, the platelets have degenerated into dislocation loops and the B nitrogen is then associated with small clusters that have been observed in electron micrographs of such diamonds in association with loops [Eva 78]. It may be noted that the amount of B nitrogen present in diamonds exhibiting a B - B' correlation is of the same order as that required to produce platelets with the Lang [Lan 64] structure (see Chapter 7).

Platelets are the major defect associated with Ia diamonds. Grown-in dislocation would appear to be low in number [Lan 79]. Evans and Phaal [Eva 62b] reported dislocation loops associated with platelets but apparently 10 to 30 times fewer in number. They believed that these lay on {111} but were unable to demonstrate this owing to the lack of sufficient movement in the microscope stage. Loops on {111} have not been reported by other authors, but Woods [Wo 76] found loops on {100}, associated with 'giant' platelets, and of similar size. These would appear to be some 20 times less numerous than the platelets [Lan 79].

ii) Type Ib

These are comparatively rare in nature, comprising about 0.1% of natural diamonds, but most synthetic diamonds are Ib. An infra-red one-phonon absorption spectrum is found which is correlated to ultra-violet absorption in the secondary absorption region below 5.5 eV and to the concentration of single substitutional nitrogen atoms [Dav 77]. The concentration of nitrogen is less than in Ia diamonds, averaging about 100 ppm [Sel 78], not all of which is present in the single substitutional form. Some is probably present in the A form [Chr 77].

No platelets are found in Ib diamonds. Small defects, approximately spherical and about 5 nm in diameter, have been found in several Ib diamonds [Hu 77b, Bus 78]. It has been suggested, without much evidence, that these are related to platelets [Hu 77b]. It is not known if they are related to the clusters of about the same size seen in Ia B diamonds with no B' features. However, no dislocation loops have been reported in the Ib diamonds and examination of micrographs of the clusters in Vandersande's diamonds indicates that the clusters do not show the 'structure factor' contrast observed in the Ib defects.

iii) Type IIa

These contain typically 20 ppm of nitrogen and it has been suggested that they are simply limiting cases of Type Ia diamonds [Dav 77]. However, many Type II diamonds are dislocation rich, apparently as a result of plastic deformation, and exhibit marked birefringence [Lan 79]. This is in marked contrast to Type I diamonds which typically contain few dislocations [Lan 79]. Many Type II diamonds have a mosaic structure. A typical dislocation density in such diamonds is $\sim 10^8$ lines cm^{-2} [Lan 79].

This would appear to be one to two orders of magnitude less than the minimum density observable in channelling [Pic 78].

iv) Type IIb

These are essentially the same as IIa diamonds as regards defects and nitrogen concentrations. They contain up to 100 ppn of boron [Lig 76, Sel 78] which acts as an acceptor to produce p-type semiconductivity [Kem 65]. IIb diamonds are often recognizable by a characteristic blue colouration caused by acceptor to valence band transitions [Dav 77].

Several conclusions can be drawn from the above in respect of the relation of channelling to diamond type. The principal lattice impurities, nitrogen in the A form and boron, are both nearly substitutional and close to carbon in charge and mass. The effect of these on channelling is thus expected to be very small, except perhaps in the case of type Ia diamonds with very high concentrations of nitrogen. These, however, are likely to contain platelets which must combine the dechannelling properties of stacking faults and dislocation loops, by virtue of their $\frac{a_0}{3} \cdot \langle 100 \rangle$ displacement vector. Typical platelet areas per unit volume are similar to the area that could be covered by distributing the nitrogen in a Lang (Lan 64) model platelet and thus the dechannelling effect of platelets will be much greater than that of an equivalent number of nearly substitutional nitrogen atoms. Because the structure of the B nitrogen centre is not known, its effect on channelling cannot be evaluated. If the B nitrogen is in small substitutional groups the effect will be small. If it is associated with larger clusters 5 nm in diameter, or platelets, the effect could be large. The effect of dislocations in a typical Type II diamond would appear to be too small to observe in channelling: this

might not be true at higher energies as the dechannelling cross-section is expected to rise as $(\text{Energy})^{\frac{1}{2}}$ [Qu 68]. The assessment of Type Ib diamonds is difficult as little work appears to have been done on the identification of defects in these. The clusters that have been observed are low in concentration (about $2 \cdot 10^{21} \text{ m}^{-3}$) and might thus be expected to give only a small effect. It would, therefore, appear that the best diamond for channelling purposes would be a Type Ia with a small A absorption and no B or B' absorption.

Type IIa and IIb diamonds are likely to give good results if the dislocation density is not above average, and Ib diamonds will probably also give good results.

4.3 SELECTION OF DIAMONDS

4.3.1 Selection Procedures

It was not possible to select diamonds from a large batch using the ideal procedure outlined above, owing to the lack of suitable resources and the non-availability of large batches of diamonds and a somewhat simpler procedure was used, albeit more relevant to ion channelling.

A group of 18 diamonds ('Di' series) had been obtained for ion channelling purposes by Dr T.E. Derry [Der 78] from Dr F.A. Raal of Diamond Research Laboratories (DRL), Johannesburg. These were chosen by DRL for good appearance and freedom from inclusions. Several were used by Derry in early experiments and several were rejected on the grounds of size and poor quality. This left twelve diamonds for ion channelling purposes, eleven of which were Ia and one a IIa. These were in the form of plates, mainly natural, 0.6 mm on a side and 1 mm thick.

A further set of 24 stones (K series) was selected from a large group of near-gem industrial diamonds. These were selected for low birefringence and good morphology. The selection was made at the main De Beers sorting rooms in Kimberley with the assistance of T.E. Derry. Two large, flat, clear stones were also lent by De Beers from their special collection, giving a total of 26 K series stones, most of which were Ia, but including one IIb.

This resulted in a set of 38 diamonds used by the author and by T.E. Derry. This set was supplemented on an ad hoc basis with diamonds which became available through the general diamond research programme in the laboratory, in particular, a large brown IIa, a good quality IIb and a Ib.

A set of diamonds on which to make definitive measurements was selected from the above group using ion channelling, under standard conditions of 1 MeV protons channelled along $\langle 110 \rangle$. As a measure of the crystal quality, the yield χ_0 , measured just behind the surface peak, and $\chi_{2.5}$, measured at 2.5 μm , were used. These measurements were taken after surface preparation as discussed in Section 4.4.

The minimum yield χ_0 was found to cluster about 2%, with a range up to about 3%. The yield at 2.5 μm was found to cluster at about 24% with the yield in some diamonds rising to about 60%. The diamonds which showed yields less than 25% were used for definitive dechannelling measurements; diamonds with yields less than 30% were judged as good crystals for general channelling use. The diamonds that showed excessive yields were predominantly Cape yellow diamonds from the K series. Infra-red

spectra showed that these were strong Type Ia's with a high concentration of nitrogen and platelets, and a group of these was chosen for further study. The spread in the minimum yield below the surface peak was quite small and tended to correlate with the yield at 2.5 μm . Extrapolation to the surface showed a clustering with a much smaller spread at about 1.5%. The critical angle at the surface was found to be the same for diamonds with high $\chi_{2.5}$ and those of the definitive set.

4.3.2 Assessment of Selection Procedures

The definitive set was found to contain diamonds that on the basis of external appearances might be judged as good crystals. Members of all four sub-groups were included; kinds which showed markedly worse characteristics were all strong Ia diamonds. It was unfortunately not possible to measure the infra-red absorption on all the diamonds, but such Ia diamonds in the definitive set that were measured showed low nitrogen and platelet concentration. It is thus concluded that the results obtained are those characteristic of diamond itself.

One possible remaining problem is that of homogeneity. Diamonds are found which are inhomogeneous in internal structure [Lan 79]. The NPRU has recently obtained a Luminoscope (Nuclide Corporation, USA) (a cathodoluminescence apparatus for attachment to a microscope stage) and the opportunity was taken to examine some of the diamonds used in this study in cathodoluminescence, which can show up many structural and spectroscopic features in a topographical manner [Ha 77].

The luminescence is produced over a range of several microns into the diamonds [Dav 79], about the same as probed by channelling and thus

features observed are directly relevant to channelling. It was confirmed that the diamonds used were essentially uniform, and that cathodoluminescence is a diagnostic indicator that will be useful in future channelling studies on diamond.

4.4 PREPARATION

4.4.1 Aims

For accurate channelling measurements the crystal surfaces should be flat, to prevent variations in the scattering geometry, and free of contaminating layers, which would scatter the incident beam. It was found that natural faces of diamond crystals inevitably gave bad channelling results. Several reasons for this may be suggested: the surface can suffer mechanical damage during the history of the diamond and during mining operation; the surface can suffer radiation damage by contact over many millions of years with rocks containing radioactive isotopes; and contaminating material can be imbedded in fissures and irregularities on the surface. The aim in target preparation was thus to prepare a fresh flat surface on the diamond. This was done by polishing or, in some cases, etching. The diamonds were then cleaned and mounted in the target holders.

4.4.2 Polishing

Diamonds were first cut to size if necessary using conventional diamond sawing techniques. They were then polished using standard diamond polishing techniques on a standard scaife (polishing wheel), with the final polish being done with 0 - $\frac{1}{2}$ μ m diamond grit. The scaife is a cast iron wheel, spinning at about 3000 rpm which is charged with a mixture of diamond grit and olive oil. Polishing is done at a linear

wheel speed of 30 - 50 m·s⁻¹. Polishing is thought to proceed by the cleavage of small (almost atomic sized) blocks from the surface [Wil 59], but a chemical attack at surface asperities has also been suggested as the mechanism [Sea 58]. The surface is not subject to plastic flow. The final surface produced retains a good crystal structure and is free of damage. It has been suggested that a network of microcracks along {111} cleavage planes could exist in the surface region to a depth of about 50 nm [Fr 64, Va 76]. It was found that annealing produced a very slight improvement in the channelling minimum yield on some diamonds, which might indicate the healing of microcracks and, for this reason, diamonds were generally annealed at 1100 °C in ultrahigh (10⁻¹⁰ torr) vacuum after polishing. No difference in yield was found between polished and annealed diamonds, and gas-etched diamonds [Der 78], and it was concluded that polishing was a satisfactory method of surface preparation.

4.4.3 Gas-Etching

This procedure has been described by Derry [Der 78]. Diamonds were etched in a stream of dry carbon dioxide at a temperature of 1000 °C. The results tended to be variable: some diamonds showed extreme pitting after etching and, for this reason, the process was used only on diamonds that would be difficult to polish, in particular, diamonds that were thin and irregular and thin diamonds that had large flat {111} faces which are extremely difficult to polish [Wil 65].

4.4.4 Cleaning

After polishing or etching, the diamonds were cleaned in a 10% solution of Contrad (Decon Laboratories, Brighton, United Kingdom, also known as Decon 90) and deionised water. Contrad is a detergent designed

for radioactive decontamination and contains a surfactant and a chelating agent. Diamonds were cleaned for half an hour in this solution in clean teflon beakers in an ultrasonic bath, after which they were rinsed three times in deionised water, also in the ultrasonic bath. This cleaning procedure was found to be as efficient as a longer procedure involving baths of boiling acid [Der 78].

4.4.5 Assessment

The effectiveness of the cleaning and surface preparation techniques was judged by backscattering and channelling measurements. The surface was found to be free of contaminants with masses higher than that of carbon, with the exception of a monolayer of oxygen. Derry [Der 79] has suggested that this is in the form of OH groups, derived from the aqueous cleaning mixture, terminating dangling bonds on the surface. The surface peak in channelling experiments was found to be consistent with that evaluated from Barrett's expression [Ba 71] and corresponded to about five monolayers [Der 78], thus indicating that surface disorder is low. These measurements were greatly aided by the low rate of hydrocarbon deposition on the target surface from the vacuum, owing to the effective trapping provided by the cryoshield held at 80 K around the target.

It was concluded that the diamonds used in this work were good crystals with clean, ordered surfaces, and could be used as confidently as well-prepared, carefully grown crystals have been in other studies.

4.4.6 Thin Diamonds

Diamonds for transmission work were prepared by D Drukker and Zon,

Amsterdam. These were Type IIa crystals, carefully polished to the final thickness of 4 - 20 μm . The diamonds used will be further specified in Chapter 8.

DECHANNELLING IN GOOD CRYSTALS

5.1 INTRODUCTION

An important aspect of the motion of channelled ions is the fact that these ions do not necessarily remain channelled as they proceed into the crystal, but can become dechannelled as a result of collisions with electrons in the channel, with thermally vibrating atoms or with defects. Thus the yield of close encounter processes increases with depth into the crystal. This is clearly shown in Figure 5.1, where channelled and random backscattered spectra taken with the same number of incident ions, are compared. The dechanneling in the best (and thus 'defect free' as far as channelling is concerned) diamonds is investigated in this chapter.

Extensive studies have been made of dechanneling in the other Group IV diamond-cubic crystals, silicon and germanium, by workers at Catania [Fot 71, Cam 71] who have shown that, for a particular axis, the results for various incident beam energies and crystal temperatures may be reduced to a single curve in which the yield is determined as a function of

$$\frac{u_2^2}{E} z$$

where u_2 is the (2-dimensional) thermal vibration amplitude, E is the incident beam energy and z is the depth into the crystal. This scaling

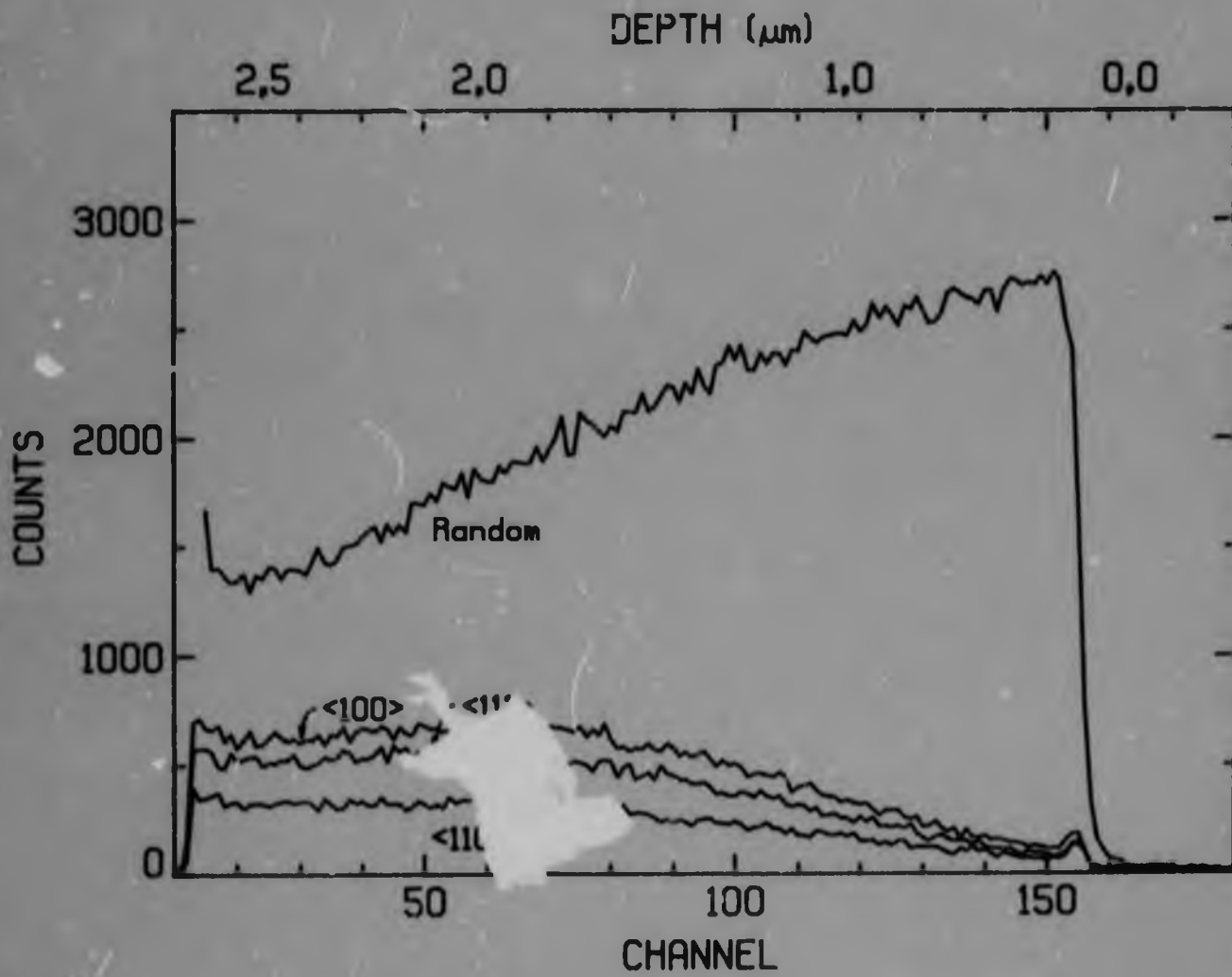


Figure 5.1: Energy spectra for 1.0 MeV protons incident on diamond in random and channelled directions.

implies that the dechannelling is largely determined by scattering from thermally vibrating atoms, although the theoretical treatment suggests a more complicated behaviour [Fot 71, Cam 71]. Similar scaling has been obtained in quartz [Abe 72b], but has not been found in tungsten [Mas 72], while some workers have been unable to repeat the silicon scaling [Fon 72]. It is of interest to examine the situation in diamond where, on the grounds of the theory of Chapter 2, it is expected that dechannelling will be dominated by the effect of scattering by electrons in the channel.

Measurements have been made of the yield as a function of depth, using protons incident along the axial directions $\langle 110 \rangle$, $\langle 111 \rangle$ and $\langle 100 \rangle$, over a range in energies from 1.0 MeV to 8.9 MeV and, at 1.0 MeV, for temperatures ranging from room temperature (20 °C) to 700 °C. Some measurements are also reported for the planes $\{110\}$, $\{111\}$ and $\{100\}$, although the emphasis of the work was on axial dechannelling. The measurements have been compared with theoretical predictions based on the steady increase model and on the diffusion model. The effect of various contributions to the dechannelling has been examined through the diffusion model.

5.2 EXPERIMENTAL METHOD AND DATA ANALYSIS

Experiments were carried out as described in Chapter 3. Data analysis was performed using the program CHANSPEC (see Appendix 1). Spectra were 'deconvoluted' by fitting a curve to the surface edge, and the surface peak was stripped off. Conversion from an energy scale to a depth scale was performed, the spectra were normalised to random and then smoothed.

A perennial problem in the comparison of dechannelling measurements to theory arises in the conversion from an energy scale to a depth scale. Well-channelled ions have a stopping power lower than the random value. Thus, in calculating the depth scale for a channelled spectrum, a lower stopping power should be used along the incident path, before back-scattering occurs. For this reason, some workers (for example [Ped 75]) have used an estimate of the channelled stopping power (generally taken as half the random stopping power) in evaluating their depth scales. However, the stopping power is trajectory-dependent, and ions which are dechannelled will have experienced a gradual increase in stopping from the value at the point at which they entered the channel, up to the stage at which they dechannelled. The appropriate stopping power for a particular depth is the average stopping power experienced by ions dechannelled at that depth [Ped 75]. This will be close to the random value (or even higher [Ros 77]) for small depths, gradually decreasing at larger depths. The actual value to be used is difficult to assess. Protons transmitted through thin diamond crystals and emerging at angles close to zero with respect to the $\langle 110 \rangle$ channel show an energy loss of $\sim 80\%$ of the random value (see Chapter 8). This group will represent mainly the best-channelled ions. One may conclude that ions that are dechannelled will have a higher energy loss than this. Thus the effective channelled stopping power to be used in the depth conversion is likely to be close to the random value, at least for diamond.

In view of these uncertainties, random stopping powers have been used along both the in-going and out-going paths, for the depth conversion in this work. However, some comments about the neglect of a lower channelled stopping power are in order. The effect of a lower channelled

stopping power on the normalised yield is dependent on the shape of the spectra and the energy dependence of the scattering cross-section, and is not necessarily equivalent to a rescaling of the depth scale, as has been implied in [Ped 75]. Thus, for depths smaller than that corresponding to the maximum in the channelled spectra in Figure 5.1, the yield will be decreased by a lower channelled stopping power while, for larger depths, the yield will be increased.

Using a value for the channelled stopping power of half the random value, the yield for $\langle 110 \rangle$ at 4.5 MeV was found to be decreased by $\sim 15\%$ at a depth of 10 μm , while it was increased at depths greater than 20 μm . The effect at 1 MeV was found to be smaller, amounting to a decrease of $\sim 10\%$ at 1 μm and 5% at 2 μm . These figures give some idea of the effect of a lower channelled stopping power on the yield: the use of a more realistic value will result in much smaller changes.

The diamonds used for this study of dechanneling represent the best diamonds in the selected set. They are thus expected to represent the dechanneling of diamond, without a contribution from defects.

5.3 CALCULATIONS

5.3.1 Diffusion Model

The full 'diffusion' equation, including absorption and damping (equation 2.5.28) was integrated numerically.

In order to provide fixed boundary conditions, the transformation

$$\epsilon_1 = \epsilon_m \tan^2 \left(\frac{\pi}{2} y \right)$$

was introduced. ϵ_m is a constant introduced to set the scale of the transformation, with $\epsilon_1 = \epsilon_m$ for $y = \frac{1}{2}$. With this transformation, the equation (2.5.23) becomes:

$$\frac{\partial f}{\partial z} = D_1 \frac{\partial^2 f}{\partial z^2} + D_2 \frac{\partial f}{\partial y} + D_3 f \quad (5.3.1)$$

with $f = f(y, z) = \frac{g(y, z)}{A(y)}$; $f(\pm 1) = 0$

and $D_1 = \frac{1}{4\epsilon_m^2} \frac{\cos^4(\pi/2 \cdot y)}{\tan^2(\pi/2 \cdot y)} D(r_1(y))$

$$D_2 = \frac{1}{2\epsilon_m} [S(\epsilon_1(y)) + S_d(\epsilon_1(y))] \frac{\cos^2(\pi/2 \cdot y)}{\tan(\pi/2 \cdot y)}$$

$$- \frac{D(\epsilon_1(y))}{4\epsilon_m^2} \frac{\cos^2(\pi/2 \cdot y)}{\tan(\pi/2 \cdot y)} [2\cos^2(\pi/2 \cdot y)$$

$$+ \cot^2(\pi/2 \cdot y)]$$

$$D_3 = \frac{1}{2\epsilon_m} \frac{\cos^2(\pi/2 \cdot y)}{\tan(\pi/2 \cdot y)} \frac{dS_d(\epsilon_1(y))}{dy} - \sigma_T \Pi_T(\epsilon_1(y))$$

where

$$S(\epsilon_1) = \frac{d\epsilon_1}{dz}$$

$$S_d(\epsilon_1) = A(\epsilon_1) \left(\frac{d\epsilon_1}{dz} \right)_{\text{damp}}$$

and $D(\epsilon_1)$ is related to $S(\epsilon_1)$ by equation (2.5.21). The equation may be solved for f and hence g for the boundary condition $f(\pm 1) = 0$. This transformation allows a wide range of ϵ_1 to be covered while retaining accuracy in the small ϵ_1 region, and allows an efficient usage of computer core. The 'small ϵ_1 ' region may be expanded or contracted by choice of ϵ_m . The results were insensitive to the value of ϵ_m and a value of $\epsilon_m = 0.5$ was generally used.

The solution of equation (5.3.1) was approximated on a grid with step-size Δz in z and Δy in y . The equation (5.3.1) was then solved on this grid using a Crank-Nicholson finite difference method [Ric 67] modified to include the second and third term in equation (5.3.1). Thus $f(z + \Delta z)$ can be obtained from $f(z)$ by solving the implicit set of equations:

$$\begin{aligned} \frac{f_{i,j+1} - f_{ij}}{\Delta z} &= \frac{D_1}{2(\Delta y)^2} \{f_{i,j+1} + f_{i,j-1} + f_{i+1,j+1} \\ &+ f_{i+1,j-1} - 2f_{i,j} - 2f_{i,j+1}\} \\ &+ \frac{D_2}{4\Delta y} \{f_{i,j+1} - f_{i,j-1} + f_{i+1,j+1} - f_{i+1,j-1}\} \\ &+ \frac{D_3}{2} \{f_{i+1,j} + f_{i,j}\} \end{aligned}$$

where i refers to the y co-ordinate grid and j to the z grid. The Crank-Nicholson scheme is stable for all choices of Δy and Δz , although the accuracy of the approximation (that is, truncation error) is obviously dependent upon them [Ric 67]. The stability of the scheme is not expected to be affected by the inclusion of the lower order terms in equation (5.3.1) [Ric 67]. The equation was generally solved with $\Delta y = 0.005$ and Δz varying from 0.0005 at small z to 0.02 at larger z . The behaviour of the program was checked by comparing numerical solutions of the simple equation (2.5.20) with $A(\epsilon_1) = 1$, $\frac{d\epsilon_1}{dz}$ constant and $g(\epsilon_1, 0)$ given by the single string model (that is, equation (2.3.9)), with the exact solution, equation (2.5.25). The two values for the yield agreed within

0.1 % and this was held to be sufficient accuracy. Greater accuracy could be achieved by decreasing Δy and Δz with a concomitant increase in computer core requirements and execution time. The yield calculated from the full equation (5.3.1) was found to be insensitive to variations in Δy and Δz .

In general, the value of $A(\epsilon_1)$ was taken to be zero for $\epsilon_1 = 0$, and the usual device, for example [Mas 75], of introducing a minimum accessible area derived from multiple scattering was not used. This necessitated the definition of $g(0,z) = 0$, which is reasonable from physical grounds, due to finite collimation and scattering in amorphous layers on the surface, as discussed in Section 2.3.2. In fact, only beam collimation (equation 2.3.8) was used to calculate $g(\epsilon_1,0)$ for the calculations in this Chapter. The introduction of beam collimation also yields a finite value for the flux at the potential minimum for $z = 0$. At larger depths, the flux, which may be calculated from I (by equation 2.3.15), becomes governed by the multiple scattering. A listing of the computer program is given in Appendix 2.

5.3.2 Steady Increase Model

The dechannelling depth $z(\epsilon_1)$ corresponding to a particular transverse energy was calculated by numerical integration of equation (2.5.16) and the yield was then calculated graphically [Gr 73].

5.4 RESULTS AND DISCUSSION

5.4.1 Energy Dependence

The yield as a function of depth, for protons incident down $\langle 110 \rangle$ at room temperature, is shown for several energies in Figure 5.2. (The

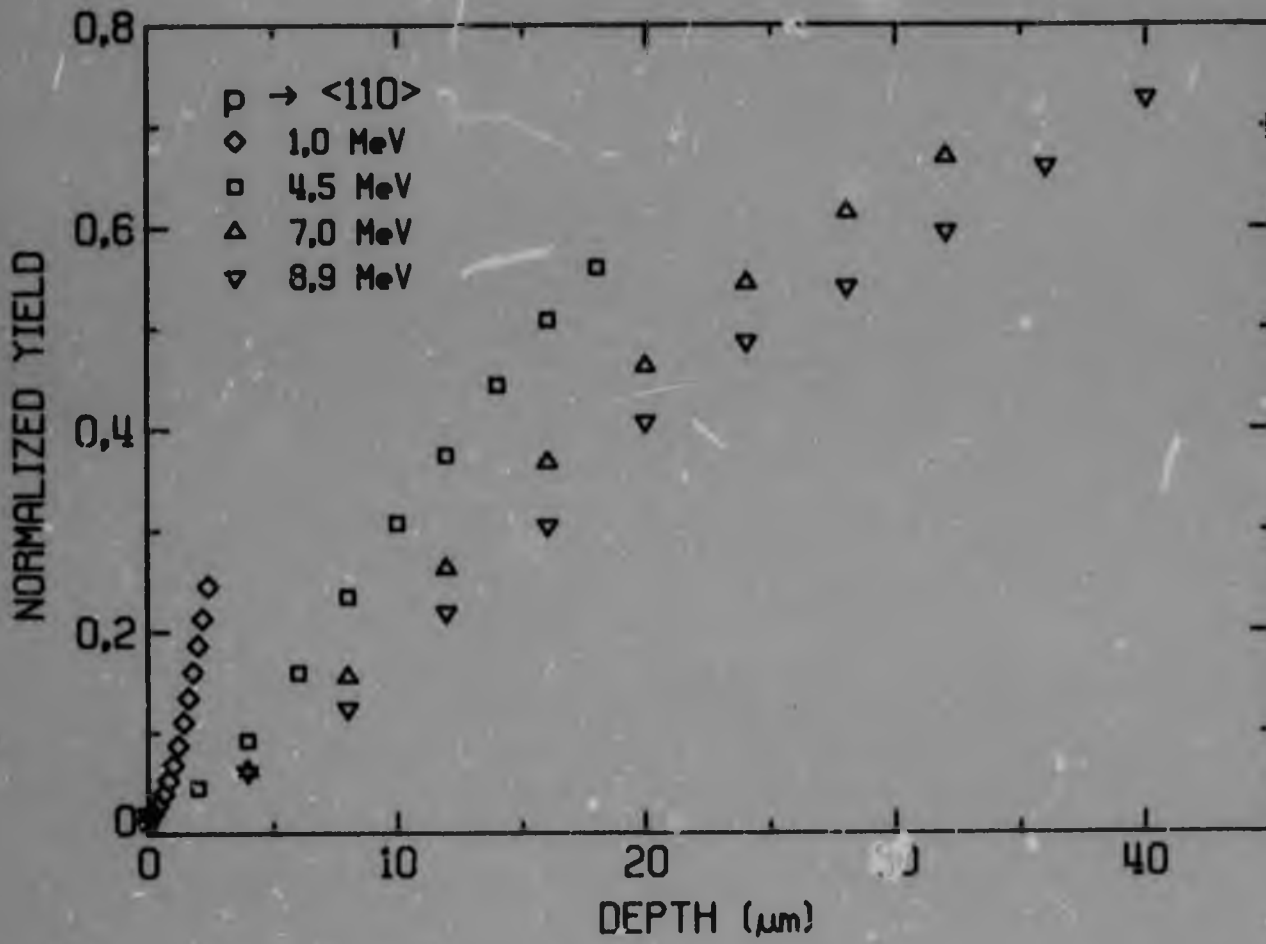


Figure 5.2: Experimental energy and depth dependence of the normalized yield, for protons along <110>.

cut-off at relatively small depths for the 1 MeV curve represents the greatest depth accessible in the backscattering spectrum for that energy). Clearly, the rate of dechannelling with depth is decreased as the energy increases. As discussed in Section 2.5, the dechannelling is expected to depend on two terms:

- i) An electronic scattering term, with an energy dependence related to that of the electronic stopping power.
- ii) A thermal term, with an approximately E^{-1} energy dependence.

In studies on silicon, germanium and quartz [Pot 71, Cam 71, Abe 72b] the dechannelling has been found to vary as E^{-1} , with the result that the yield versus depth curves for various energies collapse onto one when the yield is plotted as a function of z/E where z is the depth. This scaling fails for diamond. However, it is expected from the theory presented in Section 2.5 that the dechannelling in diamond is dominated by the electron component. Thus the energy dependence of the yield versus depth curves can be expected to be similar to the energy dependence of the change in transverse energy with depth due to electron scattering. This is essentially contained in the characteristic length (equation 2.5.9).

$$z_e = \frac{E}{\pi Z_1 e^2 L_0 N_d}$$

Values for this quantity, calculated using the same stopping power as for the depth conversion, are given in Table 5.1, as a function of energy and axis.

Table 5.1

ELECTRON SCATTERING LENGTH, z_e , FOR MAJOR AXES OF DIAMOND

Energy (MeV)	z_e (μm)		
	<110>	<111>	<100>
1.0	1.57	1.29	1.11
4.5	4.85	3.97	3.43
7.0	6.76	5.53	4.78
8.9	8.09	6.62	5.72

The yield was then plotted as a function of z/l_e and the results are shown in Figures 5.3 to 5.5 for the three axes <110>, <111> and <100>. The scaling is obviously well obeyed, although there is some indication that the 1 MeV curves lie slightly above the rest. Investigation at lower energies are not very useful in examining this trend, as the largest depth accessible in back-scattering decreases rapidly. The theoretical curves in Figures 5.3 to 5.5 are discussed below.

These results imply that electron multiple scattering is the dominant mechanism of dechannelling in diamond.

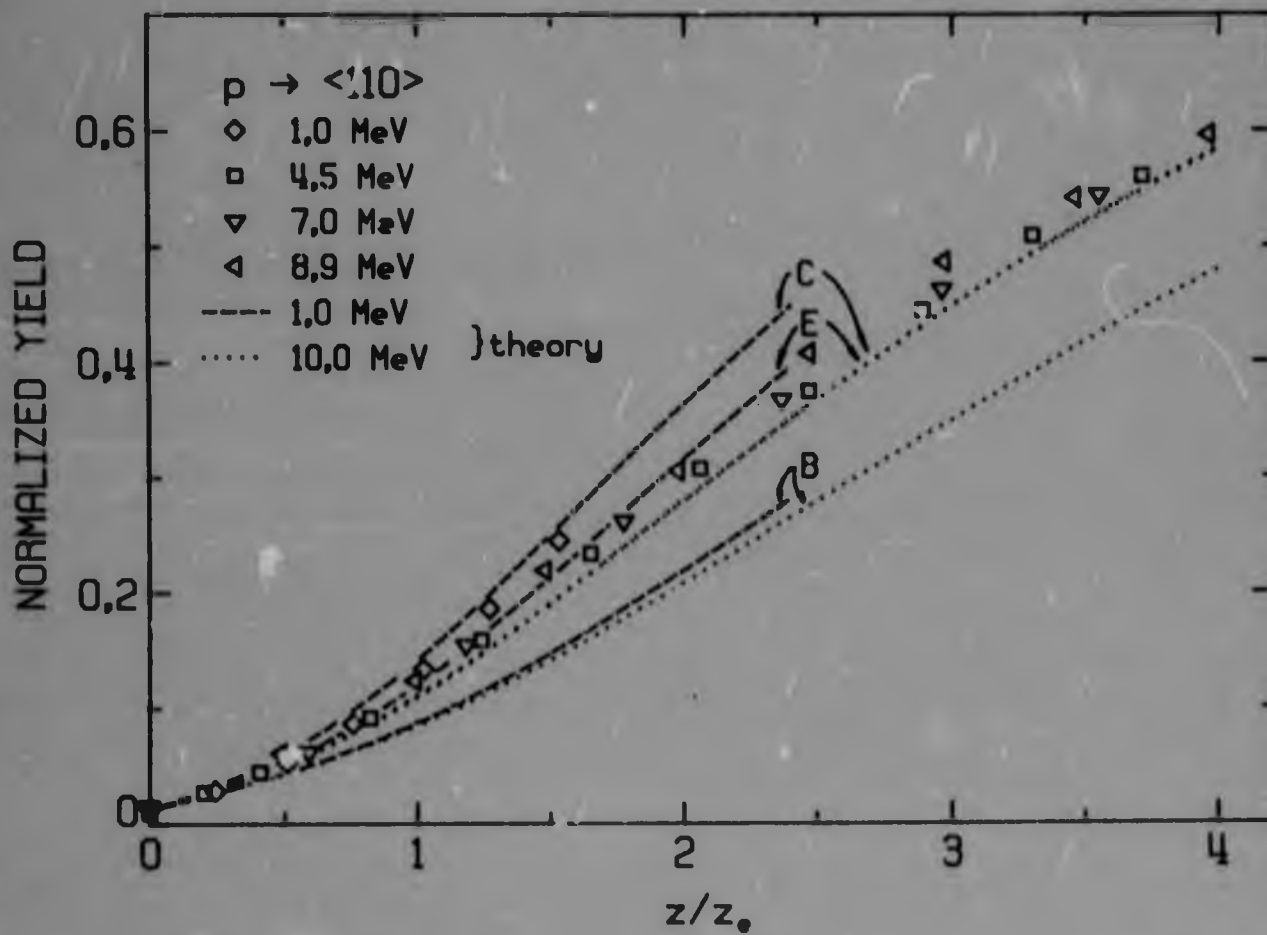


Figure 5.3: Scaled depth dependence of the normalized yield for $\langle 110 \rangle$.

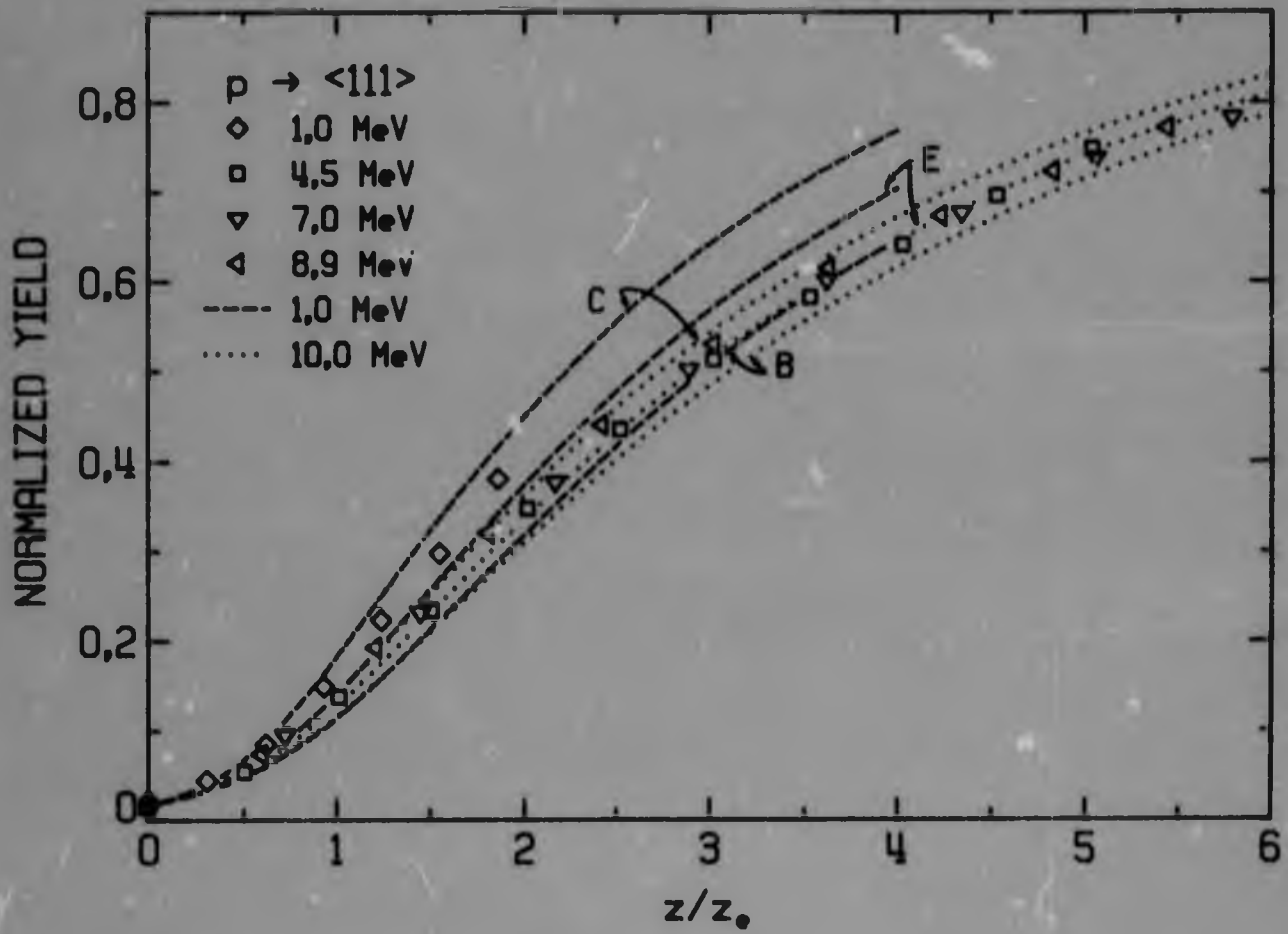


Figure 5.4: Scaled depth dependence of the normalized yield for $\langle 111 \rangle$. Theory: - - - and ····.

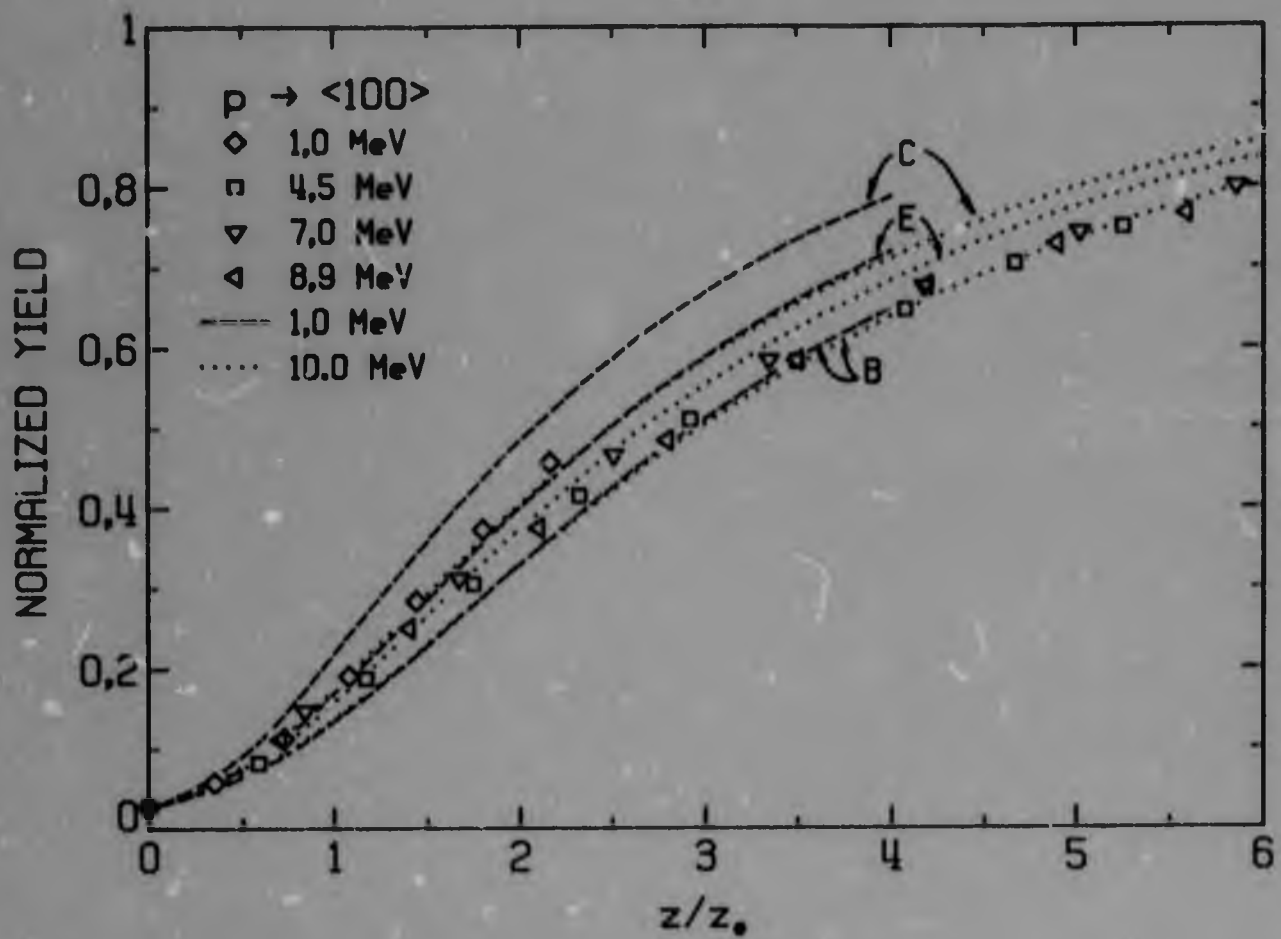


Figure 5.5: Scaled depth dependence of the normalized yield for $\langle 100 \rangle$. Theory: - - - and ····.

5.4.2 Axial Dependence

The axial dependence of dechannelling can be judged from Figure 5.3 to 5.5, and θ -yield is plotted as a function of the (unscaled) depth in Figure 5.6, for 1 MeV protons.

Both the z_e and the corresponding length, z_{11} (equation 2.5.5d), determining the scattering by thermally vibrating atoms in the channel, are proportional to $1/d$ where d is the row spacing. If the axial dependence of dechannelling were contained only in these characteristic lengths, then the three curves for $\langle 110 \rangle$, $\langle 111 \rangle$ and $\langle 100 \rangle$ could be expected to be the same function of z/z_e . However, there are other causes of differences among the three axes:

- i) The initial transverse energy distributions differ, with a larger proportion of ions having higher transverse energies in narrower axes. Thus the minimum yield at the surface increases with d [Der 78].
- ii) The minimum electron density in the channel, which determines the minimum electron scattering, is axis dependent.
- iii) The constant, A , which determines the zero of the potential in equation (2.5.5) is axis dependent.

Examination of Figures 5.3 to 5.5 indicate that axial differences in the reduced curves are not large: these figures are replotted on one set of axes in Figure 5.7. The general features are similar for all three curves. It can be concluded that the differences noted above are not important in determining the general features of the dechannelling.

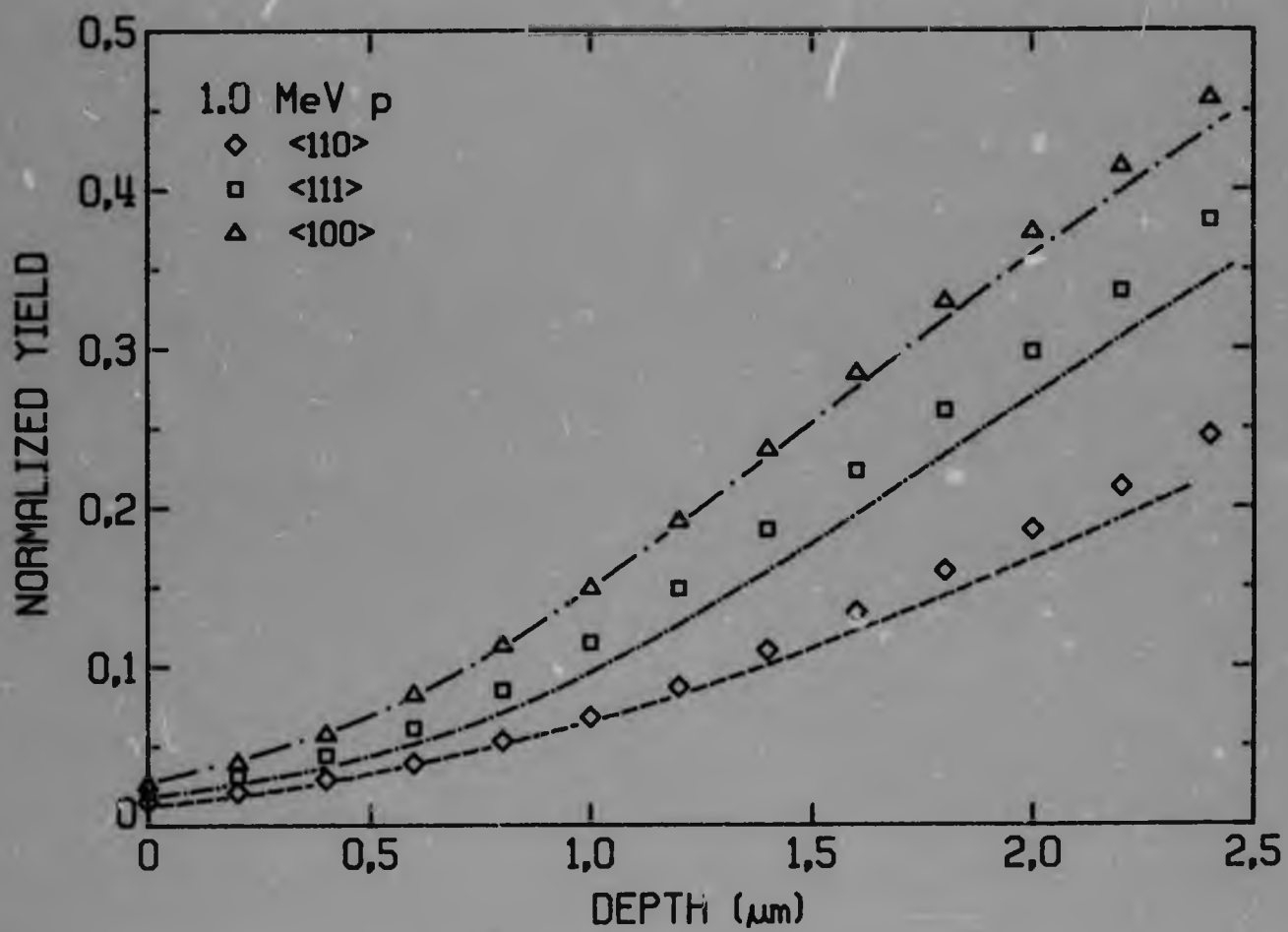


Figure 5.6: Dependence of the normalized yield on depth for the three major axes. Calculated curves:
 ----- <110>, - - - - - <111>, - · - · - · <110> .

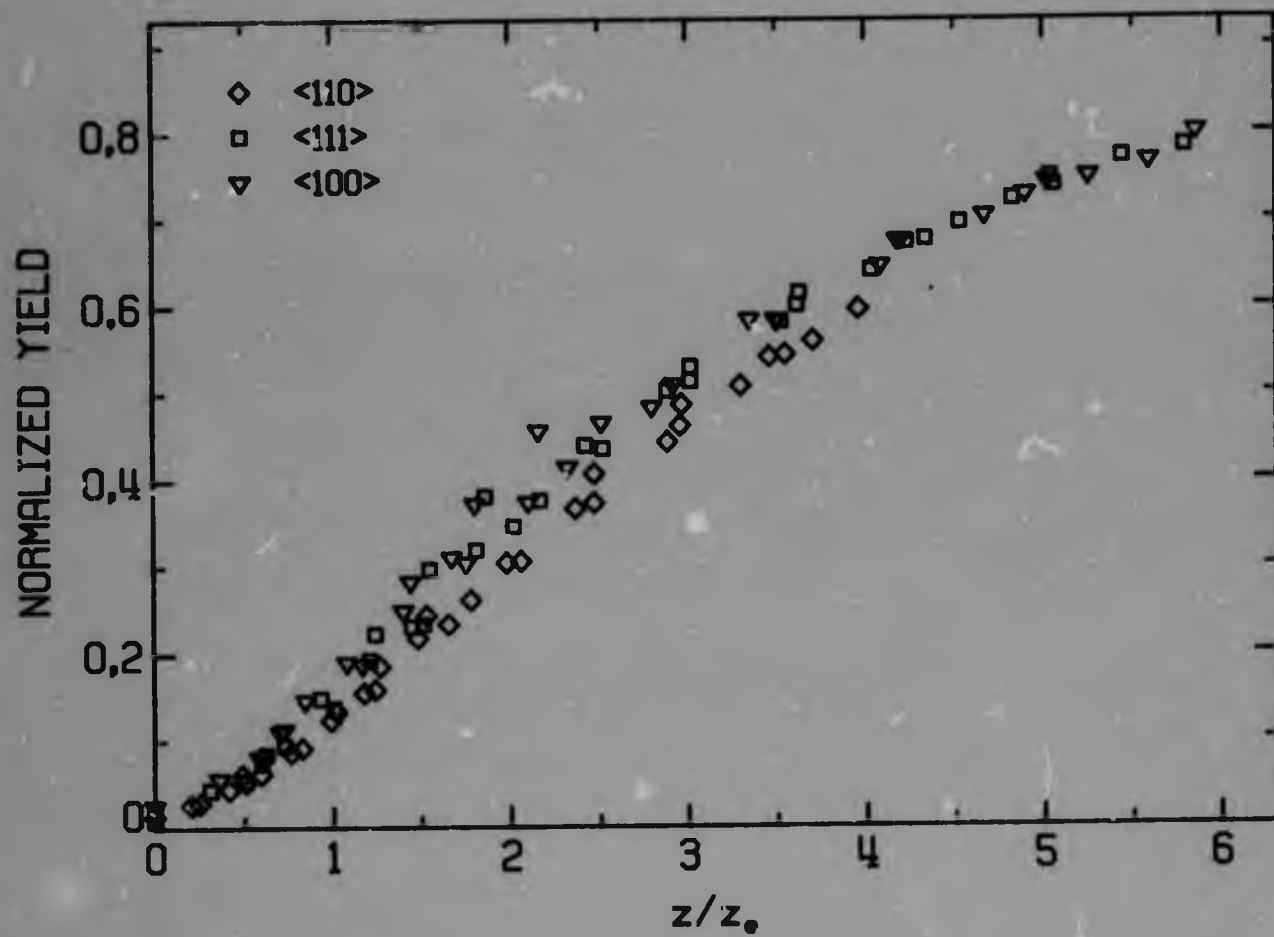


Figure 5.7: Scaled depth dependence of the experimental normalized yield for three major axes.

This is, perhaps, not too surprising. The concept of dechannelling as a diffusion process implies that small perturbations in the initial distributions will become 'washed out' as the diffusion proceeds. Also, the yield, at least at small depths, is determined by diffusion in the region $\epsilon_1 = \epsilon_1^*$ (where ϵ_1^* is given in Table 2.2) and thus the differences at $\epsilon_1 = 0$ should only become important at larger depths.

5.4.3 Temperature Dependence

The depth dependence of the yield at 1 MeV is shown as a function of temperature for the three axes $\langle 110 \rangle$, $\langle 111 \rangle$ and $\langle 100 \rangle$ in Figures 5.8 to 5.10. As can be expected from the high Debye temperature of diamond, 1860 K, the effect of temperature is quite small. Taking as a standard, a yield of 0.20 at room temperature, at 700 °C the yield has increased to 0.24. By comparison, a similar increase in temperature in silicon (Debye temperature 543 K [Ge 74]) increases the yield to 0.43 [Bod 72] and the yield in tungsten [Das 72] (Debye temperature 310 K [Ge 74]) is doubled by an increase in temperatures of 600 °C.

An attempt to find a scaling of the dechannelling with u_2^2 was made, and the yield as a function of $u_2^2 z$ is shown in Figure 5.11 for $\langle 110 \rangle$. No scaling occurs and the order of the curves is inverted.

5.4.4 Planar Dechannelling

The depth dependent yield was measured at 1 MeV for the three planes $\{110\}$, $\{111\}$, and $\{100\}$. Many workers have found that the dechannelling can be described by an exponential decay of the number of channelled particles, and the results are thus plotted as $\ln(1 - x)$ against the depth in Figure 5.12. The deviation from true exponential behaviour (that is, a straight line) is clearly small.

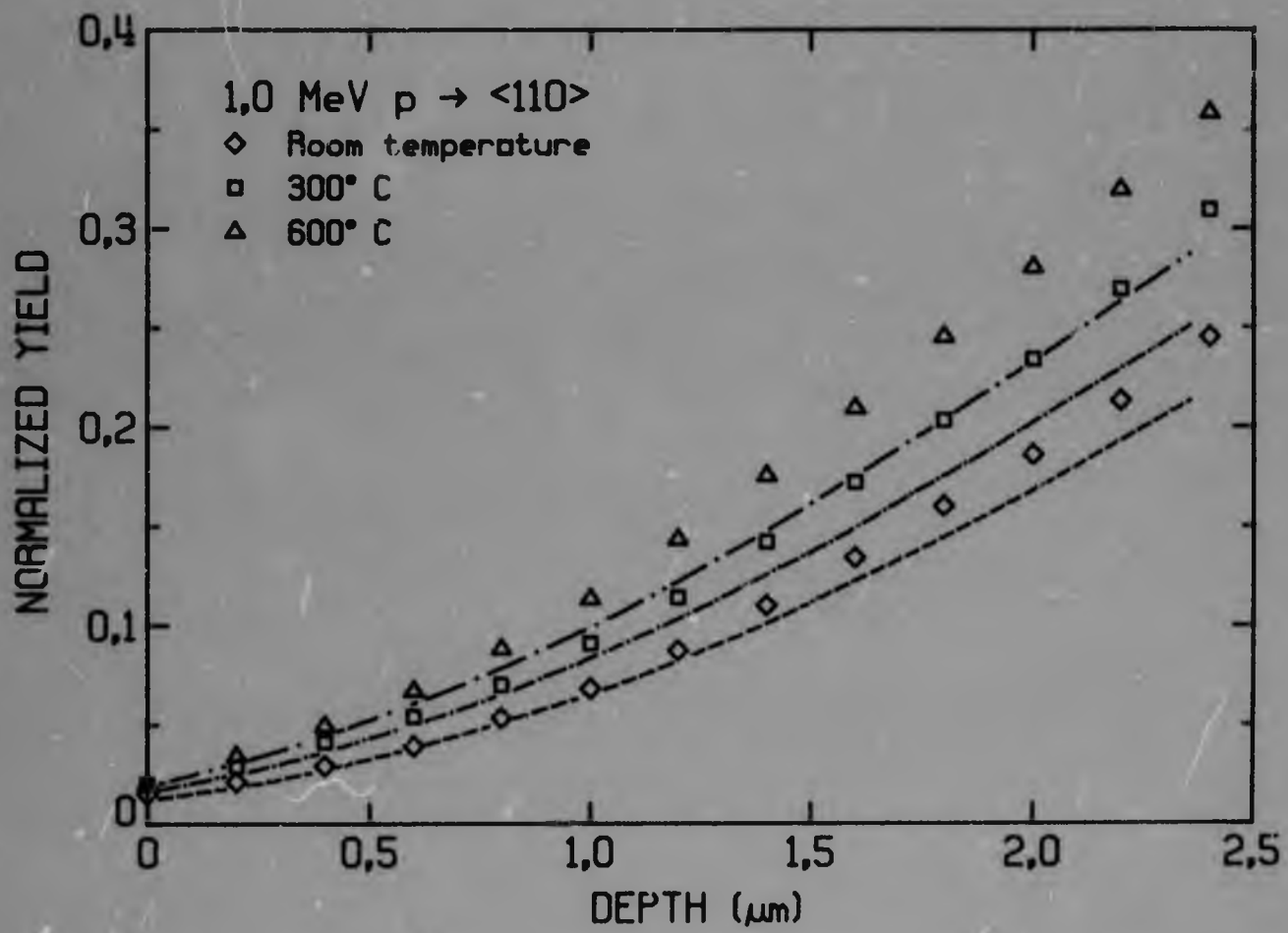


Figure 5.8: Dependence of normalized yield in <110> on depth, at various temperatures. Calculated curves: ----- room temperature, - · - · - 300 °C, - · - · - 600 °C.

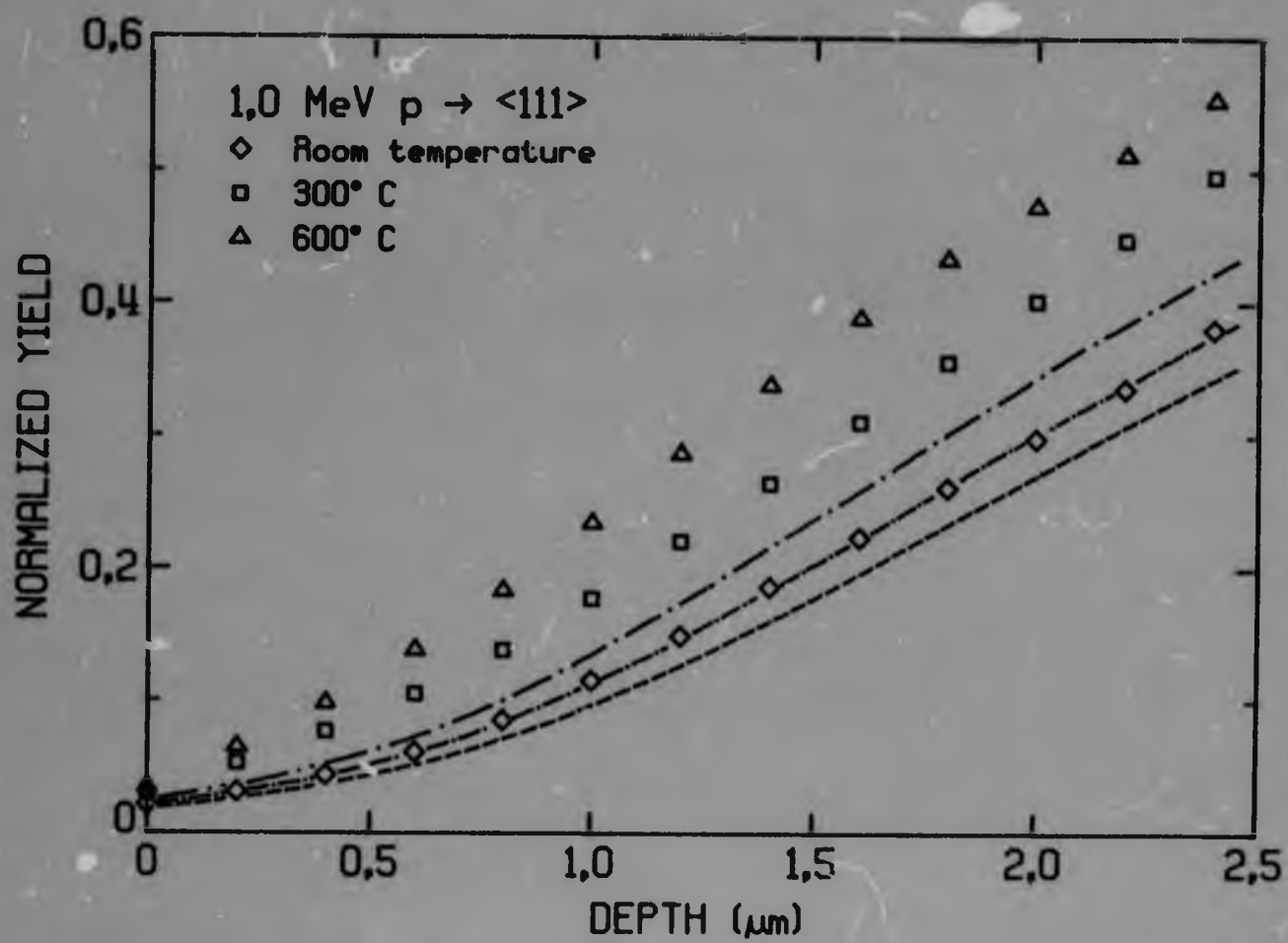


Figure 5.9: Dependence of normalized yield in <111> on depth, at various temperatures. Calculated curves: ----- room temperature, 300 °C, - · - · - 600 °C.

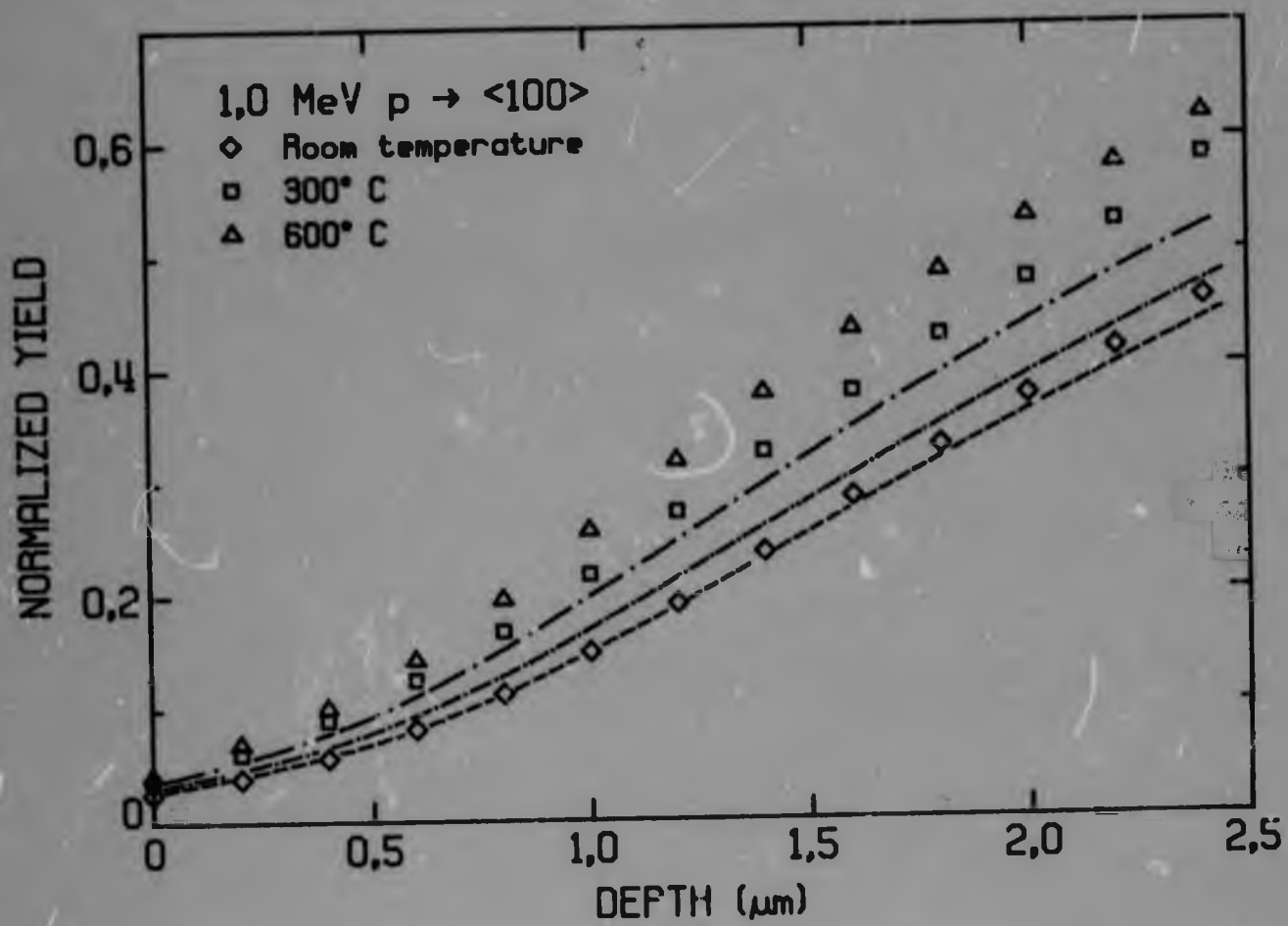


Figure 5.10: Dependence of normalized yield in $\langle 100 \rangle$ on depth, at various temperatures. Calculated curves: ----- room temperature, - · - · - 300 °C, · · · · · 600 °C.

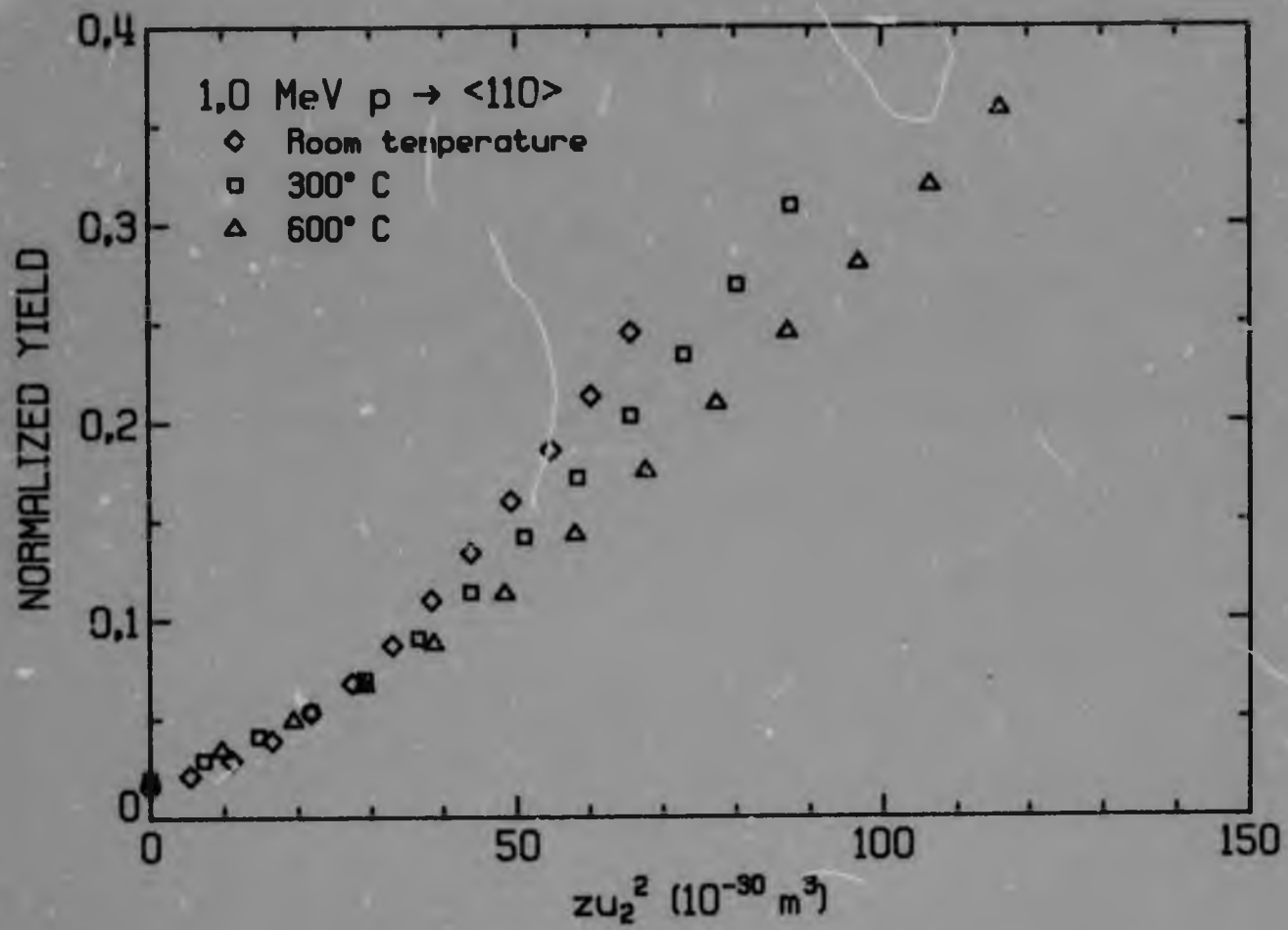


Figure 5.11: Dependence of normalized yield in <110> on zU_2^2 , for various temperatures.

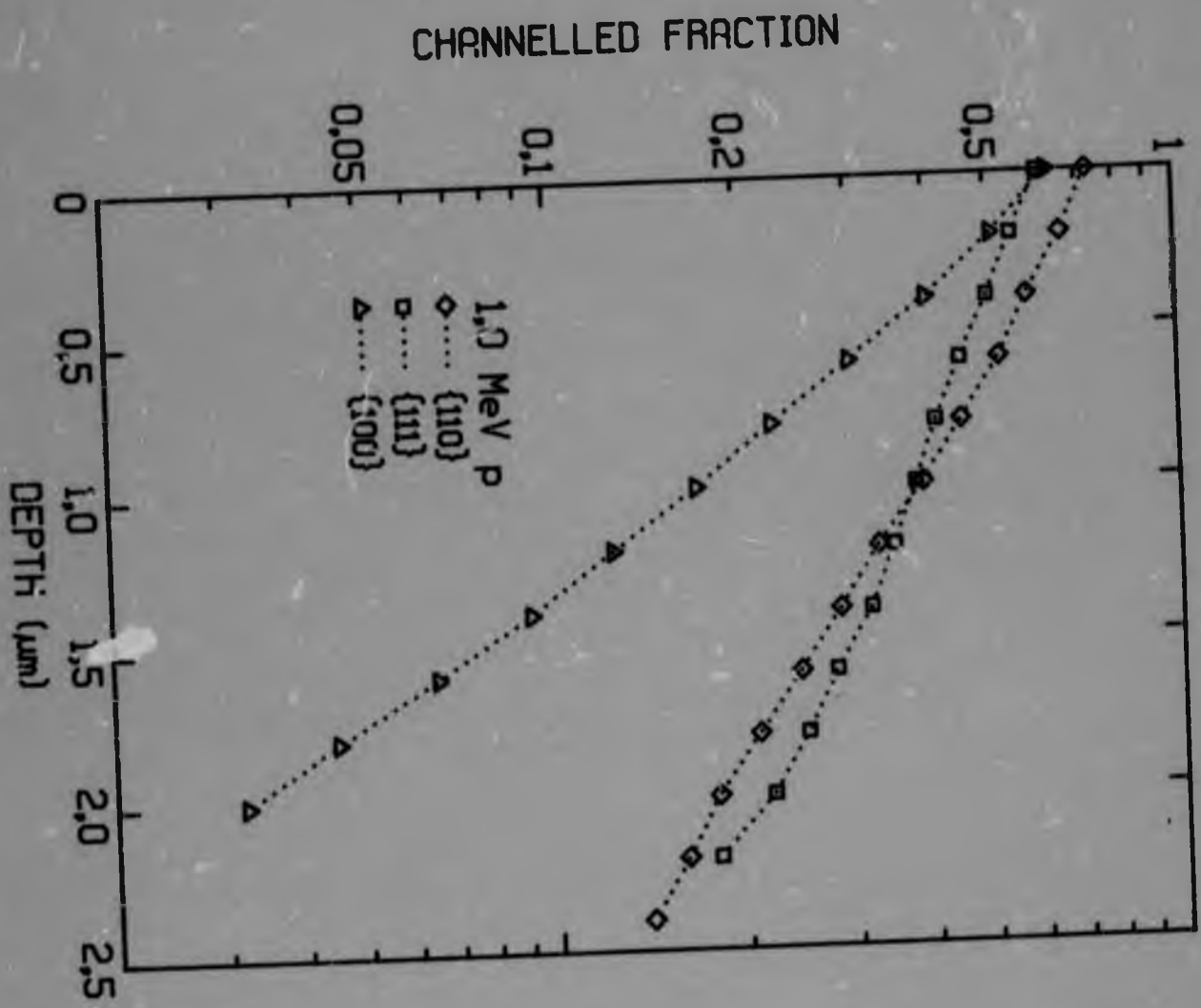


Figure 5.12: Dependence of channelled fraction of beam, 1 - X, on depth, for three major planes.

5.5 COMPARISON WITH THEORY

5.5.1 Axes: The Diffusion Model

The variation of yield with depth is determined in this model by the functions $g(\epsilon_1, 0)$, $A(\epsilon_1)$, $\frac{d\epsilon_1}{dz}(\epsilon_1)$, $\frac{d\epsilon_1}{dz}(\epsilon_1)_{\text{damp}}$ and $\Pi_T(\epsilon_1)$, with the last two being small corrections. The detailed calculation of these functions is difficult and some approximation is necessary. The results are further dependent on the potential chosen to describe the ion-string interaction. Thus the diffusion model leads to a complicated description which is subject to various approximations at different stages. It is then important to determine not only the yield, but also to what extent the calculated yield is sensitive to the various approximations and assumptions that have been made.

The basic function determining the dechannelling is the rate of change of transverse energy with depth,

$$\frac{d\epsilon_{\perp}}{dz}(\epsilon_1) = \left. \frac{d\epsilon_{\perp}}{dz} \right|_e + \left. \frac{d\epsilon_{\perp}}{dz} \right|_n$$

The form of $\left. \frac{d\epsilon_{\perp}}{dz} \right|_n$ used was based on the series expansion of Schjøtt et al ([Sc 75], note in proof). Thus the reduction factor, γ_n , was [Sc 75]

$$\gamma_n = \gamma_1 + \gamma_2 + k \frac{\gamma_2^2}{\gamma_1} \quad (5.5.1)$$

where γ_1 and γ_2 are the first and second order expansion (equations (2.5.5a) and (2.5.5b)) and k is a constant ≈ 1 . The resulting $\left(\frac{d\epsilon_1}{dz}\right)_n$ was compared with the curve calculated numerically, with scattering angles restricted to $\leq \psi_1$, and a value of $k \approx 1.5$ was found to give reasonable agreement for $\epsilon_1 \leq \epsilon_1^*$. The numerical curve and the approximation (5.5.1) are shown in Figure 5.13 for 1 MeV protons in $\langle 110 \rangle$. The approximation (5.5.1) was used until it reached the random value, and the latter was then used. This leads to an overestimate of the numerical results in the region slightly above ϵ_1^* , and some calculations were made with a straight line approximation from $\epsilon_1 = 3$ to $\epsilon_1 = 7$ as shown in Figure 5.13, in order to evaluate the effect of the simpler approximation. It should be noted that all these calculations were based on the Lindhard potential, equation (2.2.4).

For the electron scattering term, $\left(\frac{d\epsilon_1}{dz}\right)_e$, the 'general' function, equation (2.5.13), has been used with the parameters s_r and s_c calculated for various models of electron scattering. The value of z_e depends on the model stopping power. In order to provide a basis for comparison between the various models and experiment, the values of z_e in Table 5.1 were used, and the values of $\left(\frac{d\epsilon_1}{dz}\right)_e$ obtained were normalised to these values of z_e through the random stopping power as calculated in the models. The agreement between the theory and experiment should then be independent of the actual stopping power used for the depth conversion except, of course, for the effect of the neglect of the effective channelled stopping power in the depth conversion.

Three models of electron scattering have been used:

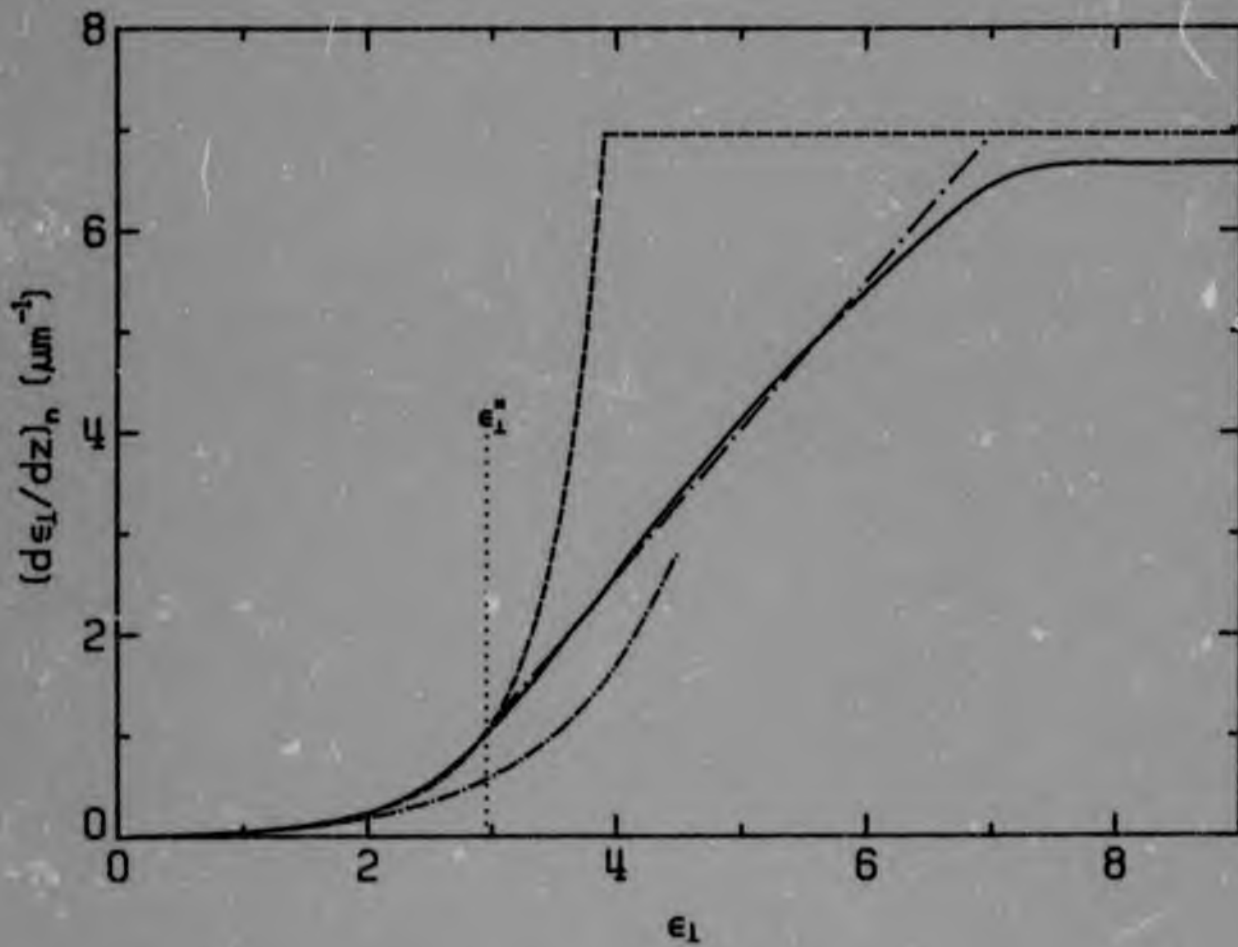


Figure 5.13: Rate of change of transverse energy with depth, due to nuclear scattering, for 1.0 MeV p in $\langle 110 \rangle$.
 (i) ——— numerical calculation, (ii) - - - - from equation (5.5.1), (iii) - · - · - straight line interpolation used with (ii), (iv) ····· first order term, equation (2.5.5b).

- 1) A simple 'equipartition' model [Lin 65] (denoted 'E' in Table 5.2

Table 5.2
PARAMETERS s_c AND s_r FOR $\left(\frac{d\epsilon_1}{dz}\right)_e$
(for description of different sets see text)

Parameter set	s_c					
	<110>		<111>		<100>	
	1 MeV	10 MeV	1 MeV	10 MeV	1 MeV	10 MeV
F	2.07	1.93	5.26	4.18	3.98	3.24
B	1.43	1.38	8.33	7.30	3.03	2.78
C	1.64	1.46	5.85	3.73	3.73	2.65
	s_r					
	E		B		C	
	1 MeV	10 MeV	1 MeV	10 MeV	1 MeV	10 MeV
	1.0	1.0	0.804	0.885	1.19	1.11

and figures) in which

$$\left(\frac{dE_1}{dz}\right)_e = \frac{1}{2} \frac{m_e}{M_1} \frac{dE}{dz} (E_1)$$

The stopping power at the potential minimum, that is, for $\epsilon_1 = 0$ has been calculated from equations (2.4.33) and (2.4.24). (The resulting stopping power is similar to that obtained from the

theory of Esbensen and Gclovchenko, equation (2.4.25). This is discussed at greater length in Chapter 8.)

- ii) The electron gas model of Bonderup et al [Bod 72], equation (2.5.10) (denoted 'B'). The electron density at the potential minimum was determined using experimental X-ray structure factors [Gor 59], and this was used to calculate the local electron scattering at the same position. The random stopping power for this model was obtained by using the local density approximation with Hartree-Fock wave functions for a free atom to give the mean ionisation potential $I = 74$ eV. The value which would be obtained from using more realistic electron densities, for example, from the X-ray structure factors is not expected to differ much from this value; in any case the resulting stopping power is not too sensitive to the value of I because of its occurrence in the logarithmic term

$$\ln \frac{2m_e v^2}{I}$$

- iii) In the third approximation (denoted 'C'), $\left. \frac{d\epsilon_1}{dz} \right|_e$ has been determined from the energy loss to close collisions only; that is,

$$\left. \frac{dE_1}{dz} \right|_e = \frac{m_e}{M_i} \left. \frac{dE}{dz} \right|_{\text{close}} (E_1)$$

$\left. \frac{dE}{dz} \right|_{\text{close}}$ was calculated using the dielectric formalism of

Section 2.4.5, from equation (2.4.14) and equation (2.4.34). A value of $k'_c = 1.25 k_c$ was used in equation (2.4.34) as this gave better agreement with the numerical calculations of Br₇₀ and Reinheimer [Br 70] for the random case.

The values of s_c and s_r for various axes and energies as calculated are given in Table 5.2. The three approximations are compared in Figure 5.14 for 1 MeV protons in $\langle 110 \rangle$.

The effect of damping was taken into account (see Section 2.5.4). Scattering by thermally vibrating atoms through angles larger than θ_1 was taken into account using an absorption term, equation (2.5.31). Both multi-string and single-string initial distributions, based on the Lindhard potential, were used.

Calculations were carried out to assess the importance of different terms and the sensitivity of the calculated yield to various parameters and approximations. The basis for comparison was the yield as calculated for 1 MeV protons in $\langle 110 \rangle$, with the set E of Table 5.2 used for the electronic term parameters, and using a multi-string initial distribution.

In Figure 5.15 is shown the effect of varying the random electronic scattering by $\pm 10\%$ while keeping the scattering for $\epsilon_1 = 0$ at the original value, and the effect of varying the value at $\epsilon_1 = 0$ by $\pm 10\%$ while keeping the random value constant. It can be seen that the greatest change in the yield amounts to $\sim 5\%$ and that the yield, as might be expected, is more sensitive to changes in the random value than in the centre channel value. This is consistent with the conclusions of Section 5.4.2. The

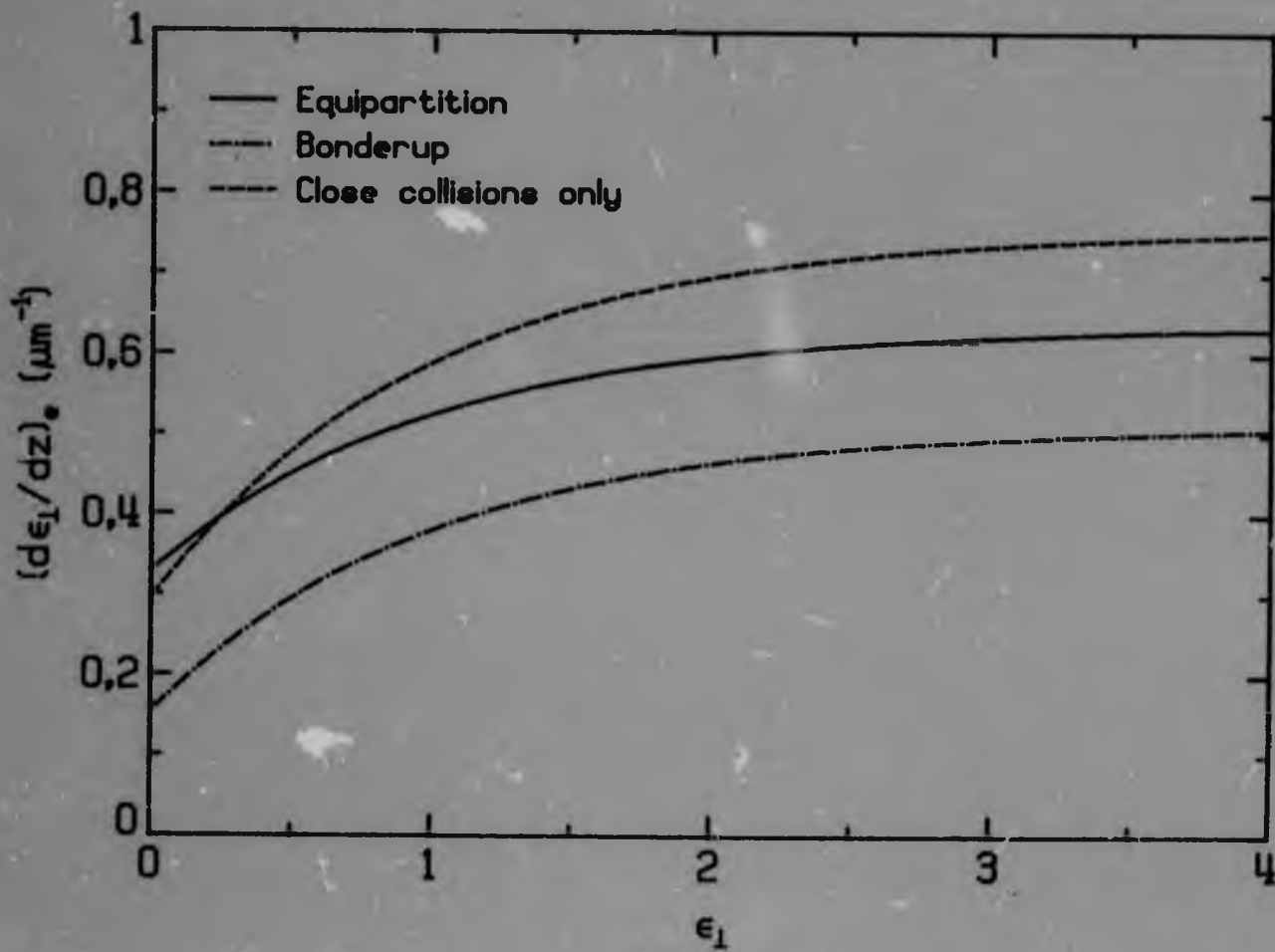


Figure 5.14: Rate of change of transverse energy with depth, due to electronic scattering, for 1.0 MeV p in $\langle 110 \rangle$.

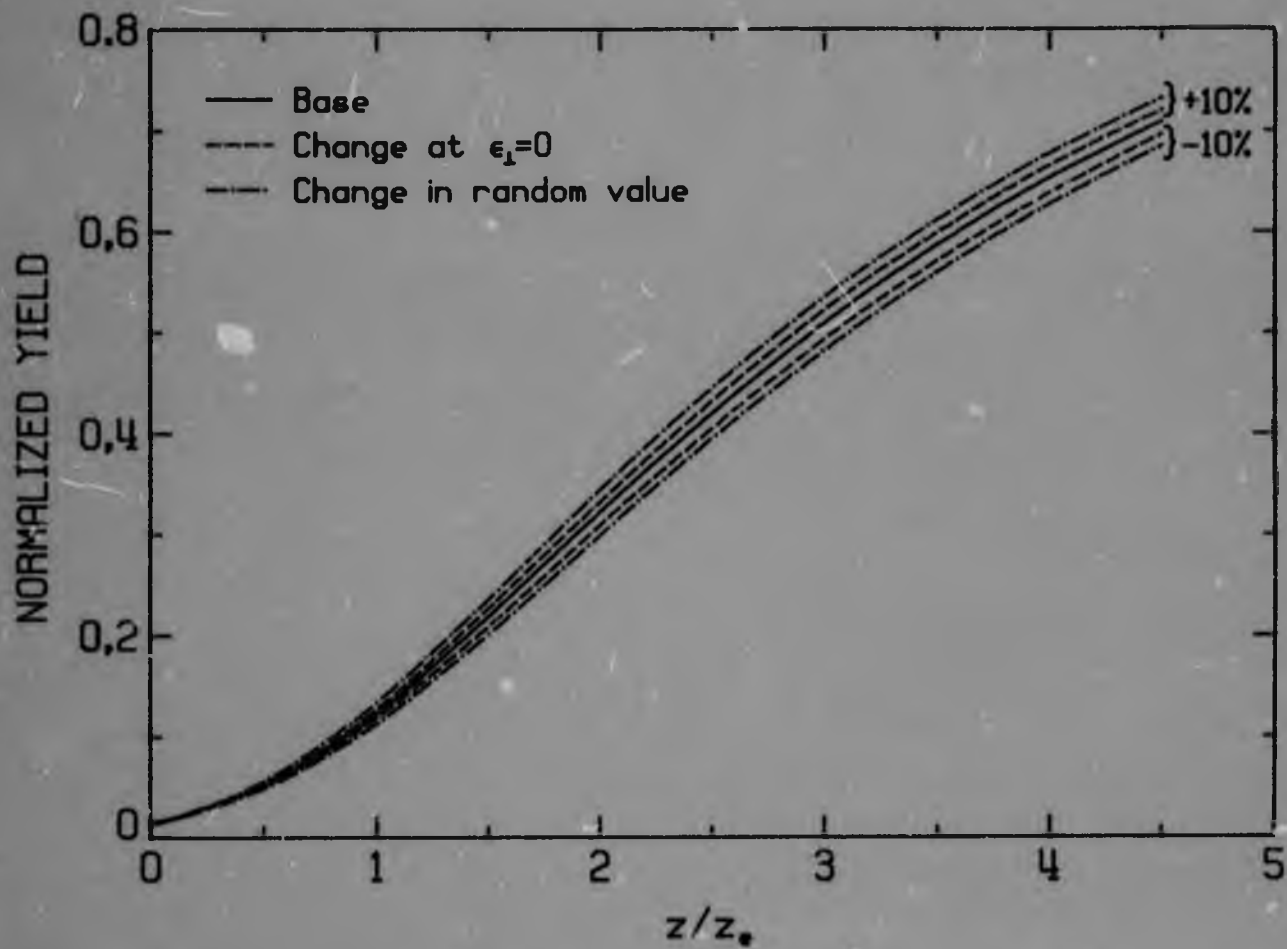


Figure 5.15: Effect of changes in electronic scattering on the yield calculated using the diffusion model, for 1.0 MeV p in $\langle 110 \rangle$.

effect of the approximation for the thermal term is shown in Figure 5.16, where the introduction of the straight line approximation in Figure 5.13 is shown to result in a small change in the yield. The effect of this is only felt for larger z/z_0 . It can be concluded that the multiple scattering in the region beyond the critical transverse energy is relatively unimportant in determining the yield, as diffusion is very rapid in this region. Also shown is the yield calculated for the single-string initial distribution. The introduction of the multi-string distribution is shown to have only a small effect on the calculated yield. The effect of the diffusion is to render the calculated yield insensitive to the initial distribution, within reason (that is, provided the yield at $z/z_0 = 0$ is similar; the case of major changes in the initial distribution due to over-laying the crystal with an amorphous film, is considered in the next chapter). Also shown in Figure 5.16 is the effect of neglecting the dependence of accessible area on transverse energy, that is, taking $A(\epsilon_1) = 1$ for all ϵ_1 . The effect of this is to increase the yield at small depths and to decrease it at larger depths; no great changes occur, however. The results calculated from the analytical solution, equation (2.5.25), are also shown. This is, of course, for $A(\epsilon_1) = 1$ and using the single-string distribution; the diffusion length, z_D , was obtained from the 'base' curve. The yield is in good agreement with the numerical solutions at smaller depths but falls below them at larger depths, when the effect of the more complex diffusion functions, varying with ϵ_1 , become apparent. It is clear that the yield at smaller depths is determined largely by the value of the functions in the region $\epsilon_1 = \epsilon_1^*$; at larger depths the effect of the region $\epsilon_1 < \epsilon_1^*$ becomes important in determining the yield. In the final analysis, the decreased multiple scattering at small ϵ_1 in the more complex models results in a slower diffusion from this region; this

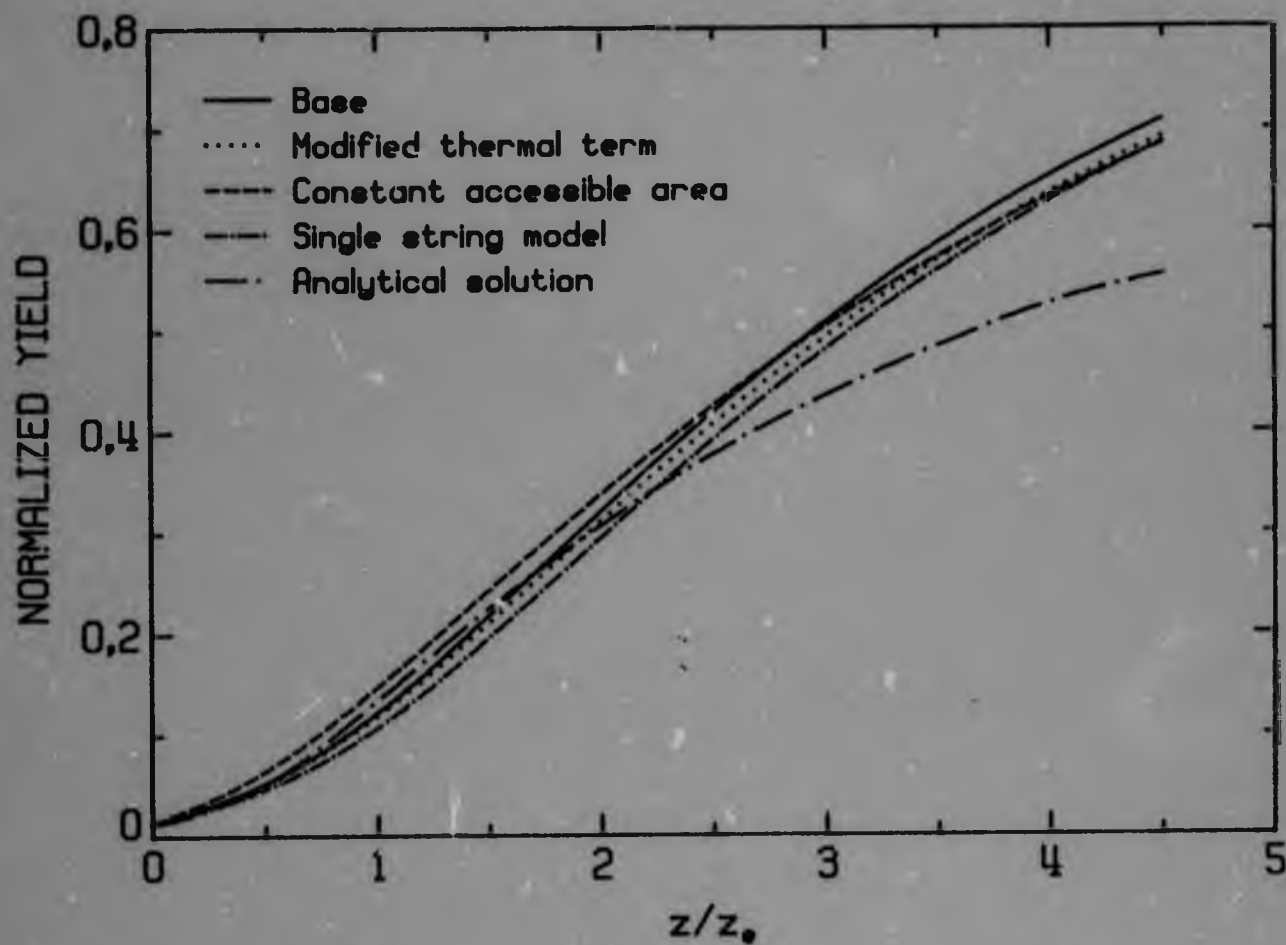


Figure 5.16: Effect of changes to various terms on the yield calculated using the diffusion model, for 1.0 MeV p in $\langle 110 \rangle$.

leads to higher gradients in the distribution which leads, at larger depths, to a greater rate of increase in yield with depth.

In Figure 5.17, the effect of the damping and absorption terms is shown. It is confirmed that the effect of these is small, but both lead to an increase in yield at larger depths. That the damping term leads to an increase in the yield at larger depths is, at first sight, paradoxical as the term causes a decrease in transverse energy. In steady increase model calculations, the term leads to a reduction in the yield [Bj 72]. In fact, the yield is reduced very slightly at smaller depths; at larger depths the yield is increased. This can be traced again to the modification of the distribution which develops a larger slope at greater depths and, hence, a greater dechanneling rate, as a result of this term. Finally, the results of neglecting the electronic and thermal terms is shown. Although the terms are not additive, as is immediately apparent, the relative importance of the two can be judged; clearly the thermal term is a relatively small (15%) correction to the electronic term.

Thus the calculated yields show no undue sensitivity to the various factors and approximations in the description. Calculated yields for the three axes are shown in Figures 5.3 to 5.5. Multi-string distributions were used and the thermal term of equation (5.5.1) was used with no straight line approximation. Both sets (E) and (C) of electronic parameters give reasonable agreement, but set (B) gives low values, especially in $\langle 110 \rangle$. This latter model gives multiple scattering that is approximately proportional to the electron density along the path; the neglect of interactions at a greater distance would appear to lie at the root of the discrepancy, that is, the local density approximation is not strictly valid.

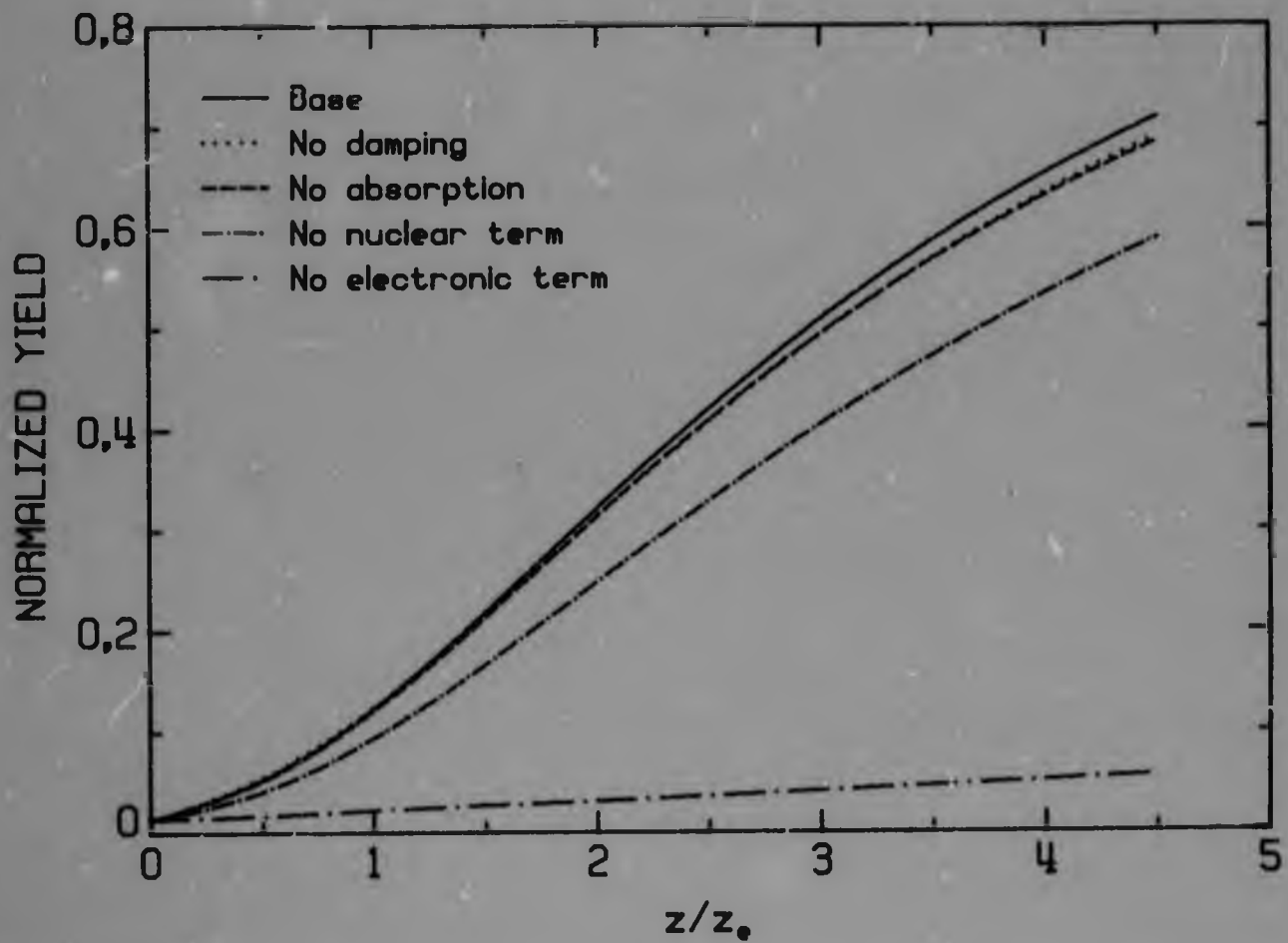


Figure 5.17: Effect of changes to various terms on the yield calculated using the diffusion model for 1.0 MeV p in <110>.

Of the two sets (E) and (C), set (E) appears to give better agreement. At the present level of accuracy of the theory, it is probably not possible to make a choice between the two; perhaps a more detailed calculation of the transverse energy dependence of the electronic term is necessary.

The calculated temperature dependence is shown in Figures 5.8 to 5.10, using set (E) values for the electronic term. It is clear that the experimental variation is larger than the theoretical variation. This suggests that a larger thermal contribution is necessary; this would tend to give a better agreement of set (E) values with experiment. There can be two sources for this inadequacy of the thermal term:

- 1) The calculation has been made with a Lindhard potential. It has been shown that a Molière potential leads to a larger thermal scattering [Cam 71]. Thus, a more accurate potential might give a larger thermal contribution. Whether a Molière potential is more accurate for diamond is not known; it is perhaps no more accurate than the Lindhard approximation as the Thomas-Fermi theory on which these potentials are based is only valid for larger atomic numbers. A potential calculated from Hartree-Fock wave functions should give a better approximation to the true potential. For comparison, the results of Campisano et al [Cam 71] for germanium have been scaled to diamond for the Molière potential, that is, they found their thermal term was increased by $\sqrt{2}$ for the Molière potential, over the Lindhard potential. Using this same factor to increase the Lindhard thermal contribution, gives the

curves of Figure 5.18 for $\langle 110 \rangle$, with the set (E) electronic parameters. The agreement is seen to be much better.

- ii) In the calculation of the thermal term, statistical equilibrium on the transverse energy shell has been assumed. Barrett [Da 73] has pointed out that this assumption is not necessarily valid, due to the presence of focusing effects in the transverse plane. Ions that have had a close encounter with one string, can be focussed onto other strings at particular transverse energies; this leads to an enhancement of close encounter processes and is responsible, for example, for the increase in yield over the Lindhard value. Such processes will undoubtedly occur in diamond and have some effect on the thermal scattering; their effect can, however, only be evaluated using a Monte-Carlo approach or detailed trajectory calculations.

Thus the diffusion model can give results that are in reasonable agreement with experiment. More detailed comparison requires a more accurate calculation of both the electronic and thermal terms, with some evaluation of a realistic ion-atom potential and the effect of focusing in the transverse plane. Such detailed comparison will also require a more accurate calculation of the depth scale, taking into account the variation of energy loss with trajectory. A possible approach to determining the effective energy loss to be used is in the work of Rudnev and co-workers [Rud 74, Ros 77].

5.5.2 Axes: The Steady Increase Model

Calculations for the steady increase model are shown in Figures 5.19

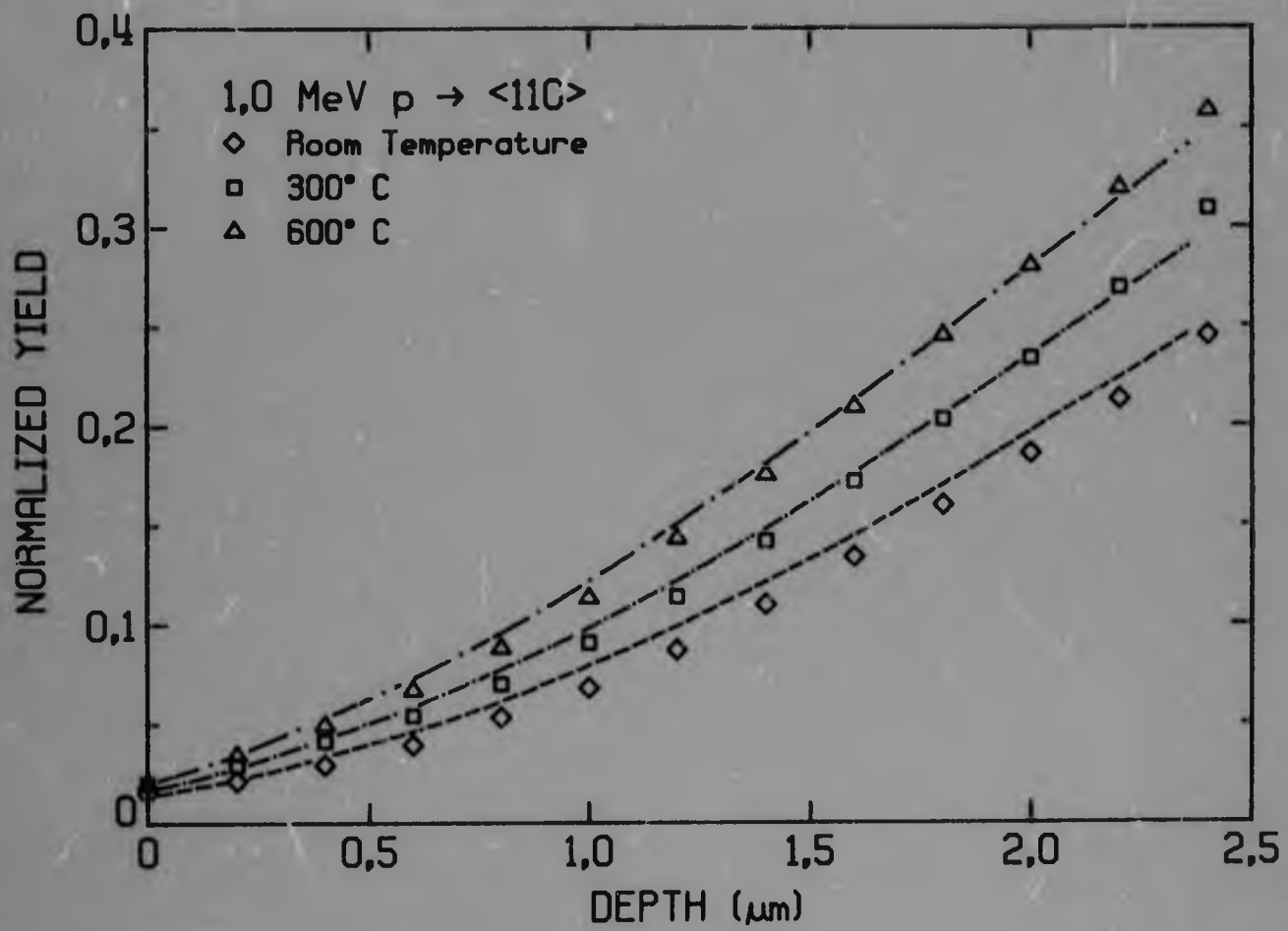


Figure 5.18: Temperature dependence of normalized yield in <110> on depth. Calculations using modified thermal description: ----- room temperature, -·-·-·-·- 300 °C, -·-·-·-·- 600 °C.

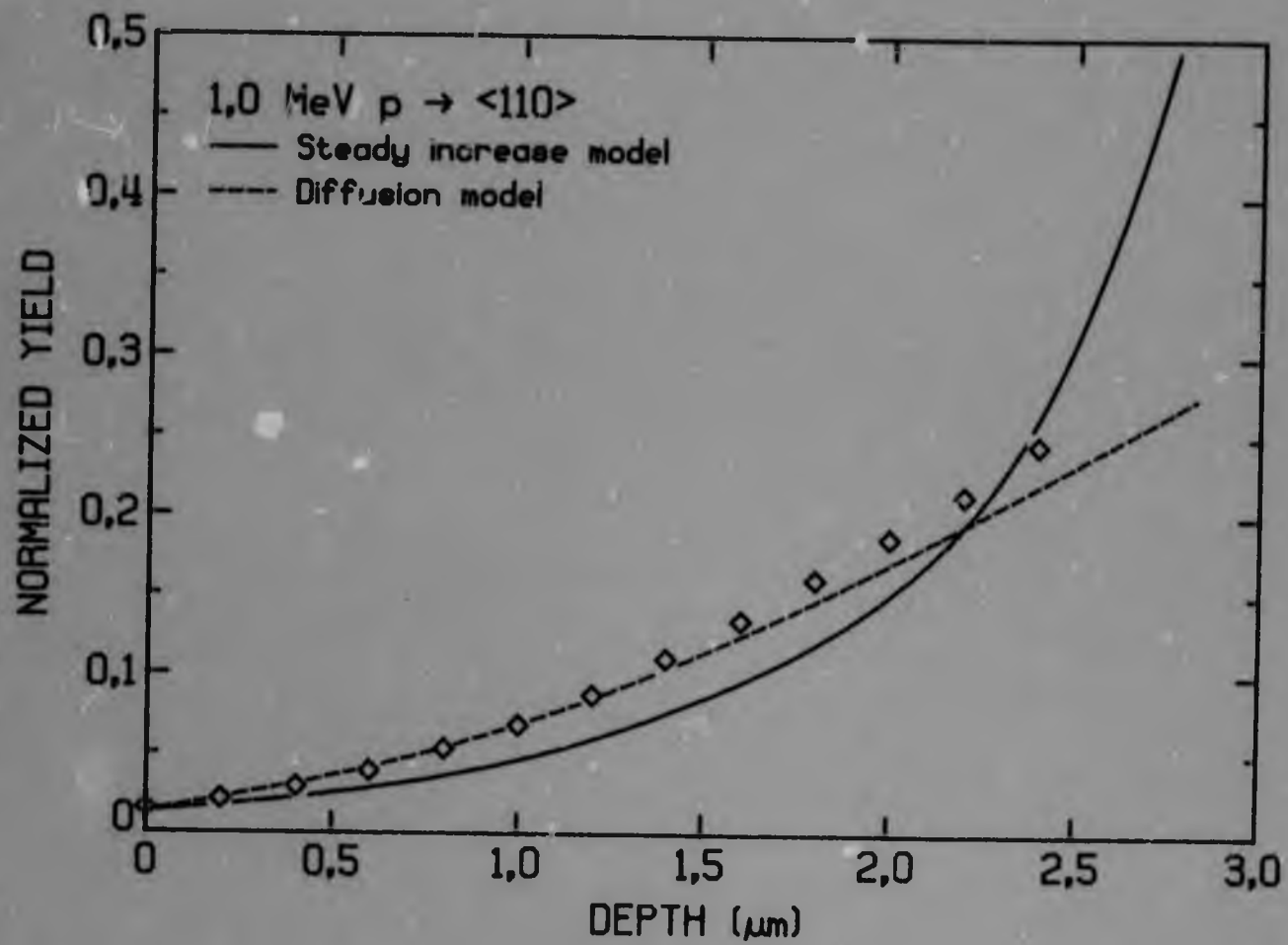


Figure 5.19: Comparison of steady increase model and diffusion model.

for $\langle 110 \rangle$. At small depths, there is some measure of agreement, but at larger depths the rapid increase in the calculated yields leads to disagreement. Thus, it can be concluded that the model is not adequate for use in diamond. This is not too surprising: the model is only valid when $\frac{d\epsilon_1}{dz}$ is changing rapidly with ϵ_1 ; in diamond where the electronic term is dominant for $\epsilon_1 < \epsilon_1^*$, diffusion becomes important.

5.5.3 Planes

The measured dechannelling half-lengths for the three planes, $\{110\}$, $\{111\}$ and $\{100\}$, found by drawing a straight line through the points in Figure 5.12, are given in Table 5.3, together with the theoretical

Table 5.3
PLANAR DECHANNELLING HALF-LENGTHS, $x_{\frac{1}{2}}$, IN DIAMOND
 (for 1 MeV protons at room temperature)

Plane	Mean d_p pm	$x_{\frac{1}{2}}^F$ (eqn 2.5.32) μm	$x_{\frac{1}{2}}^M$ (eqn 2.5.33) μm	$x_{\frac{1}{2}}$ Experiment μm
$\{110\}$	126.1	0.45	2.17	1.0
$\{111\}$	103.0	0.40	1.33	1.2
$\{100\}$	89.2	0.19	0.93	0.5

estimates of Feldman et al, equation (2.5.32) and of Morgan, equation (2.5.33). The Molière potential has been used in the evaluation of

equation (2.5.33); the Lindhard potential leads to values $\sim 10\%$ higher. For $\{110\}$ and $\{100\}$ the Feldman value underestimates the experimental value by a factor of 2, while the Morgan value over-estimates it by a similar factor. The experimental value for $\{111\}$ does not follow this progression, which follows the mean planar spacing, d_p , also given in Table 5.3. The $\{111\}$ plane, however, has two spacings of 51.5 pm and 154.5 pm. It can be expected that there are two dechannelling components, corresponding to these spacings. There is some evidence for this in Figure 5.12, and an initial 'short-lived' component with a half-length of $\sim 0.5 \mu\text{m}$, and a 'longer-lived' component with a half-length of $1.5 \mu\text{m}$ can be identified. The Morgan theory gives half-length values of $0.36 \mu\text{m}$ and $3.0 \mu\text{m}$ for the two, respectively. (The Feldman theory does not allow a distinction to be made.) The Morgan wide-spacing value is again twice the experimental value. If the narrow-spacing half-length is as small as the Morgan value suggests (that is, $\sim 0.18 \mu\text{m}$), accurate investigation of this will require high resolution detectors; the measurement can then be expected to be complicated by oscillations in the yield as a function of depth [Abe 72a].

Inclusion of nuclear scattering in the theory will reduce the half-length (although the effect is likely to be small [Bel 73]) and will thus increase agreement between the Morgan theory and experiment. The agreement can be considered reasonable in view of the simplicity of the theory. A more general approach, using numerical solution of the diffusion equation, was not undertaken because of the minor role played by planar dechannelling in this work.

5.6 CONCLUSION

The depth dependence of the yield in the axes $\langle 110 \rangle$, $\langle 111 \rangle$ and $\langle 100 \rangle$ has been investigated for diamond. The temperature dependence is small. The energy dependence has been found to be determined by the electron stopping power and a scaling of the yield with z/z_0 has been found. The axial dependence in the scaled depth variable suggests that the dechannelling mechanism in all three axes is similar, and that the processes are not too sensitive to fine details of the motion.

Calculations with the diffusion model are in satisfactory agreement with experiment. Closer investigations of the agreement will require more detailed calculations of the multiple scattering, leading to some loss of generality in the model and to much numerical complexity. The depth scale will also have to be calculated more exactly.

EFFECT OF AMORPHOUS SURFACE LAYERS ON CHANNELLING

6.1 INTRODUCTION

Measured channelling parameters, such as the minimum yield and critical angle and the yield as a function of depth, are affected by amorphous layers present on the surface of the crystal. An initially well-collimated beam is scattered in the layer, and the ions enter the crystal with a distribution of incident angles relative to the initial direction [Lin 65]. The minimum yield is increased: the yield must now be taken as an average of the yield as a function of angle, weighted with the angular distribution of the scattered beam.

It is of interest to study the effect of amorphous layers, as these layers can be present on the crystal for several reasons, for example, layers produced by surface oxidation, or by condensation of vapours from the vacuum system. Also, amorphised layers produced by radiation damage (for example, by ion implantation) can be treated in a similar fashion to surface layers [Rim 72, Got 75b] and their study is thus of importance for channelling investigations of crystal disorder. Furthermore, the scattering in the layer leads to changes in the initial transverse energy distribution in the crystal and so crystals covered with amorphous layers may be used to study dechannelling [Cam 73].

The effect of gold and aluminium layers evaporated onto silicon crystals has been studied by several workers [Rim 72, Lug 73, Cam 73,

Got 75b]. It has been shown [Rim 72] that the increase in minimum yield can be predicted by averaging the angular yield function over the plural scattering distribution of Meyer [Mey 71]. It has also been shown that an azimuthally averaged angular yield function is the most appropriate, although a square-well approximation can give good results [Lug 73]. It has also been shown that the steady-increase model of dechannelling can give a good account of the yield as a function of depth, and that this can also be determined using a depth-dependent angular yield function [Cam 73].

The use of diamond as a target material enables the comparison of theory with experiment to be extended to light mass surface atoms such as carbon, which is a common constituent of contamination layers deposited on targets in vacuum systems. The effect of carbon, aluminium and gold layers evaporated onto diamond is studied in this Chapter. The experimental method is detailed in Section 6.2, and the treatment of data in Section 6.3. Comparison of theory, outlined in Section 6.4, with experiment is made in Sections 6.5 and 6.6 where the yield as a function of larger thickness has been calculated using the plural scattering treatment of Meyer, as modified by Sigmund and Winterbon [Si 74] using several angular yield functions, and the yield as a function of depth is calculated, using the diffusion model of dechannelling.

The effect of thin layers, such as are likely to approximate contamination layers, has not been much studied. This problem is studied in Section 6.7 where several simple theoretical approximations are given which give good agreement with experiment. Also in this section, a power-law scaling rule is discussed which relates the yield due to different layers. This rule is found to have some validity, and has been used in

the correction of the aluminium thickness for small amounts of oxygen contamination. Conclusions are summarised in Section 6.8.

6.2 EXPERIMENTAL METHOD

The experiments were performed using a diamond which was regarded as a good channelling stone, although not of the best, with a minimum yield of about 2 % and a yield at 2.5 μm of about 30 % on the uncovered diamond. Measurements were taken using 1.0 MeV protons along the $\langle 110 \rangle$ axis at room temperature.

A layer of gold, aluminium or carbon was evaporated onto a polished surface of the diamond using standard evaporation techniques. An aligned spectrum was taken, the target was rotated to face the ion-sputtering gun in the chamber and a portion of the layer was removed by sputtering with argon ions of 900 eV energy. Another spectrum was then taken and the procedure was repeated until the layer had been removed.

The thickness of the layers showed no angular dependence and it was taken that these were amorphous for the purposes of the experiment. The shape of the spectrum also indicated that the crystal was covered completely by the layer.

6.3 TREATMENT OF DATA

6.3.1 Determination of Layer Thickness

The layer thickness was determined for the backscattered spectrum using the usual relation

$$N_x = \frac{C}{n\sigma d\Omega} \quad (6.3.1)$$

where N_x is the areal density of the layer (= density N times thickness x); C is the number of backscattered particles (counts) obtained by integrating the appropriate peak in the spectrum; n is the number of incident particles, obtained from the beam current integration; σ is the scattering cross-section and $d\Omega$ is the solid angle subtended by the detector.

The integration of the gold or aluminium peaks is simple as these peaks are well separated from any interference. The aluminium was found to be accompanied by a small amount of oxygen, and this peak was also integrated for later inclusion in the total layer thickness. The peak due to the carbon layer was separated from the diamond spectrum graphically as illustrated in Figure 6.1. Straight-line approximations were drawn to various parts of the spectrum and the area divided up according to the effect of instrumental resolution.

The maximum error in this procedure was estimated from various limiting possibilities of drawing the lines as about 5 %.

The solid angle subtended by the detector was measured using a calibrated thin ^{241}Am alpha source at the target position. The solid angle was determined from the number of counts recorded in a given period compared with the total number of disintegrations, known from the calibrated activity. Errors due to backscattering in the source were estimated to be negligible compared with the experimental accuracy of

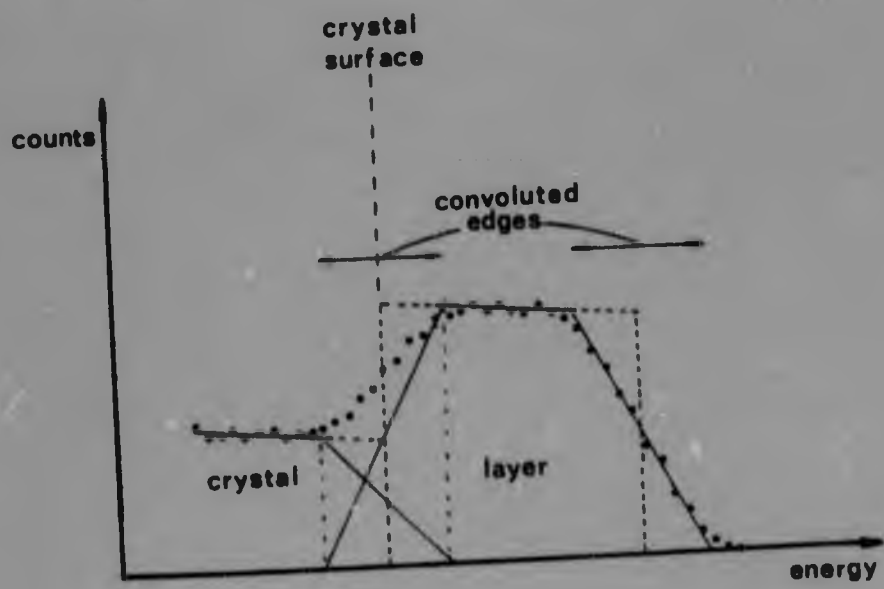


Figure 6.1: Deconvolution of spectrum of carbon layer on diamond.

about 1 %. The measured value, 4.08 m sterradians was close to that calculated from geometrical considerations.

The Rutherford cross-section was used for gold and aluminium; the latter, while essentially Rutherfordian [Aw 65], does have a narrow resonance at 991.9 keV with a width of about 100 eV. The cross-section is increased by about 15 % just above the resonance energy and decreased about the same amount just below the resonance energy [Ben 49]. The maximum error incurred by neglect of this resonance was estimated to be of the order of 1 % for protons leaving the Al layer at the resonance energy. For exit energies from the layer greater than 3 keV from the resonance, the effect of the resonance is negligible, because of the symmetrical nature of the resonance. Estimates of energy loss in the aluminium layer using tabulated stopping powers [Ans 77] showed that with none of the layers did the protons leave the layer with energies in the resonance region and so the resonance was neglected.

For carbon and oxygen measured cross-sections were used (C: [Jas 52], O: [Lau 51]), the former being accurate to 5 % and the latter to 20 %.

The energy dependence of the cross-section was taken into account for the aluminium layer. The proton energy used was that appropriate to the mean energy of the protons in the layer, calculated using tabulated stopping powers [Ans 77]. The maximum variation was 1.7 % from the value calculated for 1.000 MeV. For the other cross-sections the 1.000 MeV values were used. For carbon and oxygen, the cross-sections vary much more slowly with energy than the Rutherford cross-section, and any

correction would be much less than the uncertainties in the measured cross-section. For gold, the energy loss in the layer never exceeded 3 keV; any correction, therefore, would be less than 0.3 %. For convenient comparison of the results with the multiple scattering theory as given by Sigmund and Winterbon [Si 74], the layer thickness was calculated in terms of the dimensionless Thomas-Fermi variable

$$\tau = \pi a^2 N x \quad [\text{Si 74}]$$

where a is the Thomas-Fermi screening radius. The oxygen thickness was scaled to an equivalent aluminium thickness (see Section 6.7) and included with the τ value for aluminium. The correction to the aluminium value ranged from 3 % for the thickest layers to 12 % for the thinnest.

6.3.2 Minimum Yield

The minimum yield was determined by plotting the spectrum and drawing a smooth curve through the points, extrapolated to the surface. The surface was taken to be at that energy corresponding to halfway up the step in the spectrum at the interface between the carbon layer and diamond, or halfway down the step in the diamond spectrum for gold and aluminium or, if the minimum yield was sufficiently low for there to be a well-defined surface peak, at the peak position.

The yield thus determined was normalised to the random yield, using a random spectrum measured on the uncovered diamond but dividing by the value of the random spectrum at the energy corresponding to the equivalent surface of the covered crystal. The yield should be determined using a random spectrum measured with the same layer as the channelled

spectrum used: to keep radiation damage at a minimum this was not done. The above procedure is equivalent to using a random spectrum from a diamond covered with a carbon layer which gives the same energy loss as the actual layer on the diamond. For the carbon layer this procedure gives the same result as a crystal covered with a carbon layer, neglecting any possible chemical bonding effects on the stopping powers [Sof 61, Mat 76]. The energy loss through gold layers was less than 3 keV and any errors made by the above procedure are extremely small. For aluminium layers the procedure was estimated to give a maximum error in the random position of two analyser channels (about 10 keV). The variation in random level over this interval was much less than the statistical uncertainty in the spectrum of $\sim 2\%$ and was, therefore, ignored. It was thus concluded that the above procedure for determining the random spectra was sufficiently accurate.

6.3.3 Depth Conversion

Depth conversion was done in the usual way, taking the surface at its usual 1.000 MeV position. The equivalent depth of the true surface on the covered crystal was then used as the origin for the depth scale.

6.4 THEORY

6.4.1 Plural and Multiple Scattering

The plural and multiple scattering of ions in the keV to lower MeV energy range has been investigated by Meyer [Mey 71] and Sigmund and Winterbon [Si 74], using the Thomas-Fermi concepts of Lindhard et al [Lin 68]. Agreement of the theory with experimental multiple scattering measurements, is good, in general [Si 76]. The treatment of Sigmund and Winterbon is followed here.

The theory uses the universal Thomas-Fermi screened coulomb scattering cross-section of Lindhard et al [Lin 68].

$$d\sigma = \pi a^2 \frac{dt}{2t^{3/2}} f(t^{1/2}) .$$

The variables are defined in Section 2.4.2. With this cross-section the angular distribution of ions after traversing a thickness x of material is

$$F(x, \alpha) d\Omega = a \int_0^{\infty} da \int_0^{\infty} dz J_0(a z) \exp[-\tau \Delta(z)]$$

$$= a \int_0^{\infty} da f_1(\tau, a)$$

where

$$\Delta(z) = \int_0^{\infty} d\phi \frac{f(\phi)}{\phi^2} (1 - J_0(z\phi)) .$$

Here, α is the total scattering angle; x is the thickness of layer traversed; $d\Omega$ is the element of solid angle belonging to α ; and J_0 is the zeroth order Bessel function. a and τ are dimensionless variables

defined by

$$\tau = na^2Nx$$

$$\delta = \frac{Ea}{2Z_1Z_2e^2} \quad (6.4.2)$$

Thus, for all target and ion combinations the multiple scattering distribution is a function only of the two variables τ and δ . Meyer's treatment also includes a function $f_2(\tau, \delta)$ as a small correction to $f_1(\tau, \delta)$ [Mey 71]; this is believed to be an artifact [Si 74].

The distribution, f_1 , defined above is normalised to unity, that is

$$\int_0^{\infty} f_1(\tau, \delta) \delta \, d\delta = \int F(x, \alpha) \, d\Omega = 1.$$

For thin layers, the distribution tends to the single scattering distribution, that is,

$$\lim_{x \rightarrow 0} F(x, \alpha) \, d\Omega = N \, d\sigma(\alpha), \quad \alpha \neq 0$$

or, in dimensionless variables,

$$\lim_{\tau \rightarrow 0} \frac{a^3}{\tau} f_1(\tau, a) = f(a). \quad (6.4.3)$$

The distributions $f_1(\tau, a)$ are evaluated and tabulated for a large range of τ and a in [Si 74].

The Thomas-Fermi cross-section may be approximated by a cross-section derived from a power potential

$$V(r) = r^{-1/m}$$

over limited regions, giving

$$f(\phi) = \lambda \phi^{1-2m} \quad 6.4.4$$

for some range in ϕ , where λ depends on m . With this cross-section, the function $a^2 f_1(\tau, a)$ is a function of one variable, $\frac{a^{2m}}{c\tau}$, where c depends on m . The distribution may be evaluated analytically for certain values of m but, in general, is expressed as a power series. The summation of this power series is much easier than evaluation of the integral in equation (6.4.1). Marwick and Sigmund [Mar 75] have shown that a function $\tau(m)$ relating the τ for the Thomas-Fermi cross-section to the power cross-section parameter, m , may be defined; with this function a

Thomas-Fermi distribution may be approximated by an equivalent power-law distribution; the agreement is very good [Mar 75].

6.4.2 Yield in Channelling Measurements

On an uncovered crystal, the yield near an axial channel depends on both the polar angle ψ from the axial direction and the azimuthal angle ϕ from some reference plane intersecting the channel. With an amorphous layer on the surface of the crystal, the beam is multiply scattered with some distribution $F(x, \psi)$ and the yield, for the beam aligned with the channel, becomes

$$x_L(x) = \int F(x, \psi) \chi(\psi, \phi) \, d\Omega$$

where $\chi(\psi, \phi)$ is the yield measured on the uncovered crystal. $\chi(\psi, \phi)$ may be integrated over the azimuthal angle, giving (for small scattering angles)

$$x_L(x) = 2\pi \int_0^{\pi} F(x, \psi) \chi(\psi) \psi \, d\psi$$

where $\chi(\psi)$ is now the azimuthally averaged angular yield, introduced by Lujjjo and Mayer [Lug 73]. This may be written in dimensionless Thomas-Fermi variables

$$\chi_L(\tau) = \int_0^{\infty} \delta \, d\delta f_1(\tau, \delta) \chi(\delta) . \quad (6.4.5)$$

Thus the yield at 0° on a covered crystal may be determined by using the multiple scattering distribution together with the experimentally measured angular yield (azimuthally averaged) from the uncovered crystal. This relation holds for all depths: thus the yield at 0° as a function of depth may be determined using the angular yield measured as a function of depth [Cam 73].

A simple approximation to $\chi(\psi)$ is sometimes used: the square-well approximation [Rim 72, Lug 73]. In this approximation, the yield is taken as

$$\begin{aligned} \chi(\psi) &= \chi(0) & \psi \leq \psi_1 \\ &= 1 & \psi > \psi_1 \end{aligned} \quad (6.4.6)$$

where ψ_1 is the critical angle. With this definition of the angular yield function, the yield on the covered crystal becomes [Lug 73] (for δ_1 the dimensionless ψ_1)

$$\chi_L(\tau) = \chi(0) + (1 - \chi(0))P(\delta_1, \tau)$$

where

$$P(\bar{\alpha}_1, \tau) = \int_{\bar{\alpha}_1}^{\infty} f_1(\alpha, \tau) \alpha \, d\alpha .$$

The function $P(\bar{\alpha}_1, \tau)$ is given graphically in [Lug 73] for the multiple scattering distributions as calculated by Meyer [Mey 71].

In this work, an approximation is investigated which might be expected to agree more closely with the angular yield. This is a quartic approximation

$$\begin{aligned} \chi(\psi) &= \chi(0) + (1 - \chi(0)) \frac{\psi^4}{2\psi_1^4} ; & \psi < 2^{1/2}\psi_1 \\ &= 1 & ; \quad \psi > 2^{1/2}\psi_1 . \end{aligned} \tag{6.4.7}$$

The three yield functions are compared in Figure 6.2. Also shown in this figure is the usual angular yield measured at fixed azimuth, and the angular yield function determined from the dechannelling approach of the next section.

6.4.3 Dechannelling

The yield as a function of depth may be calculated using the depth-

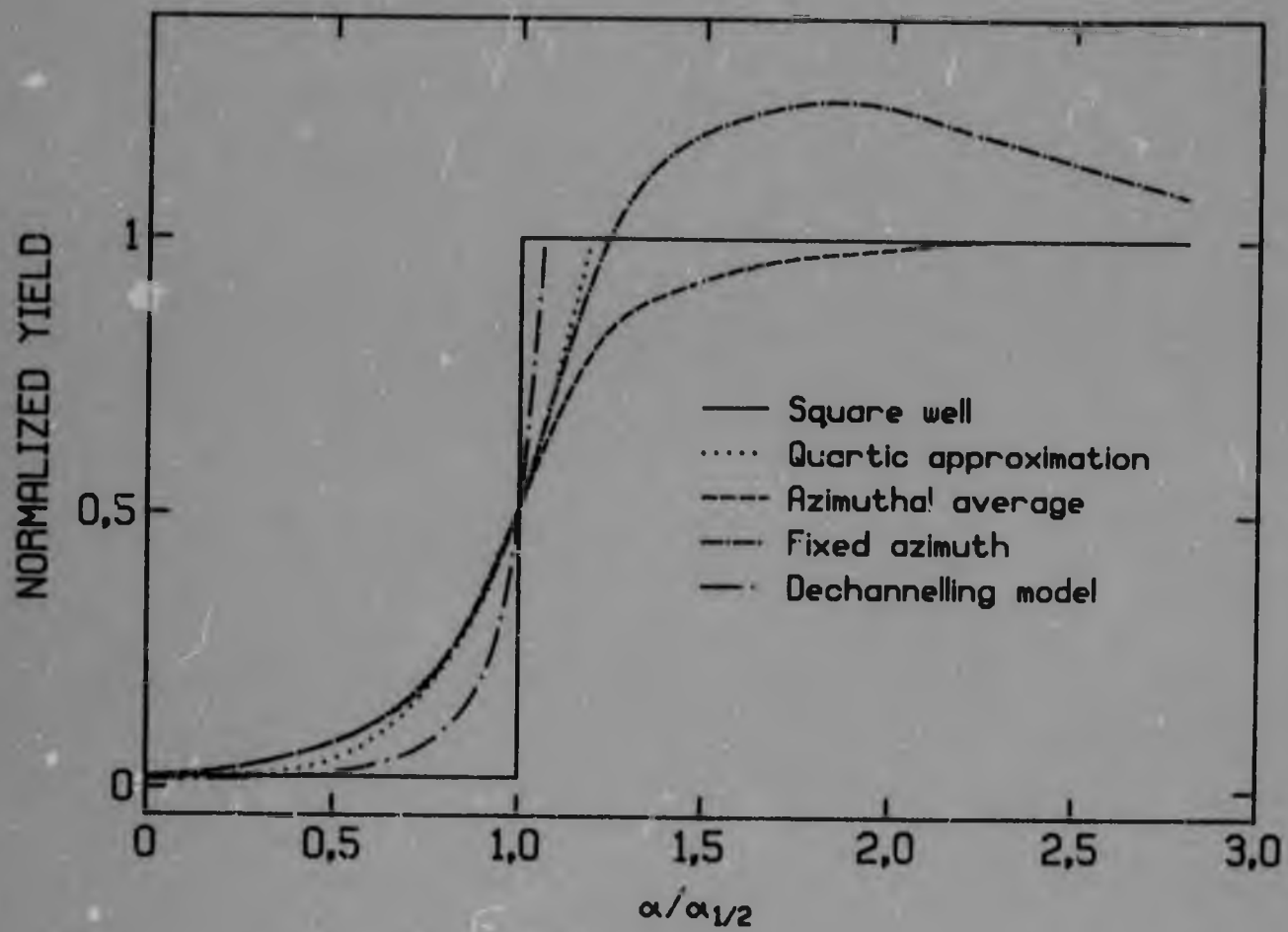


Figure 6.2: Dependence of normalized yield on angle.

dependent angular yield function. It may also be calculated using the diffusion theory of dechannelling or the steady increase model, discussed in Section 2.5. The agreement between theory and experiment should give an additional check on the validity of this theory.

In terms of this theory, the initial transverse energy distribution is modified by the multiple scattering. The multiple scattering distribution may be written, in terms of the transverse energy $E_{\perp} = E\psi^2$ or the reduced transverse energy ϵ_{\perp} ,

$$f'_1(\tau, \epsilon_{\perp}) = \frac{a_1^2}{2\epsilon_{\perp}} f_1(\tau, \dots)$$

where

$$\epsilon_{\perp} = 2 \frac{E_{\perp}^2}{E^2}$$

With this definition,

$$\int_0^{\infty} f'_1(\tau, \epsilon_{\perp}) d\epsilon_{\perp} = 1$$

Equation (6.4.5) becomes

$$\chi_L(\tau) = \int_0^{\infty} f_1'(\tau, \epsilon_1) \chi(\epsilon_1) d\epsilon_1$$

where from Equation (2.3.6)

$$\chi(\epsilon_1) = \int_0^{\infty} g(\epsilon_1' - \epsilon_1) \Pi(\epsilon_1') d\epsilon_1'$$

Thus

$$\begin{aligned} \chi_L(\tau) &= \int_0^{\infty} f_1'(\tau, \epsilon_1) g(\epsilon_1' - \epsilon_1) \Pi(\epsilon_1') d\epsilon_1' d\epsilon_1 \\ &= \int_0^{\infty} g_L(\tau, \epsilon_1') \Pi(\epsilon_1') d\epsilon_1' \end{aligned}$$

where

$$g_L(\tau, \epsilon_1') = \int_0^{\infty} f_1'(\tau, \epsilon_1) g(\epsilon_1' - \epsilon_1) d\epsilon_1 \quad (6.4.8)$$

is the initial transverse energy distribution for the covered crystal.

The diffusion equation may be solved using equation (6.4.8), to give the yield as a function of depth on the covered crystal. Similarly, the integral distribution may be obtained by integrating equation (6.4.8) and used to determine the yield using the steady increase model.

6.5 INFLUENCE OF AMORPHOUS LAYERS ON MINIMUM YIELD AT THE SURFACE

6.5.1 Results

The measured minimum yield at the surface, χ_m , is plotted as a function of τ for the three cases, carbon, aluminium and gold, in Figures 6.3, 6.4 and 6.5 respectively, together with the theoretical curves. The errors shown include, for τ , the various errors and approximations mentioned in Section 6.3, together with the error in the layer thickness owing to the counting statistics. The error in χ is estimated from a consideration of various possibilities in extrapolation of the yield to the surface, and includes the effect of errors in the random spectrum.

6.5.2 Calculation

The theoretical curves have been calculated using the Thomas-Fermi multiple-scattering distributions of Sigmund and Winterbon [Si 74]. Three different angular yield functions have been used. These are

- 1) The experimentally obtained azimuthally averaged yield, obtained on an uncovered crystal by averaging the yield obtained at 5° steps over 90° in azimuth, from a {100} to a {110} plane. The two-axis design of the goniometer necessitated the simultaneous variation of both θ and ϕ to scan along a path at a constant

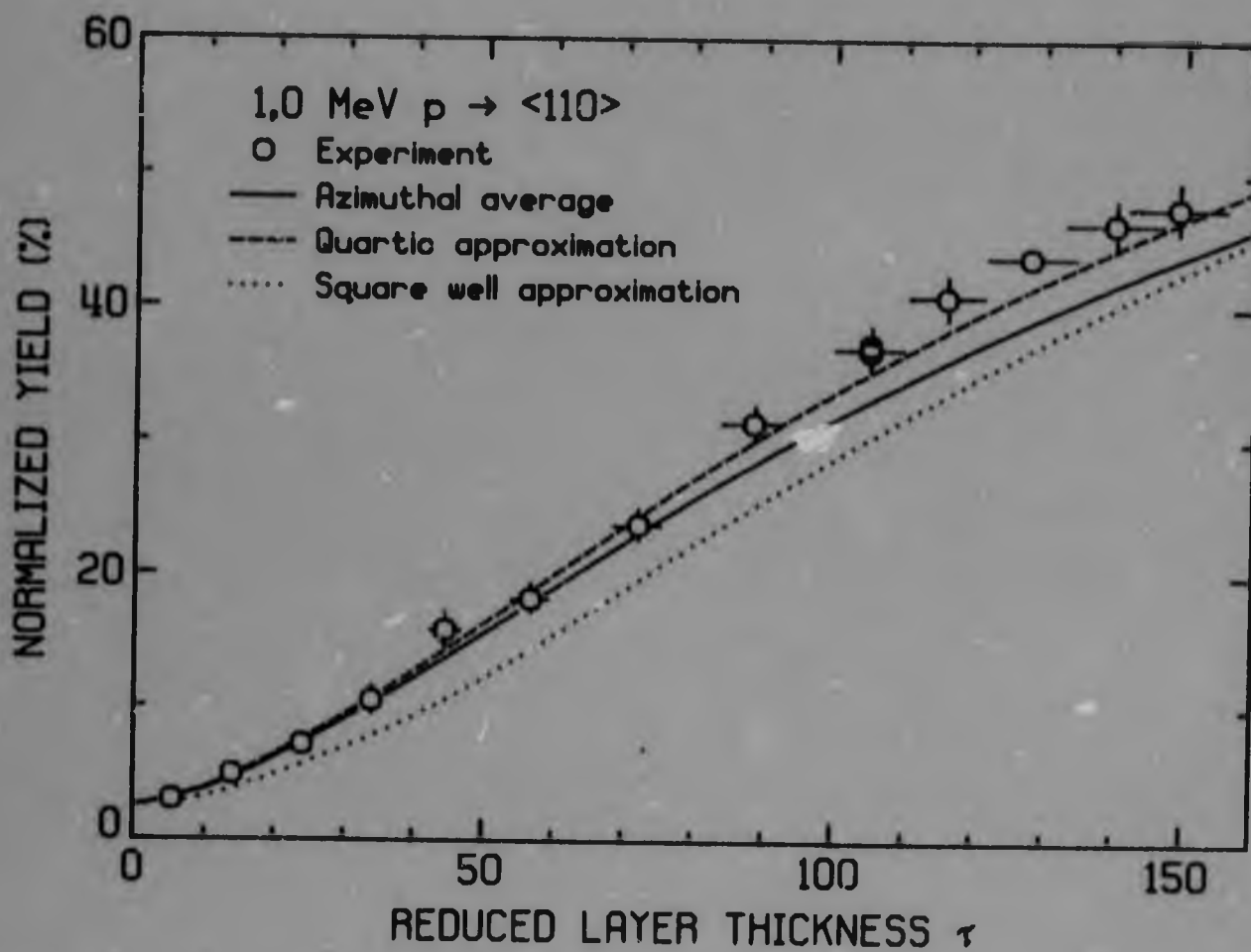


Figure 6.3: Dependence of normalized yield on reduced thickness τ , for carbon layer.

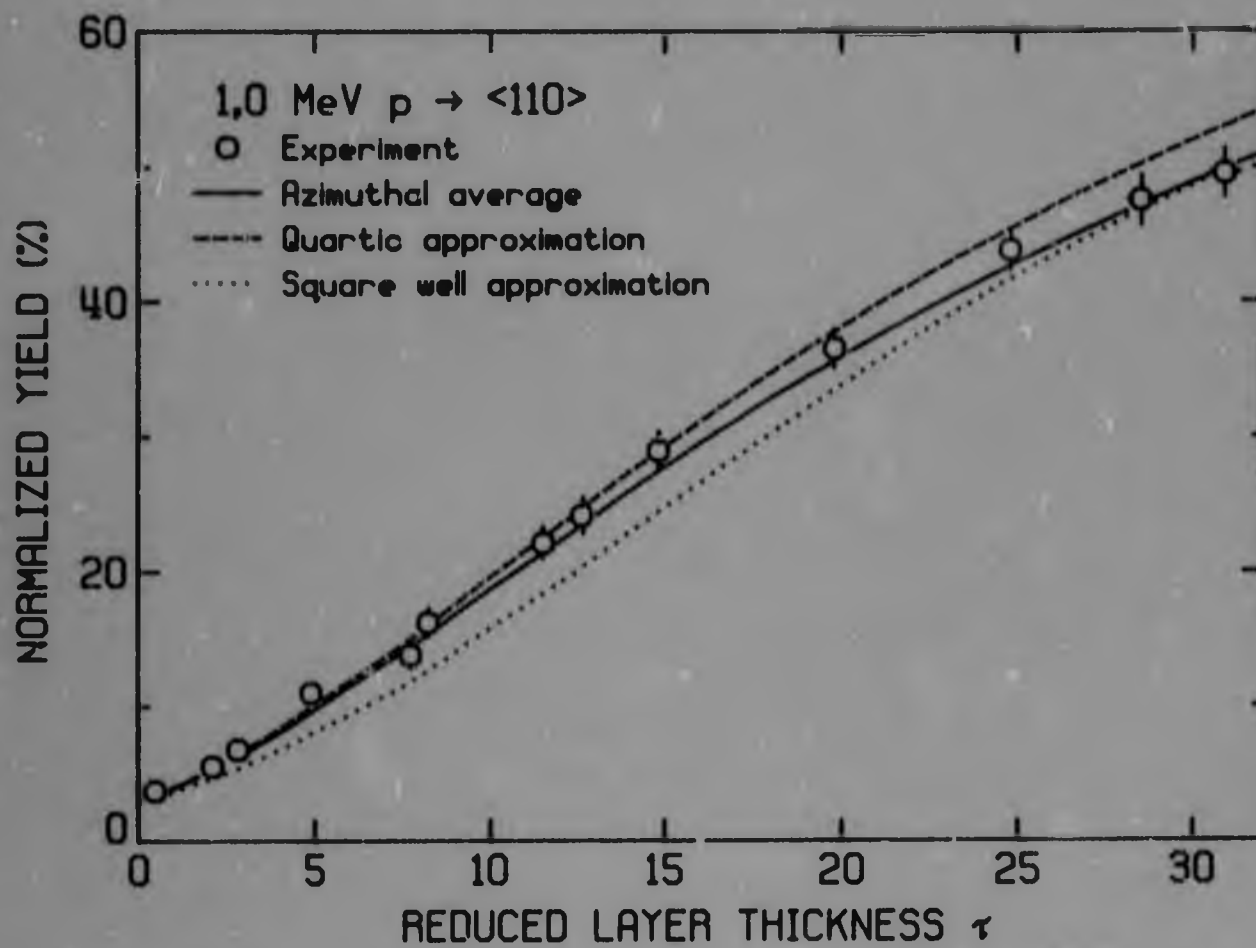


Figure 6.4: Dependence of normalized yield on reduced thickness τ , for aluminium layer.

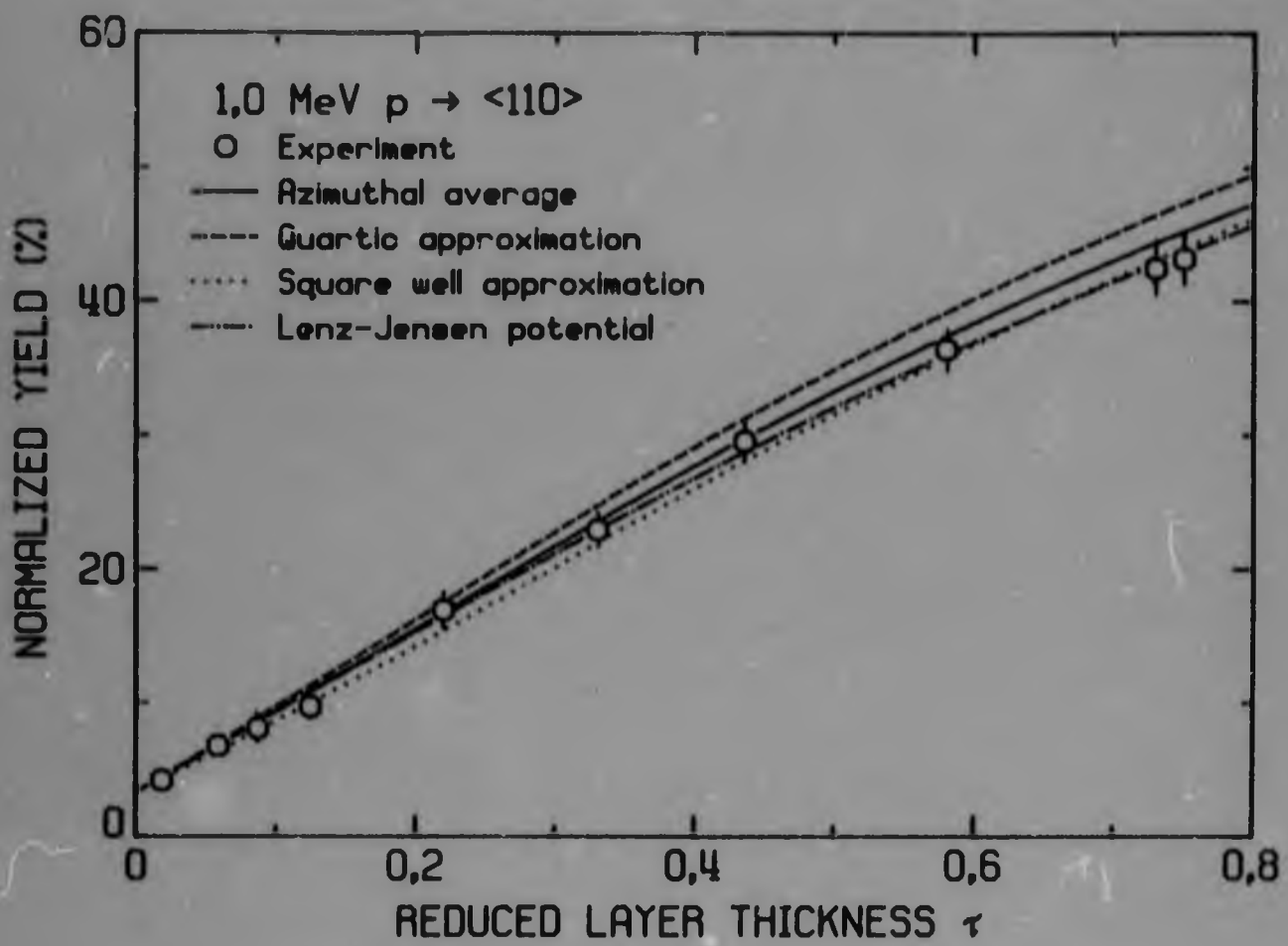


Figure 6.5: Dependence of normalized yield on reduced thickness τ , for gold layer.

angular offset from the $\langle 110 \rangle$ axis; the angular settings for each step were calculated using spherical trigonometry [Der 78]. The critical angle measured, 0.55° , agrees with that measured using the standard azimuth defined in Chapter 3 and with the measurements of Derry [Der 78].

- ii) The square-well approximation, equation (6.4.6).
- iii) The quartic approximation, equation (6.4.7).

These approximations were used with the minimum yield measured on the uncovered crystal before the start of each set of experiments.

The integral (6.4.5) is in terms of the reduced scattering angle δ which is energy dependent (equation 6.4.2). The appropriate energy for equation (6.4.2) is the average energy of the beam in the layer where the scattering takes place; this may be written as $E_0 - \frac{1}{2}\Delta E$, where E_0 is the initial energy and ΔE is the energy loss in the layer. This is a good approximation for thin layers. However, the critical angle ψ_1 which, in the form Λ_1 , defines the scale of $\chi(\delta)$ in equation (6.4.5) is also energy dependent, varying as E^{-1} ([Lin 65], shown for diamond by Derry [Der 78]). The appropriate energy for ψ_1 is that at which the beam enters the crystal, $E_0 - \Delta E$. Thus

$$\begin{aligned} \alpha_1(E_0 - \Delta E) &= \frac{a}{2Z_1Z_2e^2} [E_0 - \frac{1}{2}\Delta E] \psi_1(E_0 - \Delta E) \\ &= \frac{a}{2Z_1Z_2e^2} [E_0 - \frac{1}{2}\Delta E] \frac{E_0^{\frac{1}{2}}}{[E_0 - \Delta E]^{\frac{1}{2}}} \psi_1(E_0) \end{aligned}$$

Expanding to first order in $\frac{\Delta E}{E_0}$,

$$a_1(E_0 - \Delta E) = \frac{a}{2Z_1 Z_2 e^2} E_0 \psi_1(E_0) = a_1(E_0)$$

Thus, for thin layers, we may, to a good approximation, use the critical angle as measured at the incident energy, in this case, 1.000 MeV, and neglect any energy loss in the layer.

The tabulated multiple scattering distributions [Si 74] were fitted with a rational function which gave the same large angle behaviour as the true distribution ($\sim \frac{1}{\alpha^4}$), and the integration (6.4.5) was performed numerically. The calculated points were joined with a smooth (spline) curve and are shown plotted in Figures 6.3 to 6.5.

6.5.3 Discussion

The theoretical curves based on the averaged angular yield are seen to be in agreement with experiment within about 10 %, the greatest discrepancy being for carbon. The two approximations also give good results, especially for the quartic approximation at lower yields.

For carbon, the quartic approximation is in closest agreement with the experimental results. This might indicate that the angular yield function needs to be closer to the quartic shape. However, this is not reflected in the other results and there is no reason to expect that the angular yield profile should depend on the nature of the layer. Another possible explanation of the discrepancy is the uncertainty in the

cross-section: it does not, however, seem possible to explain all the discrepancy on this basis, especially as the fractional deviation is increasing with increasing τ . This could only be accounted for with rather drastic variations in the energy dependence of the cross-section. A more likely explanation is that an interatomic potential based on Thomas-Fermi statistical considerations is not strictly applicable between light atoms with few electrons (carbon) and protons. It is also possible that some effect of the nuclear potential is being felt by the protons. The results indicate that a potential with rather less screening than the Thomas-Fermi potential would be appropriate: this would allow more scattering and provide a higher yield. Bernhard et al [Bed 72], in measuring the multiple scattering of protons of energies up to 270 keV through thin carbon foils and analysing the results using Meyer's theory [Mey 71], have found that a screening length of 28.8 pm is consistent with their data, rather than the value of 25.8 pm used here. This increase in screening length would have the effect of reducing the screening of the potential, however, calculations indicate that the effect of this change on the results presented is very slight. Nevertheless, the agreement between the experimental and theory for carbon must be regarded as satisfactory, bearing in mind the great simplicity of the Thomas-Fermi scattering theory [Lin 68], which permits a universal description of all target-ion pairs.

For the other two layer materials, agreement of theory with experiment is found to be good. This agrees with results obtained on silicon [Lug 73, Rim 72], and extends these results to yields below 15 %, which were not measured by those authors.

At higher layer thickness, the experimental points for gold fall

below the theoretical curve and agree most closely with the square-well approximations although the deviation is rather small. Calculations were made using the multiple scattering distribution for the Lenz-Jensen potential [Si 74] and are shown in Figure 6.5. The agreement was found to be better than with the Thomas-Fermi distributions. The difference between the Thomas-Fermi and Lenz-Jensen distributions becomes smaller as the reduced thickness t is increased and the change in the curves for aluminium and carbon is very small. The difference between the two curves and the experimental results is barely of significance considering the experimental errors; however, it might indicate that the Lenz-Jensen potential is more appropriate for the gold-proton scattering.

In general, the results show that satisfactory agreement can be obtained between the theoretically calculated yields and the experimentally measured yields, using the azimuthally averaged yield functions. The two approximations are also found to give good results, considering the crudity of the approximations, and the quartic approximation is in close agreement with the experimental results for low yields. The results indicate that high accuracy and precision experiments of this type will be able to distinguish between different interaction potentials used in the calculation of multiple scattering distributions.

6.6 DECHANNELLING IN DIAMONDS COVERED WITH AMORPHOUS LAYERS

6.6.1 Results

The yields, as a function of depth, for various selected thicknesses of carbon, aluminium and gold are shown in Figures 6.6, 6.7 and 6.8 respectively. The experimental points were smoothed by drawing a

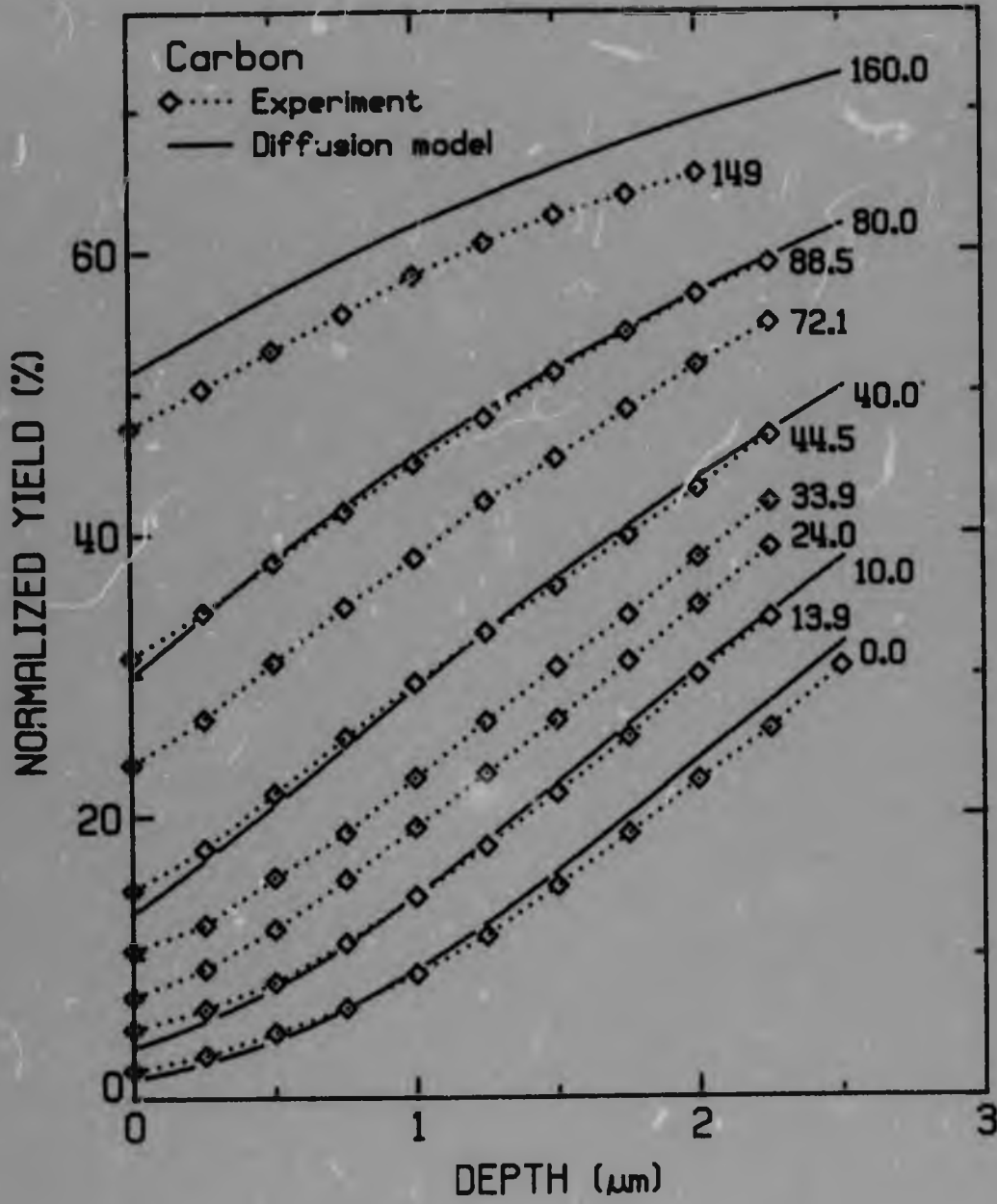


Figure 6.6: Experimental and theoretical dependence of normalized yield on depth, for various values of τ , as indicated.

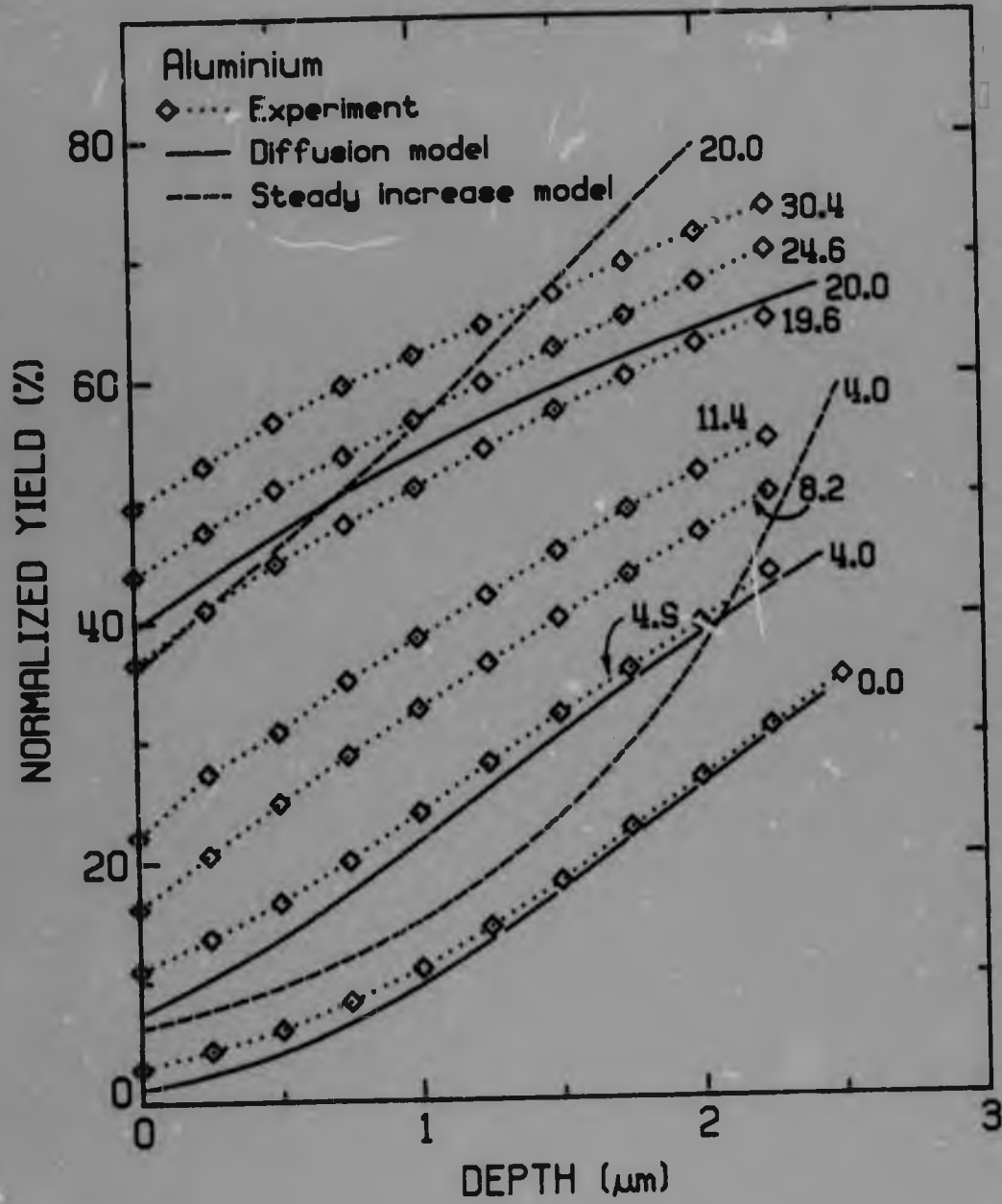


Figure 6.7: Experimental and theoretical dependence of normalized yield on depth, for various values of τ , as indicated.

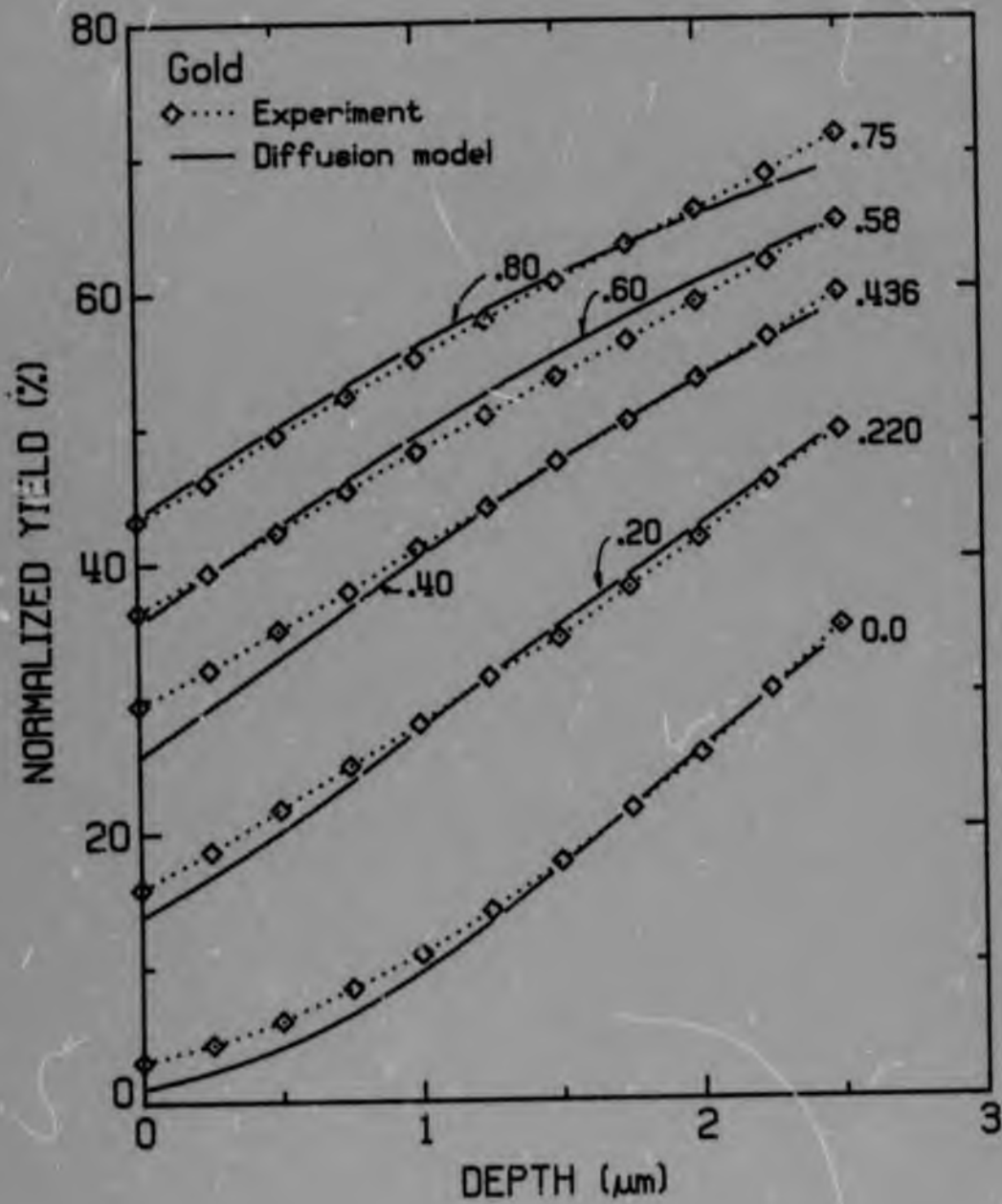


Figure 6.8: Experimental and theoretical dependence of normalized yield on depth, for various values of τ , as indicated.

smooth curve through the plotted spectrum and extracting values from the smoothed curve to calculate the yield.

6.6.2 Calculations

Calculations were performed using the diffusion model and the steady increase model. Initial transverse energy distributions were calculated using equation (6.4.8) with the multiple scattering distributions used in Section 6.5. The values of τ do not correspond exactly with actual experimental values but they are close enough for a similar behaviour to be expected. The experimental curves show that a smooth behaviour is seen as the value of τ is increased.

Because the diamond used in the experiments was not of the highest quality, the yields calculated according to Chapter 5 fall below the experimentally measured ones. For this reason, a defect scattering term was introduced in the change of transverse energy with depth, $\frac{d\epsilon_t}{dz}$ (Section 2.5.6), this term being a constant, representing a uniform distribution of defects across the channel. This form of the term was chosen as the simplest in the absence of detailed knowledge of any defects present. The size of the term was adjusted to fit the yield as measured on the uncovered diamond. The magnitude of the term was always small.

The yields were then calculated using, for the other parameters of the theory, the usual values for 1 MeV protons in $\langle 110 \rangle$. The diffusion model calculations are shown for carbon, aluminium and gold in Figures 6.6 to 6.8. The results for the steady increase model were not in very

good agreement with the experiment, as expected from Section 5.5.2 and are only plotted for aluminium in Figure 6.7.

6.6.3 Discussion

The angular yield profile which corresponds with the dechannelling model, is rather different from those used in Section 6.5 and is shown in Figure 6.2. The actual values of the yield at the surface do not agree too closely with those of Section 6.5, but the effect of variations in the yield function will be similar at all depths, thus the slope of the dechannelling curves will be insensitive to them. For this reason, the slope of the calculated curve is of more significance than the absolute magnitude, and this is what should be compared with experiment.

With this in mind, it is seen that the diffusion model of dechannelling gives a good agreement between theory and experiment. The results for the steady increase model are poor, again illustrating that this approach is not suitable for diamond.

The agreement between the diffusion model calculations and the experiment is of interest not only from the point of view of calculating the yield as a function of depth, but also from the applicability of the diffusion model. The model is complex, and requires both an initial transverse energy distribution and a rate of change of transverse energy with depth which are subject, to some extent, to wide variation from differing theoretical assumptions. These assumptions are tested in Chapter 5 by variation of axis, energy and temperature. The wide variation in initial transverse energy of distribution introduced by the evaporation of layers at the surfaces allows a further test of these

assumptions. The good agreement found over such a wide range in conditions in this Chapter and in Chapter 5 shows that the assumptions made about the various functions that enter the diffusion model are good.

6.7 APPROXIMATIONS

6.7.1 Effect of Thin Contamination Layers

The effect of thin contamination layers on the minimum yield has not been studied to any large extent. The measurements, discussed in Section 6.5, have been made down to low yields in the region of the uncovered minimum yield in order to investigate this problem. The aim of this section is to derive simple, but reasonably accurate, relationships that describe the effect of thin contamination layers.

For thin layers $\tau \rightarrow 0$ the multiple scattering distribution may be approximated via equation (6.4.3) as

$$f_1(\tau, \delta) = \frac{\tau}{\delta^3} f(\delta) \quad (6.7.1)$$

For large δ ,

$$f(\delta) = \frac{1}{2\delta} \quad [\text{Si } 72]$$

(that is, the Rutherford cross-section in Thomaz-Fermi units).

Using the square-well approximation for the angular yield

function, the yield with the crystal covered with a thin layer becomes

$$x_L(\tau) = x(0) + (1 - x(0))P_S(a_1, \tau)$$

with

$$P_S(a_1, \tau) = \int_{a_1}^{\infty} \frac{\tau}{2s^4} s \, ds$$

$$= \frac{\tau}{4a_1^2}$$

Thus

$$\begin{aligned} \Delta x &= x_L(\tau) - x(0) \\ &= (1 - x(0)) \frac{\tau}{4a_1^2} \\ &= \frac{\tau}{4a_1^2} \end{aligned} \quad (6.7.2a)$$

Returning this to dimensional form

$$\Delta x = nNx \left(\frac{Z_1 Z_2 e^2}{E} \right)^2 \frac{1}{v_1^2} \quad (6.7.2b)$$

which is just the expression derived by Lindhard [Lin 65] as the contribution to the minimum yield by an amorphous contamination layer.

If the Rutherford cross-section is used, then

$$\sigma = \left(\frac{Z_1 Z_2 e^2}{4E} \right)^2 F(\theta, M_1, M_2)$$

with

$$F(\theta, M_1, M_2) = \frac{4(\cos\theta + [1 - (\frac{M_1}{M_2} \sin\theta)^2]^{\frac{1}{2}})^2}{\sin^4\theta [1 - (\frac{M_1}{M_2} \sin\theta)^2]^{\frac{3}{2}}} \quad (\text{Pot 77})$$

where E and θ are energy and scattering angle in the laboratory frame and M_1 and M_2 are the masses of the incident ion and target atom respectively.

Using equation (6.3.1), equation (6.7.2b) becomes

$$\Delta x = 16\pi \frac{1}{v^2} \frac{C}{F(\theta, M_1, M_2)n} d\Omega$$

For $M_1 \ll M_2$,

$$F(\theta, M_1, M_2) = \sin^4 \theta/2 \quad (6.7.3)$$

and then

$$\Delta x = 16 \frac{1}{\psi_1^2} \frac{C}{n} \frac{1}{d\Omega} \frac{1}{\sin^4 \theta/2} \quad (6.7.4)$$

Thus, for light ions incident on the crystal through a heavy impurity layer, the increase in minimum yield depends only on the number of backscattered counts recorded in the spectrum, and not on the elemental nature of the layer.

The approximation of $f(\theta)$ made here is, of course, rather crude and deviation must be expected, especially for layers of heavier atoms where d_1 becomes d_1 . However, equation (6.7.4) does provide a useful first estimate and a useful rule of thumb in its prediction of the mass independence of the effect of thin layers on the yield. In this regard, it should be noted that the approximation (6.7.3) is only in error by about 25 % for the case of alpha particles incident on carbon, and thus equation (6.7.4) may be applied, with due regard to the limitations of the assumptions that are involved in it, to surface layers of essentially all masses. It should also be noted that, for protons incident on light impurity layers such as carbon or oxygen at energies of the order of 1 MeV, the cross-section is no longer Rutherfordian and equation (6.7.4) cannot be applied - equations (6.7.2a) or (6.7.2b) should be used.

A better approximation can be obtained, firstly by using a better approximation to the Thomas-Fermi cross-section and, secondly, by using the quartic approximation for the angular yield function, which was found to give good results at low yields in Section 6.5.

A better approximation to the cross-section may be obtained by piece-wise approximation of the Thomas-Fermi cross-section by power law cross-sections (for example [Win 70]):

$$\begin{aligned}
 f(\bar{a}) &= \frac{1}{2\bar{a}} & \bar{a} > 1.53 \\
 &= 0.327 & 0.0156 \leq \bar{a} \leq 1.53 \\
 &= 1.309\bar{a}^{1/3} & \bar{a} < 0.0156 .
 \end{aligned}$$

With this approximation for the cross-section, using the quartic approximation and equation (6.7.1), the yield becomes

$$\chi_L(\tau) = \chi(0) + (1 - \chi(0))P_Q(\bar{a}_1, \tau)$$

with

$$\begin{aligned}
 P_Q(a_1, \tau) &= \left(\frac{0.349}{a_1^{2/3}} + 20.8 \right) \tau, & a_1 < 0.0131 \\
 &= \left(\frac{0.367}{a_1} - 0.107 - \frac{2.06 \cdot 10^{-8}}{a_1^4} \right) \tau, & 0.0131 \leq a_1 \leq 1.29 \\
 &= \left(\frac{0.354}{a_1^2} - \frac{0.098}{a_1^4} \right) \tau, & a_1 > 1.29. \quad (6.7.5)
 \end{aligned}$$

The experimental points for small layer thickness are shown in Figure 6.9 for the three cases of carbon, aluminium and gold, together with the approximations (6.7.2a) and (6.7.5). It is clear that Lindhard's expression (6.7.2b) gives only a rough approximation to the actual increase in yield, being best for carbon where, with a critical angle $a_1 = 14.3$, equation (6.7.2) is a reasonably good approximation.

The approximation (6.7.5) is seen to give a much better agreement with experiment, within 15 % for carbon layers up to increases in yield $\Delta\chi$, of 0.05 and for aluminium and gold to about $\Delta\chi = 0.1$. Thus equation (6.7.5) may be used to provide a good description of the effect of thin amorphous impurity or contamination layers on the minimum yield.

6.7.2 An Approximate Scaling Rule.

As discussed in Section 6.4.1, the function $a^2 f_1(\tau, a)$ is a function of only one variable, $\frac{a^{2m}}{c\tau}$, for power law cross-sections. Thus,

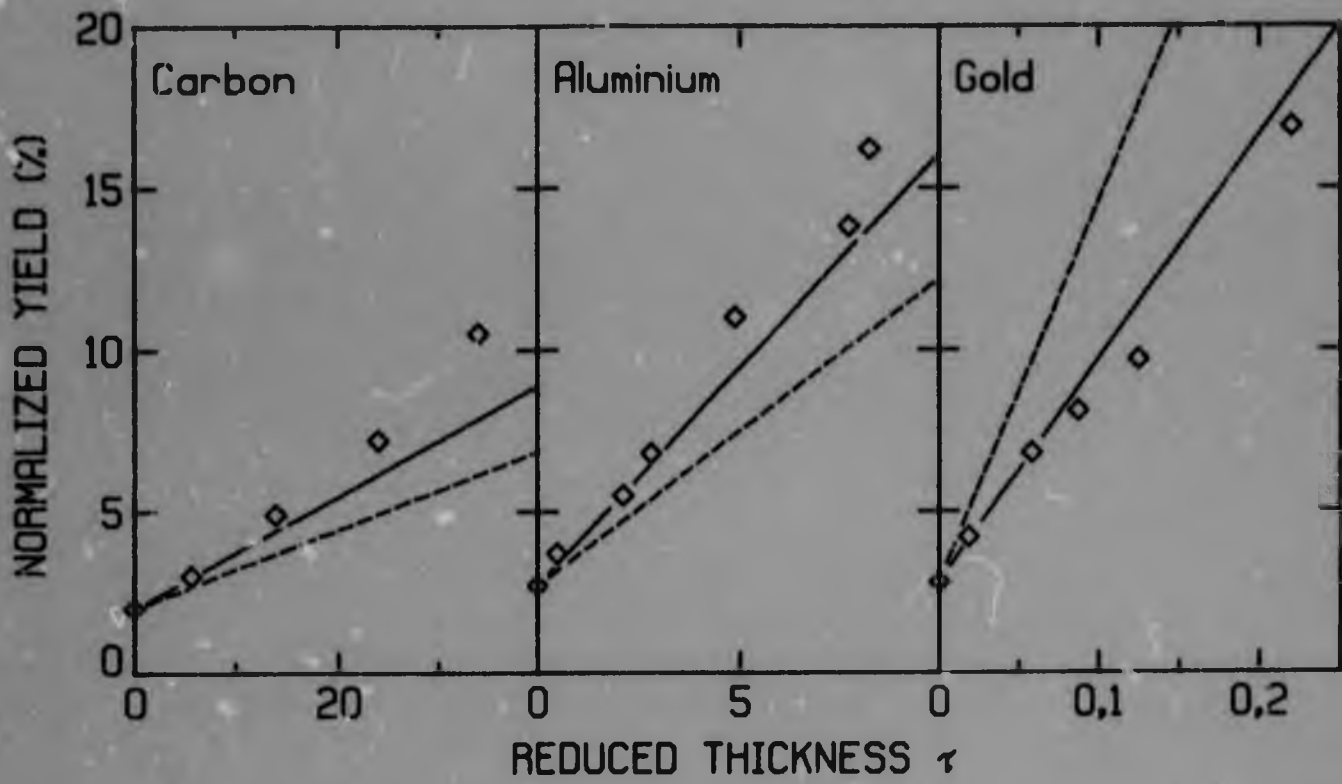


Figure 6.9: Dependence of normalized yield on τ for thin layers. — equation (6.7.5); - - - equation (6.7.2 a).

for multiple scattering distributions calculated from a power law cross-section, the yield for a layer thickness τ as calculated in Section 6.4.2 is a function of

$$\frac{a_1}{(c\tau)^{1/2m}}$$

Marwick and Sigmund [Mar 75] have shown that, for a given τ , an equivalent power cross-section can be related to the multiple scattering distributions calculated using the Thomas-Fermi cross-sections, and great simplification can be achieved in the calculation of the distribution by evaluating the simpler power cross-section expression. These authors show, that for the power cross-section equation (6.4.4),

$$f_{1P}(\tau, 0) = \text{const} \cdot \tau^{-1/m}$$

and a power m may be associated with a particular τ value for the Thomas-Fermi distribution, by

$$\frac{1}{m} = -\tau \frac{d \ln f_{1TF}(\tau, 0)}{d\tau}$$

where f_{1P} and f_{1TF} are the power and T-F multiple scattering distributions.

The possible existence of simple power-law simplification in the modification of yields by surface layers was investigated. The expression $c\tau^{1/2m}$ was evaluated as a function of τ , by matching to the value of $f_{ITF}(\tau, 0)$ in a similar fashion to Marwick and Sigmund [Mar 75]. The resultant curve is shown in Figure 6.10. This was then used to evaluate the yield as a function of $(c\tau)^{1/2m}/a_1$ for the three cases of carbon, aluminium and gold, the aluminium beam uncorrected for the small amount of oxygen contamination. This yield is shown plotted in Figure 6.11. The three elements, while falling on their own distinct curves, are grouped closely together. This suggests that it might be possible to define a 'universal' yield versus $(c\tau)^{1/2m}/a_1$ curve which would describe all three axes to an accuracy of about 30%. An approximate curve is shown sketched in Figure 6.11.

Another possible use for such a plot is in the calculation of the multiple scattering of combined layers of different substances. If the curves of the two elements in a plot such as Figure 6.11 lie close together (for example, aluminium and carbon) it is possible to use the scaling to convert an amount of one element into an equivalent amount of another element which will provide the same change in yield.

Thus, for equal yields,

$$\left[\frac{(c\tau)^{1/2m}}{a_1} \right]_1 = \left[\frac{(c\tau)^{1/2m}}{a_1} \right]_2$$

and hence

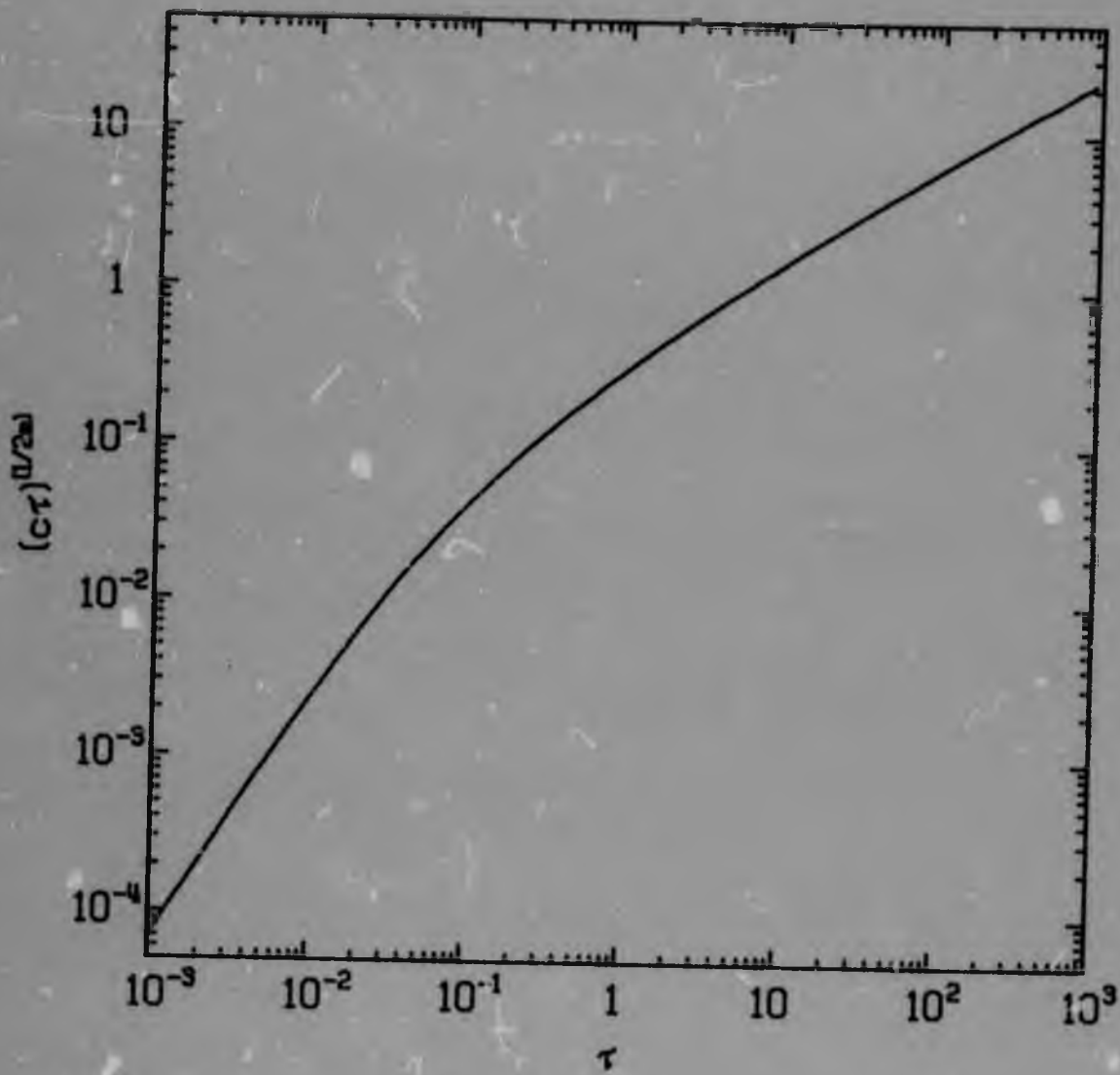


Figure 6.10: Dependence of $(c\tau)^{1/2m}$ on τ .

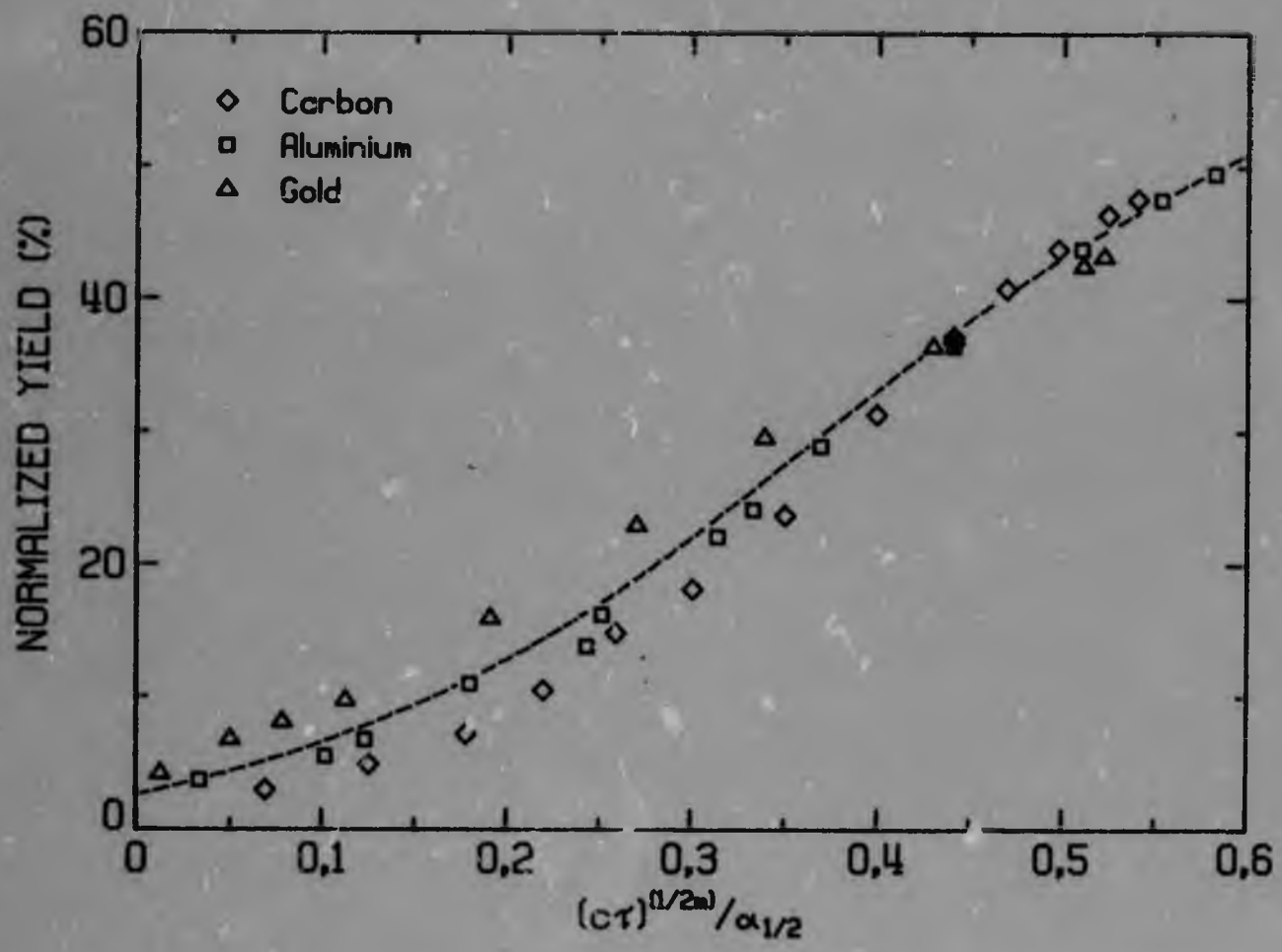


Figure 6.11: Scaling of the dependence of normalized yield on layer thickness τ .

$$\frac{[(c\tau)^{1/2m}]_1}{[(c\tau)^{1/2m}]_2} = \frac{[\delta_1]_1}{[\delta_1]_2}$$

Because $(c\tau)^{1/2m}$ is related uniquely to τ , Figure 6.10 may be used to relate τ_1 to τ_2 .

In this manner, the τ values for oxygen were converted to equivalent τ values for aluminium by assuming the oxygen curve would lie between aluminium and carbon. Since part of the yield in the case of aluminium is produced by the oxygen, the true curves are even closer together than shown in Figure 6.11, and the approximation is thus better than Figure 6.11 suggests. The equivalent aluminium values of the oxygen were added to the τ values for aluminium to give a net aluminium τ .

6.8 CONCLUSION

The Thomas-Fermi theory of multiple scattering [Mey 71, Si 74] has been shown to give good results in the calculation of the effect of amorphous surface layers in channelling. For gold and aluminium layers, the previous work has been confirmed and extended to thinner layers. The effect of carbon layers is also explicable in terms of the theory, but the need for less screening in the potential is indicated. Better agreement in the case of gold can be obtained using a Lenz-Jensen potential, but the differences between this and the Thomas-Fermi potential are small.

It has also been shown that the diffusion model of dechannelling gives a good description of the yield as a function of depth, while the steady increase model is not as successful. The good agreement found

while using the diffusion model indicates that the assumptions in the model are reasonable.

The effect of very thin layers, which approximate the case of thin impurity or contamination layers which might arise on crystals during normal use, has been investigated and an expression based on the Thomas-Fermi theory has been developed which gives a good description of the effect of these layers on the minimum yield. Finally, a power cross-section scaling law has been investigated, and the multiple scattering of mixed layers has been discussed.

DECHANNELLING BY DEFECTS IN TYPE Ia DIAMONDS

7.1 INTRODUCTION

During the selection of diamonds for ion channelling purposes outlined in Section 4.3, it was observed that certain 'Cape Yellow' diamonds, known to be strong Type Ia diamonds, that is, having relatively strong Type Ia optical absorption features, had yields in $\langle 110 \rangle$ for 1 MeV p reaching ~ 0.6 at depths of 2.4 μm compared with 0.24 - 0.3 at this depth for other diamonds. As discussed in Chapter 4, Type Ia diamonds can have up to several tenths of one percent concentration of nitrogen impurity, predominantly in two forms, the A and B aggregates, which produce characteristic infra-red absorption in the region 1000 to 1332 cm^{-1} , and contain defects known as platelets on (100) planes, which are related to an infra-red absorption peak at $\sim 1370 \text{cm}^{-1}$. Investigations were made to ascertain to what extent the enhanced dechannelling in the Cape Yellow diamonds could be understood in terms of these characteristic defects. It should be noted at the outset that the yellow colouration of these diamonds is due to the presence of nitrogen in the so-called N3 centre, thought to consist of three nitrogen atoms on next nearest neighbour sites on (111). This is a minority form of nitrogen, accounting for $< 1\%$ of nitrogen in the diamonds studied here, and it is thought that the yellow colour of these diamonds, in relation to the dechannelling, is merely an indication of their high nitrogen content and that other, non-yellow, strong Type Ia diamonds could also show the same behaviour.

The results of this investigation are presented in this Chapter. It is shown that the dechannelling probability, obtained using a single scattering model, is correlated with the infra-red absorption produced by the platelets and by the B nitrogen. The dechannelling in a diamond with absorption due to B nitrogen only, and no platelet absorption, has also been measured. A model for the dechannelling is outlined, and the relationship between the platelets and the B aggregates is discussed.

7.2 EXPERIMENTAL PROCEDURES AND RESULTS

7.2.1 Infra-red Measurements

Infra-red transmittance spectra were recorded on a Perkin Elmer 540 infra-red spectrophotometer. Absorption coefficients were calculated at selected wave-numbers from the measured transmittance, with allowance for multiple reflections [Cla 56]. Errors in the absorption coefficient were estimated at 5%. The absorption coefficient at 1282 cm^{-1} was decomposed into A and B components using the method of Davies [Dav 77]. A typical Ia spectrum is shown in Figure 7.1, with the approximate A and B contributions indicated.

7.2.2 The Diamonds

Seven Cape Yellow diamonds were initially selected for investigation. These were subsequently cut and polished into thin sections suitable for infra-red measurements, which required thicknesses $< 0.5 \text{ mm}$ in order that the transmittance was not reduced below $\sim 10\%$ at absorption peaks. (The uncertainties in calculated absorption coefficients become increasingly larger at small transmittances.) Several slices from certain diamonds were subsequently used.

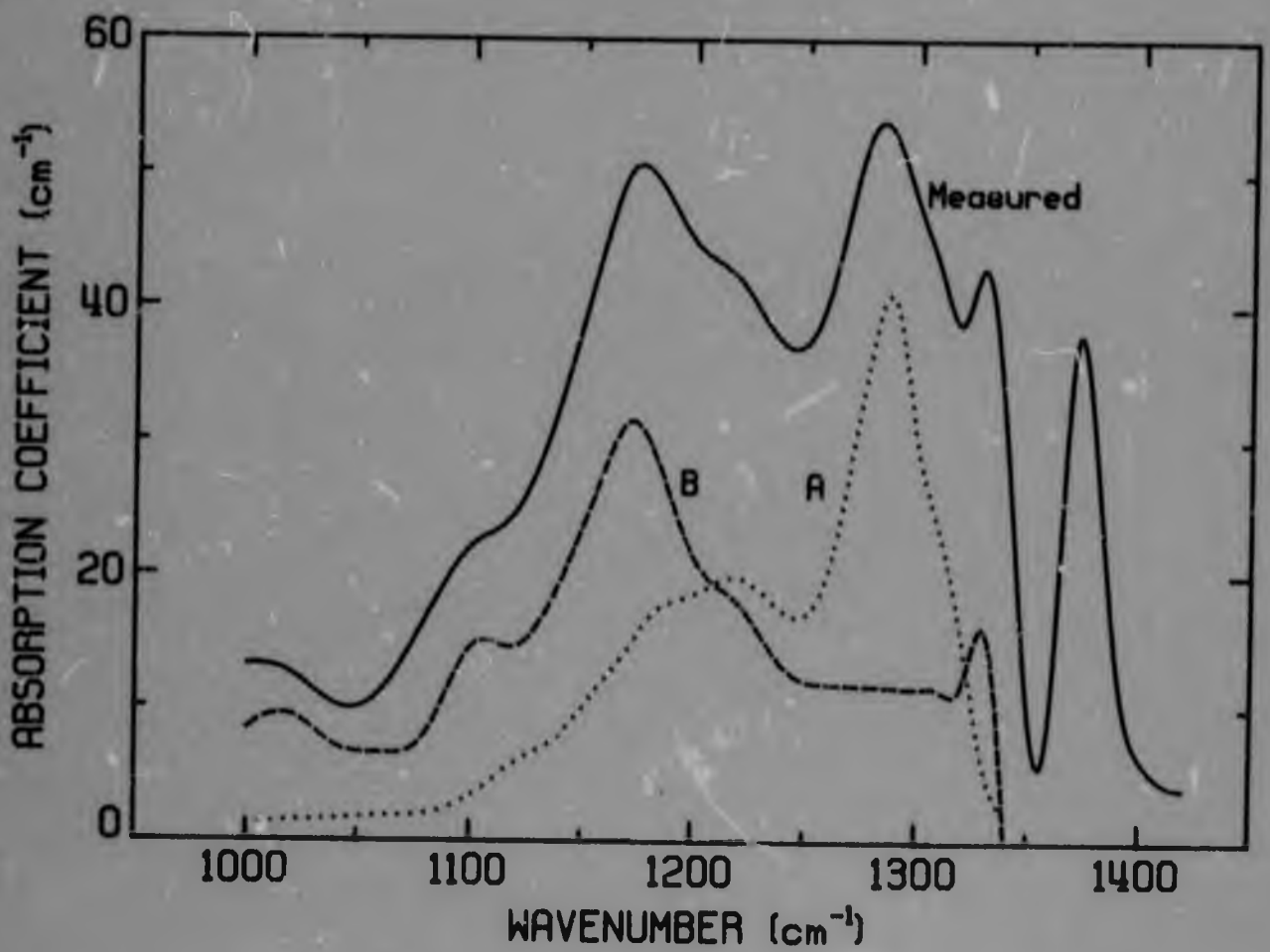


Figure 7.1: Typical Type Ia diamond infrared absorption spectrum in the one-phonon region, with approximate decomposition into A and B components.

The question of sample inhomogeneity is always a problem in work on diamond. It was noted that, in these diamonds, the infra-red absorption coefficients did not vary by more than ~30 % in slices cut from regions of the diamond several millimetres apart. On individual slices, the absorption coefficient at selected 2 μm diameter regions across the slice did not vary by more than 5 % and in reducing the thickness of several slices by more than 50 % from ~0.5 mm to ~0.2 mm, the absorption coefficients did not change more than 10 %.

Thus, it was concluded that the diamonds were reasonably homogeneous on a scale of perhaps 0.1 mm. The homogeneity on a finer scale is more difficult to assess. However, cathodoluminescence examinations under a microscope using a lumino-scope showed none of the complicated structure that is sometimes seen in cathodoluminescence studies of diamond [Ha 77, Lan 79].

A reference diamond, representing the 'perfect crystal' dechanneling for the extraction of defect dechanneling probabilities was selected from among the best diamonds. The yield at 2.4 μm in $\langle 110 \rangle$ was 0.24 for 1 MeV protons. This diamond was also Type Ia, with absorption coefficient at 1282 cm^{-1} of 1.5 cm^{-1} , due mainly to A aggregates. This represents 50 ppm nitrogen. The absorption coefficient at 1370 cm^{-1} was 0.5 cm^{-1} . By comparison, absorption coefficients in the Cape Yellow set ranged up to 63 cm^{-1} at 1282 cm^{-1} and 43 cm^{-1} at 1370 cm^{-1} . The absorption coefficients, together with the decomposition into A and B components are given in Table 7.1.

Table 7.1

ABSORPTION COEFFICIENTS AND DECIANNILLING PROBABILITIES IN TYPE 'A' SUITE

Diamond	μ (1282 cm^{-1}) cm^{-1}	μ_A (1282 cm^{-1}) cm^{-1}	μ_B (1282 cm^{-1}) cm^{-1}	μ_P (~1370 cm^{-1}) cm^{-1}	n_{D^0} <110>, 1 MeV _p μm^{-1}
D13 (ref)	~ 1.5	~ 1.5	~ 0	~ 0.5	0 by defn
C1a	53.5	50.7	5.8	20.8	0.100
C1b	47.9	41.1	6.8	17.8	0.095
C2a	48.5	36.4	12.1	40.6	0.169
C2b	54.3	42.7	11.6	41.6	0.162
C4a	23.4	13.2	10.2	38.3	0.161
C4b	28.7	18.2	10.6	31.2	0.175
F1a	55.6	48.1	7.5	26.2	0.125
F1b	51.2	43.6	7.6	22.8	0.108
F2a	57.1	48.2	8.9	42.2	0.183
F2b	56.4	46.7	9.7	33.7	0.167
K1a	43.3	38.1	5.2	24.2	0.098
K1b	56.3	48.5	7.7	31.7	0.129
K4a	62.6	56.5	6.1	25.6	0.117
K4b	43.2	37.6	5.6	18.0	0.087
B only	9.2	0	9.2	1.8	0.108

It was discovered that a diamond with only B absorption features and very small 1370 cm^{-1} peak had been used in another experiment. A $\langle 110 \rangle$ spectrum was measured but the diamond was unfortunately not available for other measurements. This diamond is denoted 'B-only' in the following.

7.2.3 Channelling Measurements

Channelling spectra were recorded and analysed in the standard fashion, using protons as the incident ion. Spectra were measured at room temperature at a standard energy of 1 MeV. On selected diamonds, measurements were made at higher energies of 2.5, 4.5, 6.0, 7.4 and 9.8 MeV in order to examine the energy dependence of the dechannelling.

The $\langle 110 \rangle$ yield as a function of depth at 1 MeV is shown in Figure 7.2 for several diamonds. The absorption coefficient at 1370 cm^{-1} is also indicated and the increase in dechannelling with absorption may be noted.

The variation of the depth dependent yield with energy is shown for a Cape Yellow diamond in Figure 7.3, which may be compared with Figure 5.2. It is clear that there is a difference in the energy dependence for the two diamonds, with the dechannelling in the Cape Yellow diamond varying less with energy.

7.3 DATA ANALYSIS AND DISCUSSION

7.3.1 Extraction of Dechannelling Probability

The yield at a depth z in a crystal of density n containing a density n_d of randomly disordered atoms may be written [Bøg 67]

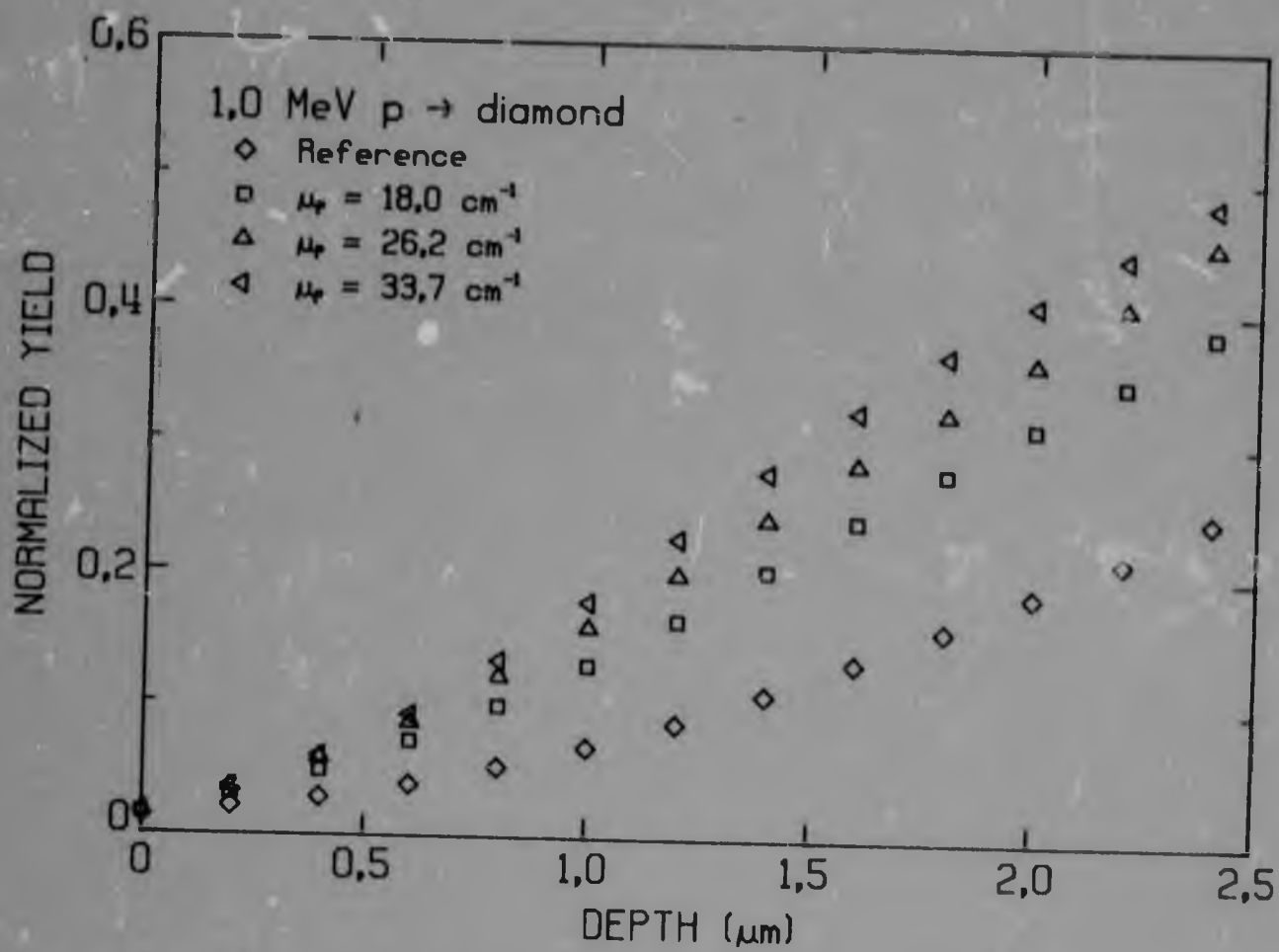


Figure 7.2: Dependence of normalized yield on depth, for Type Ia diamonds with differing absorption at 1370 cm^{-1} .

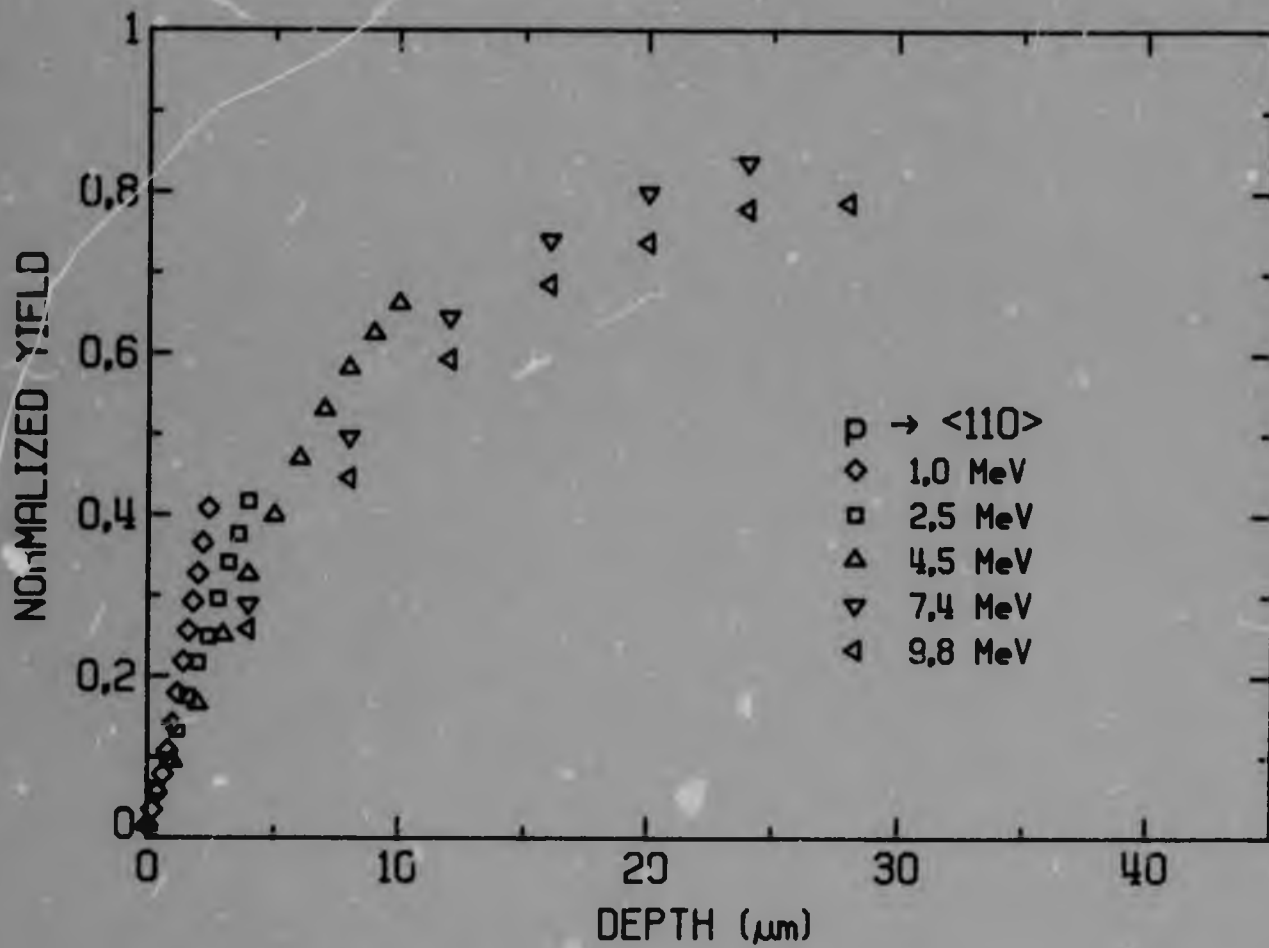


Figure 7.3: Experimental energy and depth dependence of the normalized yield, for a diamond with high Type Ia absorption.

$$\chi(z) = \chi_R(z) + (1 - \chi_R(z)) \frac{n_d}{n} \quad (7.3.1)$$

where χ_R is the random fraction of the beam at depth z , and the second term represents direct back-scattering from atoms not on lattice sites. Flux-peaking has been neglected. The random fraction of the beam, χ_R , depends on the dechannelling between the surface and the depth z . In the absence of any detailed knowledge of the defects causing the dechannelling, the random fraction of the beam may be obtained from the single scattering model [Bøg 67] which allows the defect to be described in terms of a dechannelling cross-section, σ . This model is appropriate for small concentrations of disordered atoms, where multiple scattering may be ignored, and for extended defects with large dechannelling cross-sections [Qu 76].

According to this model [Bøg 67]

$$(1 - \chi_R(z)) = (1 - \chi_p(z)) e^{-n_d \sigma z} \quad (7.3.2)$$

where n_D is the density of defects with cross-section σ and χ_p is the yield in a perfect crystal at depth z . The defects causing the direct back-scattering are not necessarily identical with those responsible for the dechannelling. It follows from equations (7.3.1) and (7.3.2) that

$$\frac{1 - \chi_D(z)}{1 - \chi_p(z)} = e^{-n_D \sigma z} \left(1 - \frac{n_d}{n}\right) \quad (7.3.3)$$

Clearly, unless $x_D = x_P$, the direct back-scattering term is only important when the concentration of disordered atoms exceeds several per cent. If it is assumed that the observed yields in Figure 7.2 are produced by atoms displaced from lattice sites, the dechannelling cross-section may be estimated from the Rutherford cross-section and equation (2.5.39) applied. This leads to concentrations of displaced atoms of 10 to 20 % being required to give the observed yields. There is no evidence for such disorder in the diamonds. It is, therefore, concluded that the dechannelling is produced by extended defects which can have a large dechannelling cross-section [10, 76]. In this case, the direct back-scattering term may be neglected and, from equation (7.3.3)

$$n_D \sigma z = \ln \left(\frac{1 - x_P(z)}{1 - x_D(z)} \right)$$

The quantity $n_D \sigma z$ is the dechannelling probability per unit length. This was determined for the spectra recorded in the experiment by fitting a straight line to the curve

$$\ln \left(\frac{1 - x_P(z)}{1 - x_D(z)} \right)$$

as illustrated in Figure 7.4. The curve does show some slight systematic deviations from linearity. There can be several reasons for this:

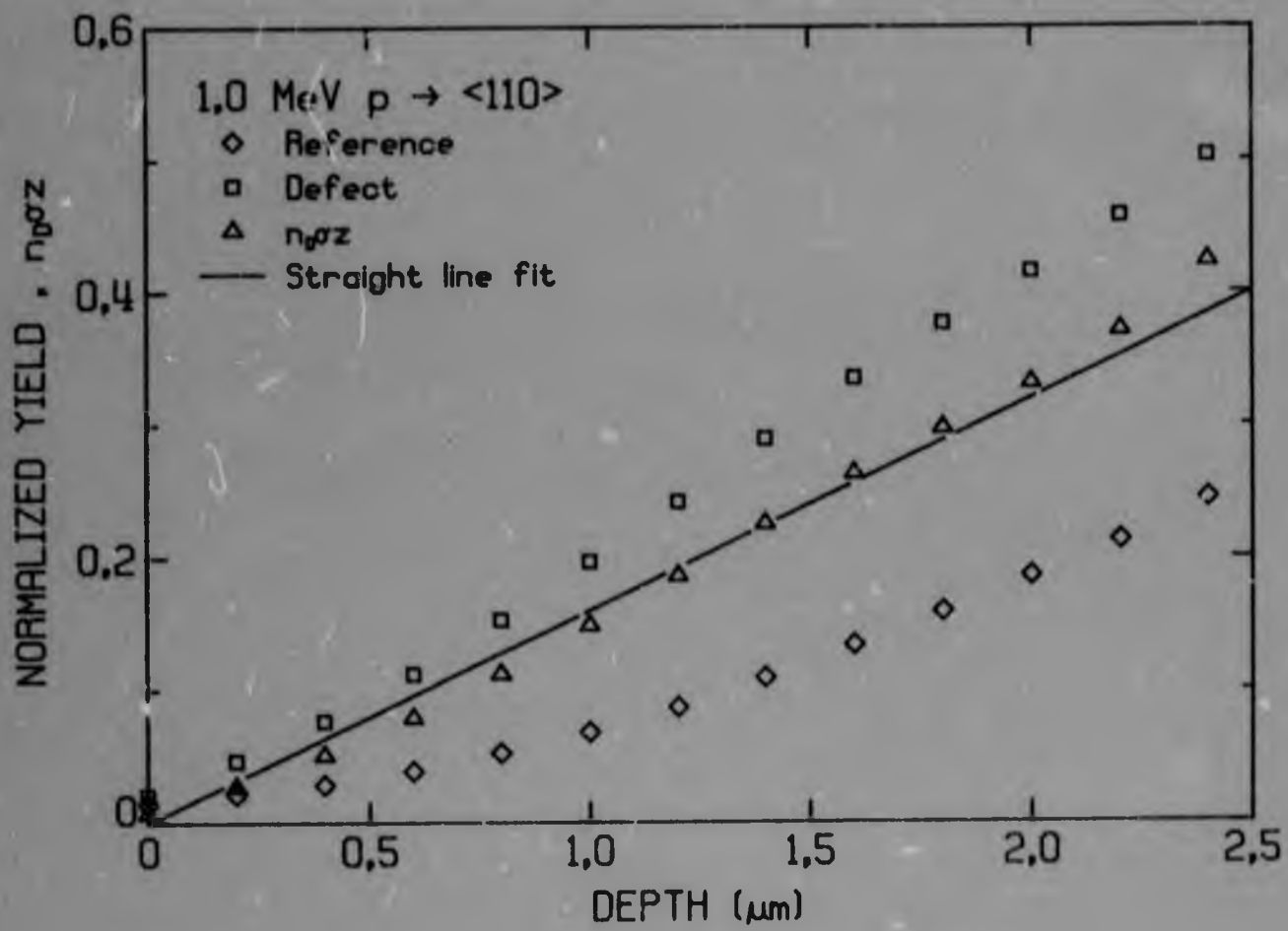


Figure 7.4: Determination of dechannelling probability, n_D^0 .

- i) A defect will modify the transverse energy distribution as well as simply dechannelling some ions [Mas 75]. This will lead to increased dechannelling at greater depths. This can be regarded as small-angle multiple-scattering which may, for example, be taken into account using a diffusion approach, if suitably detailed knowledge of the defect is available to enable the diffusion function to be calculated. The computational complexity of this approach is not justified in the present analysis. However, an analysis based on plural scattering by displaced atoms, developed for radiation damage analysis, does give a more linear dependence of 'disorder-1 atom density' on depth. The meaning of this density in terms of extended defects is rather obscure compared with the direct relevance of the dechannelling probability and this approach was not continued. It does, however, suggest that multiple scattering is the source of the deviations in Figure 7.4.
- ii) The defect dechannelling cross-section can depend on the details of the transverse energy distribution and this might depend on depth. An example will be discussed below. The quantity $n_D \sigma$ determined from the straight line fit will then represent a value of σ averaged over the depth used in analysis.
- iii) The defect concentration could be inhomogeneous, as discussed above. However, the deviations for all diamonds were similar, and it seems simpler to consider a similar mechanism in all cases than similar inhomogeneities in defect distribution.
- iv) The curvature could be an artifact of the conversion from an

energy to a depth scale, due to the neglect of variation in channelled stopping power. The effect of a reduced channelled stopping power on the yield is small for 1 MeV protons (see Chapter 5).

It was concluded that the straight-line approximation was sufficient and that the quantity $n_{\eta}\sigma$ provides a good estimate of the dechannelling probability. This quantity is also tabulated in Table 7.1.

7.3.2 Results

Initial experiments concentrated on investigating the relation between the total nitrogen concentration and the dechannelling. The nitrogen concentration was measured in the region probed by the channelled proton beam by use of the reaction $^{14}\text{N}(\alpha, n)^{17}\text{F}$ [Sel 75b], by Dr H.J. Annegarn and Mr C.C.P. Madiba of the NPRU. The concentration of nitrogen is compared with the extracted $\langle 110 \rangle$ dechannelling probability in Figure 7.5. There is clearly no correlation. The dechannelling along the three axes $\langle 110 \rangle$, $\langle 111 \rangle$ and $\langle 100 \rangle$ was also compared and is shown in Figures 7.6 and 7.7. The dechannelling probability along $\langle 110 \rangle$ correlates with that along $\langle 111 \rangle$. The correlation of $\langle 110 \rangle$ and $\langle 100 \rangle$ is less definite, although a trend is evident. It is possible that the greater scatter for $\langle 100 \rangle$ arises from greater difficulty in accurate location of the channel due to the high yields recorded.

The diamonds were then sliced and polished. Infra-red measurements were made and channelling measurements were made on the slices. The dechannelling probabilities were then compared with the infra-red absorption coefficients. No correlation was found between the dechannelling

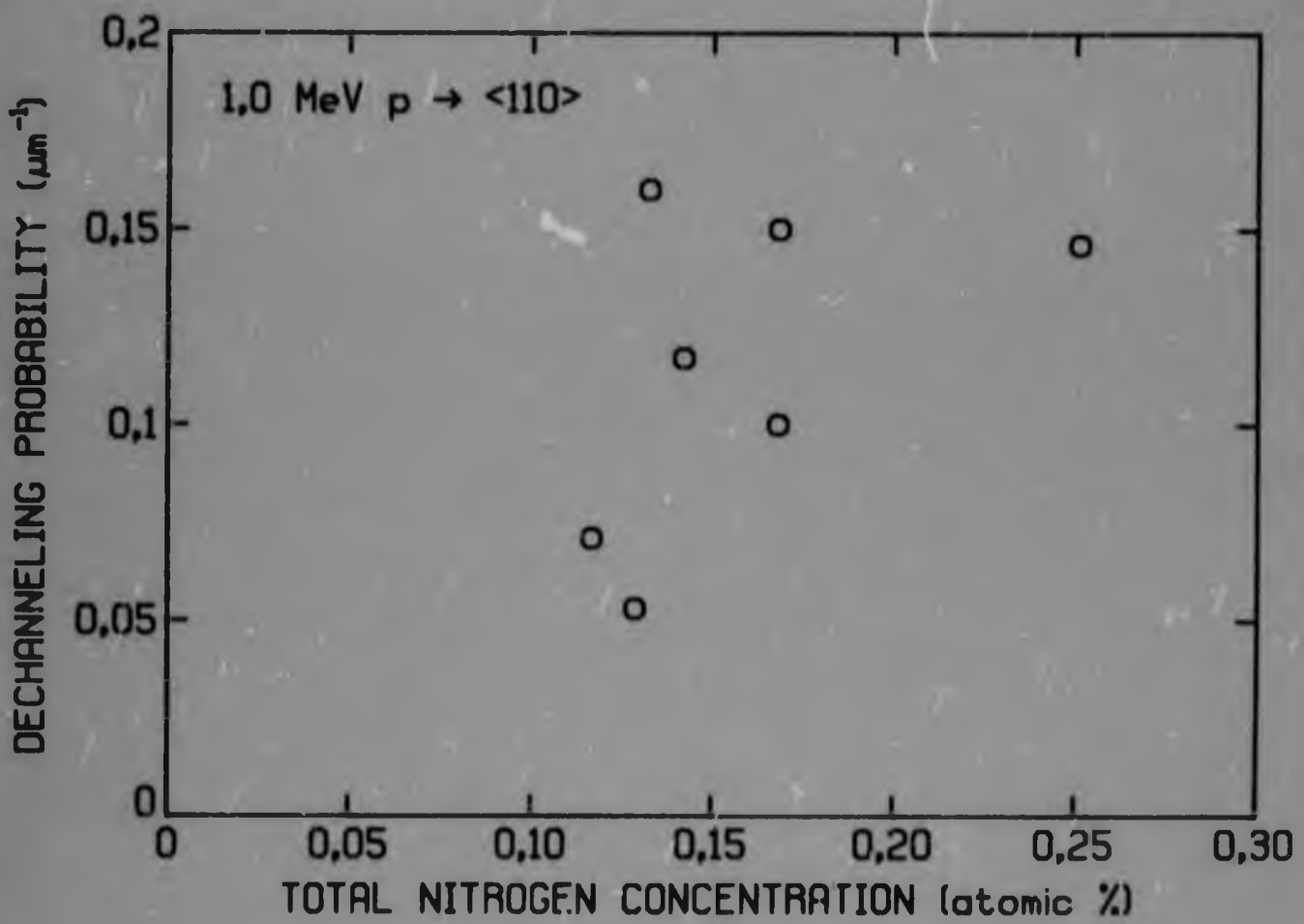


Figure 7.5: Variation of dechannelling probability with measured total nitrogen concentration.

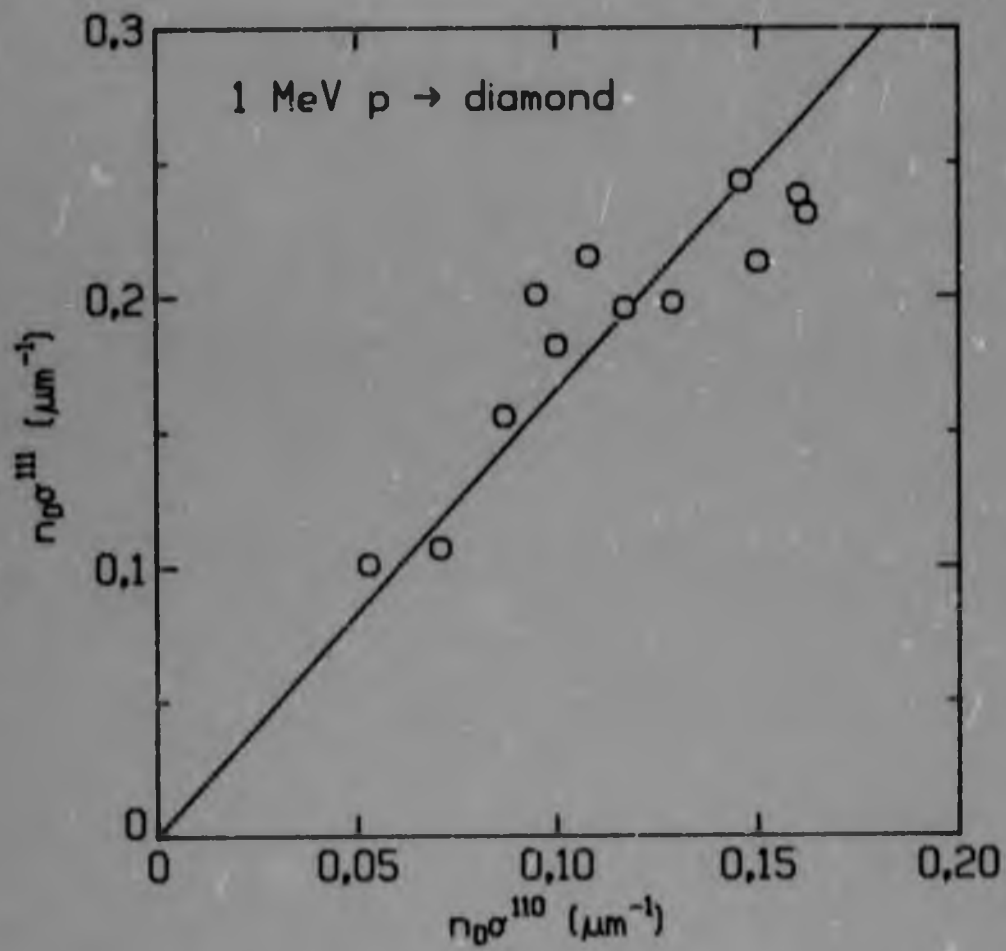


Figure 7.6: Relation of dechannelling probability in $\langle 111 \rangle$ to that in $\langle 110 \rangle$.

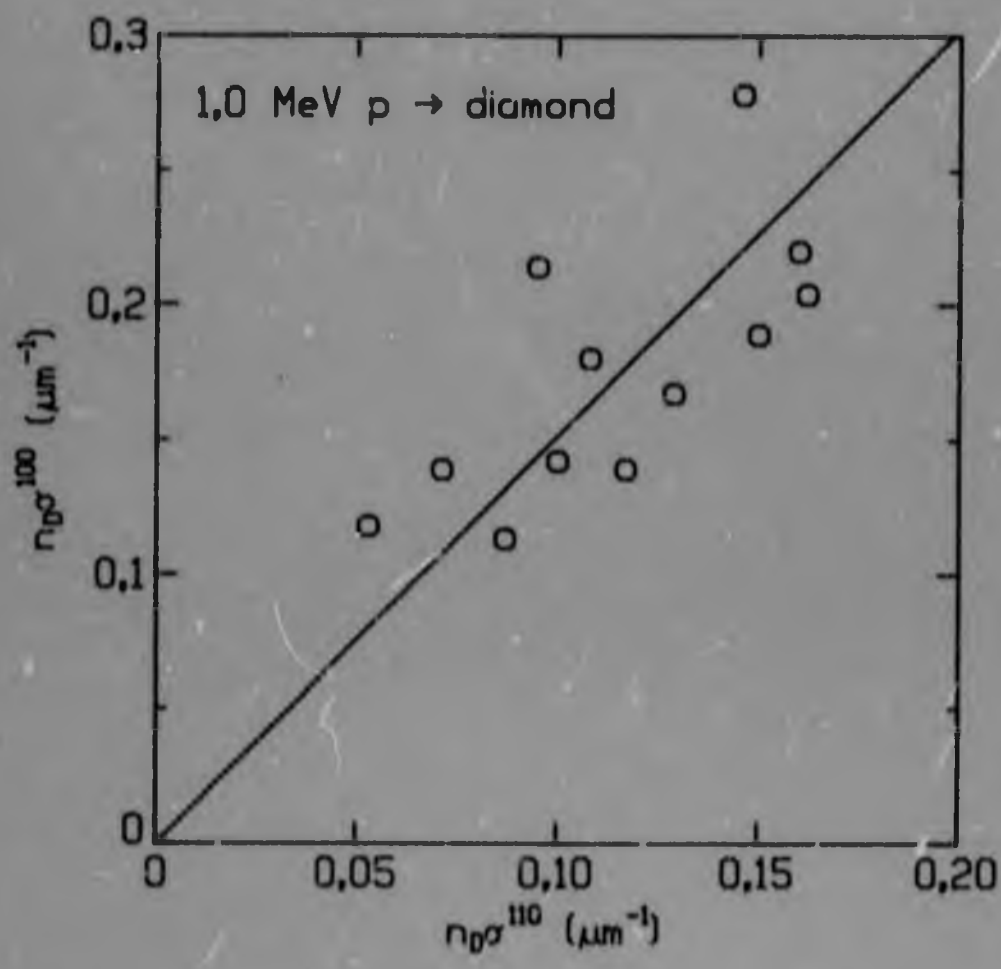


Figure 7.7: Relation of dechannelling probability in <100> to that in <110>.

probability and the total absorption at 1282 cm^{-1} or the A-aggregate absorption at 1282 cm^{-1} . A correlation was found between the dechannelling probability and both the B-aggregate absorption at 1282 cm^{-1} and the platelet absorption at 1370 cm^{-1} . These data are shown plotted in Figures 7.8 and 7.9. Also shown is the dechannelling probability for the B-only diamond, which is in general agreement with, but slightly below, the line for the no-B absorption correlation.

In order to provide further information about the defects responsible for the dechannelling, the dechannelling probability was determined for three diamonds as a function of energy. Similar behaviour was observed for all three diamonds. The results for the three axes $\langle 110 \rangle$, $\langle 111 \rangle$, and $\langle 100 \rangle$ on one diamond are shown in Figure 7.10. A similar behaviour is observed in all three axes, with the dechannelling cross-section varying with energy, E , as $\propto E^{-1/3}$.

7.5.3 Discussion

Considering the results for the Cape Yellow set first, it is clear that the dechannelling is related to the presence of B-aggregates and/or platelets. The absorption coefficients of 1282 cm^{-1} and 1370 cm^{-1} are proportional to the concentration of B-aggregate nitrogen and the area per unit volume of platelets, respectively. Thus it has been shown that the dechannelling probability is proportional to the concentrations of these defects (where 'concentration of platelets' means 'area per unit volume of platelet').

The results for the B-only diamond suggests that the platelets play little part in the dechannelling, and that it is the B-aggregates

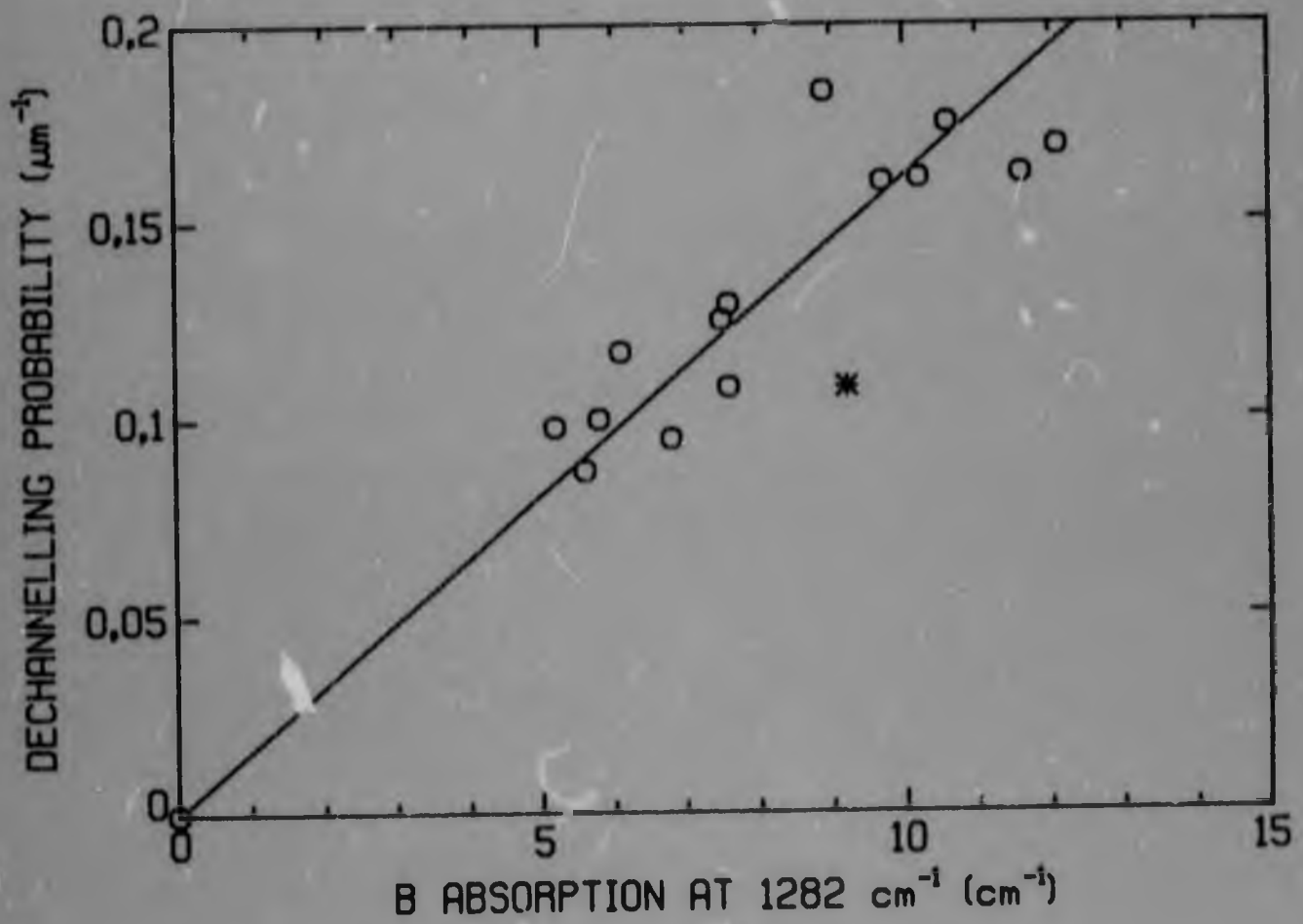


Figure 7.8: Dependence of dechannelling probability on absorption at 1282 cm^{-1} due to B aggregates.
 * : 'B only' diamond.

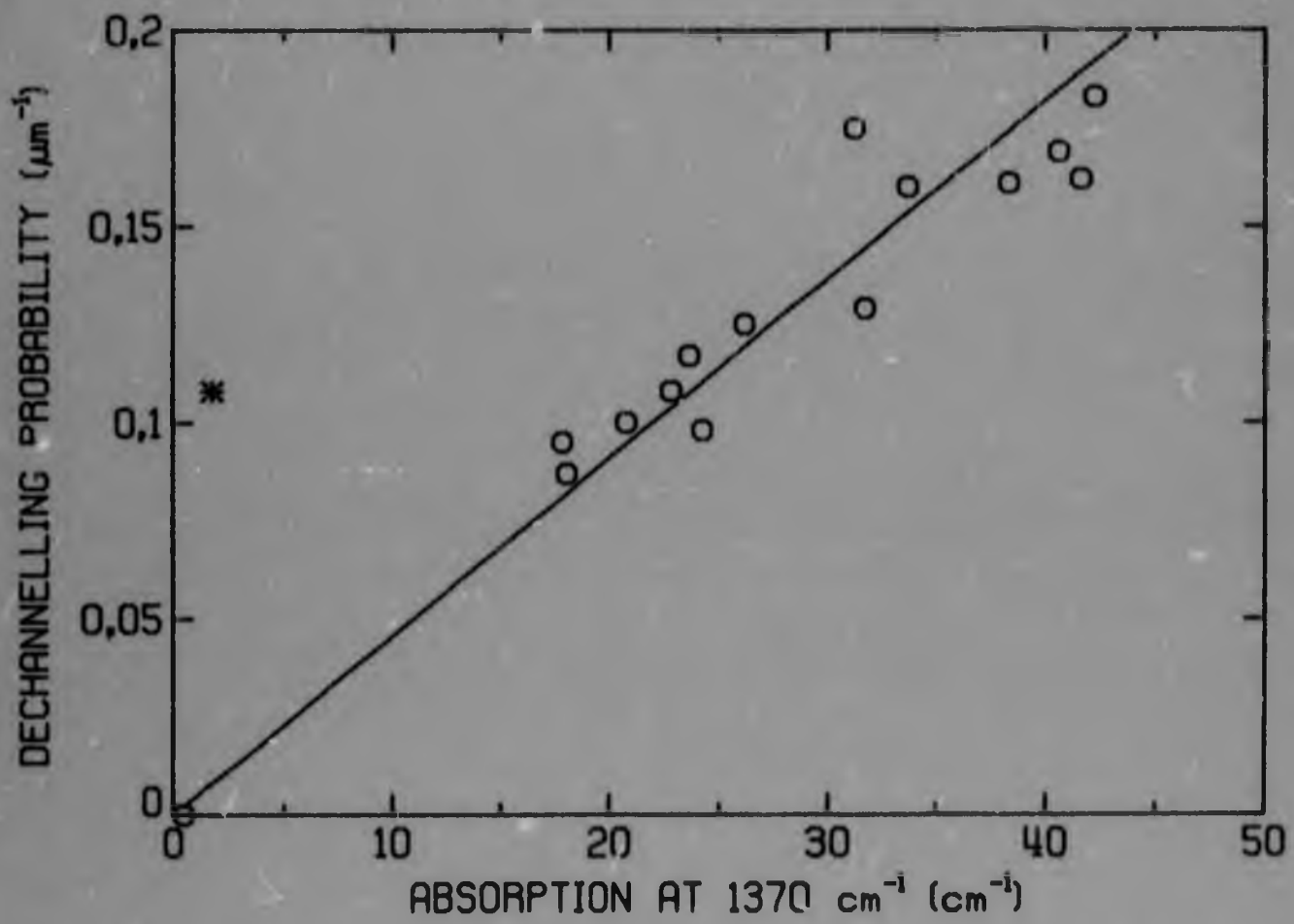


Figure 7.9: Dependence of dechannelling probability on absorption at 1370 cm^{-1} . *: 'B only' diamond.

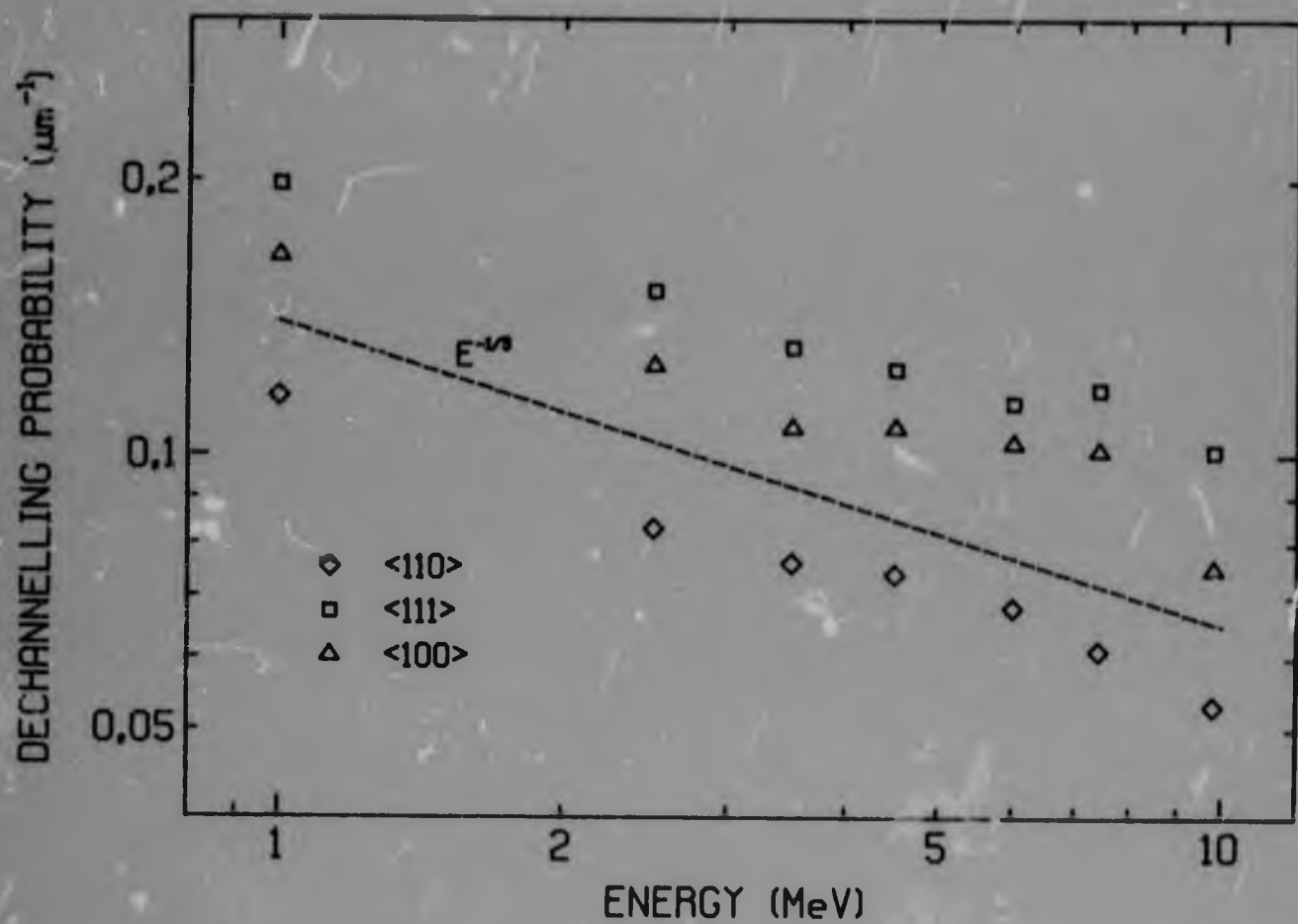


Figure 7.10: Energy dependence of dechannelling probability.

that are related to the dechannelling. It will be recalled, however, that B-only diamonds have been observed to contain concentrations of $\frac{a_0}{2} \langle 110 \rangle$ dislocation loops similar to platelet concentrations in other Ia diamonds. It is to be expected that these loops will also contribute to the dechannelling. Two situations can be considered:

- a) The B-aggregates are small clusters of nitrogen atoms, say 2 - 8 atoms, dispersed through the lattice [Dav 77]. Even if they were all in interstitial positions, the typical concentrations of 500 ppm to 1000 ppm would be too small to be a major contributor to the measured dechannelling cross-section. The major contribution must then be from the platelets in the Cape Yellow set and from dislocation loops in the B-only diamond. There need be no connection between the B-aggregates, the platelets and the loops.
- b) If the hypothesis of Evans [Eva 78] is accepted, the B-aggregates are associated with the platelets, and the dislocation loops in B-only diamonds have resulted from the degradation of platelets together with the dispersion of the B-nitrogen into the lattice. Again the major contribution from dechannelling is due to the platelets in the Cape Yellow set and the loops in the B-only diamond. In this case, the area of dislocation loops in the B-only diamond is equal to the area of platelets that were present before degradation occurred which, in turn, is related to the concentration of B-aggregate nitrogen.

Thus, both considerations lead to the conclusion that the

dechannelling is produced by platelets in the Cape Yellow set and by loops in the B-only set.

The nature of dechannelling due to the platelets can now be considered. The platelets, leaving aside the nature of the precipitated species, can be considered as a dislocation loop with a Burgers vector of type $\frac{a_0}{3} \langle 100 \rangle$. This displacement vector implies a faulted surface at the loop (that is, the loop is imperfect) and rows passing non-normally through the platelet will contain a stacking fault. The displacement of the rows for $\langle 110 \rangle$ and $\langle 111 \rangle$ is shown in Figure 7.11. The dechannelling cross-section for the platelet may be written as

$$\sigma_p = \sigma_F + \sigma_L \quad (7.3.4)$$

where σ_F is the fault contribution and σ_L is the loop contribution. The case of a loop of perfect dislocation with Burgers vector $\frac{a_0}{2} \langle 110 \rangle$ as in the B-only diamond is included in this description, with $\sigma_F = 0$.

It has been suggested that the energy dependence of the dechannelling cross-section can be used to distinguish between defects causing dechannelling [Qu 76]. In the present case, the cross-section (assuming n_D is not energy dependent!) varies as $E^{-1/3}$. Such an energy dependence has not been predicted for any defects. The dechannelling from stacking faults is expected to be energy independent [Mog 72, Cam 78]. The energy dependence of dechannelling by dislocation loops is more complicated. Dislocation lines are expected to dechannel with an $E^{1/2}$ energy dependence

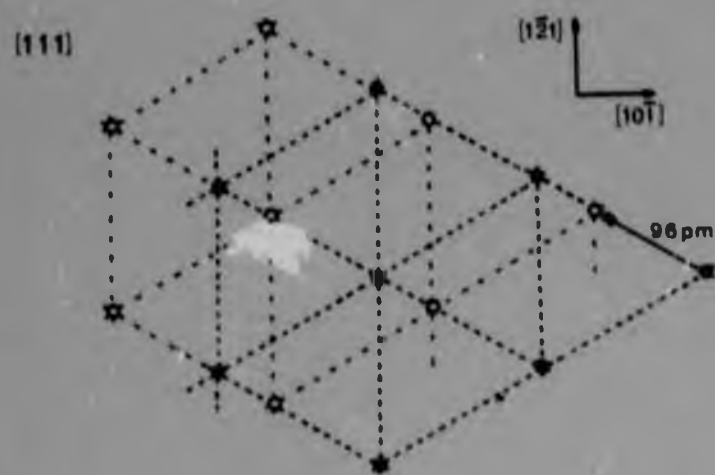
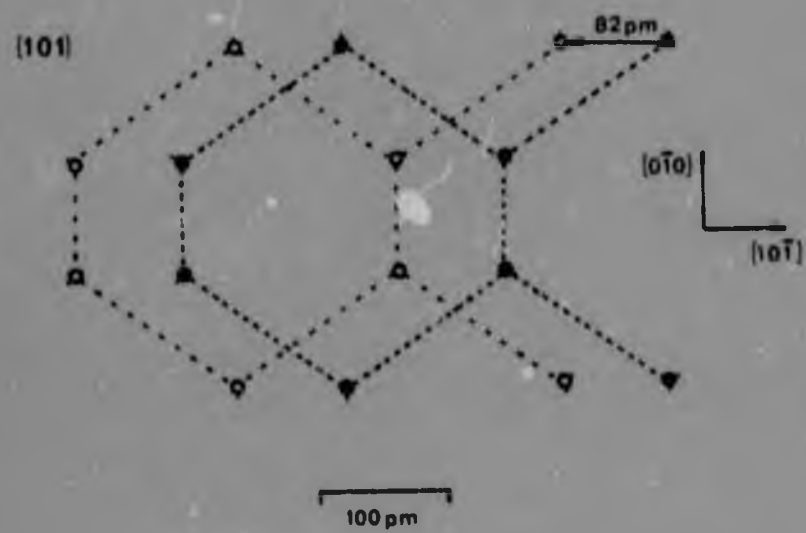


Figure 7.11: Displacement of rows by $\frac{1}{3} [100]$ fault, viewed along $[101]$ and $[111]$. ● rows before fault; ○ rows after fault.

and Quéré has suggested the same behaviour for loops [Qu 78]. However, Kudo [Kud 78] has shown that the behaviour for loops is more complicated, with an E^2 dependence at low energies changing to an energy independent region at high energies. In the intermediate region there is a peak in the cross-section, decreasing to a constant value as the energy increases. Thus the measured energy dependence leads to an indefinite result. It is interesting to note, however, that Agrawal and Sood [Ag 73] found an $\sim E^{-1}$ dependence for small imperfect loops in copper. This they interpreted as being due to the interstitial layer at the loop, however, the loop contribution is likely to be much larger [Qu 76]. This suggests that the energy dependence of dechannelling by loops is by no means simple, or understood.

Some simple estimates of the dechannelling cross-section in equation (7.3.4) can now be made. These are essentially of order-of-magnitude accuracy: a more accurate evaluation is probably only possible using computer simulation techniques or detailed solutions of the equations of motion of a large number of channelled ions. Nevertheless, some conclusions can be drawn.

To a first approximation, the channelled ions incident on the faulted surface can be treated as a parallel beam incident upon a free surface, so that the probability of dechannelling at the fault is given by the minimum yield, χ_{\min} , at the crystal surface. Then the dechannelling cross-section per row is [Cam 78]

$$\sigma_{F, \text{row}} = \chi_{\min} / Nd$$

where N is the crystal density and d the row spacing. In general, the angular distribution and flux of channelled ions at the fault must be taken into account, and the dechannelling cross-section may be written

$$\sigma_{F, \text{row}} = n(z) x_{\text{min}} / Nd$$

where n may, in general, depend on depth through the depth-dependence of the transverse energy distribution. (The dechannelling cross-section will thus also be depth-dependent.) If the projected platelet area per unit volume, normal to the channel is A , then the number of rows per unit area is NdA and hence the dechannelling probability is

$$n_D \sigma_F = n(z) x_{\text{min}} A$$

There will be no contribution to fault dechannelling from platelets parallel to the channel, and the $\frac{a_0}{3} \langle 100 \rangle$ displacement vector implies that $\langle 100 \rangle$ channels will not contain faulted surfaces. With a platelet area per unit volume of A_p , and with platelets distributed equally on all equivalent $\{100\}$ planes, the dechannelling probabilities for the three axes, $\langle 110 \rangle$, $\langle 111 \rangle$ and $\langle 100 \rangle$ become

$$n_D \sigma_F^{110} = n_{110} x_{\text{min}} \cdot \cos 45^\circ \cdot \frac{2}{3} A_p$$

$$n_{D^{\sigma F}}^{111} = n_{111}^{\text{min}} \chi_{\text{min}}^{111} \cdot \cos 54.7^\circ \cdot A_p$$

$$n_{D^{\sigma F}}^{100} = 0 \quad (7.3.5)$$

An estimate of $n(z)$ can be obtained as follows. The displaced row at the fault lies on some equipotential of the undisplaced crystal, $E_{\perp R} = U(\bar{r})$ where \bar{r} is the position of the displaced row (Figure 7.11). Ions reaching the fault with $E_{\perp} < E_{\perp R}$ will not be able to interact directly with the new row and so will not contribute directly to the dechannelling. (The perturbation of the trajectories of these ions will, of course, lead to an increase in yield due to a type of multiple scattering. This may be neglected in this estimate.) Ions with $E_{\perp} > E_{\perp R}$ will be able to interact with the displaced row. Because the axial potential varies rather steeply close to rows, it may be assumed that these ions are travelling, everywhere in their accessible area $A(E_{\perp})$, with an angle ψ to the channel given by $E\psi^2 = E_{\perp}$ (that is, the effect of the potential has been neglected). The relative interaction probability of these ions with the displaced row is then given by the angular yield function $\chi(\psi)$. The flux of such ions at the row is $\frac{g(E_{\perp}, z)}{A(E_{\perp})}$ and hence

$$n(z) = \frac{1}{\chi_{\text{min}}} \int_{E_{\perp R}}^{E_{\perp 1}} \frac{g(E_{\perp}, z)}{A(E_{\perp})} \chi(E_{\perp}) dE_{\perp} .$$

This was evaluated using $g(E_1, z)$ calculated using the diffusion model of Chapter 3, and with $\chi(E_1)$ approximated by

$$\chi(E_1) = \chi_{\min} + \frac{1}{2}(1 - \chi_{\min}) \left(\frac{E_1}{E_{1j}} \right)^2$$

that is, the angular yield as measured at the surface is approximated by a quartic [Der 78]. The resulting $n(z)$ for 1 MeV protons is shown in Figure 7.12 for the $\langle 110 \rangle$ and $\langle 111 \rangle$ axes. Because of the straight-line approximation used to calculate $n_D \sigma$, these were averaged over the depth of analysis to obtain

$$n_{110} = 5 \quad \text{and} \quad n_{111} = 4 .$$

Then the following dechannelling probabilities are obtained from equation (7.3.5), with $\chi_{\min}^{110} = 0.015$ and $\chi_{\min}^{111} = 0.018$:

$$n_D \sigma_P^{110} = 0.035 A_P$$

$$n_D \sigma_P^{111} = 0.042 A_P$$

$$n_D \sigma^{100} = 0 . \quad (7.3.6)$$

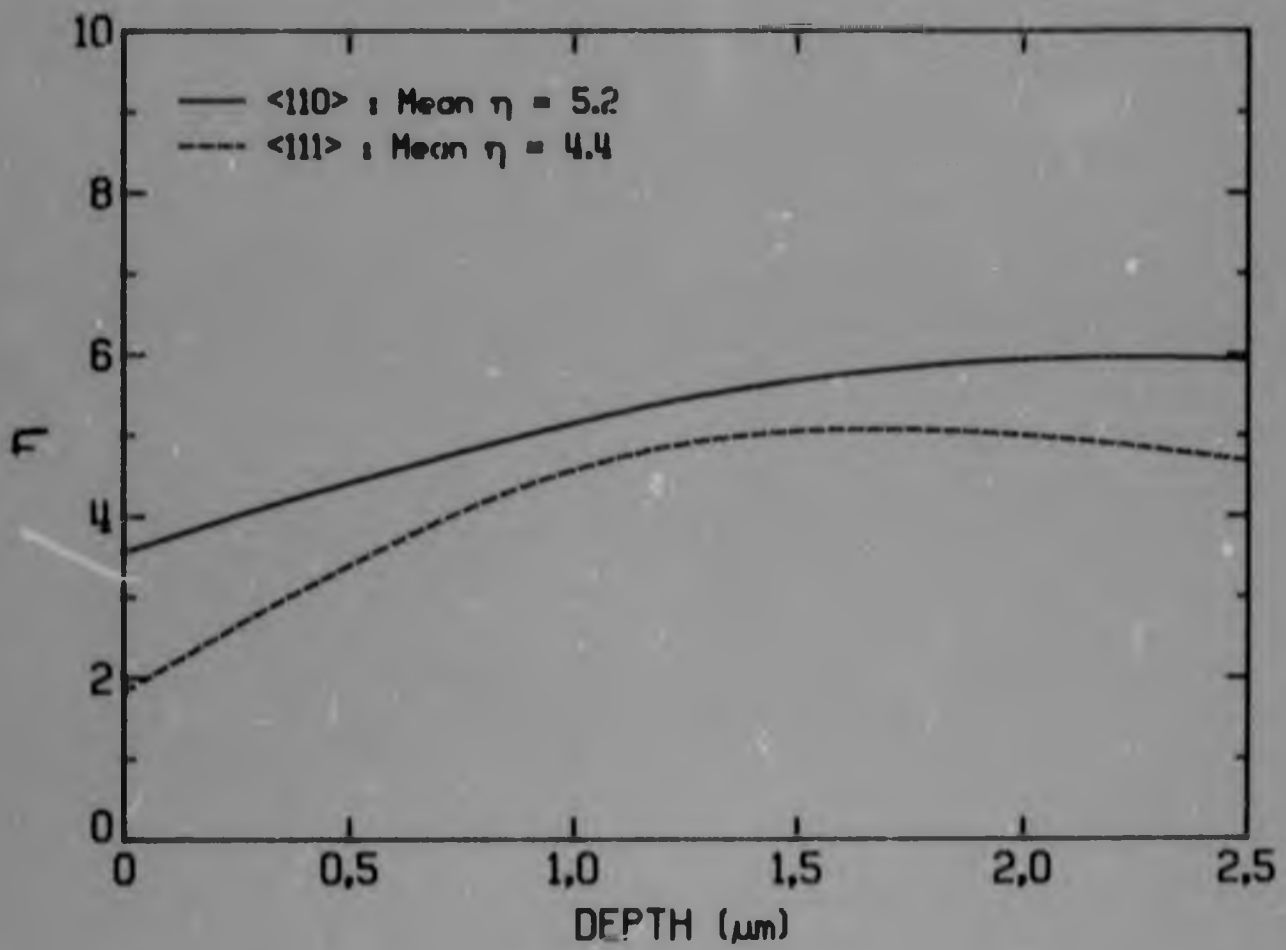


Figure 7.12: Dependence of η on depth, for $\langle 110 \rangle$ and $\langle 111 \rangle$.

The dislocation loop contribution, σ_L , is less certain. De-channelling by dislocation has been described by Quéré [Qu 68] in terms of a dechannelling diameter, λ , around the dislocation line, within which dechannelling is inevitable. Thus the cross-section for a line of length ℓ is

$$\sigma = \lambda \ell$$

For a dislocation loop, the dechannelling diameter, λ , is decreased because of the reduction in long-range strains and becomes proportional to the radius of the loop, for small loops [Qu 78]. Quéré has suggested the form [Qu 78]

$$\lambda = \lambda_m \cdot \frac{r}{r_c + r}, \quad r_c = 250 \text{ nm}$$

with

$$\lambda_m = \sqrt{0.08 \frac{Ebda}{z_1 z_2 e^2}} \quad (7.3.7)$$

as approximating the variation of λ with loop radius, r . Here, a is the Thomas-Fermi screening radius, and b is the length of the Burgers vector of the dislocation. According to equation (7.3.7), the dechannelling

diameter varies as $E^{\frac{1}{2}}$. However, Kudo [Kud 78] has shown, using numerical integration of the equations of motion of channelled ions, that the energy dependence of λ is more complicated.

At low energies, the wavelength of the trajectory of a channelled ion is much smaller than the loop size, and an $E^{\frac{1}{2}}$ dependence is obtained. As the energy and the wavelength increase, λ rises to a maximum and decreases to a constant, energy-independent, value at high energies, where the wavelength is much larger than the loop size. Kudo also found that for small loops, λ increased in proportion to r , and showed that λ must obey the functional relation [Kud 78]

$$\frac{\lambda}{r} = g \left(\frac{E^{\frac{1}{2}}}{r} \right) \quad (7.3.8)$$

where g is some (unknown) function.

Using the ideas of Kudo, the formula of Quéré (equation 7.3.7) can be reformulated to approximate the energy dependence obtained by Kudo. Equation (7.3.8) implies that r_c in equation (7.3.7) must be energy-dependent, $r_c = E^{\frac{1}{2}}$, and Kudo has suggested that the wavelength of the channelled ion trajectory is important in defining the energy dependence of λ . Trajectories with high transverse energy are the most sensitive to dislocation dechanneling [Kud 76a]. A characteristic high transverse energy trajectory is one with $E_{\perp} = E_{\perp}^2$. The wavelength of this trajectory can be estimated as follows. Suppose that the trajectory is sinusoidal.

Then the amplitude of the trajectory is approximately equal to the (single string model) 'radius' of the channel, r_0 , given by $\pi r_0^2 = 1/Nd$. At the channel centre, $U(r) = 0$ and the crossing angle $\psi = \psi_1$. Then $\psi_1 = \frac{2\pi r_0}{L_0}$ where L_0 is the wavelength of the trajectory, and hence

$$L_0 = \frac{2\pi r_0}{\psi_1} = \sqrt{\frac{2\pi E}{NZ_1 Z_2 e^2}} \quad (7.3.9)$$

Thus $r_c \sim L_0$ has the required energy dependence. It is reasonable to suppose that the critical wavelength in determining the behaviour of dechannelling by the loop is given by equating $\frac{1}{2}L_0$ to the diameter of the loop and thus $r_c = 0.25L_0$. Comparison with the results of Kudo [Kud 78, 76b] suggest that $r_c = 0.35L_0$ is more appropriate, at least to give a good fit to his results. Thus the dechannelling diameter for a dislocation may be approximated by

$$\lambda = \lambda_0 \frac{r}{0.35L_0 + r} \quad (7.3.10)$$

This is in good agreement with calculations by Kudo for aluminium [Kud 78] and gold [Kud 76b], although the peak in the energy dependence of λ is not, of course, reproduced. It is interesting to note, however, that this peak is at energies such that $r = 0.35L_0$. The value of σ for small ($r = 19$ nm) loops in gold calculated by Kudo [Kud 76] is in good

agreement with experiment [Mer 73]. Whether this will hold in general is difficult to assess. Kudo used a cosine distribution for the transverse energy distribution. Comparisons with the multi-string distribution for diamond, in Figure 7.13, shows that this over-estimates the number of ions with high transverse energy, which are the most likely to be dechannelled [Kud 76], by a factor of ~ 5 . This suggests that equation (7.3.10) might over-estimate λ for diamond by about the same amount.

The cross-section for dechannelling by the loop will be

$$\sigma_{L,\parallel} = 2\pi\lambda$$

for trajectories parallel with the loop (that is, perpendicular to b) and

$$\sigma_{L,\perp} = 2\pi\lambda$$

for trajectories perpendicular to the loop (that is, parallel to b). Kudo has shown [Kud 76a] for silicon, that for a straight edge dislocation, the dechannelling diameter for channels perpendicular to the Burgers vector and to the dislocation line is about 2.5 times that for channels parallel with the Burgers vector and perpendicular to the dislocation line.

Thus λ in $\sigma_{L,\parallel}$ should be increased by a factor of this order and, to a first approximation, the orientation of the loop with respect to the channel may be ignored to obtain the following for all channels:

$$\sigma_L = 2\pi\lambda.$$

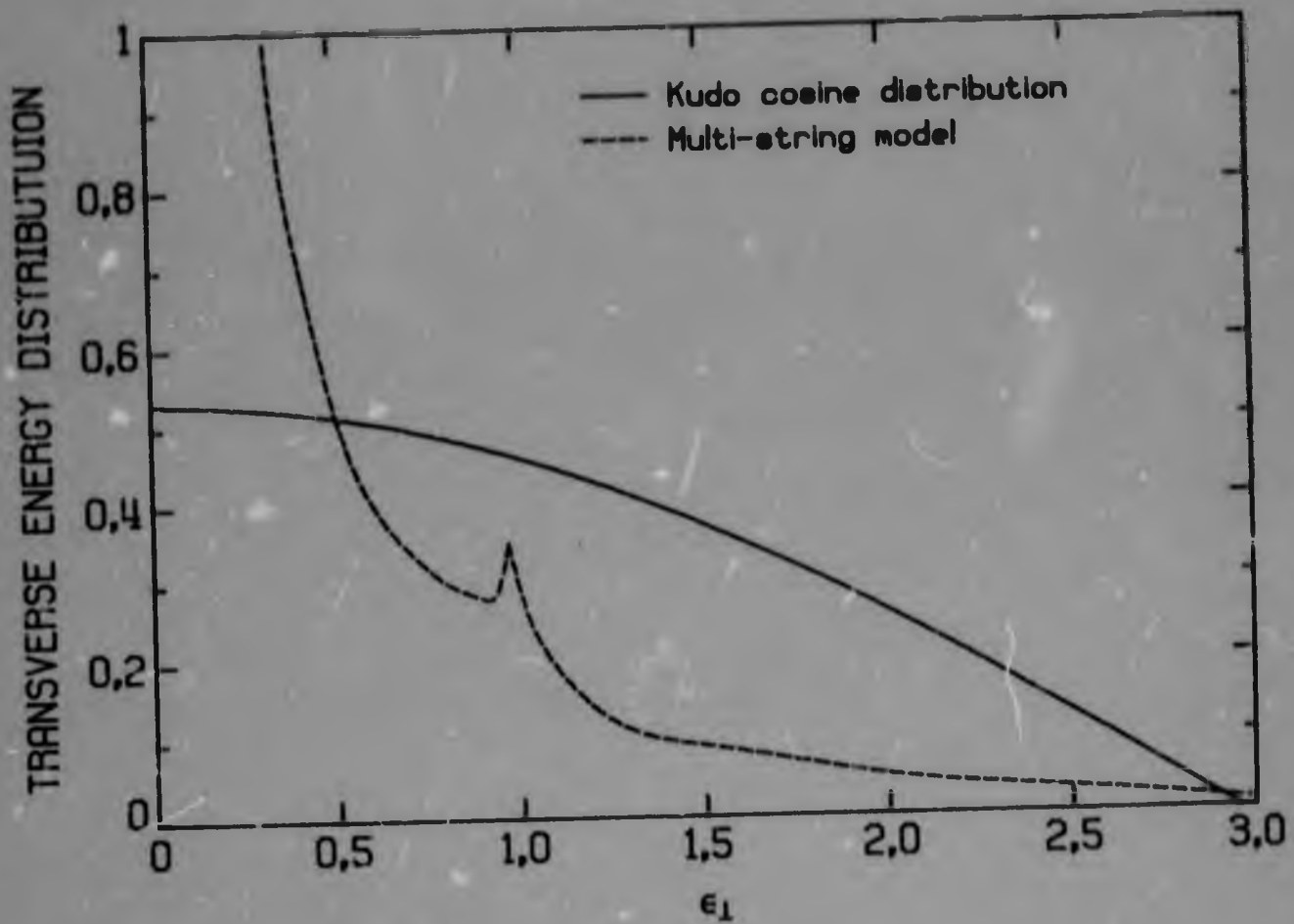


Figure 7.13: Comparison of transverse energy distribution as used by Kudo and multi-string distribution calculated for $\langle 110 \rangle$.

If the loop is small compared with r_c the dechannelling cross-section becomes proportional to r^2 , that is, the area of the loop and hence the dechannelling probability may be written, from equations (7.3.10), (7.3.9) and (7.3.7), with a factor of 0.2 introduced to take account of the transverse energy distribution,

$$n_D \sigma_L = 0.2 \sqrt{0.4 N b d a} A_L$$

where A_L is the area of loop per unit volume. Retaining the channel and Burgers vector dependence, this may be written

$$n_D \sigma_L = k \sqrt{b d} A_L$$

where k is a constant for the material, expected to be of the order of $k = \sqrt{0.016 N a} = 0.27 \text{ nm}^{-1}$ for diamond. In the case of platelets presently under consideration, $A_L = A_p$.

Then the loop contribution to platelet dechannelling becomes

$$\begin{aligned} n_D \sigma_L^{110} &= k \sqrt{b d_{110}} A_p = 0.047 A_p \\ n_D \sigma_L^{111} &= k \sqrt{b d_{111}} A_p = 0.052 A_p \\ n_D \sigma_L^{100} &= k \sqrt{b d_{100}} A_p = 0.056 A_p \end{aligned} \quad (7.3.11)$$

where the length of the Burgers vector $\frac{a}{3} \langle 100 \rangle$ is 0.119 nm. Thus $n_D^{\sigma_L}$ is of the same order as the fault contribution, equation (7.3.6).

In the B-only diamond, the dechannelling will depend on the loop contribution only,

$$(n_D^{\sigma_L^{110}})^B = k \sqrt{b'd_{110}} A_L = 0.068 A_L \quad (7.3.12)$$

where $b' = 0.252$ nm, and A_L is the area of loop per unit volume.

Thus, from equations (7.3.6) and (7.3.11),

$$n_D^{\sigma^{110}} = n_D^{\sigma_F^{110}} + n_D^{\sigma_L^{110}} = 0.082 A_p \quad (7.3.13)$$

From the correlation of dechannelling probability with the 1370 cm^{-1} absorption coefficient, μ_p , (Figure 7.8),

$$n_D^{\sigma^{110}} [\mu\text{m}^{-1}] = 0.0046 \mu_p [\text{cm}^{-1}]. \quad (7.3.14)$$

Hence, from equations (7.3.13) and (7.3.14),

$$A_p = 560 \mu_p \quad (7.3.15)$$

This is of the same order as the estimate from electron micrographs by Hudson [Hu 76],

$$A_p \sim 1000 \nu_p .$$

This suggests that the model for platelet dechannelling is reasonable. The model also gives

$$\frac{n_{D^{\sigma}111}}{n_{D^{\sigma}110}} = 1.15 \quad \text{and} \quad \frac{n_{D^{\sigma}100}}{n_{D^{\sigma}110}} = 0.68 .$$

The experimental values from Figure 7.6 and 7.7 are

$$\frac{n_{D^{\sigma}111}}{n_{D^{\sigma}110}} = 1.7 \quad \text{and} \quad \frac{n_{D^{\sigma}100}}{n_{D^{\sigma}110}} = 1.5 .$$

This agreement is not too good. However, it is possible that a more detailed treatment of the various terms, especially the directional dependence of the dislocation loop dechannelling, will improve matters.

Now, suppose that the loops in B-only diamonds are degraded platelets. Then the area of loop must equal the area of platelets existing before degradation. This hypothesis also assumes that the B-nitrogen is the species at the platelet site. Then, before degradation recurred in the B-only diamond, the dechannelling probability would have been given, at

the same B-aggregate absorption, on the line in Figure 7.8, that is,

$$(n_D^{\sigma})_{\text{before}}^B = 0.15 \mu\text{m}^{-1} \quad (7.3.16)$$

compared with a value after degradation (that is, as measured)

$$(n_D^{\sigma})_{\text{after}}^B = 0.11 \mu\text{m}^{-1} .$$

This latter contribution is due only to dislocation loops (equation 7.3.12) and thus the loop contribution to the platelets, existing before degradation, may be obtained from this value, without knowledge of k in equations (7.3.11), and (7.3.12), that is

$$\begin{aligned} (n_D^{\sigma_L})^B &= 0.11 \sqrt{\frac{b}{b'}} \\ &= 0.075 \mu\text{m}^{-1} \end{aligned}$$

and, hence from equation (7.3.16),

$$(n_D^{\sigma_P})^B = 0.075 \mu\text{m}^{-1} .$$

This implies that $n_D^{\sigma_P} = \frac{1}{2} n_D^{\sigma}$ and, hence from equations (7.3.14) and (7.3.6)

$$A_p = 650 \mu_p \quad (7.3.17)$$

which is in agreement with the value (7.3.15). Thus the concentration of defects assumed to be dislocation loops, in the B-only diamond is consistent with these loops being formed from previously existing platelets.

Suppose now that the B-nitrogen aggregates are the species at the platelet site. The correlation between B-aggregate infra-red absorption, μ_B (in cm^{-1}) at 1202 cm^{-1} and the concentration, N_B (in atomic per cent) of B-nitrogen atoms is not well-known but is given by (from Section 4.2.3)

$$\mu_B = (85 - 150)N_B .$$

The B absorption-platelet absorption correlation for the Cape Yellow set is

$$\mu_p = 3.6 \mu_B$$

and this will be taken as representative of the undegraded platelet state. Then, from equation (7.3.17),

$$A_p = 2300 \mu_B$$

and hence the number of B nitrogen atoms, n_B , per platelet area is given by

$$n_B = (0.5 - 1) \cdot 10^{20} \text{ m}^{-2} .$$

This may be compared with the number required to form nitrogen platelets with the Lang [Lan 64] structure (see Figure 7.14)

$$n_L = 0.314 \cdot 10^{20} \text{ m}^{-2}$$

With due consideration of the uncertainties in the B-nitrogen concentration and the simple model which has been used for the dechanneling cross-section, the experimental value is consistent with this value, that is, the B-nitrogen in Type Ia diamonds is present in concentrations consistent with those required to form nitrogen platelets. This conclusion must, at present, rest on data from only one B-only diamond. It would be interesting to continue these measurements if further specimens of this type become available.

7.4 SOME REMARKS ON PLATELET STRUCTURE

Evans has hypothesised [Eva78] a sequence of platelet growth and decay, whereby single nitrogen atoms are incorporated into the lattice and, under suitable conditions of temperature and pressure, combine to form first A-aggregates and then the more stable B-aggregates. These B-aggregates condense into platelets which then, under some conditions, can degrade into $\frac{a_0}{2} \langle 110 \rangle$ dislocation loops. Evans suggested that the B-aggregates would then be related to small (5 nm) defects observed in B-only diamonds with no 1370 cm^{-1} absorption. In terms of this hypothesis, the B-aggregate absorption would be a property of individual B-aggregates in the lattice, while the 1370 cm^{-1} absorption would be due to some collective property of the B-aggregates in a platelet. The results presented above for the B-only diamond are not inconsistent with this

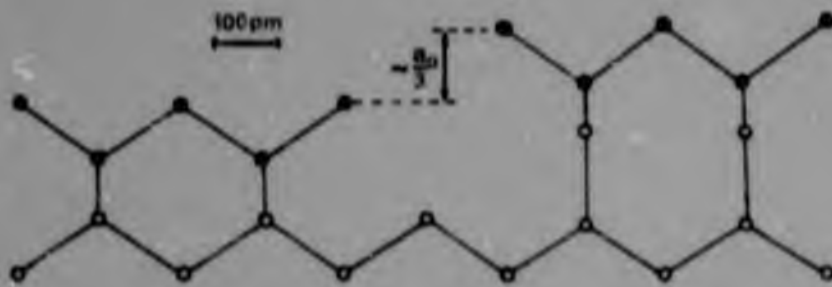


Figure 7.14: View in (110) of Lang model platelet, on right, compared with diamond, on left. Atoms depicted (○) lie in the plane of the paper, while those depicted (●) lie out of the plane.

hypothesis. Certain remarks can be made about this hypothesis, and some predictions can be made.

The Lang model for a nitrogen platelet [Lan 64], which is the simplest and most reasonable model consistent with the hypothesis and the observations, has two bonded nitrogen atoms replacing one carbon atom on (100) planes (Figure 7.14). This suggests that the B-aggregate might be identified as a pair of nitrogen atoms occupying a split <100> interstitial site. This site has been suggested as the most reasonable for carbon self-interstitials [Ma^o 71, Wei 73, Mai 78]. The self-interstitial is mobile below room temperature but it is possible that the strength of N-N and C-N bonds (stronger than C-C bonds) renders the split <100> nitrogen interstitial a more stable defect. This site has also been suggested for the site occupied by nitrogen implanted into diamond at low energies and studied by X-ray photo-electron spectroscopy [Evn 78]. The configuration studied by X-ray photo-electron spectroscopy [Evn 78]. The configuration studied was found to be relatively stable [Evn 78].

Such a bonded nitrogen pair could also be more stable than the A-aggregate which Davies [Dav 76] has suggested is a pair of neighbouring nitrogen atoms which are not bonded to each other. It is also possible that such an A-aggregate could transform into a split <100> interstitial to become a B-aggregate as in the sequence proposed by Evans. B-aggregates could then aggregate on (100) planes to form platelets.

A possible sequence for degradation can also be proposed. It is possible that, under certain conditions of temperatures and pressures, split <100> carbon interstitials could interchange with B-aggregates, being accommodated at the platelet in the form, perhaps, of a distorted

ethylene skeleton with a 90° rotation about the double bond. (This was proposed and rejected as a (carbon) platelet model by Caticha-Ellis and Cochrane [Cat 58].) Then the 1370 cm^{-1} peak would decrease in proportion to the amount of carbon present in the platelet, while the $\frac{a}{2} \langle 100 \rangle$ displacement vector would be maintained, so that no effect on X-ray spikes would be observed. This is consistent with the observations of Evans and Rainey [Eva 78]. The carbon platelet thus formed, however, would be unstable because of the high strain in the carbon bonds, and a suitable dislocation could sweep across the platelet, as proposed by Woods [Wo 76] to form an $\frac{a}{2} \langle 110 \rangle$ loop on $\{100\}$. This could then glide off the plane into the arbitrary orientation observed in B-only diamonds [Eva 78]. Presumably, the energy contained in the strained bonds would be sufficient to offset the energy deficit in turning an $\frac{a}{2} \langle 100 \rangle$ dislocation loop into an $\frac{a}{2} \langle 110 \rangle$ dislocation loop.

Evans has suggested that the B-aggregates in B-only diamonds are associated with small (5 nm) defects noted in electron micrographs. There is no compelling reason for this and these are perhaps associated with other defects. The concentration of these aggregates, in any case, is less than can be accounted for by the B-nitrogen [Va 80].

This sequence is consistent with observations, but is rather hypothetical. Certain predictions can be made from it, that can be tested. Thus, if platelets are made of B-aggregates, in all diamonds,

where equality holds if all the B-aggregates are in undegraded platelets. The results for the Cap Yellow diamonds in this work suggest $a \approx 3.6$. It is interesting to note that all published spectra and decompositions noted by the author, in which u_p can be compared with u_B , are consistent with $a \approx 4$. Thus, the existence of an upper limit to the platelet absorption in terms of the B-aggregate absorption seems reasonably well-established. Such a limit is difficult to understand if there is no close connection between the B-aggregates and the platelets. It is also interesting to note that the observed upper limit is consistent with the Lang platelet model.

Also, it is reasonable to assume that any carbon platelets formed by the above mechanism have, in the course of geological history, degraded into loops in natural diamonds. Thus in those rare B-diamonds in which $u_p = au_B$, one can predict that the number of platelets as a fraction of all platelets and loops, should be equal to the observed 1370 cm^{-1} absorption as a fraction of the maximum possible 1370 cm^{-1} absorption, that is,

$$\frac{u_p}{au_B} = \frac{\text{area of platelets}}{\text{area of (platelets and loops)}}$$

This prediction can be tested by examination of electron micrographs of suitable diamonds.

Finally, it is possible that platelets can be made to grow by implantation of suitable atoms or by radiation damage. Thus creation of

split $\langle 100 \rangle$ interstitial nitrogen pairs by ion implantation might result in platelet growth with consequent increase in 1370 cm^{-1} absorption and X-ray spike intensity. It is possible that platelet growth can also be promoted by creation of split $\langle 100 \rangle$ carbon interstitials by ion implantation or radiation damage. The above argument would imply that such growth would be accompanied by an increase in X-ray spike intensity, but not in 1370 cm^{-1} absorption. Such experiments are possible for those with suitable facilities.

7.5 CONCLUSIONS

It has been shown that the dechannelling probability in a series of Cape Yellow diamonds containing a high concentration of characteristic Type Ia defects, that is, platelets and B-nitrogen aggregates, is proportional to the quantity of these defects present. The dechannelling probability is derived using a diamond assumed to represent the perfect crystal dechannelling, and the proportionality obtained suggests that this assumption is reasonable. These results have shown that it is possible to understand dechannelling in natural crystals, and that this dechannelling can be explained in terms of defects known to be present.

It has been concluded that the primary source of the dechannelling is the platelet, and a model has been described which treats the dechannelling by platelets as the sum of a fault term and a dislocation loop term. Current models for these two terms have been improved and the values for the dechannelling probabilities obtained allow the calculation of the total platelet area per unit volume, which is in agreement with estimates from electron micrography.

The dechannelling in a B-only diamond has been examined and found to be consistent with hypothesis that dislocation loops in these diamonds result from degraded platelets. The concentration of B-nitrogen in the diamonds is consistent with the quantity required to form nitrogen platelets.

Finally, some remarks have been made on the nature of platelets and some proposals have been made for testing certain predictions that follow from the proposed platelet model.

ENERGY LOSS OF LIGHT IONS IN DIAMOND

8.1 INTRODUCTION

An important feature of channelled motion is the reduction in stopping power for channelled ions. The relatively long range excitation processes which lead to energy loss of an ion to the electrons of the medium in which it is travelling are sensitive to the trajectories of channelled ions and reductions of typically ~50 % in stopping power are observed. The study of this reduced stopping power has received much attention in recent years, both experimental [Ap 67, Clr 70, Bi 72, Dem 72, Mel 75, Jar 77, 78] and theoretical [Ap 67, Bon 69, Kcm 74, Des 77, Bel 78, Det 75, Es 78]. Extensive measurements have been made on silicon and germanium, and most theoretical studies have made predictions for these substances.

It is of interest to extend these measurements to diamond, partly because of the similarity in crystal structure and binding to silicon and germanium, but also because most of the electrons in diamond are valence electrons. In a recent theoretical treatment, Dettmann [Det 75] (and see Chapter 2) has treated the valence electrons as a uniform electron gas, with the same contribution to random and channelled stopping. In this theory, therefore, the reduction in stopping is due to the variation in the core electron contributions, which are of relatively short range. Other authors have taken the spatial periodicity of the valence electron

gas into account [Bon 69, Kom 74, Des 77] and have found a difference in valence electron stopping for channelled and random ions. It has been argued [Jar 77], however, that this localisation of the valence electrons around the atoms is irrelevant for channelled ions, because the range of interaction of such ions with loosely bound valence electrons is much larger than channel dimensions, and thus that Dettmann's treatment of them as a uniform electron gas is to be preferred. For silicon and germanium, Dettmann's theory gives predictions generally similar to other theories which have a differing valence contribution to random and channelled stopping [Kom 74, Mel 75] or which do not treat the valence electrons and core electrons separately [Es 78]. Experiment does not allow a clear-cut distinction between the theories, although the theory of Esbensen and Golovchenko is favoured [Jar 78]. This does, however, rely on some corrections to the data to account for dechanneling and trajectory dependence of the energy loss, and which may be over-simplified.

In diamond, random stopping in the MeV energy range is predominantly due to the four valence electrons, the two core electrons per atom accounting for about 10 % of the stopping, according to Dettmann's theory. These two core electrons are localised close to the atoms, and thus contribute very little to channelled stopping. Thus the theory of Dettmann predicts a maximum reduction in stopping for diamond of about 10 % with a similar reduction in all axes. Other theories (for example, [Es 78]), predict a much larger reduction, and a more pronounced axial dependence. Thus a measurement of the stopping power in diamond can provide a test of the validity of the various theories.

Measurements have been made of the stopping powers of 3 - 12 MeV

protons, 12 - 18 MeV alpha particles and 24 MeV Li-7 ions in diamond crystals 4 - 18 μm thick. The results are compared with the first principle calculations of Dettmann and of Esbensen and Golovchenko. The results indicate that the localisation of valence electrons should be taken into account in Dettmann's theory. The theory was modified by treating the valence electrons as a spatially periodic electron gas using the expression derived in Chapter 2 (equation 2.4.35). The modified theory gives predictions similar to those of the theory of Esbensen and Golovchenko. The experimental results are in closer agreement with values predicted for the major planes passing through the axis than with the minimum axial values. The random energy loss and straggling have also been measured.

8.2 EXPERIMENTAL METHODS

8.2.1 Experiment

The experiment was carried out in the Tandem scattering chamber, as described in Chapter 3. Targets were aligned by using the annular detector at forward angles as a monitor and optimising the transmitted beam detected at 0° . Beam currents were of the order of 10^{-16} A.

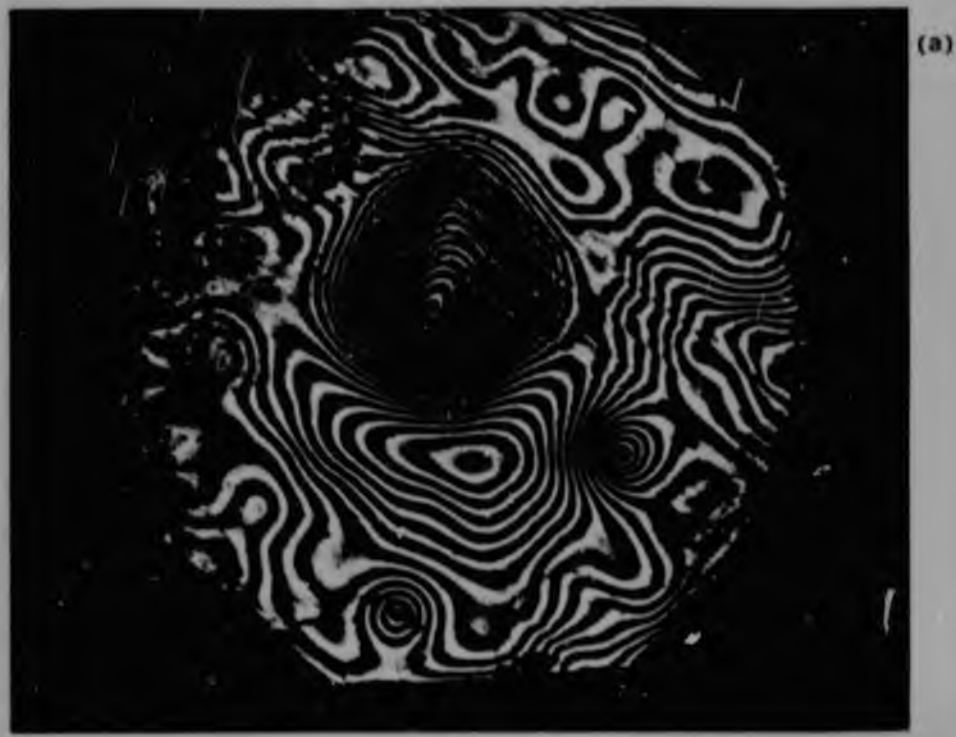
Random spectra were taken at the same goniometer tilt angle as the channelled spectra, by rotating the target off-channel. Thus the path-length for channelled and random beams in the target was the same. Incident beam spectra were recorded with the target removed and were also used to calibrate the amplifier-analyser system.

Spectra were recorded in the pulse-height analyser simultaneously with a pulse from a precision research pulser (Ortec 448 Research pulser,

specified integral linearity within 20 ppm, stability <15 ppm, accuracy of setting <10 ppm). Calibration spectra of a number of pulser peaks were also recorded at frequent intervals. These pulser spectra enabled the linearity and the gain of the system to be continuously monitored and the conversion of pulse-height analyser channel to energy was established to better than 0.1 %.

8.2.2 Thin Diamonds

Thin diamond crystals, polished to a thickness of 4 - 18 μm were obtained from D. Drukker and Zn, Amsterdam. The diamonds were natural Type IIa crystal. Other methods of preparation of thin crystals considered were ion milling and chemical etching: ion milling proceeds slowly, especially with the equipment that was available, and leads to amorphisation of the near-surface layer; chemical etching requires the use of oxidising agents at high (500 - 1000 °C) temperatures, and cannot be easily controlled under these conditions. Thus, polishing was the only realistic preparation method. Nevertheless, this is not without its difficulties. Diamond is polished on a cast-iron scaife (polishing wheel) at linear velocities of $\sim 30 \text{ ms}^{-1}$, and with relatively large loads on the diamond. This process cannot be compared with the gentle lapping used in the preparation of other thin crystals, for example, silicon. The crystals obtained varied in thickness by $\sim 10\%$ (peak to peak, corresponding to $\sim 3\%$ standard deviation) over the area of the beamspot and this uncertainty in thickness dominates the errors of the experiment. This variation is illustrated in Figure 8.1 for the two diamonds used for most of the measurements, the photographs were taken with sodium light ($\lambda = 549 \text{ nm}$) and a change of one fringe indicates a variation in thickness of 122 nm



(a)



(b)

Figure 8.1: Thin diamonds viewed in sodium light. (a) 18.7 μm diamond, (b) 4.0 μm diamond.

(refractive index = 2.42 [Pet 23]). In view of the difficulties associated with the polishing of diamond, the uniformity obtained is a tribute to the diamond polisher's art.

Sample thickness was measured by using an infrared spectrophotometer and determining the thickness from the oscillations in the observed transmittance [Ei 72]. The thickness is then

$$t = \frac{m}{2 \left(\frac{n_1}{\lambda_1} - \frac{n_2}{\lambda_2} \right)}$$

where λ_1 and λ_2 are two wavelengths separated by m fringes and n_1 and n_2 are the refractive indices at those wavelengths. The value of the refractive index over the range of wavelengths used is 2.30 (M. Seal, private communication). Measurements at selected points on the diamond were obtained by using monochromatic light to produce a fringe pattern as in Figure 8.1 and then counting the number of fringes moving past a reference point while the wavelength of light from the monochromator was varied. The thickness could then be determined in a similar fashion to the infrared determinations.

8.2.3 Data Analysis

A typical spectrum of the channelled and random transmitted beam is shown in Figure 8.2. The definition of the channelled ion energy loss is a major source of difficulty in transmission channelling

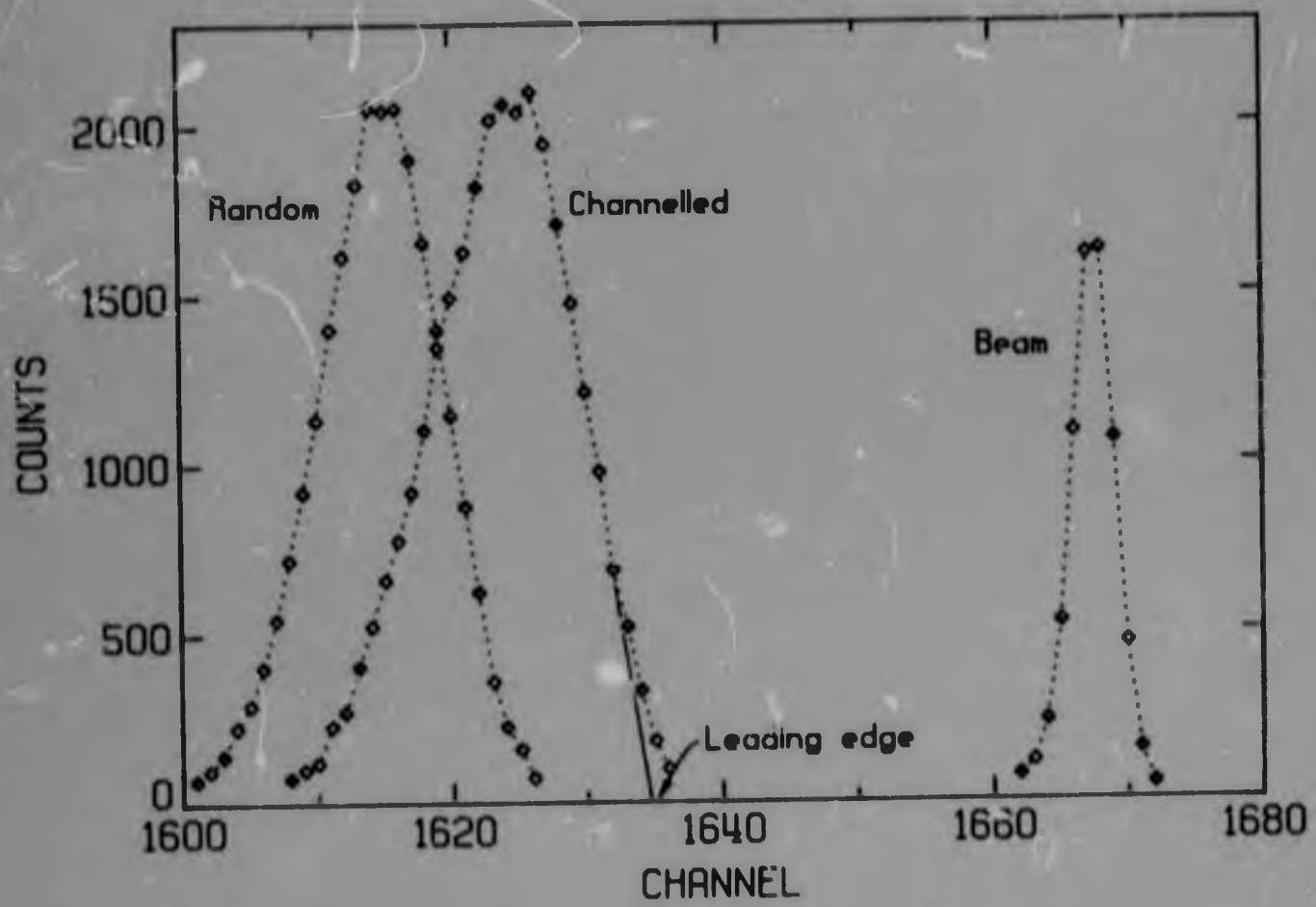


Figure 8.2: Spectra of 10.0 MeV p transmitted through 18.7 μm diamond in $\langle 110 \rangle$ and random directions, showing position of the leading edge of the channelled spectrum.

experiments. The most probable energy, that is, the energy corresponding with the maximum of the peak, can be taken as the transmitted beam energy for the incident beam and random spectra. The width of the peak in these cases can be ascribed to instrumental (detector) resolution and energy loss straggling in the target. For the channelled ion spectrum, the width is also affected by the trajectory dependence of energy loss and by dechanneling. Thus the position of the peak maximum gives the most probable energy loss for particles leaving the target at 90° and depends on the average motion of the distribution of ions through the crystal. It will depend, in general, on the thickness of the target crystal. It is not related directly to quantities predicted by theory, such as the minimum energy loss for best channelled ions. It has been suggested that the leading edge of the peak, as represented by the intercept of the tangent to the high energy side of the peak with the baseline, is representative of this least energy loss [Ei 72, Mel 75]. This can only be reasonable if the width of the peak is much greater than that expected from instrumental resolution and straggling. In this case, the width is mainly determined by the distribution in stopping powers for various trajectories and by dechanneling, and the leading edge will represent the ions with least energy loss. Thus the leading edge will give a better approximation of the least energy loss for thicker targets, and for larger energy losses in the target. In thin crystals, the peak position will be a better reflection of the least energy loss, if the width of the peak is approximately determined by straggling and resolution. In general, the true least energy loss may be expected to lie between the peak and leading edge values, and these quantities then provide upper and lower limits. The channelled energy loss was thus obtained for the peak and leading edge of the spectrum.

The position of the maximum was obtained by fitting a skewed Gaussian to the peak. The fitting function was

$$y = h \exp \left[\frac{-(c - c_0)^2}{2\sigma^2 - a(c - c_0)} \right]$$

where h is the height of the peak, c_0 is the position (channel) of the peak, σ is the 'standard deviation' and a is a skewness parameter. Fitting was done using the program MINUIT [Jan 75] with h , c_0 , a and σ used as fitting parameters. This curve gave a good approximation to the peak shape of the channelled spectrum and slightly better fits were obtained for the random and incident beam spectra (with a small skewness parameter) than with a pure Gaussian. Care must be taken to restrict the fit to regions such that $2\sigma^2 > a(c - c_0)$; outside these regions, the curve increases to infinity. In this respect the curve is not a well-defined representation of the peak. It is, however, suitable for fitting purposes. The straggling in the case of the random beam, and the beam resolution for the incident beam spectra could be obtained from the fitted standard deviations, the skewness in these cases being sufficiently small to have a negligible effect on these quantities. For the channelled spectrum, the leading edge energy value was obtained by drawing the tangent to the curve on a suitable plot.

Random stopping powers were determined from the measured energy loss $\Delta E = E_B - E_R$, where E_B is the incident beam energy and E_R the random beam energy, by

$$-\frac{dE}{dx} \Big|_{E = \bar{E}} = \frac{\Delta E}{\Delta x}$$

where $\bar{E} = \frac{1}{2}(E_B + E_R)$ is the average energy of the ion in the target, and Δx the pathlength of the beam in the target. This is, of course, an approximation which is true in the limit ΔE and $\Delta x \rightarrow 0$; however, numerical calculations for a worst case ($\Delta E/E_B = 0.3$) show that the error introduced by this approximation is in all cases less than 0.2 %.

For the channelled ions, the ratio, m , of the channelled ion stopping power to the random, was determined from

$$m(E) = \frac{E_B - E_C}{E_B - E_R} = \frac{\Delta E_C}{\Delta E_R}$$

where E_C is the channelled ion energy, either peak or leading edge value. The use of this ratio allows comparison to be made with theory, independently of the actual value of the random energy loss predicted by the theory, which might vary somewhat from the experimental value.

The straggling in the random beam was obtained from the measured standard deviation σ_R of the random peak. This contains contributions from experimental resolution (including incident beam width) and from variations in the target thickness. The former contribution can be obtained from the standard deviation of the incident beam, σ_B . The latter contribution was obtained from the estimated 3 % standard deviation in target thickness as $\sigma_T = 0.03\Delta E$, where ΔE is the measured random energy

loss. The correction introduced by this term was small only for proton beams, and the straggling was thus determined only for protons. The random straggle, σ^2 , is then given by

$$\sigma^2 = \sigma_R^2 - \sigma_B^2 - \sigma_I^2$$

8.3 THEORY

8.3.1 Random Stopping

The random stopping power was calculated from the theories of Dettmann [Det 73] and Esbensen and Golovchenko [Es 78]. These are equivalent to the usual Bethe-Bloch result, equation (2.4.6):

$$-\frac{dE}{dx} = \frac{4\pi Z^2 e^4}{\gamma_0 v^2} \cdot N Z_1 \cdot \ln \frac{2m_0 v^2}{I} \quad (8.3.1)$$

The quantity I is given in the theory of Dettmann by equation (2.4.22) and the theory of Esbensen and Golovchenko is given by equation (2.4.16), the latter being the usual local density approximation result [Lin 54]. Values of the matrix elements for equation (2.4.22) were obtained from the Hartree-Fock (single zeta) wave functions of Clementi and Roetti [Cle 74]. The same wave functions were used to obtain the electron densities for equation (2.4.16). For the valence electron term in Dettmann's theory, the stopping power for an electron gas with an energy gap, equation (2.4.12) was used. This is a slight modification of Dettmann's theory which uses a free electron gas model (equation 2.4.10) - the difference is small but

the gap model is more appropriate. A value for the energy gap of 13.6 eV was used [Br 70]. The values of the mean ionization potential $nb^* \sin \theta$ are

$$\text{(Dettmann)} I_c = 79.4 \text{ eV}$$

$$\text{(Esbensen and Golovchenko)} I_{EG} = 74.4 \text{ eV.}$$

The value from the theory of Esbensen and Golovchenko is a free atom value, approximately applicable to all carbon allotropes, while that of Dettmann is specific to diamond, because of the valence term. Thus, Dettmann's theory allows different values to be calculated for different allotropes of carbon. Allotropic differences for carbon have been observed in experiments [Sof 61, Mat 76].

A consequence of equation (8.3.1) is that the stopping power depends on the ion only through its velocity (strictly, speed) and its atomic number, Z_1 . Thus, for all ions, $-\frac{1}{Z_1^2} \frac{dE}{dx}$ should be a function only of v^2 , or equivalently of E/A_1 where A_1 is the atomic mass of the ion.

8.3.2 Straggling of the Random Beam

The energy loss of an ion due to electronic excitation of an atom is a statistical process, and thus statistical fluctuations in the energy loss along a given path lead to a broadening of the energy distribution of a beam of ions transmitted through a target. This is known as straggling.

For targets that are not too thin (that is, for energy losses in the target $\Delta E \gg I$), the energy distribution of the beam is Gaussian

to a good approximation, and the variance, σ^2 , of the distribution has been calculated by Bohr [Boh 48]

$$\sigma^2 = 4\pi Z_1^2 e^4 N Z_2 t \quad (8.3.2)$$

with t the target thickness.

For large energy losses in the target, the variance and higher moments of the energy loss distribution have been calculated by Tschalär [Ts 68] and are given in graphical form in [Ts 68].

8.3.3 Energy Loss of Channelled Ions

The energy loss of channelled ions was calculated for the three axes $\langle 110 \rangle$, $\langle 111 \rangle$ and $\langle 100 \rangle$ using the theories of Dettmann and of Esbensen and Golovchenko. Calculations were performed for the position of the potential minimum, that is, for least energy loss. For the theory of Dettmann, calculations were performed using the core term, equation (2.4.24) and the valence term given by the electron gas with a gap, equation (2.4.12). The stopping power was also calculated using the Dettmann core values, with the valence stopping given by the expression (2.4.33) for the stopping in a spatially periodic electron gas, which gives channel dependent stopping powers and which reduces to the electron gas with a gap for random stopping. This is referred to below as the modified Dettmann theory. For this valence calculation, the valence electron X-ray scattering factors are required. These were obtained by subtracting the core scattering factors calculated by Keating and Vineyard [Keu 66] from the experimental X-ray scattering factors, measured by Gütlicher and Nüfel [Gor 59]. The values of the scattering factors

obtained are given in Table 8.1 as a function of the reciprocal lattice vector Q . Scattering factors for other, non-equivalent Q vectors are negligible. X-ray scattering factors are also required in the evaluation of the theory of Esbensen and Golovchenko. The experimental values [Gor 59] were used and were supplemented (for Q not given in [Gor 59] and for higher order Q) by values calculated by Doyle and Turner [Do 68]. The electron density required for the evaluation of equation (2.4.28) was obtained from Clementi wave functions [Cle 74], as for the random case. This is perhaps slightly inconsistent with the use of experimental X-ray structure factors, but the results (for the ratio of channelled to random stopping) are not very sensitive to the electron density and closely similar values were obtained by using the electron density calculated from the Lenz-Jensen atomic model [Je 52], as used by Esbensen and Golovchenko. Convergence of the series in equation (2.4.25) is not fast, because of the large spread of the highly localised core electrons in reciprocal space, and ~150 different Q vectors were required for adequate convergence.

The channelled stopping powers obtained were normalised to the relevant random stopping powers to obtain the ratio m of channelled to random stopping at the position of minimum channelled stopping power.

Calculations were also carried out for the planes (110) and (111) using the modified Dettmann theory. These planes are the major planes of the planes intersecting at axes $\langle 110 \rangle$ (that is, (111)), $\langle 111 \rangle$ and $\langle 100 \rangle$ (that is (110)). The (111) planes have two interplanar spacings:

Table 8.1

VALENCE ELECTRON SCATTERING AND STRUCTURE
FACTORS FOR DIAMOND

G	Scattering factor $F_V(G)$	Structure factor $ F_V(G) $
111	1.400	7.92
220	0.174	1.39
113	- 0.065	0.37
222	0.15	1.2
004	- 0.142	1.14
331	0.021	0.12
224	- 0.026	0.21
440	- 0.054	0.43
335	- 0.003	0.02

NOTE: $F_V(G) = f_V(G) \sum_{k=1}^8 e^{iG \cdot \mathbf{r}_k}$

where \mathbf{r}_k is the position of the k'th atom in the unit cell.

$$\frac{a}{\sqrt{3}} \quad \text{and} \quad \frac{\sqrt{3} a}{4}$$

where a is the lattice parameter. Calculations were performed for the wider spacing. The stopping power ratio was calculated for a position midway between planes to determine the minimum planar energy loss. The valence contribution was calculated from equation (2.4.33) using only the vectors \mathbf{G} perpendicular to the plane (that is, of type $\pm n(hkl)$ for $\{hkl\}$), the others vanishing upon averaging over the plane. The core contribution was calculated by averaging the core contribution (2.4.24) over a strip along the plane perpendicular to the ion path to obtain the energy loss per plane as a function of distance, b :

$$-\frac{dE}{dx} \Big|_{\text{core, plane}} = N_d p \frac{8Z_1^2 e^4}{m_e v^2} \cdot \frac{1}{b_j} \int_0^{\infty} [K_0^2(\sqrt{a^2 + y^2}) + K_1^2(\sqrt{a^2 + y^2})] dy ,$$

$$(a = \frac{b}{b_j}) .$$

8.4 RESULTS AND DISCUSSION

8.4.1 Random Stopping

Values of the random stopping power are given in Table 8.2 and are plotted in Figure 8.3 for all ions, in units of $-\frac{1}{z_1^2} \frac{dE}{dx}$ versus E/A . The major source of error is the uncertainty in target thickness, amounting to 3 %, the second largest errors are in the peak position as obtained from the fit to the measured peaks, amounting to 2 % in $\frac{dE}{dx}$ for the thick target and 4 % for the thin target. The observed scatter in the data for the different crystals is consistent with these errors. It is clear that agreement amongst the data for different ions is good, indicating that an effective charge of the incident ion [Ans 77] does not need to be considered at the velocities considered here. Also shown are the curves obtained from the theories outlined in Section 8.3, and the values of proton stopping in carbon given in a recent compilation by Andersen and Ziegler [Ans 77]. Agreement amongst the various theories is quite good and the results are in agreement with these, and with the recommended values of Andersen and Ziegler, within the experimental uncertainties. The errors are such, unfortunately, that differences due to allotropic effects cannot be investigated.

8.4.2 Straggling

The straggling in the random proton beam is shown in Figure 8.4, plotted as Ω/\sqrt{t} against the relative energy loss, $\Delta E/E_B$, in the target. Also shown is the Bohr value given by Equation (8.3.1). The agreement is good for low energy loss, but the experimental values become increasingly larger for larger relative energy losses. The predictions of the Tschalmr theory, also shown in Figure 8.4, are in general agreement with this trend, but underestimate both the magnitude of the straggling

Author Fearick R W

Name of thesis Studies of Ion channelling and dechannelling in diamond 1980

PUBLISHER:

University of the Witwatersrand, Johannesburg

©2013

LEGAL NOTICES:

Copyright Notice: All materials on the University of the Witwatersrand, Johannesburg Library website are protected by South African copyright law and may not be distributed, transmitted, displayed, or otherwise published in any format, without the prior written permission of the copyright owner.

Disclaimer and Terms of Use: Provided that you maintain all copyright and other notices contained therein, you may download material (one machine readable copy and one print copy per page) for your personal and/or educational non-commercial use only.

The University of the Witwatersrand, Johannesburg, is not responsible for any errors or omissions and excludes any and all liability for any errors in or omissions from the information on the Library website.